Experimental study on wave bending moments of a zero-speed rigid containership model in regular, irregular, and equivalent design waves

Shinwoong Kim

MEMOIRE DE DOCTORAT DE

L'ECOLE CENTRALE DE NANTES

ECOLE DOCTORALE N° 602
Sciences de l'Ingénierie et des Systèmes
Spécialité : *Mécanique des Milieux Fluides*

Par
Shinwoong KIM

Experimental study on wave bending moments of a zero-speed rigid containership model in regular, irregular, and equivalent design waves

Projet de recherche doctoral présenté et soutenu à l'Ecole Centrale de Nantes le 12 janvier 2023
Unité de recherche : UMR 6598, Laboratoire de recherche en Hydrodynamique, Énergétique et Environnement Atmosphérique (LHEEA)

Rapporteurs avant soutenance :

Spyros HIRDARIS	Associate Professor, Aalto University (Finlande)
Jun ZANG	Full Professor, University of Bath (Royaume-Uni)

Composition du Jury :

Président :	Laurent DAVID	Professeur des universités, Université de Poitiers
Examinateurs :	Francisco HUERA-HUARTE	Associate Professor, Universitat Rovira i Virgili (Espagne)
	Spyros HIRDARIS	Associate Professor, Aalto University (Finlande)
	Jun ZANG	Full Professor, University of Bath (Royaume-Uni)

Directeur de recherches doctorales:	Pierre FERRANT	Professeur des universités, École Centrale de Nantes
Co-enc.de recherches doctorales :	Benjamin BOUSCASSE	Chargé de recherche, École Centrale de Nantes

Titre : Étude expérimentale sur les moments de flexion des vagues sur un modèle de porteconteneurs rigide à vitesse nulle dans des vagues régulières, irrégulières et focalisées

Mots clés : Expérimentation, Modèle rigide, Moments de flexion des vagues, HOS-NWT, FORM

Résumé : La thèse vise à étudier les mouvements et les chargements internes d'un modèle de porte-conteneur rigide formé de 9 segments dans des vagues extrêmes. L'étude est principalement expérimentale et est réalisée avec une maquette sans vitesse d'avance dans une houle de face et une houle oblique (-120 degrés). L'étude aboutit à des résultats soulignant l'importance de la prendre en compte les aspects non linéaires des vagues et des réponses structurelles correspondantes.
Dans des conditions de mer de face, trois types de vagues sont testés. Des vagues régulières sont utilisées pour s'assurer que le modèle se comporte de manière similaire à la campagne précédente effectuée avec la même maquette. Une approche de type Monte Carlo avec un certain nombre de réalisations de 2 heures 30 de vagues irrégulières est ensuite utilisée pour construire des données de référence. Enfin, des vagues equivalentes de design (EDW) sont générées pour vérifier, en particulier, la faisabilité d'une approche EDW irrégulière appelée First Order Reliability Method (FORM). Un algorithme numérique FORM couplé avec le solveur HOSNWT est développé et validé par rapport aux résultats Monte Carlo. Les caractéristiques géométriques des signaux EDW et VBM ainsi que leurs statistiques sont étudiées. L'étude vise peut-être deux quantités. Le premier est la hauteur de crête de la vague dans un scénario de vague seule, et le second est le VBM du modèle segmenté. L'utilisation du solveur de génération d'onde non linéaire HOS-NWT, permet une validation croisée avec la mesure expérimentale car les vagues générées sont comparables. Dans la condition de vagues obliques, l'étude est limitée aux vagues régulières avec différentes cambrure de vagues afin de fournir des données de référence pour les futures études. L'effet de non-linéarité des vagues sur les moments de flexion horizontaux et verticaux des vagues avec une cambrure variable est démontré.

Title : Experimental study on wave bending moments of a zero-speed rigid containership model in regular, irregular, and equivalent design waves

Keywords : Experiment, Rigid model, Wave bending moments, HOS-NWT, FORM

Abstract : The present thesis aims to study the motions and the internal loads of a 9-segmented rigid containership model in extreme waves. The study is mainly experimental and is carried out on a zero-speed model in a 180-degree head sea and a -120 degree oblique sea. The study leads to results highlighting the importance of the consideration of nonlinear wave descriptions and corresponding nonlinear structural responses.
In head sea conditions, three wave approaches are considered. Regular waves are used to ensure that the model behaves similar to the earlier campaign. A Monte Carlo approach with a number of full scale 2h30 irregular wave realizations is used to have reference data. Finally, irregular equivalent design waves (EDW) are studied to check, in particular, the feasibility of one irregular EDW approach called First Order Reliability Method. A numerical algorithm coupling with the HOS-NWT for the FORM EDW is developed and the validation compared to the Monte Carlo results is performed in terms of geometrical characteristics of the EDW and IW signals along with their statistics. The study targets mainly two quantities. The first is the wave crest in a wave-only scenario, and the second is the VBM of the segmented model. The use of the HOSNWT, a nonlinear wave generation solver, enables cross-validation with experimental measurement.
In the oblique wave condition, the study is limited to regular waves with various wave steepness with the intent to provide reference data for future benchmark studies. The wave nonlinearity effect on the horizontal and vertical wave bending moments with varying steepness is shown.

Doctoral Thesis

Experimental study on wave bending moments of a zero-speed rigid containership model in regular, irregular, and equivalent design waves

by

Shinwoong Kim

École Centrale de Nantes

Nantes, 2023

ABSTRACT

This thesis presents experimental investigations of a zero-speed rigid containership model's behavior and load response characteristics under extreme wave conditions. All experiments presented in the thesis are carried out for a 1/65 scale containership model that maintains its heading with four horizontal soft mooring lines. The thesis consists of two main subjects.

First of all, in head sea conditions, vertical bending moment (VBM) responses of the model induced by three wave approaches namely, long-time irregular waves (Monte Carlo reference), and regular and irregular equivalent design waves (EDW) are experimentally analyzed. Intuitive comparative analysis is performed between VBMs induced by each approach, and the characteristics and applicability of each approach are identified.

The first focus of this thesis is on the application of a fully nonlinear wave solver, HOS-NWT, to generate and validate nonlinear (non-)breaking sea states that consist of a number of 2h30min wave elevations with different random phase sets. The long-time (non-)breaking sea states are calculated first in a numerical wave tank (NWT), and the calculated waves are reproduced in an actual experimental wave tank (EWT). Through quantitative and qualitative comparisons of experimental and numerical wave spectrum and crest distributions to assess the wave quality, it is verified that the HOS-NWT provides sufficiently similar wave elevations as a result of physically acceptable energy dissipation mechanisms for wave-breaking phenomena.

A new irregular EDW calculation procedure based on First Order Reliability Method (FORM) that makes use of the HOS-NWT model is developed to find the most probable point and consider the nonlinear irregular EDWs. The nonlinear irregular EDW can be calculated through the developed algorithm that takes advantage of the interesting features of existing numerical calculation methods. The application of the HOS-NWT in the EDW calculation procedure solves the inaccuracy issue of the existing EDW methods, which describe waves with a linear model when applying the computed EDW to the experiments. It contributes to drastically reducing the experimental wave calibration process. The developed EDW calculation procedure is first tested for the wave crest-targeted EDW considering wave parameters only, followed by experiments for the VBM-inducing EDW calculated by considering a linear VBM RAO combined with the HOS-NWT wave elevation.

Validation of the FORM-based nonlinear EDW is carried out by comparing it to the long-time irregular wave results (Monte Carlo reference results). Both the geometrical similarity of EDW and VBM time signals and their statistics are reviewed. Compared to the Monte Carlo reference results, it tends to show lower VBM responses. However, the overall trend shows qualitatively good agreement, confirming that the developed nonlinear EDW calculation procedure is well-formulated.

Through a correlation analysis between the given wave parameters and the measured VBM by the FORM-based EDW, an empirical formula estimating nonlinear VBM is derived from the linear VBM estimate.

For the second subject of this thesis, limited to regular design waves, the nonlinear response characteristics of the model's 6-DOF motions and horizontal (HBM) and vertical (VBM) bending moments are identified with various wave steepness ranging from $H/\lambda =$ 0.01 to 0.105 in a -120 degree oblique wave condition.

The focus was on the analysis of time signals and RAO of responses at the HBM peak period. The changing trend of the nonlinear response with increasing wave steepness is identified. It is confirmed that the steeper wave contributes to the increase in the higher-order harmonic components including slamming events in the bending moments measured. The change in the HBM and VBM response characteristics according to the change in wave steepness is found to be very different from the linear response.

A detailed discussion is made on the influence of the mooring system on the asymmetric HBM and the change in the average yaw motion. Experiments with and without a mooring system under the same wave condition are conducted, and the effect of the mooring system is identified. It is qualitatively confirmed that the mooring system's restoring moment correlates with the asymmetric HBM and average yaw movement change.

ACKNOWLEDGEMENTS

The Ph.D. program in which I participated was carried out under the supervision of Professor Pierre FERRANT, Professor Guillaume DUCROZET, and Doctor Benjamin BOUSCASSE. This work was performed as part of the Bureau Veritas (BV) - Ecole Centrale Nantes (ECN) Research Chair. The financial and technical support from BV-ECN chair is gratefully acknowledged.

First of all, I would like to thank my supervisor Prof. Pierre FERRANT, co-directors Prof. Guillaume DUCROZET, and Dr. Benjamin BOUSCASSE for their deep and sharp insight into the issues I faced during my Ph.D. They helped me a lot in understanding the knowledge related to my research, and it became the foundation for my further growth.

I would also like to express my deepest gratitude to Jeremy OHANA, Felicien BONNEFOY, Arnaud MERRIEN, Stephane LAMBERT, and Anne LEVESQUE for their assistance and advice, who spent a lot of time together preparing and conducting the experiments.

Maxime CANARD and Sylvain DELACROIX's tremendous dedication and professionalism for the successful completion of several experiments have to be recognized. The experience we faced and solved many unexpected problems together in the wave tank over the months will be a memorable one.

Guillaume DE HAUTECLOCQUE and Charaf Ouled-HOUSSEINE of BV deserve thanks for conceptualizing the research and sharing the numerical code of the equivalent design wave. Their interest in experimental research has been very helpful in producing good-quality results, including 3(1) journal(conference) papers.

I would also like to thank Seung-Yoon HAN, Gaspard ENGEL, and Ruddy KURNIA for their time in discussions about my research. I have always been thankful for their sincere efforts in helping me with never-ending discussions. CROUS's 3 euro lunch with you was always enjoyable, and I will not forget about the days of having beers after work.

Lastly, I would like to express my sincere gratitude to my wife, Jin-ah KIM, and my family in South Korea. Their warm support and encouraging words have been the motivation that kept me going.

TABLE OF CONTENTS

LIST OF FIGURES

LIST OF TABLES

NOMENCLATURE

Latin symbols

$\overline{GM_L}$	Longitudinal metacentric height
$\overline{GM_T}$	Transverse metacentric height
a	Added mass coefficient
b	Damping coefficient
F	Force
K	Restoring coefficient
M	Moment
Q	Shear force
x	Position vector
$\{b\}$	Body-fixed frame
$\{n\}$	Inertial reference frame
$\{s\}$	Seakeeping frame
A_{wp}	Water plane area
c_g	Wave group velocity
C_x	Crest velocity
C_{corr}	correction factor
H_s	Significant wave height
L_{pp}	Length between perpendiculars
R_b	Radius around the oscillating body
R_c	Bernoulli constant
T_p	Peak period
U_x	Fluid particle velocity at crest

X	Response
X_{wm}	Wavemaker motion
A	Wave amplitude
B	Stream function amplitude
c	Wave phase velocity
g	Gravitational acceleration
H	Wave height
h	Water depth
k	Wave number
N	Total number of modes
S	Spectral density
T	Wave period
u	Fluid velocity in x direction
V	Volume of displacement
v	Fluid velocity in y direction
w	Fluid velocity in z direction

Greek symbols

β	Wave heading angle
β_{FORM}	Reliability index
η	Wave elevation
λ	Wave length
ν	Mean out-crossing rate
ν_{eddy}	Eddy viscosity
ϕ	Velocity potential
ψ	Stream function vector
ρ	Water density
ξ	Perturbation of a ship

Abbreviations

CDF Cumulative density function

COG Center of gravity

CRRW Conditional random response wave

DOF Degree-of-freedom

EDW Equivalent design wave

EWT Experimental wave tank

FORM First order reliability method

HBM Horizontal bending moment

HL Hasofer and Lind

HOS-NWT Higher order spectral-Numerical wave tank

MHLGA Modified Hasofer and Lind with Goldstein-Armijo

MLER Most likely extreme response

MLRW Most likely response wave

MLW Most likely wave

POE Probability of exceedance

RAO Response amplitude operator

RCW Response conditioned wave

VBM Vertical bending moment

VSF Vertical shear force

Chapter 1

Introduction

1.1 Background

About 90 % of world trade is carried out by maritime transport. Under the influence of the economies of scale and the demands for increased fuel efficiency, shipping companies operate larger vessels, and are required to comply with ever-stringent environmental regulations. This trend is expected to continue [2, 85].

Figure 1.1 – A container ship sailing in rough waves. (C) Hapag-Lloyd

However, its side effects that lead to an increase in safety accidents can be a major issue. Operation in extreme environments and the increase in ship size may be directly related to the increase in safety accidents and the amount of potential loss. This ultimately affects environmental pollution. For example, container ships account for 40 % of the total ship loss over the past 10 years (350/900) among vessels over 100 gross tonnages (GT). An average annual container loss is around 1500 and the loss peaked in 2020 with more than 3000 containers [2]. In order to improve safety accident records, the nonlinear behavior and loads of large vessels under various operational conditions should be estimated with high accuracy. Consequently, improved rules and regulations for the classification of ships should account for these effects with the ultimate aim to improve ship design for safety.

The estimation of ship wave load in extreme conditions is a key indicator for ship safety and efficiency. In practice, ship design is based on safety requirements-related rules presented by class societies and the IMO (International Maritime Organization). The rules account for various loading (e.g. cargo and wave loading) and operational conditions (e.g. vessel speed, heading, wave height, and general hydro-meteorological conditions). Wave loads under extreme operational and sea conditions may be prone to strong nonlinearities.

Numerical investigations based on nonlinear potential flow solutions have been broadly applied to ship hydrodynamics. Reynolds Averaged Navier Stokes (RANS) based Computational Fluid Dynamics (CFD) solvers have been developed and broadly validated. However, their application is limited to short simulation cases due to the high demand for computational resources.

For motions and loads induced by large and steep waves, non-linear effects related to large motions, the continuously changing ship's wetted surface and incoming waves, and the interaction between the ship and waves must be properly accounted for.

In addition, depending on application cases, accuracy issues are often involved in estimating the results with various theories. Nevertheless, from a practical point of view, a linear or weakly nonlinear time-domain numerical analysis may be widely used as they provide reasonable estimates at a more reasonable computational efficiency. Yet, for the accurate estimation and further development of the numerical codes, high quality model tests are still required and considered essential.

From a structural point of view, the shear force and bending moments amidships can be said to be the most important loads to be considered in the design of ships and ship-like floating offshore installations. In head sea conditions, the vertical loads of a ship are taken into account as the most important factor, and as the wave heading condition changes from head to beam seas, horizontal shear forces and bending moments overtake the largest proportion of the response.

The wave-induced loads include hydrostatic and hydrodynamic components. The hydrodynamic loads include not only the wave frequency loads but also the high-frequency loads such as slamming, whipping, and springing. The nonlinear responses induced by the complex mechanism of the wave-structure interaction in severe wave conditions justify the need to develop reliable time domain analysis methods and tools. Those should be satisfied by well-established model tests.

Time domain analysis is usually run in irregular sea states. Following the assumption that a given sea state follows a stationary process, a spectral density $S(f)$ of the sea state can be defined by specific parameters that characterize the wave conditions. Key variables considered in design models are the significant wave height H_s and the

peak period T_p. The extreme events associated with the wave spectrum specified with those parameters depend on the duration of the measurement. A typical choice is a 3-hour duration. Given that the average ship life span is around 25 years, the analysis through only one wave spectrum is referred to as a short-term analysis [95].

As shown in Table 1.1, a wave scatter diagram provides a number of 3-hour short-term sea states characterized by the significant wave height H_s and zero up crossing period T_z with a corresponding occurrence probability. The wave scatter diagram includes information on possible sea conditions that occur in a specific region.

Table 1.1 – Wave scatter diagram of the North Sea [19]

$H_s(m)$ \ $T_z(s)$	**5**	**6**	**7**	**8**	**9**	**10**	**11**	**12**	**13**	**14**	**15**
1	73	1416	4594	4937	2590	839	195	36	6	1	0
2	5	356	3299	8001	8022	4393	1571	414	87	16	3
3	0	62	1084	4428	6920	5566	2791	993	274	63	12
4	0	12	318	1898	4126	4440	2889	1301	445	124	30
5	0	2	89	721	2039	2772	2225	1212	494	162	45
6	0	1	25	254	896	1482	1418	907	428	160	50
7	0	0	7	85	363	710	791	580	311	131	46
8	0	0	2	27	138	312	398	330	197	92	35
9	0	0	1	8	50	128	184	171	113	58	24
10	0	0	0	3	17	50	80	82	59	33	15
11	0	0	0	1	6	18	33	37	29	17	8
12	0	0	0	0	2	7	13	15	13	8	4
13	0	0	0	0	1	2	5	6	6	4	2
14	0	0	0	0	0	1	2	2	2	2	1
15	0	0	0	0	0	0	1	1	1	1	0

During long-term analysis, the analysis accounts for vessel response in all sea conditions that a vessel may encounter throughout her lifetime. This is reasonable from a fatigue analysis point of view, but, it is inefficient in terms of determining the most probable extreme loads for use in ship design.

To determine the most severe sea state among various possible sea states available in a wave scatter diagram, the directional probability (P_d) of each sea state should be identified. In addition, taking the lifetime operating condition of a containership as an example, the ship experiences various load conditions containing full load and ballast, and the percentage of each load condition in the total operational period of a ship (P_l) should be correctly defined.

The internal loads such as wave bending moments and shear forces can be referred to as an index identifying the dominant load condition. For each load condition, the wave-induced load $RAO(f|\beta)$ at a specified position (mostly at the COG of a ship) is estimated. Usually, it is recommended to calculate the $RAO(f|\beta)$ with 15 degrees

intervals in wave heading β. With the scatter diagram given, the response spectrum $S_R(f)$ in the sea state (i, j) corresponding to the i^{th} significant wave height H_{s_i} and the j^{th} wave period T_{p_j} in the scatter diagram is calculated as follows:

$$S_R(f|H_{s_i}, T_{p_j}, \beta) = |RAO(f|\beta)|^2 S(f|H_{s_i}, T_{p_j}) \tag{1.1}$$

Considering that the short-term response follows the Rayleigh distribution (narrow-banded), the probability of exceedance (POE) of a response amplitude X exceeding a particular value X_C is given by the following equation:

$$POE_{ij}(X > X_C) = exp\left(-\frac{X_C^2}{2m_{0_{Rij}}}\right) \tag{1.2}$$

where

$$m_{0_{Rij}} = \int_0^\infty S_R(f|H_{s_i}, T_{p_j}, \beta)df \tag{1.3}$$

Then, the probability exceeding the specified response X_C in the long-term analysis can be as follows [55]:

$$\{POE(X > X_C)\}_L = \sum_{ij}\sum_{d}\sum_{l} P_{ij}P_dP_l\{POE_{ij}(X > X_C)\} \tag{1.4}$$

where P_{ij} denotes the occurrence probability of a sea state $S(f|H_{s_i}, T_{p_j})$. As a result, the contribution of each sea state for the response X_C can be expressed as a ratio of probability of each short-term sea state to the long-term probability in Eq. (1.4). Finally, the sea state most contributing to the generation of the response X_C is selected and used for the short-term analysis. For the ship design, usually, classification rules or IACS requirements estimate 20 - 25 years as a minimum wave return period, thus the corresponding wave scatter diagram has to be properly identified.

$$\text{Contribution} = \frac{\sum_d \sum_l P_{ij}P_dP_l\{POE_{ij}(X > X_C)\}}{\{POE(X > X_C)\}_L} \tag{1.5}$$

1.2 Wave loads analysis with various design approaches

Numerical analysis of wave-structure interactions applying not only practical codes based on potential flow theory but high-fidelity CFD simulations based on Reynolds-averaged Navier–Stokes (RANS) equations has been widely performed along with experimental tests over the past years [88, 40].

Various attempts have been made to determine the influence of related factors on

wave-induced loads, such as the vessel's flexibility-induced springing and whipping, vessel speed, geometry, sloshing, and green water on deck with the design approaches mentioned above. The experiment itself has been studied as one of the methods and has served as a reference to compare and validate the numerical results [31, 58, 21, 75, 70, 56, 84].

Table 1.2 summarizes the main research studies showing their objectives and methods applied. Each study applied a different wave type for the analysis of mostly VBM, heave, and pitch motion. Those research have been referenced in this thesis as key papers for each wave type introduced. Details are covered in the following sections.

Table 1.2 – Summary of key research papers referenced in this thesis

Research carried out by	Objectives	model rigidity	wave type considered
Kim and Kim (2016) [53]	Review of 17 numeric code results based on experimental results (VBM, heave, pitch)	Flexible	Regular EDW
Vásquez et al. (2016) [91]	Hull geometry influence on VBM in extreme wave conditions.	Rigid	Irregular wave
Dietz (2005) [19]	Application of new EDW method (MLRW) and (CRRW) to VBM analysis.	Rigid and flexible	Response conditioned wave (irregular EDW)
Bennett et al. (2012) [4]	Wave nonlinearity effect on rogue waves. Comparison of 3 EDW methods for heave and pitch:	Rigid	Wave parameter-conditioned wave (irregular EDW)

1.2.1 Monte Carlo approach to short-term sea state

Once the most contributing sea state $S(f)$ is determined, the corresponding 3-hour response signal can be calculated with a response RAO of interest. The response amplitude of each frequency component is evaluated as follows:

$$A_R(f) = \sqrt{2S_R(f)df} \tag{1.6}$$

Applying the linear superposition over the frequency range considered, response time series can be obtained:

$$X(x,t) = \sum_{i=0}^{N-1} A_R(f_i)\cos(2\pi f_i t - k_i x + \epsilon_i + \psi_i) \tag{1.7}$$

where ϵ and ψ are the phase angles of wave and RAO respectively. In this study, ϵ_i for each wave component is randomly chosen between 0 and 2π, and ψ_i is determined by calculation through a potential flow solver, Hydrostar [93]. It is noted that $X(x,t)$ represents a typical 3-hour response time series in the selected sea state.

Various studies have been conducted to identify the wave loads in short-term irregular wave conditions in relation to the aforementioned design parameters. Chen et al.

(2019) [14] focused on comparing and analyzing the experimental vertical bending moment (VBM) and horizontal bending moment (HBM) of a high-speed flexible vessel for different wave headings with numerical results. In the case of a research by Zhu et al. (2011) [102], the response spectrum of wave bending moments and the corresponding POE distribution were analyzed with respect to ship speed and wave headings. Vásquez et al. (2016) [91] observed full scale 3-hour VBM response in a mild and a severe sea state to check the effects of vessel geometry. An attempt was made to determine the response characteristics of hogging and sagging by directly comparing the VBM POE distribution of two types of vessels. The measurement data of these studies correspond to the maximum 3 hours or less in full scale for the given sea state, and the response characteristics of wave loads according to the variables mentioned, and their contribution were emphasized.

In the 3-hour short-term irregular wave elevation, approximately 1000 peak events in a first-order hydrodynamic response of a ship may occur, and the probability of exceedance (POE) distribution reaching 10^{-3} levels can be obtained. However, the closer to the tail of the POE curve, the fewer events occurred, and the convergence reliability of the curve gradually decreases accordingly.

For the design purpose, it is thus necessary to determine the representative response at each POE level with a sufficient number of runs (realizations) of simulations or measurements having different wave phase sets. Figure 1.2 shows the short-term VBM POE curves of N 3-hour simulation results with N different wave phase sets as an example, showing the spatial distribution at each POE level. The result shows that the reproducibility of the short-term VBM response is extremely variable depending on the change of the wave phase set.

As mentioned, the lower the response exceedance probability, the greater the variance in the POE value between each realization. This becomes even more evident in very harsh sea conditions with strong nonlinear effects. To put it in another way, with randomly selected wave phase sets, a variability of the short-term sea state and the corresponding structural responses can be observed.

According to Korean Register (2017) [55], assuming that N responses at each POE level follow the normal distribution (red curve at a particular POE level in Figure 1.2), the representative value for each POE level can be estimated as follows:

$$X_{C_{cor}} = \mu + 3\sigma \tag{1.8}$$

where μ is the mean of the normal distribution of N responses at the same POE level and σ is its standard deviation.

The variability in wave and response in a given short-term sea state leads us to con-

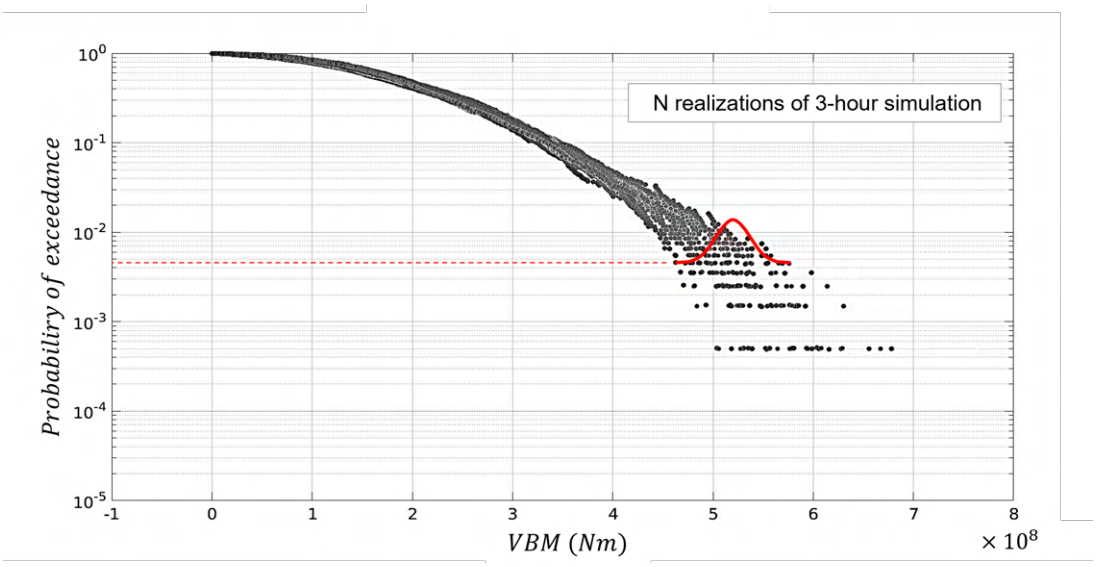

Figure 1.2 – Exceedance probability distributions of 3-hour realizations and its variability

sider the Monte Carlo approach to the 3-hour irregular waves having various random phase sets. The main purpose of this approach is to obtain statistically converged inputs (wave) and outputs (response) by considering various scenarios of a given short-term sea state. With a sufficiently large number of realizations, the Monte Carlo approach enables the estimation of the most likely extreme structural response in a given duration for a given sea state. According to Korean Register's guidance note [55], at least 30 realizations of 3-hour full scale wave simulations (or measurements) with different sets of random wave phase sets need to be carried out to determine the reliable design load where the exceedance probability is close to 10^{-3}. A detailed description can be found in [94, 55].

From a practical point of view, the main problem with this approach is that it is computationally costly. Specifically, in determining the design load, only few events located at the tail part of exceedance probability (POE) are of interest among the huge amount of data obtained through long-time calculations, and in fact, most of the remaining data are of less interest in ship design.

1.2.2 Deterministic approach

As an alternative to the Monte Carlo approach, a deterministic approach has been introduced for the design of marine and offshore structures. A key aspect of applying the approach is to reduce computational costs. The deterministic design approach corresponds to a method to generate a desired extreme response estimate at a certain

level of exceedance probability with a short wave sequence calculated by taking into account the characteristics of a given wave condition (and the response of interest). The deterministic approach includes an equivalent design wave (EDW) method, and it is divided into a regular and an irregular EDW [92]. The definition and application of the regular EDW, which has been introduced in the IACS Common Structural Rules (CSR) [45], as well as irregular EDW are introduced.

Regular EDW

The regular EDW approach is a commonly accepted method for the calculation of design loads as implemented in the IACS CSR [45]. It is a classic method of observing responses by generating a sinusoidal wave with a known specific wave height and period. This regular EDW is commonly referred to as a regular design wave.

In general practice in the industry, wave parameters to be defined for the regular EDW are estimated by considering a linear Response Amplitude Operator (RAO). Thus, the corresponding statistical estimate (e.g. short- or long-term extreme response) can be determined by spectral analysis [92]. Once the linear RAO of a physical quantity of interest for each wave heading (β) is calculated, and among them, the wave frequency (f_{EDW}) corresponding to the maximum response of the RAOs is sought (see Figure 1.3). The amplitude of the regular EDW is determined by the ratio of the target response X_C and the linear RAO as follows:

$$A(f_{EDW}) = \frac{X_C}{|RAO(f_{EDW}|\beta)|} \tag{1.9}$$

This study followed the above regular EDW (regular design wave) calculation procedure presented in the IACS CSR [45]. If the regular EDW is applied to a linear system, the EDW is supposed to induce a response equal to the target value at a specific POE level. In the case of a regular EDW applied to a nonlinear system as in an actual experiment with a model, a nonlinear response is expected to be induced, and the relationship with the linear response can be analyzed.

Kim and Kim (2016) [53] performed a comprehensive review of benchmark regular wave test results on a 6750-TEU containership. The emphasis was on the investigation of the competence of various seakeeping analysis codes based on the most widely applied methods such as 2D strip, wave Green's function or Rankine source-based 3D BEM (Boundary Element Method) and RANSE.

The experimental investigation on the same flexible target ship was conducted to use its results as a reference. 17 commercial or in-house codes were applied. Regular wave conditions in head sea conditions were considered, where the effect of wave-

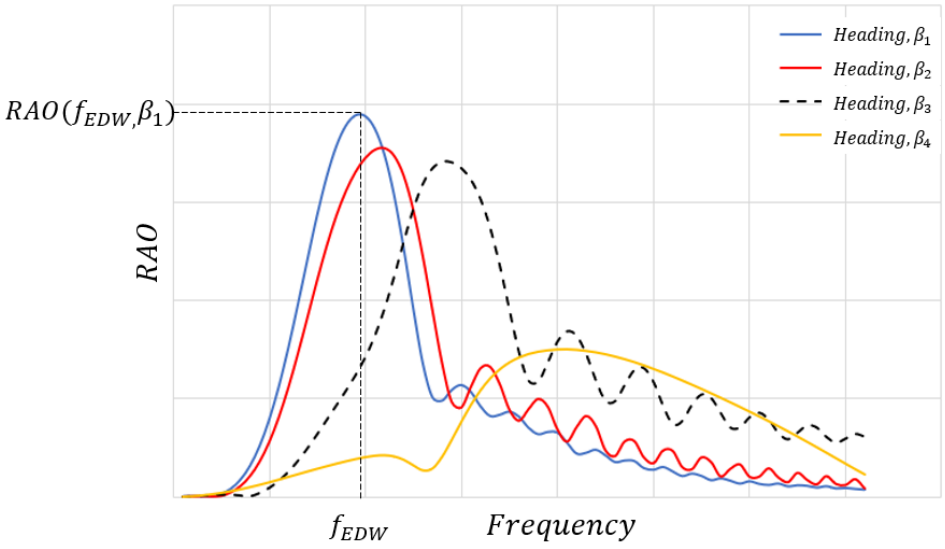

Figure 1.3 – Definition of regular EDW with consideration of linear RAOs for various wave heading conditions

induced vibration (whipping and springing) and forward speed on the motions, in particular heave and pitch, and vertical bending moment can be quantitatively compared between the codes.

The estimation of linear RAO under a zero-speed condition with test cases of $H/\lambda < 0.01$ was first carried out. For reference, in this paper, the wave steepness H/λ has been expressed in percentage units ($H/\lambda \times 100$) for convenience of expression. The average response RAO of the numerical codes was found to be mostly in good agreement with the experimental results, but a fairly significant variance was observed between the numerical codes in the VBM results even for the linear conditions. In addition, it is noteworthy that in the experimental RAO curve, some points tended to deviate from the curve, which was different from the numerical results.

When the wave steepness increased from $H/\lambda = 2$ % to 3.5 % or more under the same regular wave condition, the wave-induced hull vibration was generated and affected the increase of discrepancy between experiments and numerical calculations. As a result of considering the two different speeds in the same wave steepness condition, the same increasing trend in discrepancy as well in motion time signals was observed at a faster forward speed. The author stated that the scattered results of the numerical codes, including i) the deviation of numerical results for each position in the longitudinal direction of the model and ii) large discrepancy in the test case of the higher wave frequency may be attributed to the numerical errors related to large waves or ship speed and the limitation of the theory applied to the codes. The 3D BEM code applying the Rankine source showed relatively stable results. However, the tendency

to have a large error as compared to the average of numerical results was not strictly limited to a specific code. It varied on a case by case basis.

Irregular EDW

The irregular EDW is a method intended to generate the most probable irregular wave scenario among waves having a specific magnitude. The EDW approach was introduced for the purpose of computational efficiency. It calculates a specific wave event intuitively, thus it has advantages over the Monte Carlo approach which needs to generate long-time irregular waves, but at the same time has limitations. In detail, the profile of the irregular EDW consists of only one short wave packet with a bell-shaped envelope centered on the target wave event. Therefore, the memory effect of the vessel's response induced by the previous waves can be reflected less conservatively compared to the typical irregular wave results.

Several analytical and numerical models for the irregular EDW have been introduced. However, the general idea behind each model and the parameters considered in the calculation process are quite similar.

Wave parameter conditioned EDW The NewWave theory, introduced by Tromans et al. (1991) [90], computes the most probable extreme wave profile by application of the Slepian theory (refer to Lindgren (1984) [62] for more details). Given the result obtained by Lindgren (1970) [63] that the dominance of the most probable surface elevation is closely related to the increase in crest, the NewWave elevation at a target location x_0 and at a target time t_0 is formulated with the autocorrelation function $r(x - x_0, t-t_0)$ scaled by a target crest C_{target} with Eq. (1.10). Autocorrelation is the correlation of a signal with the same signal to which a variable delay is applied, measuring a repeating pattern between them.

$$\begin{aligned}\eta_{New}(x - x_0, t - t_0) &= C_{target} r(x - x_0, t - t_0) \\ &= C_{target} \frac{\sum_{i=1}^{N} S(f_i) \cos(2\pi f_i (t - t_0) - k_i (x - x_0)) df}{\sigma^2}\end{aligned} \tag{1.10}$$

$$\sigma^2 = \sum_{i=1}^{N} S(f_i) df \tag{1.11}$$

where σ^2 is the variance of the free surface elevation of a given sea state, $S(f)$ is the power spectral density, f_i and k_i are the wave frequency and wave number of the i^{th} wave component and df is the frequency increment. With the formulation above, the

target crest C_{target} is generated at a given time t_0 and at a target location x_0. The corresponding wave amplitude A_i for each wave component can be calculated as described below :

$$A_i = \frac{C_{target} S(f_i) df}{\sigma^2} \qquad (i = 1, ..., N) \tag{1.12}$$

It is simply calculated based on the linear superposition of N wave components of a given wave spectrum. However, the linear superposition method involves the issue of accuracy of the solution, thus it is necessary to consider a second or higher-order term for large abnormal wave cases in which the higher-order effect of the wave becomes significant [96].

Hansen and Nielsen (1995) [35] introduced the Most-Likely Wave (MLW) based on the New Wave theory but with conditioning on the random instantaneous frequency. When the instantaneous frequency is $2\pi f = m_1/m_0$ the mean wave frequency, the MLW corresponds to the NewWave profile.

The NewWave has been experimentally studied and has been widely used in various applications [97, 101, 44]. The method namely Constrained NewWave literally constrains the NewWave into regular or irregular waves. The main concept of the Constrained NewWave is embedding the NewWave profile in a random sea to have an effect of previous waves. A limitation of the concept is that as nonlinear wave-wave interaction is expected, it is not easy to generate a targeted abnormal wave.

Bennett et al. (2012) [4] carried out a numerical and experimental study on the generation of abnormal waves with the NewWave and the Constrained NewWave. For each model, numerical calculations were first performed, and the comparative analysis was done with the experimentally measured wave profile of each method. The study showed that the measured NewWave was in agreement with the solution obtained with linear or second-order wave theory. However, it was difficult to reproduce a targeted wave profile via the Constrained NewWave approach. This study also analyzed another method called ‘optimized sea’. This method creates a target abnormal wave by optimizing the random phase of wave components of a random sea, and the study pointed out the limitations of the NewWave and the Constrained NewWave.

A calibration process to deterministically reproduce a given wave sequence was introduced by Schmittner et al. (2009) [81]. The iterative correction process was applied not only for the wave amplitude but also its phase following the application of the phase corrective concept for the generation of a desired focusing wave at a target location proposed by Chaplin (1996) [12]. A method to trace back the wavemaker’s input motion based on the estimated wave spectrum data at the target location was considered. Long- and short-crested deterministic wave profiles were generated and

compared with the actual wave scenario [80]. Overall, the experimental results were in good agreement, while the authors emphasized the need for wave calibration in order to improve the wave quality embedded in a local extreme event. Clauss and Schmittner (2007) [16] applied an overall similar process for local wave sequences. In their work the wave propagation very similar to the target wave profile was generated by setting criteria for the wave height, zero down crossing period, crest, and target time. Notwithstanding this several iteration processes were required.

In the NewWave approach, a linear description of the free surface wave elevation is applied, and second or higher-order effects have to be taken into account separately for large abnormal waves. However, the actual wave profile and associated wave kinematics contain nonlinear properties, which become more pronounced as the wave conditions become more severe. Thus the methodology based on a linear theory is not considered advantageous.

Over the last few years, several formulations have been derived for a "weakly nonlinear process". In this case, the conditional focusing wave and wave kinematics have been approximated by the Gram-Charlier series [48, 65] to capture the nonlinearities [47]. Jensen (1996) [49] presented explicit second-order formulas by application of Stokes' second-order deepwater theory for the slightly non-Gaussian process, and compared the wave profile with the one derived by linear waves. In these methods, the derived wave profile is calculated by considering the stochastic properties of the wave spectrum with the second-order term. It was therefore confirmed that the wave profile is more realistic than the one based on linear wave theory.

Walker et al. (2004) [96] conducted a study on the effect of the wave's higher-order phenomena on the shape of a freak wave using the NewWave method. The NewWave method was used as a first-order contribution, and correction for the higher-order contribution of the freak wave called the New Year wave was estimated with Stokes-type corrections and exact second-order wave theory. The modified NewWave wave profile with the higher-order corrections up to fifth-order showed very good agreement with the measured New Year wave profile, whereas linear NewWave showed considerable discrepancy with the measurement. With linear or weakly nonlinear fluid models, the difficulty of reproducing a wave elevation time trace with sufficient accuracy in experiments or other nonlinear frameworks such as computational fluid dynamics (CFD) is a drawback. A solution is to use fully nonlinear methods, but from a practical point of view, compatibility of the method used to calculate the wave train for experiments or other solvers should be first confirmed.

Response conditioned EDW Since the aforementioned methods apply only wave-related properties to the EDW calculation without considering the characteristics of the structural response of interest, it is not possible to calculate the focused wave that induces a structural response corresponding to a specific probability of occurrence. With a structure having dynamic responses, an extreme wave event in a given sea state does not necessarily induce an extreme response of interest, for example, if the natural period of the response is away from the peak wave period.

In this regard, several Response Conditioned Wave (RCW) methods that literally consider the response of interest in the calculation of the irregular EDW have been introduced. The RCW was first applied to generate the most likely extreme storm wave by Tromans et al. (1991) [90]. The main concept of the RCW is based on the Most Likely Response Wave (MLRW) method suggested by Adegeest et al. (1998) [1]. By changing the wave spectrum $S(f)$ to the response spectrum $S_R(f)$ in Eq. (1.10), the most likely extreme response profile having the target response X_C at the target time t_0 is simply derived as follows:

$$X(t) = \sum_{i=1}^{N} A_{Ri} \cos(2\pi f_i (t - t_0)) \tag{1.13}$$

with

$$\begin{aligned} A_{Ri} =& S_R(f_i) df \times \frac{X_C}{\sigma_R^2} \qquad (i = 1, ..., N) \\ \sigma_R^2 =& \sum_{i=1}^{N} S(f) |RAO(f)|^2 df \end{aligned} \tag{1.14}$$

where A_R and σ_R^2 denote the response amplitude and the variance of the response spectrum. With consideration of the linear transfer function and the wave spectrum $S(f)$, the design wave generating the response profile above is then defined as follows:

$$\eta(t) = \sum_{i=1}^{N} A_i \cos(2\pi f_i t + \epsilon_i) \tag{1.15}$$

with

$$\begin{aligned} A_i =& \frac{A_{Ri}}{|RAO(f_i)|} \\ =& S(f_i)|RAO(f_i)|\Delta f \times \frac{X_C}{\sigma_R^2} \\ \epsilon_i =& -2\pi f t_0 - phase(RAO(f_i)) \end{aligned} \tag{1.16}$$

where A_i and ϵ_i are the wave amplitude and phase that are obtained from the RAO data. In the scope of linear analysis, the response induced by the RCW has the Most Likely Extreme Response (MLER), corresponding to the average shape of all random

responses having the target response X_C. Validation of the MLER process was carried out for the wave-induced bending moment of a ship by comparing it with experimental measurement [1].

Other methods which consider not only the linear structural response but also the wave spectrum in the EDW calculation have also been introduced. Dietz (2005) [19] performed a comprehensive study on the vertical bending moment amidships induced by the most likely response wave (MLRW) as well as the conditional random response wave (CRRW) corresponding to the MLRW embedded in the random wave elevation. The author compared his results against those induced by irregular sea state. Drummen et al. (2009) [22] conducted an experimental and numerical study on the exceedance probability distribution of MLRW and CRRW-induced amidships vertical bending moment of a flexible and rigid model. Although both methods accurately estimated the vertical bending moment probability distribution of a rigid hull, some discrepancies were found for flexible hulls due to strong nonlinear effects. The aforementioned methods can be a good indicator in estimating the nonlinear response, but as they apply a linear description of the response and assume that the nonlinear (higher-order) effects are small as compared to the linear effects [73], a large discrepancy in the estimate can be expected for a strong nonlinear wave response (e.g. parametric roll).

The First Order Reliability Method (FORM) has been introduced as an alternative solution for the nonlinear problem [50]. In this method, a nonlinear hydrodynamic model of interest can be explicitly defined in the time domain and the FORM, a linear optimization process, is taken into account with a limit state function to find a solution constituting a deterministic EDW profile. Ghadirian et al. (2017) [34] investigated the shape of FORM calculated based on first and second-order wave theory as well as the corresponding inline forces of a slender body in irregular waves. The difference between the measured inline load and the numerically calculated load by the FORM-based EDW was found to be significant. This highlights the importance of considering higher than second-order terms for the waves and the need to define an accurate nonlinear hydrodynamic model.

Jensen (2009) [46] conducted a study on the FORM method focusing on statistical analysis. Several procedures were compared to assess the vertical bending moment of a containership with various analytical methods including FORM. In the results, it was found that FORM tended to estimate the conservative (higher) mean up-crossing rates. The agreement between the overall results and the Monte Carlo (ensemble of realizations) simulation of the flexible hull in waves was acceptable. This confirms that the FORM method provides a comparable solution for strongly nonlinear problems.

Although many studies have been conducted to improve the efficiency and accuracy

of design load estimations by applying the above-mentioned approaches, it is relatively difficult to find data openly available for each case. Therefore, this paper mainly aims to analyze the structural responses of a ship in extreme wave conditions and to comprehensively understand each approach at the same time. A study on the load responses and characteristics of each approach including statistics for a specific ship model in extreme wave conditions is expected to facilitate the design load estimation process.

1.3 Objectives and outline of the thesis

Given the results in Kim and Kim (2016) [53], it is seen that the complexity of the system, along with the nonlinearity of the waves, may further trigger inconsistency factors that cannot be clearly identified among numerical simulations. This, in turn, increases the ambiguity in the analysis of results. Also, the experimental results sometimes showed deviating results from the average of the numerical ones, showing the need for a solid reference for numerical simulations.

This led us to the conclusion that structural response characteristics of 'a rigid containership model' under 'nonlinear extreme wave conditions' are to be clearly identified first. As a result, this thesis aimed to address the following objectives indicated by bullet points.

• Validation of nonlinear wave solver HOW-NWT applied to the generation of long-time irregular seas:

- The ability of an open source wave generation solver, Higher-Order Spectral-Numerical Wave Tank (HOS-NWT), to reproduce long-time nonlinear irregular waves (Monte Carlo reference) considering the wave breaking condition is evaluated. From the estimation of wave-related parameters, the numerically generated waves are compared with experimental measurements to check whether the energy dissipation mechanism is reasonably implemented from the result of wave-wave interactions in a numerical wave tank.

• Validation of a newly developed nonlinear irregular EDW calculation procedure to which the FORM and the HOS-NWT are applied and its applicability on the VBM response estimation:

- The first application of the developed EDW procedure is made for wave parameter-conditioned EDWs. The EDW generating a target wave crest having a certain exceedance probability level is calculated and measured. Results are then compared with the Monte Carlo reference results in terms of geometrical and statistical charac-

teristics.

- Then, the possibility of applying the developed nonlinear EDW calculation algorithm to VBM analysis is confirmed. The characteristics of the VBM response induced by the three wave approaches (IW, Regular EDW, and irregular EDW) in head sea conditions are experimentally analyzed. Monte Carlo reference results are applied as a reference for the other approaches. The measured nonlinear VBM induced by each approach is compared with each other in terms of shape and statistics. To identify the wave nonlinear effect, the measured nonlinear VBM compared to the linear VBM estimate for given wave conditions is further discussed in relation to the given wave parameters.

• The influence of wave nonlinearity on seakeeping performance in -120 degree oblique regular waves:

- The characteristics of 6-DOF motions and wave bending moments of a rigid containership model in various regular wave conditions are analyzed. Although the wave is limited to regular waves, various wave steepnesses series are applied to observe the effect of wave nonlinearity on the responses. The wave period range of each series is intended to cover the peak of the wave bending moment transfer functions. Through comparative analysis with the linear response calculated from a numerical tool, the influence of wave nonlinearity is emphasized.

- The contribution of the mooring system to the HBM response and 6-DOF motions is discussed in detail. For a ship model that maintains its heading angle with four horizontal mooring lines, it is intended to confirm that the tension on each mooring line generates an additional restoring moment and can affect the model behavior. From a qualitative point of view, the extent to which it affects the HBM response is analyzed.

Based on the stated objectives, this thesis has been organized and written. The outline of the thesis explained chapter by chapter is as follows.

Chapter 2 introduces the methodologies applied. Starting with the description of a rigid body model, the chapter deals with nonlinear wave generation. A stream function-based nonlinear regular wave is first presented, and a Higher-Order Spectral-Numerical Wave Tank (HOS-NWT), a nonlinear wave solver modeling the wave propagation in a numerical wave tank for irregular waves, is then presented. Then, a specific numerical model for the irregular equivalent design wave coupling with the HOS-NWT is described.

Chapter 3 gives overall information on the experimental setup applied including the introduction to a segmented model with its main principles. Sensor instrumentation

and the description of the data post-processing are briefly presented. The Response Amplitude Operator (RAO) calculation process, which is the most representative result calculated using the post-processed measurement (or simulation) data, is also introduced.

Chapters 4 and 5 present the numerical and experimental EDW results showing the feasibility of the FORM method in the estimation of the VBM. A developed numerical algorithm coupled with the HOS-NWT for the nonlinear FORM-based EDW calculation is introduced, and the experimental validation results are then presented. Comprehensive comparative analysis with the Monte Carlo reference results is performed from a geometrical and statistical point of view.

Chapter 6 introduces an experimental study of seakeeping performances of a moored ship in a -120 degree oblique wave condition. The effects of wave nonlinearity on the responses and the contribution of a mooring system to motions and wave-induced internal loads are discussed.

Chapter 7 summarizes the conclusions and contribution of the present study and draws some perspectives for future work.

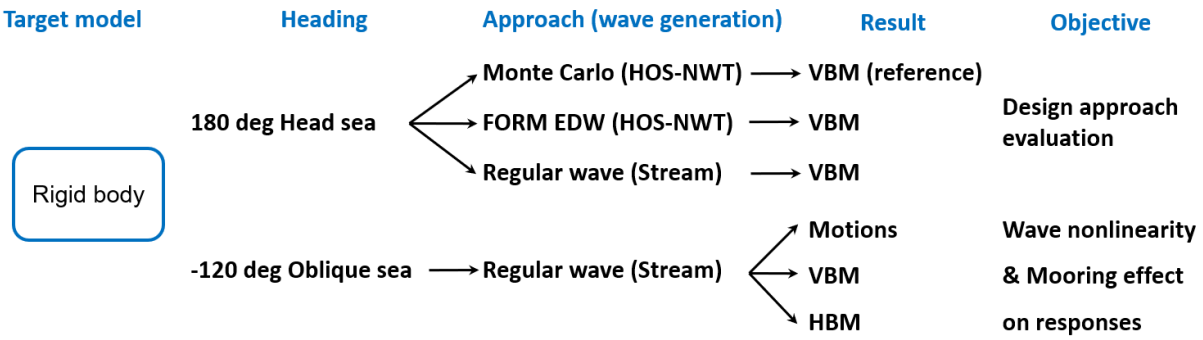

Figure 1.4 – Schematic diagram of detailed subjects of the present study

The present thesis comprises a part that evaluates the design approach using EDW with a rigid ship in head sea configuration and another part that deals with the nonlinear effect of increasing steepness of regular waves in the oblique sea configuration. Both studies are performed in a zero-speed experimental setting, and the model is set up with four mooring lines, their effect on the horizontal loads during the oblique sea tests is investigated. Figure 1.4 shows a schematic diagram of the subjects covered in this thesis. Methodologies applied to each part are addressed in the following sections.

In the former case, one key objective is the EDW generation through the application of the HOS-NWT within the FORM algorithm. This is the difference from the existing FORM-based EDW method. The main advantage is a better reproduction of the computed EDW in an experimental or CFD-based numerical wave tank. The improved EDW

method is then evaluated by comparing it with the Monte Carlo reference results. The Monte Carlo approach consists in generating a large number of irregular wave (IW) series in a nonlinear potential flow numerical wave tank and an experimental wave tank with random phases. The IW and EDW methods are compared in terms of the statistics and the geometrical shape of the response signals. This intuitive comparison allows us to determine the feasibility of the EDW methods. It is first done with a wave-only case and then with a wave-structure interaction case.

The latter case is on the investigation of the influence of nonlinear waves through motion and wave load analysis with various wave steepness series. In particular, it is noteworthy that the effect of the experimental setting of the zero-speed model (especially the mooring line) on loads and motions was identified in detail from a qualitative point of view.

Chapter 2

METHODOLOGIES

At first, this chapter presents a mathematical model for the evaluation of shear forces and bending moments from experimental measurements. Then, the linear sea-keeping model used in the FORM algorithm for the EDW study and as a reference for the oblique regular wave (RW) study is briefly summarized. The wave generation methodology is subsequently presented, for both regular waves (RW) and irregular waves (IW). The quality of the calculated and measured waves is controlled through the wave calibration procedure presented following the wave generation methodology. The procedure to calculate the equivalent design waves (EDW) is finally provided with a detailed description of the FORM optimization algorithm coupled with the HOS-NWT.

2.1 Rigid body model experiments

All cases in this paper deal with motion and wave load analysis for the zero forward speed model. The experimental setup for zero-speed conditions allows for mooring lines. Accordingly, the equations of motion of the experimental segmented model are defined with external force components including the mooring system. Shear forces and bending moments at each section are finally derived according to Bouscasse et al. (2022) [6].

The mathematical notations used to identify the physical quantities such as position, velocity, and acceleration at a position of interest of the model are defined according to Fossen (2011) [33]. The coordinate system $\{n\} = (x_n, y_n, z_n)$ with origin o_n is fixed in the wave tank and can be considered as an inertial reference frame. The moving body-fixed frame is referred to as $\{b\} = (x_b, y_b, z_b)$ with origin o_b amidships, in the longitudinal symmetry plane, and in the waterline plane (see Figure 2.1). Considering the Newton-Euler equations of motion for a rigid-body, shear forces and bending moments at a position of interest, A (x_A, y_A, z_A), expressed in the body-fixed frame can be obtained by Eq. (2.1).

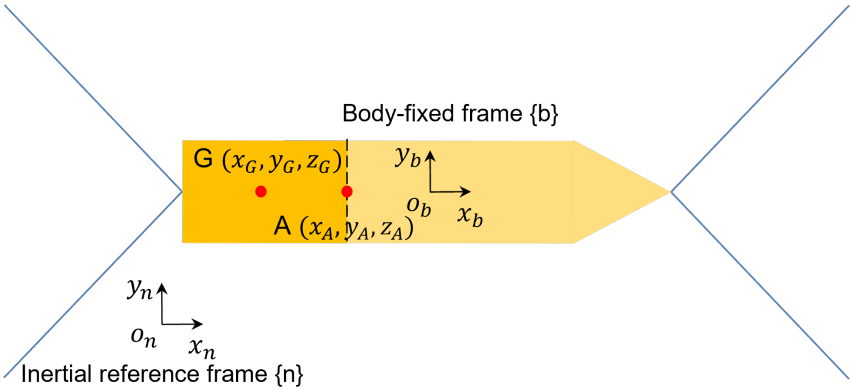

Figure 2.1 – Schematic view of model configuration with mooring system and reference frames

$$\begin{aligned}
\mathbf{Q} &= -\mathbf{F}_{ext}^{x<x_A} + m^{x<x_A}\left(\frac{d\mathbf{V}_{b/n}^{b}}{dt} + \mathbf{\Omega}_{b/n}^{b} \times \mathbf{V}_{b/n}^{b} + \frac{d\mathbf{\Omega}_{b/n}^{b}}{dt} \times \mathbf{r}_{A}^{G^{x<x_A}} + \mathbf{\Omega}_{b/n}^{b} \times (\mathbf{\Omega}_{b/n}^{b} \times \mathbf{r}_{A}^{G^{x<x_A}})\right) \\
\mathbf{M^A} &= -\mathbf{M}_{ext}^{A} + \mathbf{I}^{x<x_A}\frac{d\mathbf{\Omega}_{b/n}^{b}}{dt} + \mathbf{\Omega}_{b/n}^{b} \times \left(\mathbf{I}^{x<x_A}\ \mathbf{\Omega}_{b/n}^{b}\right) + (m\mathbf{r}_{A}^{G})^{x<x_A} \times \left(\frac{d\mathbf{V}_{b/n}^{b}}{dt} + \mathbf{\Omega}_{b/n}^{b} \times \mathbf{V}_{b/n}^{b}\right)
\end{aligned} \tag{2.1}$$

where $m^{x<x_A}$ and $\mathbf{I}^{x<x_A}$ are the mass and the moment of inertia of $0 < x < x_A$ portion of the model; $\mathbf{V}_{b/n}^{b} = [u, v, w]^\top$ and $\mathbf{\Omega}_{b/n}^{b} = [p, q, r]^\top$ correspond to a linear velocity vector and an angular velocity vector of $\{b\}$ relative to $\{n\}$ expressed in the body-fixed frame $\{b\}$ both; $\mathbf{r}_A^G = [(x_G - x_A), (y_G - y_A), (z_G - z_A)]^\top$ stands for the position vector of position A relative to G, the center of gravity of $x < x_A$ section of the model, expressed in $\{b\}$; $\top$ denotes the transpose, and this is intended to be explained in the same order of expression in the 6-DOF equations of motion below. The complete definition of the wave bending moments and the shear stresses with $y_G - y_A = z_G - z_A = 0$ for simplicity is as follows:

$$\begin{pmatrix} Q_x \\ Q_y \\ Q_z \\ M_x^A \\ M_y^A \\ M_z^A \end{pmatrix}^{x=x_A} = -\begin{pmatrix} F_{extx} \\ F_{exty} \\ F_{extz} \\ M_{extx}^A \\ M_{exty}^A \\ M_{extz}^A \end{pmatrix}^{x<x_A} + \begin{pmatrix} m[\dot{u} + qw - rv - (x_G - x_A)(q^2 + r^2)] \\ m[\dot{v} + ru - pw + (x_G - x_A)(qp + \dot{r})] \\ m[\dot{w} + pv - qu + (x_G - x_A)(rp - \dot{q})] \\ I_x\dot{p} - I_{xy}(\dot{q} - rp) - I_{zx}(\dot{r} + pq) + (I_z - I_y)qr + I_{yz}(r^2 - q^2) \\ I_y\dot{q} - I_{yz}(\dot{r} - pq) - I_{xy}(\dot{p} + qr) + (I_x - I_z)rp + I_{zx}(p^2 - r^2) - m[(x_G - x_A)(\dot{w} + pv - qu)] \\ I_z\dot{r} - I_{zx}(\dot{p} - qr) - I_{yz}(\dot{q} + rp) + (I_y - I_x)pq + I_{xy}(q^2 - p^2) + m[(x_G - x_A)(\dot{v} + ru - pw)] \end{pmatrix}^{x<x_A} \tag{2.2}$$

where dot (˙) notation denotes time derivative. The external force vector acting on $0 < x < x_A$ of the ship model, $\mathbf{F}_{ext}^{x<x_A}$, and the external moment vector at x_A, $\mathbf{M}_{ext}^A$, can be derived as follows:

$$\begin{pmatrix} F_{extx} \\ F_{exty} \\ F_{extz} \\ M_{extx}^A \\ M_{exty}^A \\ M_{extz}^A \end{pmatrix}^{x<x_A} = \begin{pmatrix} \mathbf{F}_{hydro/h} + \mathbf{P} + \mathbf{F}_{moor} \\ \mathbf{M}_{hydro/h}^A + \mathbf{r}_A^G \times \mathbf{F}_{hydro/h} + \mathbf{r}_A^G \times \mathbf{P} + \mathbf{M}_{moor}^A \end{pmatrix}^{x<x_A} \tag{2.3}$$

where $\mathbf{F}_{hydro/h}$, $\mathbf{M}_{hydro/h}$, and $\mathbf{P} = m\mathbf{g}$ are the fluid force, moment and the weight of the $x < x_A$ hull portion; $\mathbf{F}_{moor}$ and $\mathbf{M}_{moor}^A$ correspond to restoring forces and moments by the mooring lines installed at the $x < x_A$; Assuming that the x and y components horizontal to the mooring line are dominant in the restoring force by the mooring system, its restoring force for $x < x_A$ and moment at x_A can be simplified as follows:

$$\mathbf{F}_{moor}^{x<x_A} = \begin{Bmatrix} F_{x\,moor} \\ F_{y\,moor} \\ 0 \end{Bmatrix}^{x<x_A} \qquad \mathbf{M}_{moor}^A = \begin{Bmatrix} 0 \\ 0 \\ M_{z\ moor}^A \end{Bmatrix} \tag{2.4}$$

The equations above were applied when determining the wave loads, in particular, vertical shear force (VSF) and VBM at the location between each segment called 'intersegment' with measured data from the load sensor at each segment. The process is

called reconstruction. Starting with the model description, sensor instrumentation and the reconstruction of VSF and VBM are detailed in Chapter 3 with a description of how to obtain all the components.

2.1.1 Linear seakeeping model

The FORM algorithm applied in this study requires the evaluation of the ship response on a large set of waves (see Section 2.3.2). It consequently relies on a rapid numerical model to make it usable. This makes meaningful the use of linear theory, in particular, linear transfer functions as an input for the FORM algorithm. It was also used as a linear reference in the oblique study and applied for comparison with experimental results.

To solve the boundary value problems, a numerical tool applying the potential flow model, Hydrostar developed by the Bureau Veritas (BV) was used [93]. Its capability has been validated for decades through comprehensive comparative analysis with other numerical solvers and experimental results. Hydrostar is applicable for floating structures with or without forward speed (encounter frequency approximation) in deep and finite-depth waters in the frequency domain.

Potential flow theory allows for the use of integrals over the boundaries of the fluid domain. The three-dimensional boundary element method (panel method) can be used to solve the three-dimensional potential and the corresponding wave-structure interaction problem. The integral equation for the velocity potential is solved by distributing the wave source potential as a Green function that satisfies the free surface boundary condition on the boundary surface. When the solution for the velocity potential is completed, the hydrodynamic coefficient can be obtained by integrating the pressure calculated from the Bernoulli equation on the wetted surface S_B (see Figure 2.2).

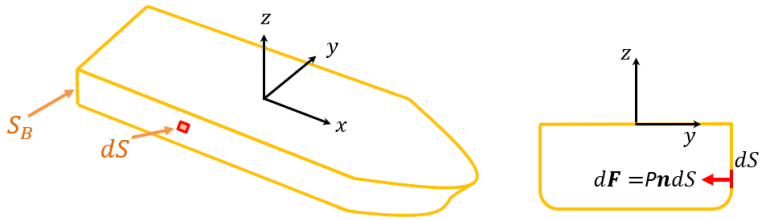

Figure 2.2 – Conceptual view of fluid pressure integral acting on the wetted surface S_B.

The linear frequency domain solver is suitable for analyzing the response of a zero-forward speed slender body to a periodic wave whose wave height is small enough as compared to the wavelength. It is assumed that the floating structure undergoes

small amplitude oscillatory motions about a fixed mean position, under the action of a given incident wave. Furthermore, all the fluid force components by the incident, diffracted, and radiated waves are estimated with the average wetted surface, not the actual wetted surface area of the ship. This means that when analyzing responses caused by a nonlinear large and steep wave, the result may include an error due to those simplifications.

Although the motions and wave loads induced by a large wave would contain nonlinear harmonic components, the first harmonic component accounts for mostly the largest portion of the total response. For large structures the Keulegan–Carpenter (KC) number describing the size of the structure to a given wave is expressed as per Eq. (2.5) and is less than 2.0. Thus, by definition, the inertia term is dominant and viscous effects are almost negligible.

$$KC = \frac{2\pi A}{L} \tag{2.5}$$

In the above expression, A is the wave amplitude and L is the characteristic length scale of the system. This corresponds to the system applied in the present thesis and explains that the linear seakeeping results based on the potential flow theory can still be a good indicator in estimating extreme responses. A detailed description of the potential flow-based linear seakeeping analysis is introduced in Appendix C.

2.2 Wave generation and nonlinear wave models

In this section, the overall description of nonlinear waves including the wave generation and calibration in experiments and numerical analysis are introduced in detail by wave type: RW, IW, and irregular EDW.

2.2.1 Regular waves

Considering that the irregular sea state is composed of numerous sinusoidal waves, a regular wave of a specific frequency among the irregular wave components can be used as excitation for a floating structure to observe the corresponding structural response. In other words, it has the advantage of being able to directly calculate or measure the response of the structure to a specific wave component. Most importantly, such an approach requires much less CPU cost or measurement time than the one with irregular waves.

For less steep waves, a linear description can be applicable. However, as the linear wave theory is an approximation, it is not suitable for real cases. According to Le

Méhauté (2013) [57] demonstrating the applicability of various wave theories in terms of a given wave steepness and a water depth, even for the wave case with $H/\lambda = 1$ % which is considered a relatively small amplitude wave, at least a second-order wave description depending on the relative water depth (see Figure 2.3) is necessary.

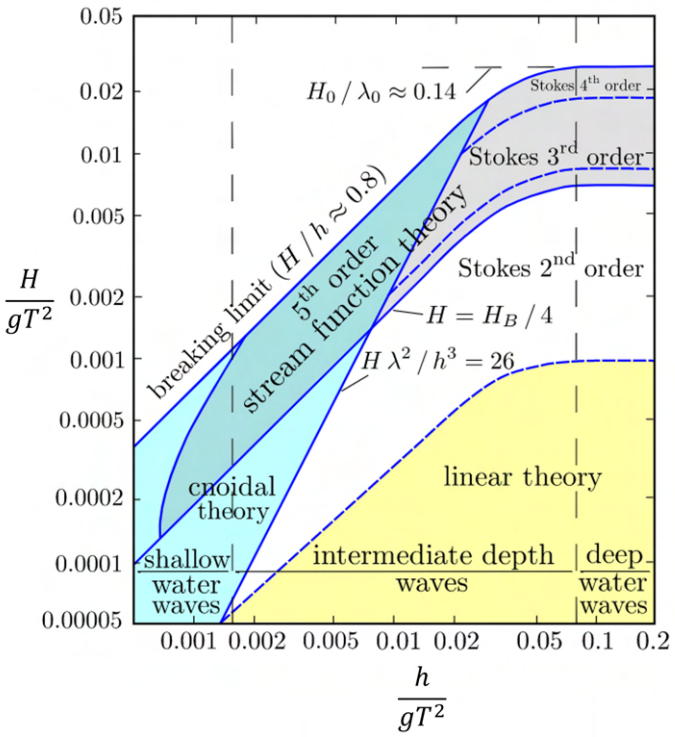

Figure 2.3 – Applicability of various wave theories presented by Le Méhauté [57]

In general, the target response of the regular design wave is estimated with the peak frequency data of the RAO or response spectrum as follows:

$$\tau_0 = A_R(f_p) = \sqrt{2S_R(f_p|\beta)df} \tag{2.6}$$

thus, the amplitude of the regular design wave is,

$$A(f_p) = \frac{\tau_0}{|RAO(f_p|\beta)|} \tag{2.7}$$

For the vertical bending moment, one tends to consider the response spectrum data associated with the frequency at $\lambda = L_{pp}$. With the defined wave height $2A(f_p)$ and period $T = 1/f_p$, the corresponding nonlinear regular wave profile is then generated.

Nonlinear regular waves

A representative theory for either linear or nonlinear regular waves can be the method of Stokes waves, which is an analytical method based on perturbation theory, and stream functions [17, 11, 76]. According to Ducrozet et al. (2019) [26], stream functions are more suitable for expressing a steep wave condition close to the breaking wave limit. On the other hand, perturbation functions have limited accuracy in terms of obtaining the converged Fourier coefficients corresponding to the higher-order terms of a given regular wave.

Given that one purpose of this study is to analyze the effect of wave nonlinearity on the global performance of a ship with a high-accuracy level under regular wave conditions, nonlinear regular waves derived from the stream functions seem more suitable. The formulations of the stream function are briefly described in Appendix D, and further information can be found in Ducrozet et al. (2019) [26].

2.2.2 Irregular waves

In ship design, wave conditions are by far the most important factor directly related to ship safety. As mentioned earlier, seakeeping analysis under irregular sea conditions is one of the classically performed design approaches. The vessel responses induced by such continuous random wave scenarios are considered to be the most realistic with physically reasonable wave-structure interactions.

Ocean wave spectra

Ocean waves are affected by transport time, distance, and wind speed associated with topography and climate. As such, the wave description may vary in terms of time and space of the observation point and special care must be taken to properly express the waves of the target sea area.

Pierson-Moskowitz (PM) spectrum is one of the most used models. It is suitable for a fully developed deep sea with a steadily blowing wind for a long time. It was developed by Pierson Jr and Moskowitz (1964) [71] and is based on measurements in the North Atlantic Ocean, describing the energy distribution as a function of wave frequency f_0 related to the wind speed U at a height of 19.5 m above the sea surface. The PM spectrum is defined as:

$$S(f) = \alpha \frac{g^2}{(2\pi)^4 f^5} exp\left[-0.74\left(\frac{f_0}{f}\right)^4\right] \tag{2.8}$$

where $\alpha = 8.1 \times 10^{-3}$ is the Phillips parameter and g is the gravitational acceleration. The peak frequency of the spectrum, f_p, has the following relationship with f_0:

$$\begin{aligned} 2\pi f_0 &= g/U \\ f_0 &= \frac{f_p}{0.877} \end{aligned} \tag{2.9}$$

thus, the PM spectrum can be expressed as a function of f_p:

$$S(f) = \alpha \frac{g^2}{(2\pi)^4 f^5} \exp\left[-\frac{5}{4}\left(\frac{f_p}{f}\right)^4\right] \tag{2.10}$$

The two-parameter wave spectrum models for the generation of the fully developed sea such as ITTC (1978) and ISSC (1968), in which the main parameters are significant wave height (H_s) and average wave period (T_0), were introduced based on the one-parameter PM spectrum expressed in Eq. (2.10).

JONSWAP spectrum applied in the present study was derived from a vast amount of wave measurements in the North Sea, and it was found that the sea state never reaches the fully developed conditions [39]. Thus, the JONSWAP spectrum applies a peak correction factor γ^r fitting the PM spectrum to the North Sea condition:

$$\begin{aligned} S(f) &= \alpha \frac{g^2}{(2\pi)^4 f^5} \exp\left[-\frac{5}{4}\left(\frac{f_p}{f}\right)^4\right] \gamma^r \\ r &= \exp\left[-\frac{(f-f_p)^2}{(2\sigma^2 f_p^2)}\right] \\ \sigma &= \begin{cases} 0.07 & \text{when } f \leq f_p \\ 0.09 & \text{when } f > f_p \end{cases} \end{aligned} \tag{2.11}$$

where γ is the peakedness parameter. For the North Sea, $\gamma = 3.3$ is typically taken and $\gamma = 1$ corresponds to the PM spectrum. Since the JONSWAP spectrum does not correspond to a fully developed sea, it has a relatively high peak and a narrow banded shape, enhancing the nonlinear wave-wave interactions [38].

Directional wave

The wave spectrum $S(f)$ corresponds to uni-directional waves. Long-crested waves may physically make sense for swell conditions, but actual sea states are mostly multi-directional. To accurately estimate the response of a ship to an actual sea state, it is necessary to consider multi-directional waves so-called short-crested waves. A spreading function is used to impose the two-dimensional effects on the unidirectional spectrum (point spectrum), $S(f)$. The spreading function represents the spread of the spec-

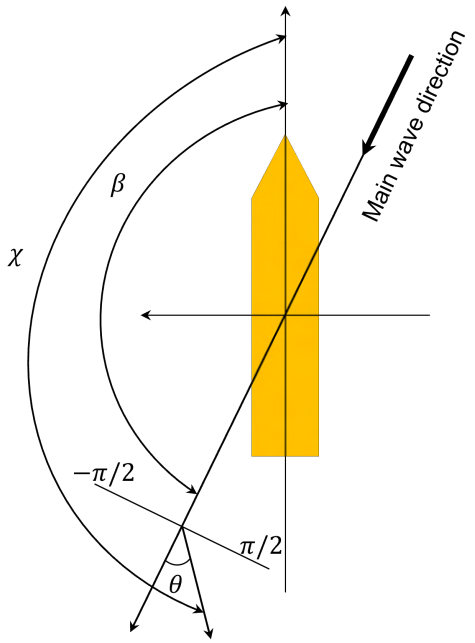

Figure 2.4 – Definition of spreading angles

tral energy of each wave frequency component that contains a dominant wave at β and component waves over the range of (see Figure 2.4):

$$\begin{aligned} \beta - \frac{\pi}{2} < \chi < \beta + \frac{\pi}{2} \\ \chi = \theta + \beta \end{aligned} \tag{2.12}$$

In the above equation, β denotes the predominant wave direction and θ is the angle of component waves to the predominant wave direction. The multi-directional spectrum can be related to the unidirectional spectrum $S(f)$ and the spreading function $D(f, \chi)$ as follows:

$$S(f, \chi) = S(f)D(f, \chi) = S(f)D(\chi) \tag{2.13}$$

$$D(\chi) = \frac{\Gamma(1 + n/2)}{\sqrt{\pi}\Gamma(1/2 + n/2)} \cos^n(\chi - \beta) \tag{2.14}$$

where Γ is gamma function, n is wave spreading parameter (for wind-generated sea, n=2 to n=4). The spreading function $D(\chi)$ satisfies:

$$\int_{-\frac{\pi}{2}}^{\frac{\pi}{2}} D(\chi) d\chi = 1 \tag{2.15}$$

From (2.13) and (2.15), we may conclude that the integral of multi-directional wave spectra is equal to the integral of unidirectional wave spectrum as expressed below:

$$\int_0^\infty S(f)df = \int_{-\frac{\pi}{2}}^{\frac{\pi}{2}} \int_0^\infty S(f,\chi)df d\chi = m_0 \tag{2.16}$$

where m_0 is the variance of the wave spectrum.

One typical wave spectrum for a given sea condition generates an irregular wave elevation of 3 hours. This is the reason why there is a limit to observing all possible responses corresponding to the sea conditions encountered by a ship with a lifespan of about 25 years. The estimation of the responses that occurred in the most severe sea condition is mainly performed for the ultimate response analysis. This emphasizes the importance of the consideration of nonlinear wave propagation containing nonlinear wave-wave interaction that the linear superposition process cannot account for.

To consider all the possible wave nonlinearities, a Higher-Order Spectral (HOS) method-based nonlinear wave propagation solver, HOS-NWT was considered. The HOS-NWT generates the fully nonlinear wave elevation in a numerical wave tank (NWT) and therefore allows for comparative analysis against experimental results.

HOS-NWT

Figure 2.5 shows a 2D configuration of a wave tank. A basin coordinate system is defined with origin O at a wavemaker location and in way of the waterline. This frame is used to indicate a location of the wave elevation (e.g. target location x_0).

This tank configuration relies on the accurate definition of the free surface elevation at a target location $\eta(x_0, t)$ (see Figure 2.5). In order to achieve a high degree of accuracy with reduced computational effort, we choose to use a Numerical Wave Tank (NWT) based on potential flow formalism.

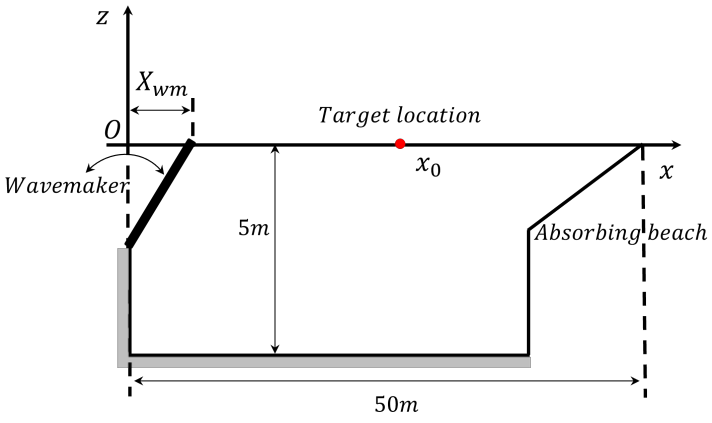

Figure 2.5 – 2D schematic view of a wave tank configuration

In this framework, the HOS method [20, 99] is known to be an efficient way of solving numerically the wave propagation [24]. An open-source Numerical Wave Tank based on the HOS method has also been developed by Ducrozet et al. (2012) [25]. This HOS-NWT model has been extensively validated and used in different configurations [5, 23, 87], thus demonstrating its accuracy and efficiency.

Apart from the numerical details and performances that can be found in Ducrozet et al. (2012) [25], the specificity of the HOS-NWT is that it reproduces all the features of an Experimental Wave Tank (EWT), namely i) the waves are generated thanks to the wavemaker through the control of its movement, ii) the sidewalls of the computational domain are fully reflective and iii) an absorbing beach is located close to the wall opposite to the wavemaker, to absorb reflective waves.

Finally, it has to be noted that the wave conditions of interest in this study (see Section 4.3) range from mildly nonlinear to extreme conditions. Breaking waves are expected to occur during wave propagation and those cannot be directly simulated by potential flow hydrodynamics. Accordingly, a specific procedure has been developed to detect breaking waves prior to their appearance and to locally dissipate some energy to allow wave propagation to pursue [83, 82].

Formulation of HOS-NWT The HOS method [20, 99] was introduced to solve nonlinear wave propagation in time in an open fluid domain. Potential flow theory is the basis of the method, thus the fluid is assumed to be incompressible and inviscid satisfying the Laplace equation $\nabla^2\phi = 0$. Although the original HOS method can simulate highly nonlinear wave evolutions, its application was limited to the unbounded fluid domain defined with periodic boundary conditions with the prescribed initial free surface elevation $\eta(x, t = 0)$. To extend the application range of the HOS and to enable comparisons against experiments, the HOS in a numerical wave tank (HOS-NWT) was developed and validated [27].

The simulation assumed a 2D rectangular fluid domain with a finite and constant water depth h. The domain $L_x \times L_y$ depicted in Figure 2.6 corresponds to the dimensions of the NWT in the x and y-axis respectively. The left side wall corresponding to $x = 0$ is the location of the wavemaker and the opposite side corresponds to the location of the wave absorbing beach. The other two sides of the rectangle corresponding to the section $(x, y) = (0 : L_x, 0)$ and $(0 : L_x, L_y)$ are perfectly reflective side walls.

Following Zakharov (1968) [100], the kinematic and dynamic boundary condition at the free surface can be written with respect to surface elevation $\eta(\mathbf{x}, t)$ and surface velocity potential $\phi^s(\mathbf{x}, z = \eta(\mathbf{x}, t), t)$, where $\mathbf{x}$ is the horizontal (x, y) vector.

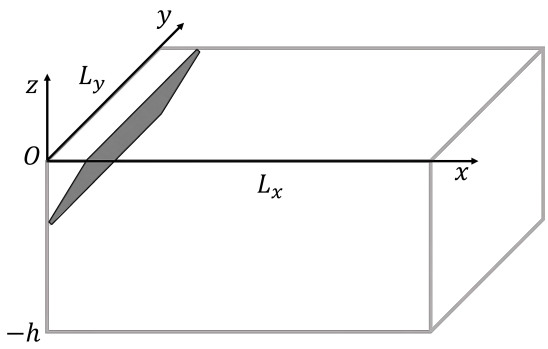

Figure 2.6 – Numerical wave tank scheme

$$\frac{\partial \eta}{\partial t} = (1 + \|\nabla \eta\|^2)W - \nabla \phi^s . \nabla \eta \tag{2.17}$$

$$\frac{\partial \phi^s}{\partial t} = -g\eta - \frac{1}{2}\|\nabla \phi^s\|^2 + \frac{1}{2}(1 + \|\nabla \eta\|^2)W^2 \tag{2.18}$$

$\nabla = \frac{\partial .}{\partial x}\mathbf{i} + \frac{\partial .}{\partial y}\mathbf{j}$ stands for surface gradient and $W = \frac{\partial \phi}{\partial z}$ is vertical flow velocity at the free surface.

In the case of the HOS-NWT, an additional velocity potential has been taken into account to model the wave generation by a wavemaker. The total potential ϕ, expressing the solution to the boundary value problem, is decomposed as $\phi = \phi_{spec} + \phi_{add}$ where ϕ_{spec} denotes the potential describing the free surface evolution in the fluid domain and ϕ_{add} the potential describing the wavemaker. The additional potential acts as a forcing term in the equations, and thus the wave evolution of a physical wave tank starting from a calm water condition can be reproduced in the NWT [25]. In addition to this set of equations, a periodic wave variation (η, ϕ) is assumed in the (x,y) plane. Therefore, η and ϕ^s can be expressed using the Fourier series:

$$\eta(\mathbf{x}, t) = \sum_{m=0}^{+\infty}\sum_{n=0}^{+\infty} A_{mn}^{\eta}(t)\cos(k_m x)\cos(k_n y) \tag{2.19}$$

$$\phi^s(\mathbf{x}, t) = \sum_{m=0}^{+\infty}\sum_{n=0}^{+\infty} A_{mn}^{\phi^s}(t)\cos(k_m x)\cos(k_n y) \tag{2.20}$$

with $k_m = m\frac{\pi}{L_x}$ and $k_n = n\frac{\pi}{L_y}$.

The spectral decomposition is performed with a given number of modes (m, n) that correspond to the number of points in the physical domain. Thanks to the discrete Fourier transform, the free surface boundary conditions (FSBC) in Eq. (2.17) and (2.18) are efficiently solved by computing products in physical space and space derivatives

in spectral space. As described in Figure 2.7, the vertical velocity W is computed with knowing η and ϕ^s using the HOS scheme. The calculation procedure is dependent on a series expansion in wave steepness ϵ power ($\phi^{(m)} = O(\epsilon^m)$) up to an order M, the so-called wave nonlinearity order. A detailed formulation and description applied to the solver can be found in [25].

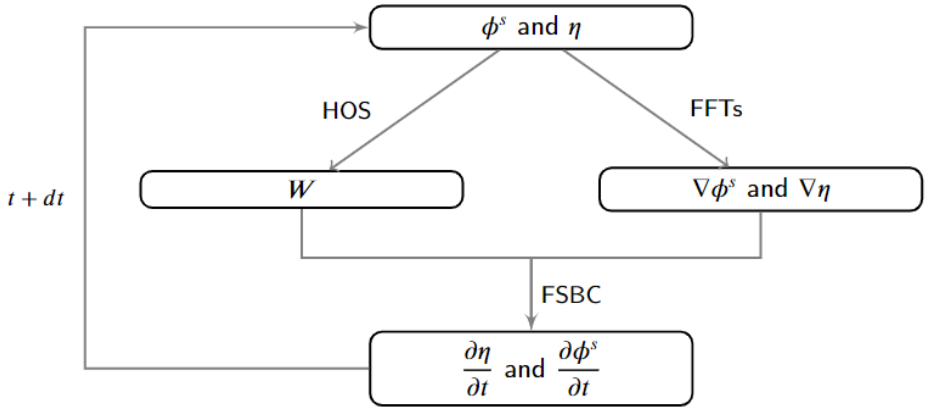

Figure 2.7 – Time stepping in the HOS scheme

Breaking waves In the case of actual wave conditions, when the steep wave continues to develop or when its speed reaches a certain limit, a breaking wave can occur, which is associated with (strong) wave energy dissipation and the generation of vorticities. However, simplified numerical models cannot simulate the complex underlying physics of the breaking events. The HOS-NWT is such a case, as it is defined based on the potential flow theory modeling the wave propagation and evolution without taking into account the viscosity of the fluid. As a solution to these limitations, an eddy viscosity model was applied to the HOS-NWT, following [89, 83, 82]. The breaking onset is estimated based on the breaking criterion [3], i.e. the ratio of fluid particle velocity at the crest U_x to the crest velocity C_x. Following Seiffert et al. (2017) [83], a threshold is set to 0.85.

$$\frac{U_x}{C_x} > \text{threshold} \tag{2.21}$$

At every time step, a breaking event is detected if the wave exceeds the criterion. Free surface boundary conditions applying the eddy viscosity as a diffusion term (see Eq. (2.22) and (2.23)) are implemented to estimate the energy dissipation by the breaking event.

$$\frac{\partial \eta}{\partial t} = (1 + \|\nabla\eta\|^2)W - \nabla\phi^s.\nabla\eta + 2\nu_{eddy}\nabla\cdot\nabla\eta \tag{2.22}$$

$$\frac{\partial \phi^s}{\partial t} = -g\eta - \frac{1}{2}\|\nabla\phi^s\|^2 + \frac{1}{2}(1 + \|\nabla\eta\|^2)W)^2 + 2\nu_{eddy}\nabla\cdot\nabla\phi^s \tag{2.23}$$

Eddy viscosity ν_{eddy} is estimated by considering the active breaking time, falling wave crest height, and horizontal breaking length as defined in Tian et al. (2010) [89].

2.2.3 Wave calibration

One of the objectives of this thesis is to simulate and measure qualified regular waves and irregular wave spectra, and to study the related wave characteristics in relation to the response of the vessel. Therefore, to qualitatively confirm that the responses are the ones induced by a given qualified wave, the wave calibration process in the EWT or NWT must be taken into account. In both environments, if a location at a certain distance from the wavemaker is selected as a target location, and the resulting nonlinear mechanism is considered, wave quality at the target location must be identified and adjusted through the wave calibration process. The waves are generated from one side of the computational domain. In this case, for example, the wave spectra will evolve in space but not in time. In this configuration, at each location, the wave field is a stationary process.

The point to note here is that the wave elevation at a certain distance from the wavemaker would be inconsistent as compared to the target one due to nonlinear wave-wave interactions and dissipation as the wave propagates along the numerical wave tank. Nevertheless, as the wave elevation at each location of the fluid domain is stationary in time, a calibration process with the wavemaker motion can be carried out to obtain the qualified wave at the target location x_0.

Regular waves

The regular wave calibration procedure applied for both measurement (EWT) and simulation (NWT) is described in Figure 2.8. With the parameters, H and λ or T, stream function theory calculates the free surface elevation at the target location x_0, consisting of wave amplitudes of harmonic frequency components up to a specified order M (see Figure 2.8). Then, for the generation of the wave elevation in the NWT or EWT, the linear wavemaker theory can be applied, which takes the first-order wave amplitude A_1 as input. With a linear transfer function of the wavemaker TF, its first modal amplitude X_{wm1} is calculated to generate the wave elevation.

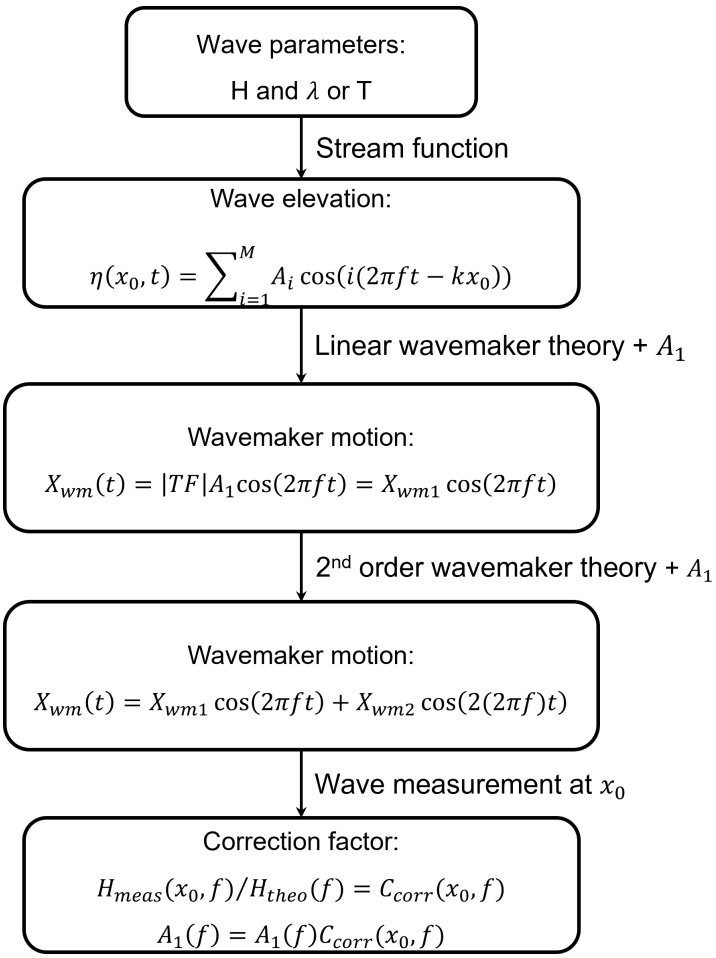

Figure 2.8 – Regular wave calibration procedure for the wave at the target location x_0

It has to be noted that in case the wavemaker is operated according to linear wavemaker theory, the second-order frequency component of the generated wave elevation may include parasitic free waves. According to Schäffer (1996) [79], these parasitic free waves can be predicted by second-order wavemaker theory and eliminated by generating opposite free waves via a correction of the wavemaker motion. Such a process is applied in the present study. The second modal amplitude of the wavemaker, $X_{wm2} = f(A1, f, k, d)$ is introduced accordingly, and the free surface elevation generated by the second-order wavemaker motion is finally reproduced and measured at x_0.

For the wave calibration, it is performed by comparing the theoretical wave height, $H_{theo}(f)$ with the actual wave height measured, $H_{meas}(x_0, f)$. The correction factor $C_{corr}(x_0, f)$ corresponding to the ratio $H_{meas}(x_0, f)/H_{theo}(f)$ is finally identified for a given wave with frequency f.

Fig 2.9 shows the time history of the wave measured and its reference crest and

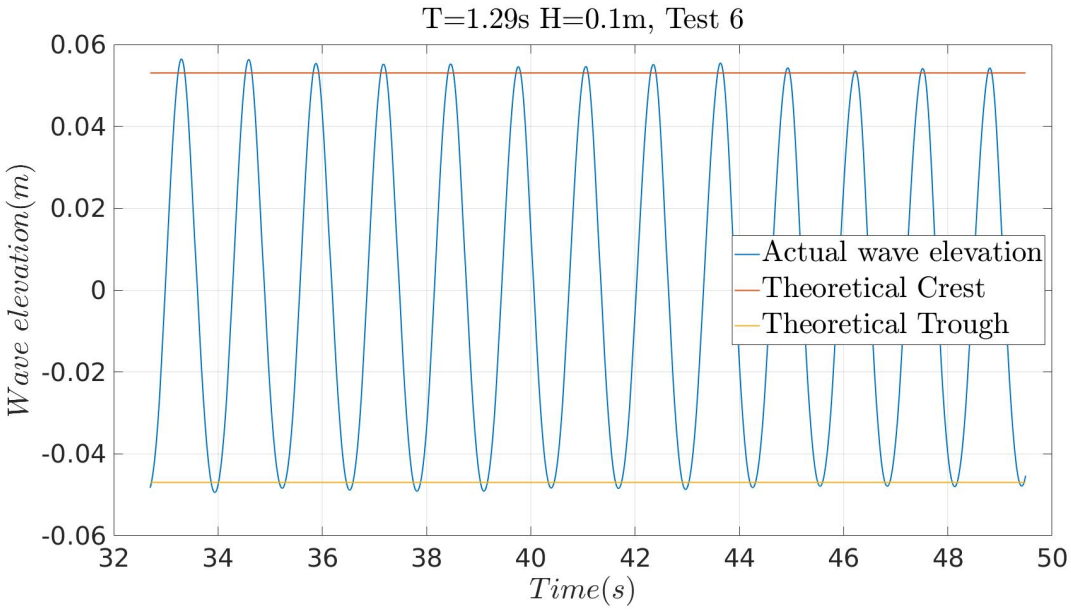

Figure 2.9 – Regular wave time signal from wave calibration test and its reference reference crest and trough

trough with horizontal solid lines as an example of the wave calibration. $H_{meas}(x_0, f)$ corresponds to the average of wave heights in a manually selected time window where the signal shows a stable state. Once the correction factor, $C_{corr}(x_0, f)$ is identified, it is then applied to A_1 described in the last part of Figure 2.8.

According to the second-order wave generation theory by Schäffer (1996) [79], the first-order wave amplitude A_1 directly involves in the calculation of the second-order wave amplitude A_2 and the first- and second-order wave maker amplitude (X_{wm1} and X_{wm2}) and is proportional to those values. Thus, by applying C_{corr} only to A_1, the corresponding wavemaker motion calibrated can be obtained for a given regular wave. Finally, with the modified wavemaker motion input, an additional wave calibration test in the EWT (or numerical simulation in NWT) is carried out again to check its validity.

As the mechanical performance of the wavemaker depends on the condition of a given wave, the iteration process may be necessary if the wave condition is out of the wavemaker's range providing good quality (see Figure 3.2).

Irregular waves

A typical design problem is to compute the probability of occurrence of a certain extreme event in a given sea state, and the most straightforward way to do so is through the Monte Carlo approach with a number of realizations for a given sea state, generating different irregular seas with different sets of wave phases. Regarding the wave crest, which is a problem of interest in this study, the probability of exceedance of the

wave crest obtained with the linear wave theory follows the Rayleigh distribution. It becomes the Forristall distribution with second-order wave theory [32], and the problem largely complexifies within the framework of nonlinear theory in a wave tank environment, where the crest POE will depend on the distance between the wavemaker and the target location and the characteristics of the spectrum (significant wave steepness and peakedness in particular) [10].

Computing a fully nonlinear solution of the wave elevation in time and space is one subject of research. The fully nonlinear wave equations induce some interactions between the spectrum components, and as mentioned above, the definition of a sea state is usually done with a spectrum shape.

When this solution is chosen, the wave spectra should be correctly reproduced at a certain reference location. This may however involve the need for some corrections to the wavemaker inputs to realize this spectrum. The wave quality at the target location x_0, where an environmental condition should meet the target condition depends also on practical reasons (such as the experimental setup and the length of the tank) as well. A calibration methodology will modify the spectrum at the wavemaker (calibrated $S_{wm}(f)$) to achieve the target spectrum $S_{targ}(f)$ at the target location x_0.

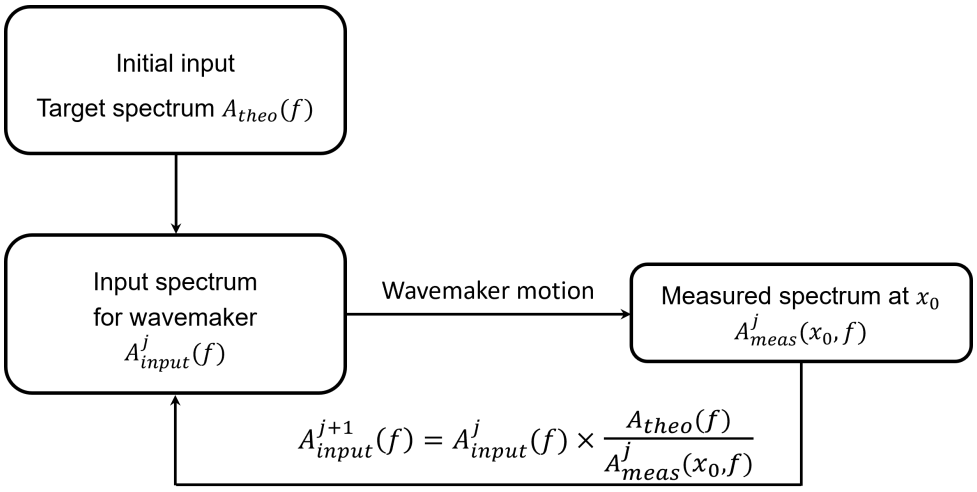

Figure 2.10 – Iterative correction process to obtain the target spectrum $S_{targ}(f)$ at x_0

Figure 2.10 shows an overview of the wave calibration procedure applied. The target wave amplitude $A_{theo}(f)$ is used to construct the wavemaker motion using linear theory where,

$$A_{theo}(f) = \sqrt{2S_{theo}(f)df} \tag{2.24}$$

The target wave amplitude $A_{theo}(f)$ is initially applied as an input for the wavemaker and is generated. Then, through a linear iterative process taking into account the ratio of

$A_{theo}(f)$ and $A_{meas}(x_0, f)$ at the target location x_0, the spectrum data at the wavemaker location are iteratively calibrated until the wave spectrum at the target location has a comparable result to the target spectrum. The ratio $A_{theo}/A^j_{meas}(x_0, f)$ at the j^{th} iteration is applied as a correction factor $C^j_{corr}(x_0, f)$ to obtain the calibrated wave amplitude $A^{j+1}_{input}(f)$ at the wavemaker for $j + 1^{th}$ step.

$$C^j_{corr}(x_0, f) = \frac{A_{theo}}{A^j_{meas}(x_0, f)} \tag{2.25}$$

$$A^{j+1}_{input}(f) = A^j_{input}(f) \times C^j_{corr}(x_0, f) \tag{2.26}$$

According to [9], the criterion in $C_{corr}(x_0, f)$ with its deviation $\pm 5\%$ is applied to wave components in the range $3/4 f_p$ to $3/2 f_p$.

$$\left| \frac{A_{theo}(f) - A_{meas}(x_0, f)}{A_{theo}(f)} \right| < 5\% \quad for\ f \in \left[\frac{3}{4} f_p; \frac{3}{2} f_p \right] \tag{2.27}$$

where f_p is the peak frequency of the target spectrum.

2.3 FORM method

The FORM approach is considered an effective solution when the hydrodynamic response distribution is not explicitly known, which is true when the problem is nonlinear. In that case, a solution cannot be derived with analytical EDW methods. In response to this, the FORM method applies a numerical minimization process that determines a non-linear solution through linear approximation. In principle, any response can be estimated in the time domain regardless of its nonlinearity [50]. Based on a given sea state and a properly defined hydrodynamic model of interest $\tau(x, t)$, FORM calculates a deterministic short irregular wave train yielding a target response τ_0. In addition, the probability of exceedance of the specified target crest generated by EDW can be estimated from the procedure.

2.3.1 Formulation of FORM-based EDW

The FORM procedure is introduced in three parts: i) the input process, in this case, the wavemaker, ii) the FORM optimization process, and iii) its solution. The wave characteristics in the wave tank are taken into account in i) and ii), and through this, the most probable nonlinear wave profile, the solution of the FORM, is estimated.

Input process

Wave elevation and the associated wave kinematics have to be accurately defined. In the FORM method, the wave, an input process of the FORM, is assumed to be a stationary stochastic process, and a linear description of the wave following the Gaussian process may be applied for the moderate sea state.

For severe wave conditions where the nonlinear wave effects become important, Jensen and Capul (2006) [50] suggested applying additional corrections to account for this nonlinearity of the waves in the FORM method. Considering our specific case where the wave may behave nonlinearly as it propagates in the NWT or EWT, a more sophisticated approach that can consider the characteristics of the wave tank needs to be considered. A typical way to generate nonlinear waves is through the use of a numerical wave tank (NWT).

If we assume a 2D wave propagation, the wave generation is controlled by the wavemaker motion $X_{wm}(t)$ on one side, defined in Eq. (2.28). This will be the Gaussian input to FORM.

$$\begin{aligned} X_{wm}(t) &= \sum_{i=1}^{N} |\mathsf{TF}_i| A_i \cos(2\pi f_i t + \epsilon_i) \\ &= \sum_{i=1}^{N} (u_i c_i(t) + \bar{u}_i \bar{c}_i(t)) \end{aligned} \tag{2.28}$$

where TF_i is i^{th} the wavemaker transfer function in N frequency components and $u_i, \bar{u}_i$ are the i^{th} uncorrelated and normal distributed parameters, which are related to the wave amplitude and phase A_i and ϵ_i:

$$\begin{aligned} |\mathsf{TF}_i| A_i &= \sigma_{wmi} \sqrt{u_i^2 + \bar{u}_i^2} \\ \epsilon_i &= \tan^{-1}(\bar{u}_i / u_i) \end{aligned} \tag{2.29}$$

$c_i(t)$ and $\bar{c}_i(t)$ for each frequency component can be expressed as follows:

$$\begin{aligned} c_i(t) &= \sigma_{wmi} \cos(2\pi f_i t) \\ \bar{c}_i(t) &= -\sigma_{wmi} \sin(2\pi f_i t) \\ (\sigma_{wmi})^2 &= |\mathsf{TF}_i|^2 S(f_i) df \end{aligned} \tag{2.30}$$

where σ_{wmi} denotes the variance of each frequency component of the wavemaker motion. $S(f)$ and df are the wave spectrum and the constant increment between wave

frequencies.

Limit state function

Once the wavemaker input process is defined, the FORM will look for a standard normal vector set, $\mathbf{u} = \{u_i, \bar{u}_i\} = \{u_1, \bar{u}_1, u_2, \bar{u}_2, ..., u_N, \bar{u}_N\}$ generating a given target response τ_0 at a given time t_0 with the highest probability among a number of $\{u_i, \bar{u}_i\}$ sets. The limit state function can be used to estimate a solution as expressed below [18]:

$$G(\mathbf{u}) = \tau_0 - \tau(t_0|\mathbf{u}) = 0 \tag{2.31}$$

where $\tau(x_0, t_0|\mathbf{u})$ is a hydrodynamic response amplitude induced by the EDW wave components **u** at $t = t_0$ and $x = x_0$.

In Figure 2.11, the limit state surface in u-space is defined with a number of $\{u_i, \bar{u}_i\}$ sets. The design point is where the distance from the point on the surface border G(**u**)=0 to the origin is the shortest among the realizations. The design point with $\mathbf{u}^*$ which is a solution of the following optimization problem in Eq. (2.32) is sought with the FORM linearization.

$$\beta_{FORM} = \min \sqrt{\sum_{i=1}^{N} (u_i^2 + \bar{u}_i^2)} \qquad \text{subject to} \qquad G(\mathbf{u}) = 0 \tag{2.32}$$

It has to be noted that FORM can estimate the exact solution when the original limit state function is linear, and the variables have normal distributions. In other words, in the general case of a nonlinear limit state function, the solution of the FORM may contain some discrepancy related to the curvature of the existing limit state function and variables.

Given the limit state function is described by standard normal distributed parameters **u**, the FORM may estimate a solution that is close to the exact solution with the linear approximation (first-order polynomial) at the design point. Therefore, finding an appropriate linearization point is important, and this leads to an iterative process [72] (see Section 2.3.2 for details).

The deterministic EDW wave episode yielding a specified target response ϕ_0 is obtained as $\mathbf{u}^*$ at a design point. This shortest distance is called the FORM reliability index, β_{FORM}, a function of $\{u_i^*, \bar{u}_i^*\}$ expressed in Eq. (2.33).

$$\beta_{FORM} = \sqrt{\sum_{i=1}^{N} (u_i^{*2} + \bar{u}_i^{*2})} \qquad \text{and} \qquad G(\mathbf{u}^*) = 0 \tag{2.33}$$

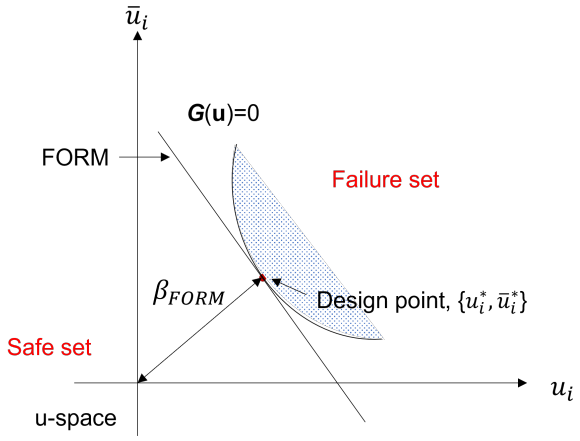

Figure 2.11 – Limit state function $\mathbf{G}$ and β_{FORM} in u-space, [18]

Mean up-crossing rates and exceedance probability

The mean out-crossing rate of the target response, $\nu(\tau_0)$ in a given sea state can be estimated with β_{FORM} and a set of $\{u_i^*, \bar{u}_i^*\}$:

$$\nu(\tau_0) = \frac{1}{2\pi\beta_{FORM}} e^{-\frac{1}{2}\beta_{FORM}^2} \sqrt{\sum_{i=1}^{N}(u_i^{*2} + \bar{u}_i^{*2})(2\pi f_i)^2} \tag{2.34}$$

For an exceedance probability of the target response in a given sea state with a narrow banded wave spectrum, the number of zero-up crossing events corresponds to the number of peaks E_0 in a given time T, with $E_0 = \nu(0)T$. In the same context, the number of out-crossing events exceeding the target response corresponds to $E_{\tau_0} = \nu(\tau_0)T$. Thus, the exceedance probability of the individual response τ_0 in a given time T can be expressed as a ratio of $\nu(\tau_0)$ to $\nu(0)$ as expressed in Eq. (2.35). By selecting several τ_0 in a given sea state, the distribution of POE estimated by the FORM can be obtained, and a comparison with the empirical POE distribution of the corresponding sea state can be carried out.

$$\begin{aligned} &\text{Prob}(\tau<\tau_0) = \text{CDF}(\tau_0) = 1 - \nu(\tau_0)/\nu(0) \\ &\text{Prob}(\tau>\tau_0) = \text{POE}(\tau_0) = 1 - \text{CDF} \end{aligned} \tag{2.35}$$

where CDF stands for the cumulative density function and $1/\nu(0)$ corresponds to the mean zero-crossing period T_z of numerically calculated wave elevation of a given sea state in the HOS-NWT.

Note that the physical quantity of target response τ_0 and associated hydrodynamic model τ are arbitrary, and we can apply the same procedure to different physical properties such as wave elevation or structural response. In this study, wave and VBM

response-related EDW studies were performed separately. This implies that τ_0 and τ were expressed with different notations depending on the physical quantity considered.

2.3.2 FORM algorithm for Most Probable Point (MPP) search

Background of the algorithm applied

According to Kim et al. (2022) [52], the numerical algorithm applied in this study is based on a specific class of the FORM optimization algorithms namely HL to denote the algorithm proposed by Hasofer and Lind (1974) [37]. In the classical HL algorithm the MPP is evaluated using the following iterative scheme:

$$\mathbf{u}^{k+1} = \frac{1}{\|\nabla G(\mathbf{u}^k)\|^2}\left(\nabla G(\mathbf{u}^k)\mathbf{u}^k - G(\mathbf{u}^k)\right)\nabla G(\mathbf{u}^k) \tag{2.36}$$

where subscript k denotes k^{th} iteration process. Usually, this iteration is not used alone (algorithm may fail to converge), but with a merit function to monitor the convergence [60].

Although the HL-based algorithms have been shown to be efficient, they may be unstable depending on the application case [60]. With the latter in mind, it was considered essential to introduce some modifications in the algorithm to improve its robustness with a reasonable CPU cost. Liu and Der Kiureghian (1991) [64] proposed the following merit function in their modified HL-RF (Rackwitz and Flessler (1978) [74]) algorithm:

$$m(\mathbf{u}) = \frac{1}{2}\left\|\mathbf{u} - \frac{\nabla G(\mathbf{u})\mathbf{u}}{\|\nabla G(\mathbf{u})^2\|^2}\nabla G(\mathbf{u})\right\|^2 + \frac{1}{2}cG(\mathbf{u})^2 \tag{2.37}$$

where c is the positive constant weight factor that can be taken in the range from 10 to 10,000 [15]. According to the modified HL-RF algorithm, the optimal design point $\mathbf{u}^*$ (=$\{u_i^*, \bar{u}_i^*\}$) is determined using a line search procedure [64]:

$$\mathbf{u}^{k+1} = \mathbf{u}^k + \alpha^k \mathbf{d}^k \tag{2.38}$$

with:

$$\mathbf{d}^k = \frac{1}{\|\nabla G(\mathbf{u}^k)\|^2}\left(\nabla G(\mathbf{u}^k)\mathbf{u}^k - G(\mathbf{u}^k)\right)\nabla G(\mathbf{u}^k) - \mathbf{u}^k \tag{2.39}$$

where α^k is determined through a line search in the $\mathbf{d}^k$ direction to decrease $m(\mathbf{u})$.

However, in this algorithm, $\nabla G(\mathbf{u})$ is required to compute $\mathbf{d}^k$ first and then $m(\mathbf{u}^k)$ at each internal loop iteration in order to evaluate α^k. This results in a huge number

of function calls, which is proportional to the number of optimization components. For this reason, the modified HL-RF algorithm is considered to be expensive since many function calls are needed to evaluate $\nabla G(\mathbf{u})$ [51].

To deal with the issue in CPU cost, Jensen et al. (2017) [51] suggested using the improved HL algorithm with circle and line search (HL-CL) [15]. The HL-CL computes $\nabla G(\mathbf{u})$ only one time by iteration to find $\mathbf{d}^k$. Then a circle search is performed to minimize $G(\mathbf{u})$:

$$\mathbf{u} = argmin_{\zeta} \left(\frac{\left\| \mathbf{d}^k + \mathbf{u}^k \right\|}{\left\| \zeta \mathbf{d}^k + \mathbf{u}^k \right\|} (\zeta \mathbf{d}^k + \mathbf{u}^k) \right) \tag{2.40}$$

where $\mathbf{u} = \xi \tilde{\mathbf{u}}$, and the sclar ξ is determined with the condition on the limit state function expressed in Eq. (2.41). A secant method search is used to locate $\mathbf{u}^{k+1}$ on the feasible region $G(\mathbf{u}) = 0$. A detailed description of the HL-CL algorithm can be found in Choi et al. (2017) [15].

$$\mathbf{u}_{k+1} = \xi \tilde{\mathbf{u}}, \qquad G(\xi \tilde{\mathbf{u}}) = 0 \tag{2.41}$$

As a result, a huge reduction in CPU time can be achieved [51] by avoiding gradient computation. Despite this important advantage, while coupling the HL-CL with the HOS-NWT, it was noted that the algorithm applying the secant method failed during the line search stage after a few iterations. In particular for the cases with a high HOS order $M > 2$, even with a reasonable H_s value. This problem seems to be related to the use of the zero search algorithm that does not converge when the limit state function G has a high convexity variation (see Figure 2.12). In this case, the secant algorithm keeps oscillating between two solutions or leads to unrealistic wave elevation values causing the HOS simulation divergence. This behavior was observed during the tests.

Modified Hasofer and Lind with Goldstein-Armijo (MHLGA) algorithm

As outlined above, an HL-based algorithm denoted MHLGA was implemented in the present study. The MHLGA procedure developed by Bureau Veritas (BV) takes benefits from the previous two algorithms. That is, the MHLGA i) uses a merit function to avoid the zero search procedure and ii) does not require any gradient evaluation of G. With this in mind, we can introduce the following merit function [78]:

$$m(\mathbf{u}) = \frac{1}{2} \|\mathbf{u}\|^2 + \frac{c}{2} G(\mathbf{u})^2 \tag{2.42}$$

The line search is conducted with Eq. (2.38) and Eq. (2.39). It has been proved that $\mathbf{d}^k$ is a descent direction for the merit function at any $\mathbf{u}$ point under the following

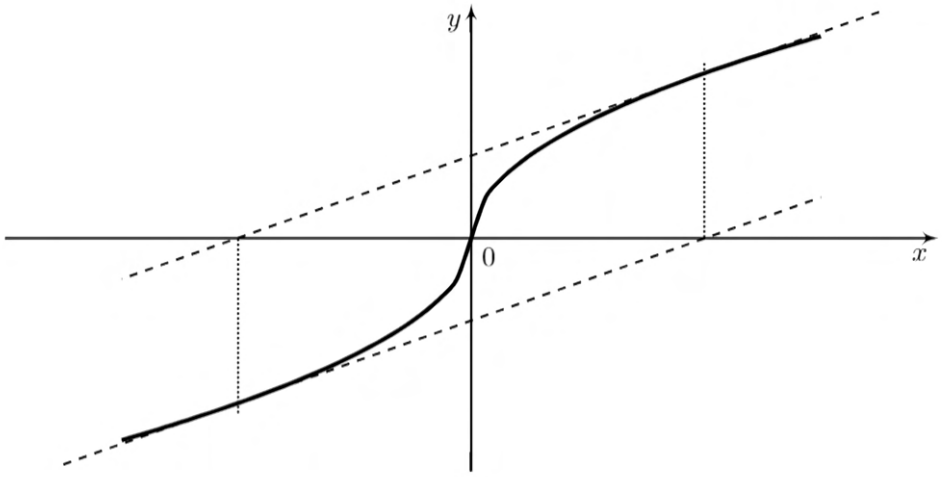

Figure 2.12 – Example of Newton's / secant method failure, the algorithm remains stuck in an infinite loop

condition [78] :

$$c > -\frac{1}{G(\mathbf{u})}\frac{\nabla G(\mathbf{u})\mathbf{u}}{\|\nabla G(\mathbf{u})\|^2} \tag{2.43}$$

where $G(\mathbf{u}) \neq 0$. α^k is determined as:

$$m(\mathbf{u}^k + \alpha^k \mathbf{d}^k) < m(\mathbf{u}^k) \tag{2.44}$$

Imposing the condition in Eq. (2.44) only may lead to a very small step α^k and then a poor algorithm performance. It is therefore recommended to use this condition with a step adjustment algorithm in order to conserve a reasonable step length [78, 60]. One solution is to use the Goldstein-Armijo (GA) rule (see Figure 2.13) [69]:

$$\alpha\mu_2 \nabla m(\mathbf{u}^k)\mathbf{d}^k \leq m(\mathbf{u}^k + \alpha\mathbf{d}^k) - m(\mathbf{u}^k) \leq \alpha\mu_1 \nabla m(\mathbf{u}^k)\mathbf{d}^k \tag{2.45}$$

with

$$\nabla m(\mathbf{u}^k) = \mathbf{u}^k + c^k G(\mathbf{u}^k)\nabla G(\mathbf{u}^k) \tag{2.46}$$

where $0 < \mu_1 < \mu_2 < 1$. This search rule has the advantage of not requiring any gradient computation. The MHLGA algorithm can be presented as follows:

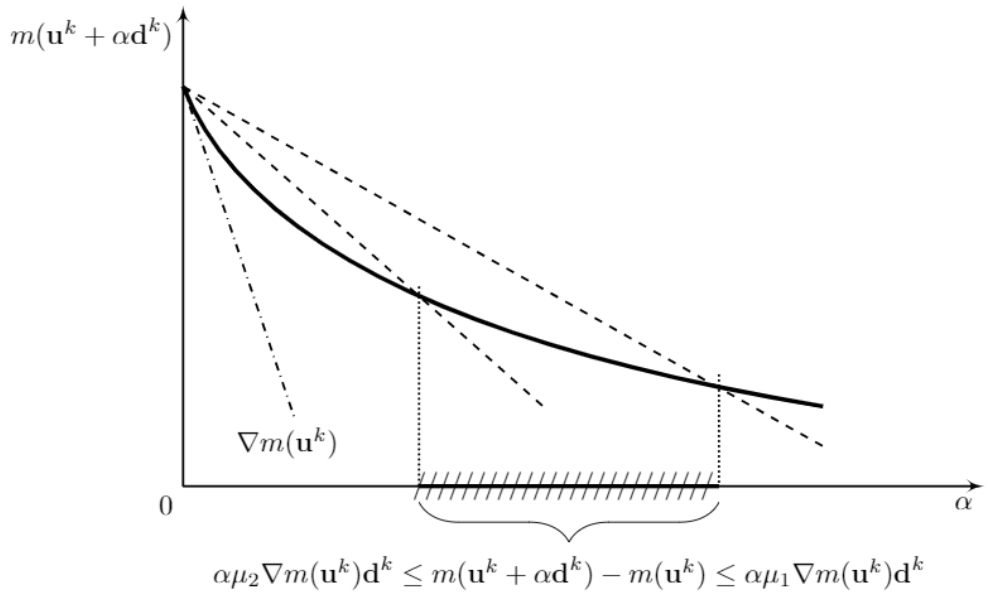

Figure 2.13 – Goldstein-Armijo line search method

(MHLGA): Modified Hasofer and Lind with Goldstein-Armijo search

Inputs: Initial solution $\mathbf{u}_0$, $k = 0$

Parameters: $A > 0$,$B > 0$, $0 < r_1 < 1$, $r_2 > 1$, $0 < \mu_1 < \mu_2 < 1$

1. Compute limit state function gradient $\nabla G(\mathbf{u}^k)$
2. Compute search direction $\mathbf{d}^k$
3. Compute c^k
   - If $G(\mathbf{u}^k) = 0$ choose $c^k = B$
   - Else $c^k = A \left| \dfrac{1}{G(\mathbf{u}^k)} \dfrac{\nabla G(\mathbf{u}^k)\mathbf{u}^k}{\|\nabla G(\mathbf{u}^k)\|^2} \right|$
4. Line search (start with $\alpha = 1$). While Goldstein-Armijo rule is not satisfied:
   - If $m(\mathbf{u}^k + \alpha \mathbf{d}^k) - m(\mathbf{u}^k) > \alpha\mu_1 \nabla m(\mathbf{u}^k)\mathbf{d}^k$:
     $\alpha = r_1 \alpha$
   - Elseif $\alpha\mu_2 \nabla m(\mathbf{u}^k)\mathbf{d}^k > m(\mathbf{u}^k + \alpha \mathbf{d}^k) - m(\mathbf{u}^k)$:
     $\alpha = r_2 \alpha$
5. $\alpha^k = \alpha$
6. $\mathbf{u}^{k+1} = \mathbf{u}^k + \alpha^k \mathbf{d}^k$
7. $\beta = \left\| \mathbf{u}^{k+1} \right\|$
8. $k = k + 1$
9. Check stopping criterion in β (see Eq. (4.3)).

The advantage of using the nonlinear wave solver is that the numerically computed wave elevation can in principle be reproduced deterministically in the experimental wave tank. The calculation procedure coupling with the HOS-NWT is applied to i) crest-targeted EDW and ii) VBM-targeted EDW, respectively, and a detailed description will be dealt with in each section (see Sections 4.2 and 5.2.3).

2.3.3 Initial wave set $\mathbf{u}^0$ for the algorithm

In the EDW calculation procedure for each subject, crest- and VBM-targeted FORM, the corresponding linear EDW method is applied when determining the initial condition of the FORM algorithm. Starting with the initial values close to the solution makes the procedure effective. For the crest-targeted FORM EDW in Chapter 4, the NewWave method explained in Section 1.2.2 was taken into account for the calculation of initial wave components $\mathbf{u}^0$. For the VBM-targeted FORM EDW in Chapter 5, the initial wave components $\mathbf{u}^0$ were determined by applying the RCW method addressed in Section 1.2.2.

The concept of the NewWave and RCW seems very similar to the FORM approach, but, both are frequency domain-based analytical approaches using spectral data and the linear description of the wave in the calculation. Thus, the FORM-based EDW approach that calculates the EDW with the consideration of nonlinear waves in the time domain is distinguished, providing not only a more accurate target response as an indicator but also a more realistic EDW profile.

Chapter 3

Experimental process

3.1 Test facility

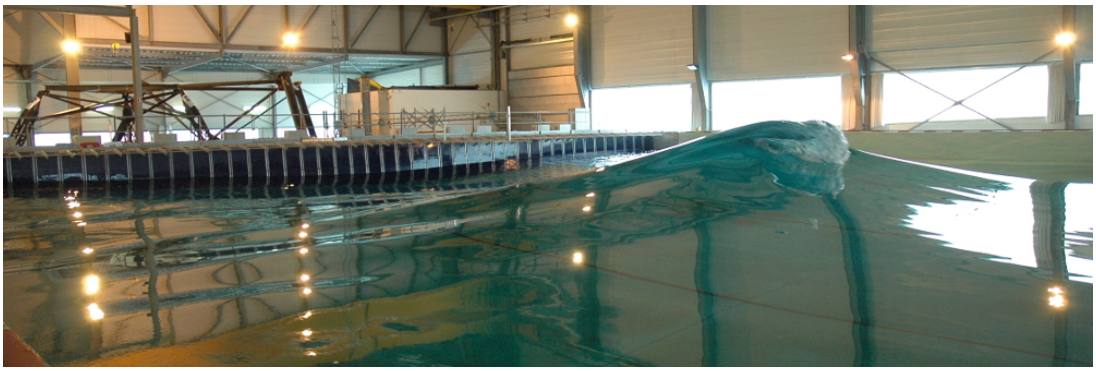

Figure 3.1 – Ocean engineering basin at LHEEA, Ecole Centrale de Nantes. The picture is taken from LHEEA's website

The ocean engineering basin of LHEEA at Ecole Centrale de Nantes measuring 50 m in length, 30 m in width, and a constant depth of 5 m, is where all the experimental studies of the present thesis were performed. A wavemaker that consists of 48 individual flaps is located on one side of the basin, capable of the generation of multi-directional waves as well as unidirectional waves. An absorbing beach on the opposite side of the wave basin is present. The beach absorbs waves, preventing disturbance by the reflected waves.

As presented in Figure 3.2, the ocean engineering basin is capable of generating waves in the range from 0.5 s to 5.0 s in wave period with a maximum H of 1.0 m for regular wave and a maximum H_s of 0.8 m for irregular waves. Most of the wave conditions considered in this thesis are within the green range. In the case of irregular waves (IW), the conditions containing breaking waves are intentionally considered, and in the case of very steep regular waves (RW), the maximum height is out of the range.

Wave calibration was basically preceded for all cases including the severe cases through the wave calibration process mentioned in Section 2.2.3. In the case of irregular waves, since all wave components of a given sea state are measured in one test,

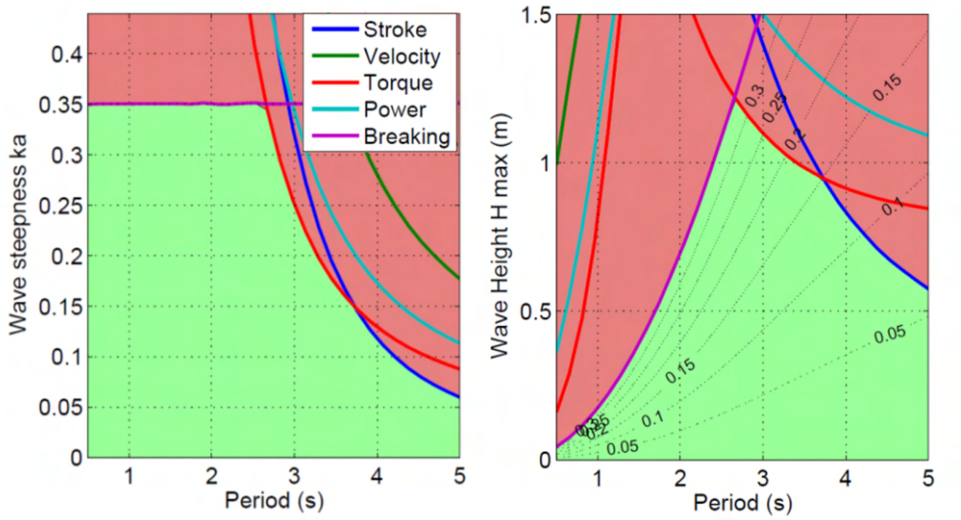

Figure 3.2 – Reproducible wave ranges of the ocean engineering wave basin at LHEEA in terms of wave steepness and wave height.

those can be corrected through one test simultaneously, although an additional wave calibration process may be required depending on the wave condition.

Conversely, regular waves were calibrated on a test-by-test basis, and even if the duration of each test case is shorter than the IW cases, an average interval of about 20 minutes was required between tests to minimize the effect of the residual waves. On this basis, correction for all the RW cases was considered time-consuming. Given that the correction factor is assumed to not vary much for waves of the same steepness and similar period, the calibration was performed on a selected subset of waves with the same steepness. Then, the correction coefficient was interpolated for each wave.

3.2 Description of the model and instrumentation

As mentioned in the introduction, the voyage of containerships is sometimes conducted in a harsh environment such as the North Sea, so that the response in such conditions can be expected to be (strongly) non-linear. To estimate the nonlinear effects induced by the waves on internal loads and motions, we use a 9-segmented 6750-TEU containership model with a scale ratio of 1/65 [6]. The physical quantities of interest measured and analyzed in this study are as follows:

- 6-DOF motions at the COG of the model
- Vertical bending moment (VBM) at 8 intersegments
- Horizontal bending moment (HBM) near the COG of the model

Sign conventions of the physical quantities above are based on the Bureau Veritas (BV) Rule Note NR 625 [8]. In the case of 6-DOF motions, the first three motions correspond to translational motions namely, surge, sway, and heave along the x, y, and z axes of the body-fixed reference frame $\{b\}$ defined with the origin o_b amidships in the waterline (see Figure 3.4). Where the positive direction of the motions follows the positive x, y, and z direction of the body-fixed frame. The last three called roll, pitch, and yaw refer to rotations about the respective x, y, and z axes, and their positive rotations follow the right-hand screw convention.

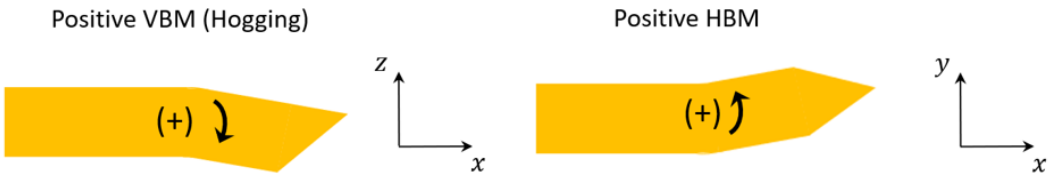

Figure 3.3 – Sign conventions for VBM and HBM

In the case of the wave bending moments, as presented in Figure 3.3, the positive VBM (hogging) and HBM are when the compressive stress is induced in the bottom and the port side of a ship respectively.

The main dimensions of the model are the same as the one used in the ITTC-ISSC benchmark study carried out by Kim and Kim (2016) [53] (see Table 3.2). Most of the experiments considering the segment model have applied backbone-type beam structures and attached a strain gauge to an appropriate location according to the internal loads to be measured in the section of interest, for example, VBM and HBM. The strain gauges measure the strain of the beam structure at the corresponding location, and the conversion process of strain to forces or moments is carried out [41, 61]. Lee et al. (2011) [59], as part of WILS II (Wave Induced Loads on Ships) Joint Industry Project organized by KRISO (Korea Research Institute of Ships and Ocean engineering), carried out a numerical and experimental investigation on the effect of springing and whipping on VBM responses of a flexible containership model applying an open cross-section backbone. Wave type was limited to mostly regular ones (one irregular sea state for whipping analysis), but various wave heights and ship speeds were taken into account. In the case of the whipping test, a comparison between the numerical and experimental results was made in the irregular wave case, and it was confirmed that the overall trend of the time series was comparable with each other. However, this was the result of applying different wave signals with two different wave phase sets for the same wave spectrum, thus the quantitative comparison of the VBM signal could not be made, but only the response spectrum was compared from a qualitative point of view. The study

found that springing also occurred by the encounter wave frequencies which are multiples of the natural hull vibration frequency, but the numerical simulation appeared to provide VBM estimates quite different from the experimental results in magnitude.

In this study, prior to applying the flexible model, the focus was on clearly understanding the effects of wave nonlinearity with various conditions on the rigid model. Therefore, a closed beam structure was designed and reflected. A 6-DOF load sensor is installed between segments (denoted as 'intersegment') near amidships to directly measure internal loads. Additionally, hydrodynamic loads by fluids are measured with 3-DOF load sensors in each segment, and reconstruction of internal loads at desired locations with the measurement data of 3-DOF load sensors at each segment is performed.

The experimental configuration of this thesis not only intuitively provides the size of the internal loads through direct measurement at the location of interest but also enables verification of the experimental measurement results through comparison with the reconstruction process results, increasing the reliability of the experimental results. Four tensiometers attached to the four mooring lines are used to qualitatively analyze how the restoring moment due to line tension affects ship behavior and HBM response. The mooring system's sensitivity to responses [102] has not been discussed in detail so far in previous studies, and therefore, this experimental setup can be considered the strength of this thesis.

Table 3.1 – Principal dimensions of 6750-TEU containership

	Prototype	**Model**
Scale	1/1	1/65
L_{pp} **(m)**	286.6	4.409
B (m)	40	0.615
H (m)	24.2	0.372
d (m)	11.98	0.188
Displacement	85663.8 (ton)	311.93 (kg)
KG (m)	16.562	0.257
LCG from AP (m)	139.56	2.146
kxx (m)	14.4	0.222
kyy (m)	71.5	1.109
kzz (m)	71.4	1.106

The sensors and instrumentation are selected at proper locations according to the quantities of interest, identical to what was done in the first campaign performed with the same model [6]. The main principles of each segment are presented in Table 3.2. Where the longitudinal (LCG) and vertical (KG) center of gravity of each segment are expressed based on AP and baseline respectively. As presented in Figure 3.4, the

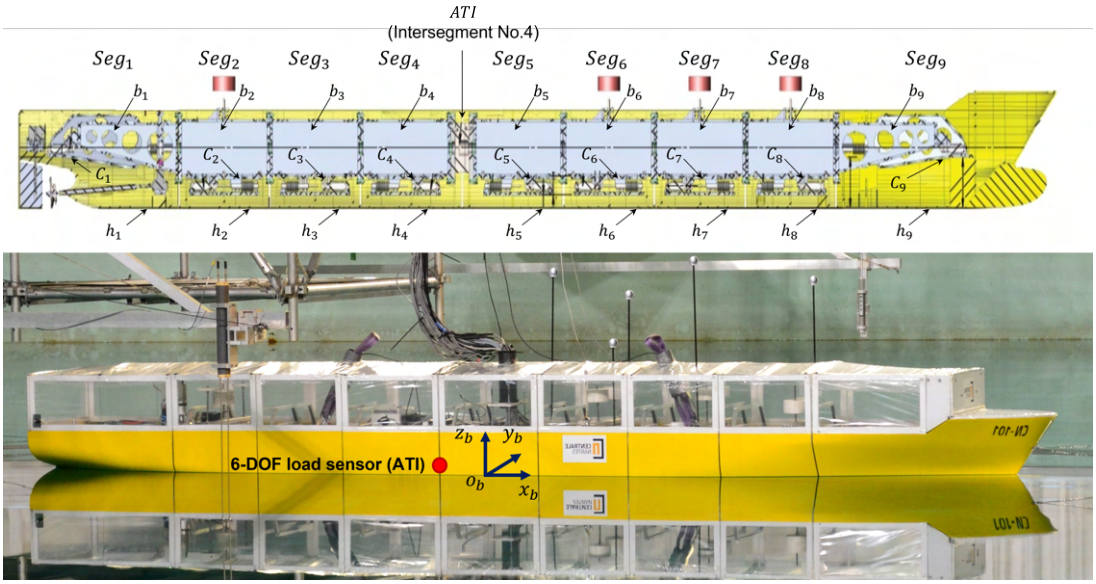

Figure 3.4 – 9-segmented 6750-TEU containership model and load sensor location

model consists of 9 segments from the stern (Seg_1) to the bow (Seg_9), each of which is equipped with a 3-DOF load sensor (C_i). The 3-DOF load sensor consists of 3 HBM Z6FC3 load cells and connects the beam part (b_i) to the hull part (h_i) (see Figure 3.7). Thus, a total of 27 HBM sensors are used and the maximum measurement range of the HBM load cells applied in this study is 30 kg to 100 kg.

The segments are connected to each other with bolts through their element b_i and set as a rigid model (see Figure 3.5). The beam structures from segments No.2 to No.8 have a constant shape close to a rectangular parallelepiped, and in each segment, the 3-DOF load sensor that measures the force in z (F_z) and the moments in x and y (M_x and M_y) is attached between the beam structure and the hull. Therefore, it measures both the wave hydrodynamic loads and inertial terms. The beam structure of the bow and stern is designed to fit the shape of the hull as shown in Figure 3.6. A 6-DOF load/torque sensor, Omega 191 made by a company ATI denoted as ATI sensor in this study is installed between beams b_4 and b_5 corresponding to the intersegment No.4 to directly measure the 6-DOF internal loads at the location (see Figure 3.7). This model setup can be used to measure a large range of loads up to 1400 Nm for moments.

Figure 3.8 shows the process of data measurement and acquisition through sensors installed in the model and relevant devices. At first, when the wavemaker is run through a wavemaker control computer, two other computers, one for 6-DOF motions and another for accelerations and wave loads are triggered. From that moment, data measurements start with the relevant sensors presented in Figure 3.8.

Thus, motions, accelerations, and wave load data measurements are automatically synchronized with wave elevation measurements. The data measured from the sensors

Table 3.2 – Main principles of each segment

Segment	Included appendages	Mass (kg)	LCG (m)	KG (m)	x InterSeg (m)	Inertia (kg.m^2)			
						Ixx	Iyy	Izz	Ixz
Seg_1	h_1, b_1, c_1	32.604	0.322	0.265	0.628	0.891	1.876	1.85	0.061
Seg_2	h_2, b_2, c_2	28.713	0.827	0.252	1.038	1.487	1.47	1.029	-0.237
Seg_3	h_3, b_3, c_3	26.195	1.242	0.206	1.448	0.718	0.72	0.869	0.002
Seg_4	h_4, b_4, c_4	27.483	1.660	0.204	1.905	0.821	0.778	0.976	-0.007
ATI	-	31.634	1.905	0.252	-	0.3	0.191	0.191	0
Seg_5	h_5, b_5, c_5	28.621	2.148	0.209	2.362	0.836	0.82	1.014	0.007
Seg_6	h_6, b_6, c_6	37.503	2.565	0.291	2.772	1.715	1.553	1.065	-0.017
Seg_7	h_7, b_7, c_7	35.006	2.996	0.283	3.182	1.41	1.363	1.017	0.165
Seg_8	h_8, b_8, c_8	34.314	3.385	0.297	3.592	1.219	1.269	0.905	0.193
Seg_9	h_9, b_9, c_9	29.852	3.957	0.280	4.587	0.557	1.863	1.896	0.041
Full Model	-	311.925	2.146	0.257	-	10.616	383.317	381.864	-5.835

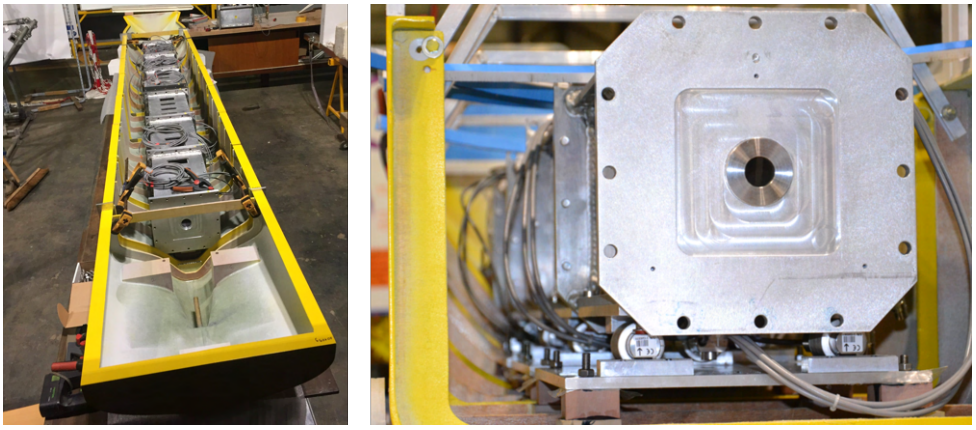

Figure 3.5 – Arrangement of beam structures (b_i and c_i) for segments No.2 to No.8

are conditioned through a data acquisition system called QuantumX device and a wave gauge conditioner, and the data is finally transmitted to the corresponding PC. All the sensors measure signals with a 100 Hz sampling rate.

The 6-DOF motions at the center of gravity (COG) of the model are measured through an optical motion tracking system, $Qualisys$. The reference coordinate system of $Qualisys$ is defined through its calibration at $x = 18.2$ m in the waterline, and a total of 4 cameras are installed to track the motion of several reflective markers attached to the model (see Figure 3.4) to measure the motion of the COG with respect to the initially defined reference frame.

Three accelerometers are installed at (0.163, 0, 0.340), near amidships (2.258, 0, 0.363), and (3.66, 0, 0.385) based on the aft perpendicular (AP) and the baseline of the model. The measured acceleration data is mainly used to calculate the inertia force component of each segment in the internal load reconstruction process with 3-DOF load sensor measurement.

The model is moored with four horizontal lines respectively at α of $45°, -45°, -135°, 135°$ (from Line 1 to 4 in Figure 3.9) with respect to the positive x_b of the body-fixed frame $\{b\}$. The stiffness of each mooring line was soft enough with the stiffness of 58 N/m

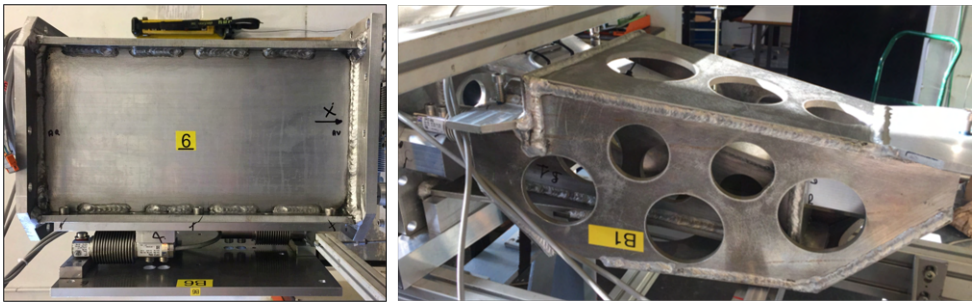

Figure 3.6 – Segment 2 to 8 beams (left) and 1 and 9 segment beam structures (right)

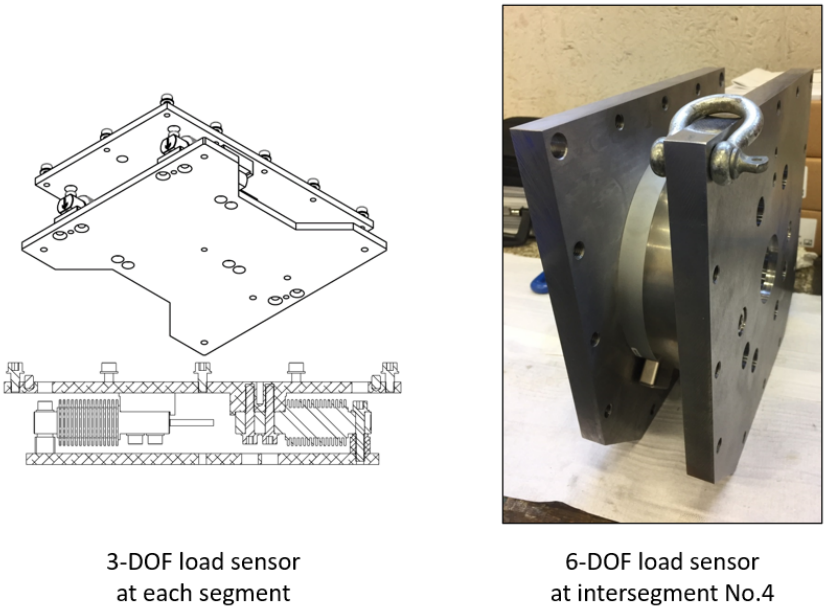

Figure 3.7 – Schematic view of 3-DOF load sensors (c_i) installed at each segment (left) and 6-DOF load sensor ATI installed at intersegment No.4 for direct measurement of internal loads (right)

used to minimize its effect on the model's response. Taking into account the theoretical added mass of 93 kg, the theoretical natural period of the moored system is 9.41 s, and it is found to be 10.1 s (around 80 s in full scale) in experiments. More details about the sensors and the experimental setup can be found in [6].

Tension measurement of the four horizontal mooring lines is performed using a tensile/compressive force transducer, HBM U9C, which can measure a nominal force of up to 500 N. The two mooring lines at the bow and the other two mooring lines at the aft are installed at (4.520, 0, 0.257) and (-0.091,0, 0.257) based on AP and baseline respectively, and each tensiometer (total of 4) is attached to the fairlead, connecting each mooring line to the model.

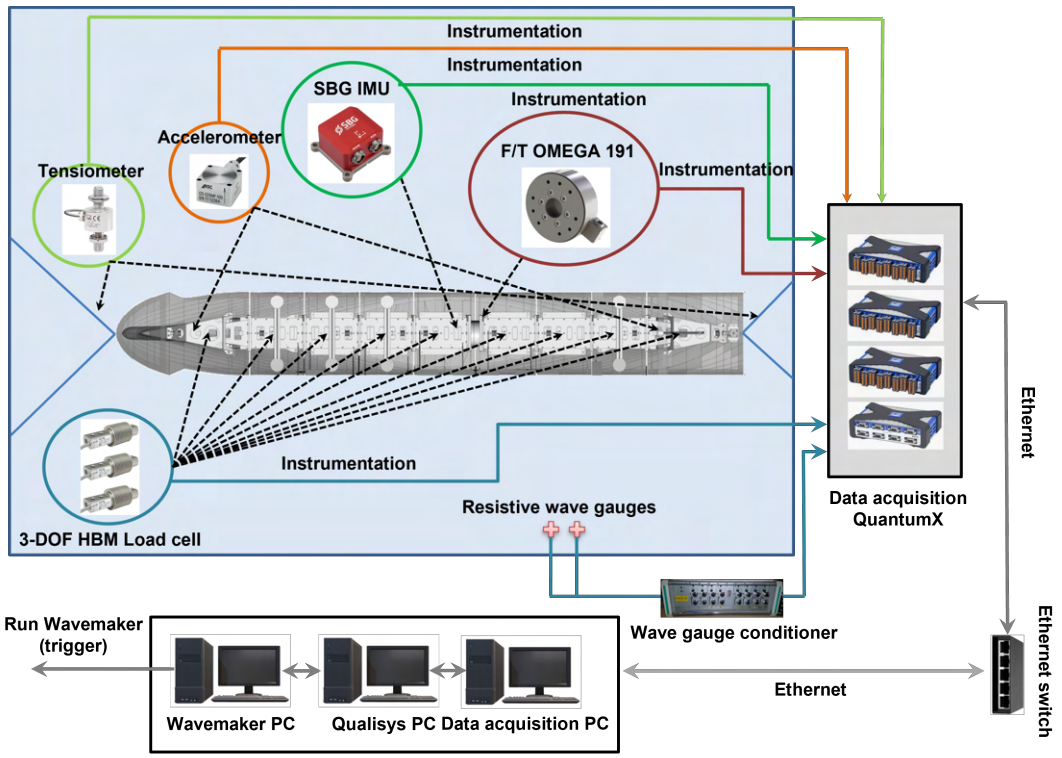

Figure 3.8 – Schematic diagram of sensor position, data measurement, and acquisition process

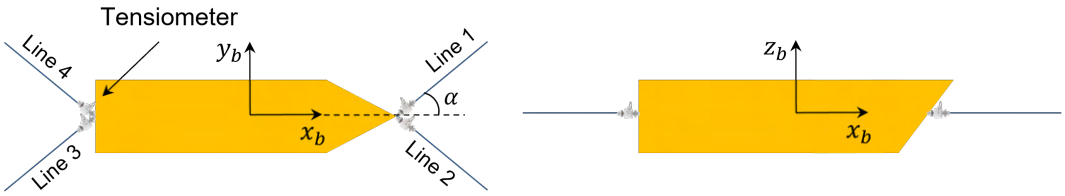

Figure 3.9 – Schematic configuration of a horizontal mooring system with tensiometer installed at each line

3.3 Reconstruction of VSF and VBM

Considering that the 3-DOF load sensors at each segment measure both forces and moments namely F_z, M_x, and M_y, the reconstruction can be carried out for VSF and VBM. The simplified form of Eq. (2.2), expressed only in the vertical plane, is:

$$\begin{pmatrix} Q_x \\ Q_z \\ M_y^A \end{pmatrix}^{x=x_A} = - \begin{pmatrix} F_{extx} \\ F_{extz} \\ M_{exty}^A \end{pmatrix}^{x<x_A} + \begin{pmatrix} m\left[\dot{u} + qw - (x_G - x_A)\, q^2\right] \\ m\left[\dot{w} - qu - (x_G - x_A)\, \dot{q}\right] \\ I_y\, \dot{q} - m\,(x_G - x_A)\,(\dot{w} - qu) \end{pmatrix}^{x<x_A} \tag{3.1}$$

with $F_{z_{moor}} = M_{y_{moor}} = 0$. The external force vector acting on $0 < x < x_A$ of the ship model, $\mathbf{F}_{ext}^{x<x_A}$, and the external moment vector at x_A, $\mathbf{M}_{ext}^{A}$, can be derived with the data of j-1 segments corresponding to the number of segments in $x < x_A$ as follows:

$$\begin{pmatrix} F_{extx} \\ F_{exty} \\ F_{extz} \\ M_{extx}^{A} \\ M_{exty}^{A} \\ M_{extz}^{A} \end{pmatrix}^{x<x_A} = \begin{pmatrix} \sum_{i=1}^{j-1}(\mathbf{F}_{hydro/h_i} + \mathbf{P}_i) \\ \sum_{i=1}^{j-1}\left(\mathbf{M}_{hydro/h_i} + \mathbf{r}_A^{G_i} \times \mathbf{F}_{hydro/h_i} + \mathbf{r}_A^{G_i} \times \mathbf{P}_i\right) \end{pmatrix}^{x<x_A} \tag{3.2}$$

where $\mathbf{F}_{hydro/h_i}$, $\mathbf{M}_{hydro/h_i}$, and $\mathbf{P}_i = m_i\mathbf{g}$ are the fluid force, moment and the weight of the i^{th} segment.

To obtain the unknown fluid force and moment in Eq. (3.2) with the 3-DOF load sensor measurement, the Newton-Euler equations of motion for the hull part h_i of the i^{th} segment can be applied:

$$\begin{aligned} m_{h_i}\left(\frac{d\mathbf{V}_{h_i/n}^{b}}{dt} + \mathbf{\Omega}_{b/n}^{b} \times \mathbf{V}_{h_i/n}^{b}\right) &= \mathbf{P}_{h_i} + \mathbf{F}_{hydro/h_i} \quad \text{for each segment } i \\ I_{h_i}\frac{d\mathbf{\Omega}_{b/n}^{b}}{dt} + \mathbf{\Omega}_{b/n}^{b} \times I_{h_i}\mathbf{\Omega}_{b/n}^{b} &= \mathbf{M}_{P_{h_i}} + \mathbf{M}_{hydro/h_i} \quad \text{for each segment } i \end{aligned} \tag{3.3}$$

where $\mathbf{m}_{h_i}$ and $\mathbf{I}_{h_i}$ are a mass and a moment of inertia, $\mathbf{P}_{h_i}$ and $\mathbf{M}_{P_{h_i}}$ are the weight and the corresponding moment of the hull part of each segment. The fluid force, $\mathbf{F}_{hydro/h_i}$, and moment, $\mathbf{M}_{hydro/h_i}$, induced by a given wave condition can be obtained with the measurement data ($\mathbf{T}_{c_i}$ and $\mathbf{R}_{c_i}$) through the 3-DOF load sensors c_i as expressed in Eq. (3.4). This assumes that the position of c_i coincides with $\mathbf{G}_{\mathbf{h_i}}$, the COG of the hull part of each segment. The physical quantity of the 3-DOF load sensor of each segment corresponds to the net force and moment acting on each segment.

$$\begin{aligned} \mathbf{T}_{c_i} &= \mathbf{F}_{hydro/h_i} + \mathbf{P}_{h_i} - m_{h_i}\left(\frac{d\mathbf{V}_{h_i/n}^{b}}{dt} + \mathbf{\Omega}_{b/n}^{b} \times \mathbf{V}_{h_i/n}^{b}\right) \\ \mathbf{R}_{c_i} &= \mathbf{M}_{hydro/h_i} + \mathbf{M}_{P_{h_i}} - \left(I_{h_i}\frac{d\mathbf{\Omega}_{b/n}^{b}}{dt} + \mathbf{\Omega}_{b/n}^{b} \times I_{h_i}\mathbf{\Omega}_{b/n}^{b}\right) \end{aligned} \tag{3.4}$$

Once the fluid forces and moments of the hull part of each segment are calculated, Eqs. (3.1) and (3.2) allow the reconstruction of the vertical shear force Q_z and the vertical bending moment M_y at each intersegment, thus providing their longitudinal distribution along the model. This enables cross-validation with the loads directly measured via a 6-DOF load sensor ATI (see right hand picture in Figure 3.7) installed between the beam elements b_4 and b_5. This intersegment corresponds to the intersegment No.4

counting in ascending order from the stern to the bow (see Table 3.2).

3.4 Data processing

3.4.1 Zeroing

Each test undertaken in the wave tank started from a calm water condition. Accordingly, the wavemaker motions were ramped. In the measurement, all types of signals were synchronized and measured from the start of the wavemaker. Thus, the response time signals contained successive intervals of i) calm water conditions, ii) transients, iii) periodic or irregular responses and iv) deceleration. Note that for the EDW cases the transient is the interval of interest, for RW the data analysis considers only the periodic oscillations around the dynamic equilibrium position reached by the model, and for IW cases the data analysis considers the oscillations after the transients vanish.

The response of the model at rest in calm water corresponds to the effect of the hydrostatic pressure. Thus, to analyze only the hydrodynamic responses induced by a given wave condition, 'zeroing' is first performed by subtracting the signals at rest from the total measurement. Hydrostatic results are effectively used not only to check the experimental setup but also for the total force estimation.

3.4.2 Filtering

As per Bouscasse et al. (2022) [6], a hammer test in calm waters was conducted and was found that the natural frequency of the beam in M_y is around $f_R = 14$ Hz, giving the ratio of the first mode VBM's natural frequency to the peak wave frequency of each sea state $f_R/f_p > 20$. This showed that the rigidity of the beam is sufficient. It also indicates that applying 7 Hz low-pass filtering frequency to eliminate the effect of the structural deformation (vibration) on the responses of interest is reasonable. More details can be found in previous research with the same model [6, 42].

3.5 Response Amplitude Operator

The theoretical linear RAO is based on the linear theory presented in Appendix C. In general, as the nonlinearity of a given wave condition increases, the resulting response of interest may become more sensitive to nonlinearities. Accordingly, the model is likely to behave differently. This section focuses on the calculation of RAO

magnitudes. Changes in phase with respect to a given wave condition are explained in Appendix A.

In the RAO calculation, the numerator can be optionally defined as either the response from a direct measurement or its decomposed n^{th} harmonic response. The former case is obtained from the measurement, while the latter is computed by applying a Fast Fourier Transform (FFT). Both are taken into account in the calculation of distinct RAOs, and the contribution of the nonlinear wave effects to the response of interest can be qualitatively estimated through the comparison of different RAOs computed at different wave steepness (refer to [6]).

3.5.1 Regular waves

Selection of the time window for the analysis

For regular wave cases, data measurements are typically carried out from the start of the wave generation to when the reflected wave affects the incident wave field. Thus the acquisition time varies depending on the period of a given wave, but generally, it lasts for a couple of minutes. The selection of a 'good' time interval among the whole acquisition time is the first task to be accomplished prior to data post-processing. The data in the selected time window (T_w) should present a relatively steady response and not be disturbed by reflected waves. In this study, the whole time signal has been processed by using a FFT-based function, helping to assess the wave quality in magnitude and periodicity over the whole time signal. Specifically, the entire time signal is divided into several segments having a length of T, and the Fourier Transform is performed segment by segment. Then the n^{th} harmonic coefficients of each segment are compared with the neighboring ones to check their consistency with each other. The definition of the n^{th} series coefficient c_n applied on a function f_c is given by:

$$c_n(t, f, f_c) = \frac{1}{T} \int_{t-\frac{T}{2}}^{t+\frac{T}{2}} f_c(x, \tau)\, e^{-i(n2\pi f \tau)}\, d\tau \tag{3.5}$$

where c_n is the complex Fourier coefficient and T is a period of one segment and f is frequency of a given wave. Since Eq. (3.5) is applied only to the calculation of response RAO for the regular wave cases, a wave period of a given regular wave can be designated as T. More details can be found in Bouscasse et al. (2022) [6].

RAO calculation

The RAOs are by definition linear operators and only valid for very small wave steepness following Section 2.1. For the study case presented in this thesis, the motions

and loads of the structure are induced by steep nonlinear waves up to 11 % in H/λ, i.e. meaning that the wave and wave-induced responses are highly likely to contain (strong) nonlinear effects. Finding the nonlinear effects in the RAOs imposes some rigor on data processing. The fully nonlinear solution for the motions and the wave loads could be represented as:

$$X(t) = \mathbb{R}\left[\sum_{n=-\infty}^{\infty} c_n e^{i2\pi f_n t}\right] \tag{3.6}$$

where f_n is n^{th} harmonic excited motion frequency corresponding to a given wave frequency generated, and c_n is the complex Fourier coefficient which is calculated by using Eq. 3.5. It should be noted that the c_n is the coefficient calculated from the selected time window.

Then, the calculation of motion and bending moment RAOs is performed. All the RAO results are expressed in dimensionless quantity, and half the wave height, $H/2$, applied as one of the denominators corresponds to the theoretical values. The physical quantity of a numerator takes the n^{th} harmonic amplitude ($= |c_n|$) from the Fourier decomposition in Eq. (3.6). The n^{th} harmonic RAO of the arbitrary response $X(t)$ is thus expressed as:

$$|RAO^{(n)}| = \frac{\mu_n |c_n|}{\text{Denominator}} \tag{3.7}$$

$$\mu_n = \begin{cases} 1, & n = 0 \\ 2, & n > 0 \end{cases} \tag{3.8}$$

Additionally, by using direct measurement data that includes all harmonic components, the average of positive or negative peak events in the selected time window (T_w) can be applied as a numerator of the RAO:

$$\overline{X^{(+)}} = \frac{1}{N}\sum_{i=1}^{N}(X_i^{(+)}) \qquad \text{for N positive peaks in } T_w \tag{3.9}$$

The corresponding RAO can be expressed as follows:

$$|RAO^{(+)}| = \frac{\overline{X^{(+)}}}{\text{Denominator}} \tag{3.10}$$

The same goes for $|RAO^{(-)}|$ calculated with the negative peak events measured in the selected time window, T_w. Regarding the denominator of the RAO for translational and rotational motions, and wave bending moments, the following physical quantities are applied:

$$\begin{aligned} &\text{Translational motion} && = H/2 \\ &\text{Rotational motion} && = kH/2 \\ &\text{Bending moment} && = \rho g L_{pp}^2 BH/2 \end{aligned} \tag{3.11}$$

where k is the wave number calculated through the linear dispersion relation corresponding to the depth of the wave tank (5 m).

3.5.2 Irregular waves

The spectral density of a given wave with frequency f_i is defined as:

$$S(f_i)df = \frac{1}{2}A(f_i)^2 \tag{3.12}$$

where A is the amplitude of a given frequency component. The same applies to the response spectrum:

$$S_R(f_i)df = \frac{1}{2}A_R(f_i)^2 \tag{3.13}$$

BY using Eq $(\mathrm{C}.23)$, the magnitude of $RAO(f_i)$ is simply obtained from the square root of the ratio between the response and the wave spectrum:

$$|RAO(f_i)| = \frac{A_R(f_i)}{A(f_i)} = \sqrt{\frac{S_R(f_i)df}{S(f_i)df}} \tag{3.14}$$

In the case of irregular waves, the component decomposition of the wave and response signals is performed by the FFT-based Welch's overlapped segment averaging estimator [98]. Welch's method provides power spectral density and phase for each discrete frequency component. This study applies the Welch's method with a duration window of 50 s long and 50 % overlap. Then, the RAO amplitude of all discrete wave frequency components considered is obtained using the relationship in Eq. (3.14). Figure 3.10 shows the flow chart of the RAO estimation for the irregular wave case.

Appendix A deals with the validation of nonlinear hogging and sagging RAO estimation with the direct measurement data from the ATI sensor and includes a detailed process related to the irregular waves and the corresponding VBM responses spectrum covered in this section.

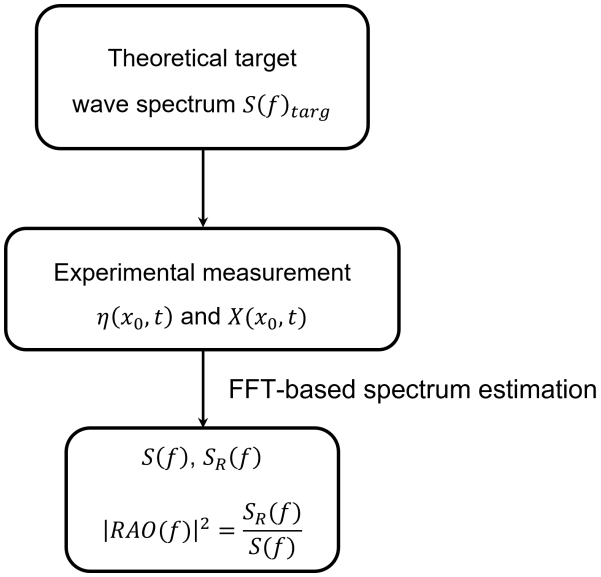

Figure 3.10 – RAO calculation with the Welch's spectral estimation method

Chapter 4

Numerical and experimental application of EDW approach

4.1 Introduction

This chapter presents the numerical and experimental validation of the practicality of a FORM-based EDW approach by comparing it with the Monte Carlo approach (i.e. the ensemble of all realizations with various wave phase sets) having a converged wave crest POE distribution [77]. The overall procedure is presented in Figure 4.1. In numerical and experimental configurations, the FORM-based EDW applying the HOS-NWT is evaluated against the corresponding (numerical or experimental) Monte Carlo reference results, respectively, and additionally, comparisons between results of the numerical and experimental configurations are performed.

Five sea states, mostly breaking sea states, are considered with H_s varying from 6 m to 17 m and T_p from 12.25 s to 17.0 s. Each sea state consists of a number of realizations (2h 30min time series after cutting off the transients) with various random wave phase sets. The spectra are calibrated experimentally to achieve the target spectrum at the target location. The same wavemaker motions obtained after calibration are also used numerically in the HOS-NWT so that a Monte Carlo reference is obtained both experimentally and numerically. This allows for the comparison of the wave spectrum and the crest POE with each other for each sea state. There are some differences between the physical and the numerical wave tanks. The former has physical and mechanical limitations, and the latter considers only the main characteristics of the physical wave tank. Furthermore, the breaking model is quite simple in the numerical wave tank and cannot reproduce accurately the complexity of the physical breaking. In this regard, a slight difference can be observed in the wave spectrum when comparing numerical and experimental results. Including the POE curve and estimated main spectral parameters, the agreement between experimental and numerical results in wave quality seems sufficient for it to be used as a reference for EDW cases.

For each sea state, three different EDW are studied, corresponding to different POE levels (see Figure 4.1). As part of the cross-validation of the EDW approach, the same

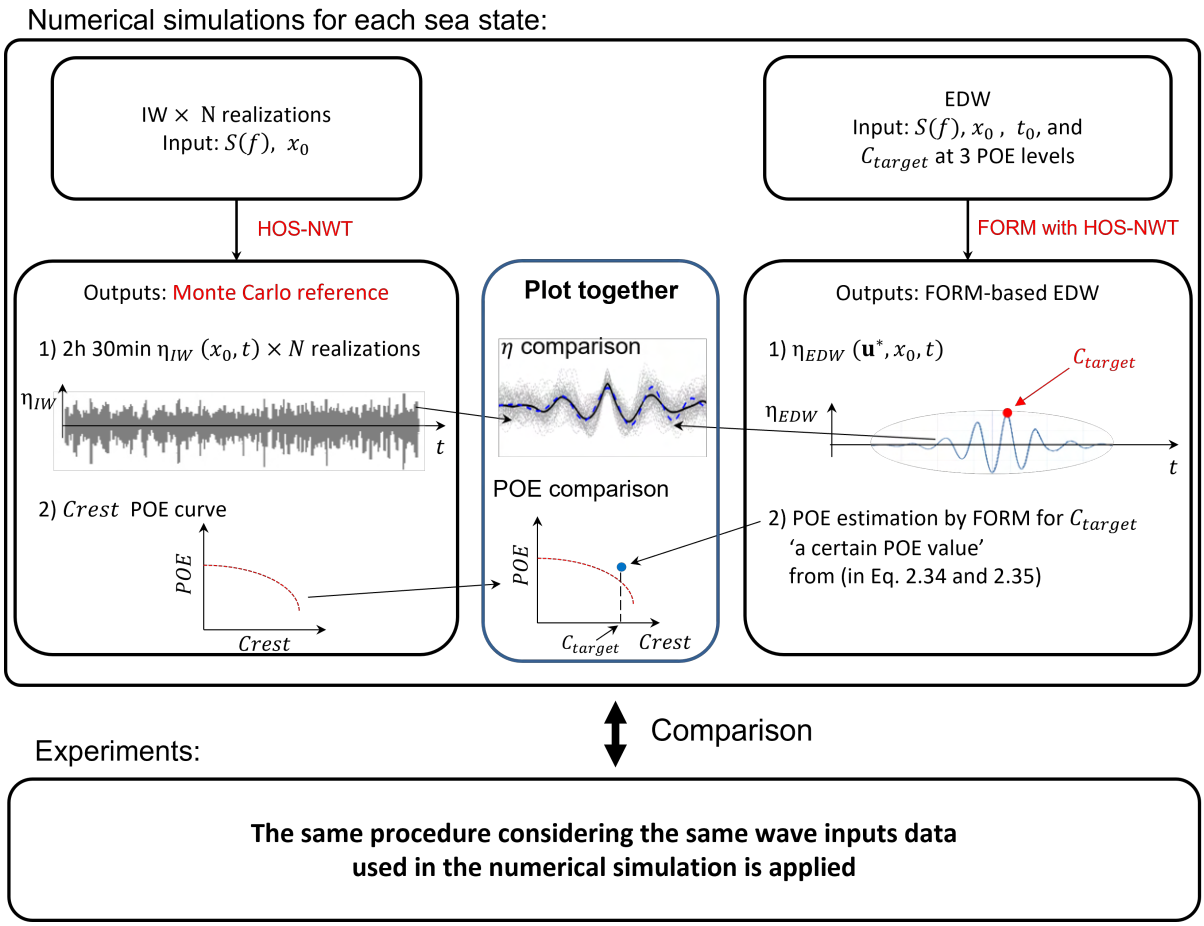

Figure 4.1 – FORM-based EDW validation procedure in numerical and experimental with Monte Carlo reference results.

EDW cases are generated in the experiment and the numerical wave tank. The original FORM approach proposes to use a linear wave elevation formula for the calculation of a certain EDW case in moderate sea states and suggests applying a second or higher-order term in the formula if the wave condition is harsh. In this case, there would be a possibility that the calculated EDW may contain uncertainty due to this conditional selection of the wave's nonlinearity depending on the severity of the sea condition. This would make the comparison, such as changes in shape characteristics, between EDW results ambiguous. Hence, in this study, a new EDW calculation procedure described in Section 2.3 is used. This method applies the same nonlinear wave model in the calculation of EDW in all sea states considered.

As shown in Figure 4.1, the study focuses particularly on a geometrical similarity review of the calculated EDW wave profile by directly comparing it with the corresponding irregular waves having a similar crest amplitude. Statistical analysis is performed as well with the crest POE distribution of a given irregular sea state and the POE of the related EDW cases estimated by the novel FORM method. The geometrical simi-

larity between the measured EDW wave signal and the corresponding irregular wave signals measured in a given sea state confirms that the FORM-based EDW generates a wave profile comparable to the most probable wave profile. In the statistical analysis, results show that in relatively severe sea states, the POE of individual EDW cases estimated by the novel HOS-NWT based FORM in Eq.(2.35) appears conservative as compared to the empirical wave crest POE distributions. The estimated POE for EDW cases in moderate sea states is in good agreement with the Monte-Carlo wave crest POE distribution of a given sea state.

4.2 Crest-targeted FORM calculation with HOS-NWT

Following Section 2.3 and Eq. (2.31) , a crest-targeted FORM EDW is calculated with the limit state function expressed as:

$$G(\mathbf{u}) = C_{target} - \eta^{HOS}(x_0, t_0|\mathbf{u}) = 0 \tag{4.1}$$

where $\eta^{HOS}(x_0, t_0|\mathbf{u})$ is calculated by the nonlinear wave solver HOS-NWT (detailed in section 2.2.2). The FORM optimization results in the most probable wave profile composed of $\mathbf{u}^*$ yielding a target crest amplitude C_{target} at $t = t_0$ and $x = x_0$. C_{target} will be dependent on the sea state and the target POE level considered.

With $\mathbf{u}^*$ and its β_{FORM}, the mean out-crossing rate of the target crest $\nu(C_{target})$ for the stationary stochastic process can be estimated following Eq. (2.34) [46]. The FORM reliability index β_{FORM} is inversely proportional to the mean out-crossing rate, meaning that the $\mathbf{u}^*$ at the MPP generates the most probable deterministic EDW wave episode inducing the specific target crest C_{target} among realizations that satisfy $G(\mathbf{u})$=0. The corresponding POE can be estimated with the relation below:

$$\begin{aligned} \text{Prob}(C < C_{target}) = \text{CDF}(C_{target}) &= 1 - \nu(C_{target})/\nu(0) \\ \text{Prob}(C > C_{target}) = \text{POE}(C_{target}) &= 1 - \text{CDF}(C_{target}) = \nu(C_{target})/\nu(0) \end{aligned} \tag{4.2}$$

At first, the numerical algorithm (see Figure 4.2) helps specify a target crest C_{target} having a specific exceedance probability level in a sea state of interest. The result is based on the so-called Forristall distribution [32] (see Section 2.2.3). Then, by applying the NewWave method (see Eq. (1.12)) with C_{target} and the wave spectrum of interest, the set of amplitudes and the corresponding phases of each wave frequency component (=$\mathbf{u}^0$) are first calculated to define the initial wavemaker motion as explained in Sections 1.2.2. The superscript k=0 in the **u** term denotes the initial "assumed" value.

Once the initial wavemaker motion is defined, the algorithm starts to iterate through successive HOS-NWT simulations with the aim to identify the most probable point (MPP), which consists of frequency components $\mathbf{u}^*$ satisfying a criterion in β. The criterion corresponds to the difference between β at k^{th} and $k+1^{th}$ iteration process as follows:

$$\beta^{k+1} - \beta^k < 0.002 \tag{4.3}$$

Initial β^0 is set to 0, and in the subsequent iteration, it is replaced by the newly calculated value with a set of $\{u_i, \bar{u}_i\}^k$ using Eq. (2.32). This means that the wavemaker motion is also modified according to the calculated $\mathbf{u}$ at each iteration.

$$G(\mathbf{u}^k) = C_{target} - \eta^{HOS}(x_0, t_0|\mathbf{u}^k) \tag{4.4}$$

At every iteration k of the EDW calculation process, $\mathbf{u}^k$ is computed by running the HOS-NWT. The process seeks $\mathbf{u}^* = \mathbf{u}^k$ when $\mathbf{u}^k$ satifies the criterion given in Eq. (4.3). In detail, with $\mathbf{u}^k$ in the k^{th} iteration, the wave time series $\eta^{HOS}(x_0, t|\mathbf{u}^k)$ is exported to compare its elevation at the target time t_0, $\eta^{HOS}(x_0, t_0|\mathbf{u}^k)$ with C_{target} (Eq. (4.4)). If the $\mathbf{u}^k$ meets the tolerance criterion in β (Eq. (4.3)), the iteration process ends and provides outputs, namely i) the wave elevation time series $\eta^{HOS}(x_0, t|\mathbf{u}^*)$ inducing C_{target} at the target time t_0 and ii) the corresponding wavemaker motion. Thus, as described in Section 2.2.3, the time-series data at the target location, represent the most probable wave profile.

4.3 Test cases

4.3.1 Irregular wave (IW) case

As listed in Table 4.1, five sea states defined by the JONSWAP spectrum are considered for the irregular wave conditions with H_s (T_p) ranging from 6 m (12.3 s) to 17 m (15.5 s). Note that all the cases referred to as SS6 to SS17 are simulated on a scale of 1/65 and all the results are presented as dimensionless quantities or as model scale quantities. For each sea state 35 realizations are simulated in the numerical wave tank (HOS-NWT), and the ensemble of realizations (i.e. the result from Monte Carlo simulations) is used as a reference for the EDW case. The simulation time of every single run is 1200 s at model scale and the length of the time window for the analysis is 1080 s (2h 30min at full scale). By considering the travel time of the shortest wave component as $3.5f_p$ at the target location x_0 based on x_0/c_g (c_g being the group velocity), fully devel-

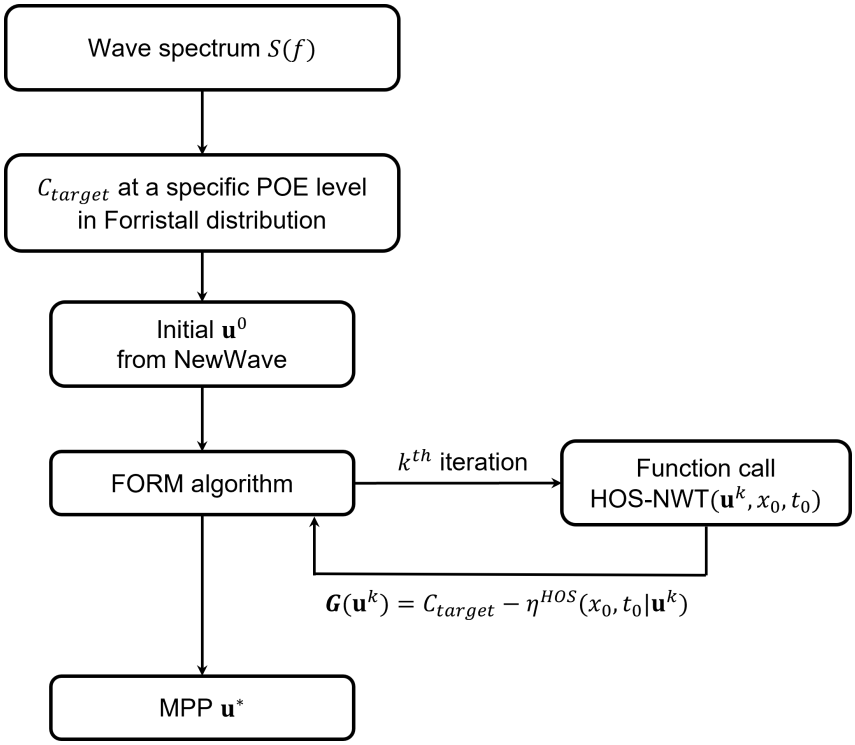

Figure 4.2 – HOS coupling with FORM

oped wave elevation data without any transient period are used in the post-processing analysis for each sea state.

Table 4.1 – Description of irregular sea state cases (full scale)

Case	H_s **(m)**	T_p **(s)**	γ	**Number of realization**		**Remark**
				EXP	**HOS**	
SS6	6.0	12.2	1.0	8	35	No breaking wave
SS8	8.3	14.0	1.5	12	35	Breaking waves
SS10	10.0	14.0	1.5	10	35	Breaking waves
SS12	12.0	14.0	1.5	8	35	Breaking waves
SS17	17.0	15.5	2.6	12	35	Breaking waves

4.3.2 EDW case

Each sea state is associated with 3 individual FORM-based EDW cases with different POE, and all EDW cases are calculated to have a target crest C_{target} at $x_0 = 18.2$ m from the wavemaker at $t_0 = 45$ s. The target crest C_{target} of each EDW case corresponding to a certain POE level is selected based on the Forristall distribution of each sea state as described in Table 4.2.

For reference, given that the wave energy of each sea state is dominant within $0.5f_p - 2.5f_p$ ($0.33 - 1.65$ Hz for SS6 and $0.26 - 1.30$ Hz for SS17), the reduced frequency range $0.35 - 1.6$ Hz for the EDW calculation is applied. Then, the target time $t_0 = 45$ s is decided based on the travel time of the highest frequency component (1.6 Hz) to the target location 18.2 m ($x_0/c_g = 37.2$ s). Under the given condition, the spectrum is discretized into $N = 78$ components ($df = 0.016$ Hz) with repeat period longer than $t_0 = 45$ s. The corresponding repeat period is $1/df = 62.5$ s, thus the repetition of the EDW time series before the target time $t_0 = 45$ s can be avoided. Hence, with the given discretized wave components, the EDW elevation can be generated at the wavemaker in calm water conditions with no waves and therefore will reach the target location without any disturbance by repeated waves. According to the previous sensitivity study on the number of frequency components by Ghadirian et al. (2017) [34], $N = 78$ may be considered sufficiently large enough to give a highly accurate resolution for the EDW elevation.

Table 4.2 – Description of EDW cases of each sea state ($1/65$ scale) at $x_0 = 18.2$ m and $t_0 = 45$ s

Case		H_s (m)	T_p (s)	Designated POE	C_{target} (m)
	SS6-1			10^{-1}	0.0523
SS6	**SS6-2**	0.092	1.519	10^{-2}	0.0753
	SS6-3			5×10^{-3}	0.0810
	SS8-1			10^{-1}	0.0724
SS8	**SS8-2**	0.128	1.736	10^{-2}	0.1042
	SS8-3			5×10^{-3}	0.1121
	SS10-1			10^{-1}	0.0882
SS10	**SS10-2**	0.154	1.736	10^{-2}	0.1274
	SS10-3			5×10^{-3}	0.1372
	SS12-1			10^{-1}	0.1073
SS12	**SS12-2**	0.185	1.736	10^{-2}	0.1557
	SS12-3			5×10^{-3}	0.1675
	SS17-1			10^{-1}	0.1530
SS17	**SS17-2**	0.262	1.923	10^{-2}	0.2223
	SS17-3			5×10^{-3}	0.2398

4.4 Numerical validations

The numerical Monte-Carlo simulations are first performed with the HOS-NWT for five sea states. Each sea state case consists of 35 realizations of 2h 30min wave simulation. It is to obtain the reference numerical solution. In this regard, the capability

to reproduce a given wave spectrum along with main spectral parameters is assessed. The resulting wave crest POE curve is used as a reference.

Then, the calculation of EDW is performed with the new FORM algorithm to which the HOS-NWT is applied. Based on the Monte Carlo reference of a given sea state, the accuracy of the algorithm to provide the EDW corresponding to the most probable wave profile at a given POE level is discussed. The geometrical characteristics of the calculated EDWs and their POE estimates by the FORM method are then discussed.

4.4.1 Numerical wave tank setup

The reproduction of the wave elevation generated in the experiment is done for cross-validation in a 2D numerical wave tank measuring 35 m in length (L_x) and 5 m in depth (L_z). It should be noted that the NWT applied is a digital twin of the ocean engineering basin at ECN, but with a smaller L_x. This is because the reference location x_0 targeted is 18.2 m from the wave maker, so a shorter numerical tank is implemented to save computational effort; this modification does not affect the result. The main parameters are listed in Table 4.3. All the HOS-NWT numerical parameters listed in the table are applied to the irregular wave as well as to the EDW wave calculation. They have been chosen after a careful convergence analysis.

Table 4.3 – Numerical wave tank setup

Parameter	Value
x_0	18.2 m
N_x	230
N_z	17
k_{max}/k_p	15
M	5
$Tolerance$	10^{-4}
$f_{sampling}$	20 Hz

N_x and N_z correspond to the number of modes on the free surface and the wavemaker respectively. N_x is related to the maximum wave number, $k_{max} = N_x\pi/L_x$, and the number of modes in x is chosen based on a constant ratio of $k_{max}/k_p = 15$ providing effective and stable resolution for the whole energetic range of frequency $f < 2.5f_p$. The resolution of the wave evolution in time is conducted by applying an adaptive 4th-order Runge-Kutta Cash-Karp scheme with a time tolerance of 10^{-4}. The nonlinearity order M relative to series expansion in wave steepness is set to 5. The time step of the output wave signal is set to 20 Hz ($f_{sampling}/f_p = 40$). Further details can be found in Bonnefoy et al. (2010) [5] and Ducrozet et al. (2012) [25].

4.4.2 Numerical simulation results

Figures 4.3-4.7 show the estimated wave spectrum and the corresponding wave crest POE curve results at the target location for given sea states. The wave spectrum plotted is the average of 35 numerically calibrated realizations and is compared with the target JONSWAP wave spectrum. Spectrum results are displayed as dimensionless quantities with their corresponding target values. The estimation of the wave spectrum is carried out with the Welch's overlapped segment averaging estimator with time windows of 50 s long and 50 % overlap. Relevant spectral parameters (e.g. H_s, T_z, and T_p) are estimated by considering spectral moments of wave frequency components. A trapezoidal method is applied for the calculation of the spectral area of each wave frequency component. Here, inputs consist of equidistant wave frequencies and their corresponding spectral densities estimated by Welch's method [98].

The estimated power spectral density of most of the frequency components depicted comparable results to the target spectrum, but some differences were observed in the range over $1.2f_p$. The discrepancy near $f/f_p = 1$ appears to increase as the sea condition becomes severe. The main parameters of the wave spectrum for each sea state are listed in Table 4.4. As presented in Figures 4.3-4.7, the maximum differences in significant wave height and peak period are found to be (4.8 %) and (1.3 %) in SS17 respectively, while T_z (4.8 %) and T_1 (4.6 %) are observed in SS6, the mildest sea condition. This shows that the HOS-NWT is able to reproduce the wave spectrum of various sea conditions with small differences.

Table 4.4 – The ratio of the calculated main parameters to target values

	$\frac{H_{s_{HOS}}}{H_{s_{target}}}$	$\frac{T_{p_{HOS}}}{T_{p_{target}}}$	$\frac{T_{z_{HOS}}}{T_{z_{target}}}$	$\frac{T_{1_{HOS}}}{T_{1_{target}}}$
SS6	$+1.8\,\%$	$+1.1\,\%$	-4.8 %	-4.6 %
SS8	-2.1 %	$0.0\,\%$	$+0.7\,\%$	-0.4 %
SS10	-2.3 %	$0.0\,\%$	-0.9 %	-1.4 %
SS12	-3.0 %	$0.0\,\%$	-2.3 %	-2.3 %
SS17	-5.8 %	-1.3 %	$+0.9\,\%$	$+0.5\,\%$

In each graph, the wave crest exceedance probability (POE) distribution of a given sea state is also presented. The crest height in the abscissa is expressed as a dimensionless quantity with respect to the measured significant wave height. For the comparison with the second-order wave-based Forristall distribution, the POE of a single realization consisting of 35 individual cases (gray markers) and its ensemble (red curve) are plotted together. In most cases, the ensemble POE of all realizations is distinct from the Forristall distribution (yellow curve), and the gap increases as the POE level decreases. Following Huang and Zhang (2018) [43], it can be said that the For-

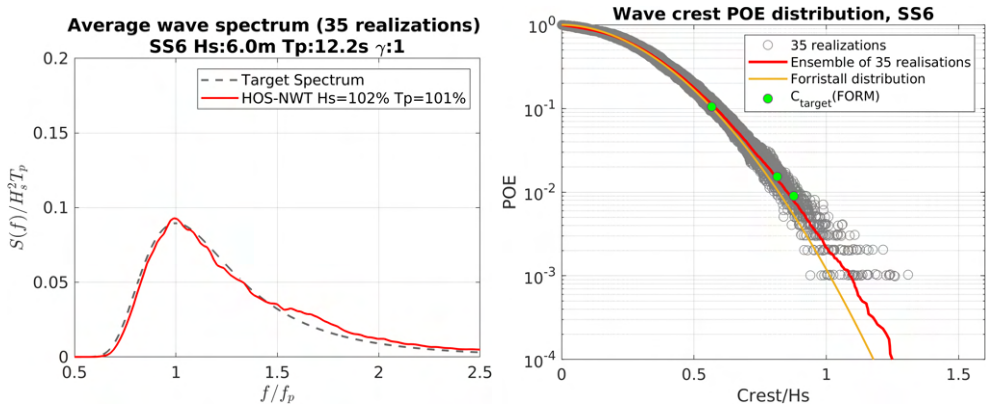

Figure 4.3 – Average wave spectrum of 35 realizations and corresponding wave crest probability distributions, SS6

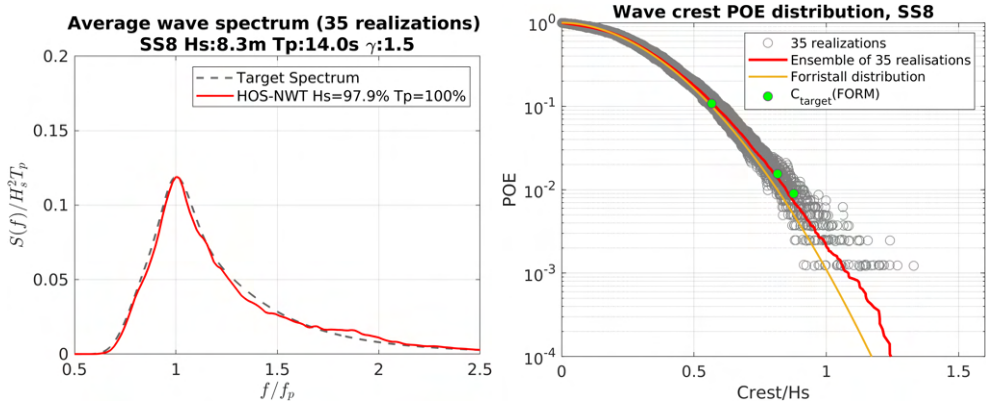

Figure 4.4 – Average wave spectrum of 35 realizations and corresponding wave crest probability distributions, SS8

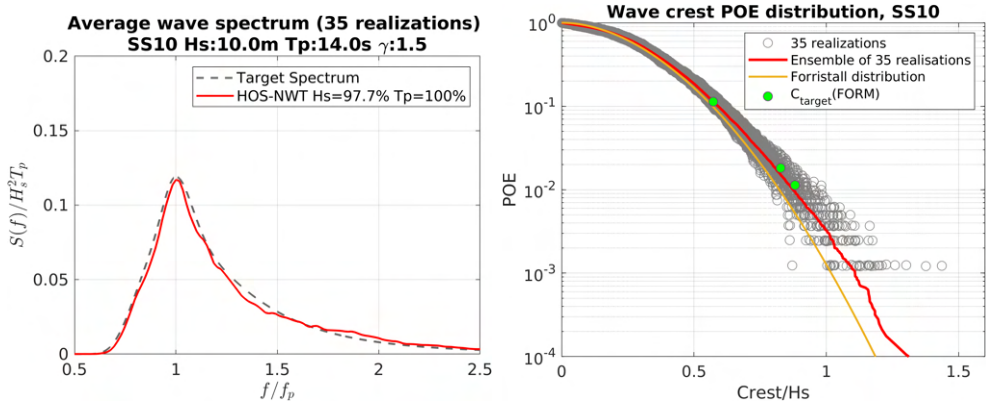

Figure 4.5 – Average wave spectrum of 35 realizations and corresponding wave crest probability distributions, SS10

ristall distribution is derived based on the second-order wave theory and the HOS-NWT considers higher-order effects responsible for the gap between the ensemble distribution and the Forristall distribution. The large scatter of each individual POE curve (in

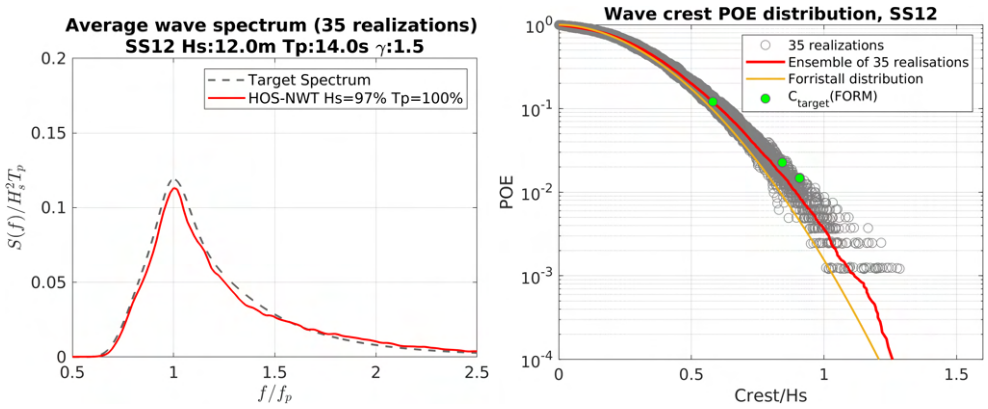

Figure 4.6 – Average wave spectrum of 35 realizations and corresponding wave crest probability distributions, SS12

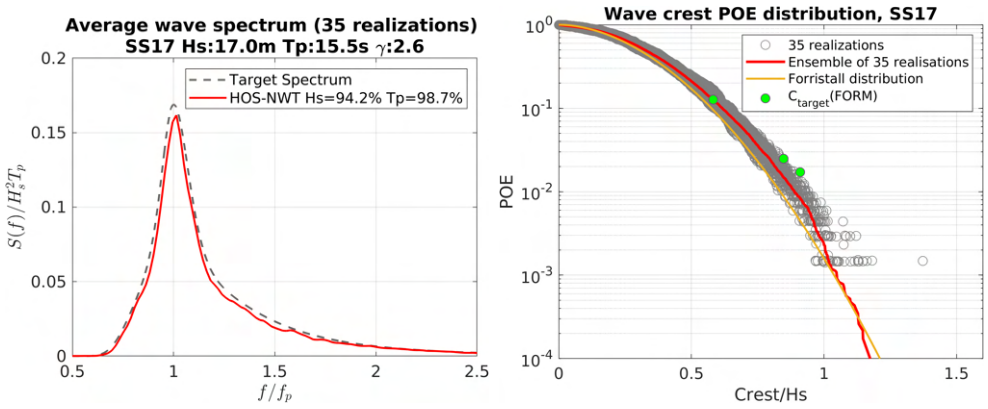

Figure 4.7 – Average wave spectrum of 35 realizations and corresponding wave crest probability distributions, SS17

particular at the low POE level) computed on a 2h 30min full scale time series is observed in all sea states, explaining the need for a large number of realizations to have reliable results on the low POE level.

The estimation of the POE of the target crest C_{target} in a given sea state by the FORM method is also done and the results are represented in the graphs by green points. The estimated POE value using (2.34) and (2.35) with $\mathbf{u}^*$ yielding the target crest C_{target} shows fairly good agreement with the ensemble distribution for 35 realizations in moderate sea states. However, it appears to produce a conservative POE value for C_{target} under harsh wave conditions such as SS12 and SS17 with significant breaking waves. To find out whether the POE estimation result of the FORM method is related to the sea conditions and characteristics of individual EDWs, the ratio of C_{target} to λ_p of a given sea state corresponding to the crest steepness and the crest error defined as $1 - C_{target}/C_{ensemble}$, are summarized in Figure 4.8 and Table 4.5. $C_{ensemble}$ corresponds to the crest value having the POE estimated by the FORM on the ensemble POE

curve of a given sea state. In other words, it is the crest on the red curve that intersects horizontally with the three green points in Figures 4.3-4.7.

As shown in Figure 4.8, it can be seen that the crest error gradually increases as the sea state becomes more severe and the individual EDW becomes steeper, and the trend seems quite clear. In Table 4.5, which summarizes the same results, when the crest steepness (C_{target}/λ_p) is 2.4 % or more, the crest error starts to have a difference of about 5 % or more. For cases with C_{target}/λ_p of 3.3 % to 4.1 % (SS12-2, SS12-3, SS17-2, and SS17-3), the crest error increases at a relatively high rate, from 8.6 % to 15.6 %. The facts that the energy dissipation mechanisms due to the strong nonlinear phenomena including the breaking waves are expected to be more active as the sea state becomes more severe from SS6 to SS17, and no breaking wave occurred in all EDW cases could be possible reasons for the result. Although it cannot be determined with only one parameter, the relationship between the crest size of individual EDW and λ_p of a given sea state seems to be somewhat related to the FORM POE estimation result.

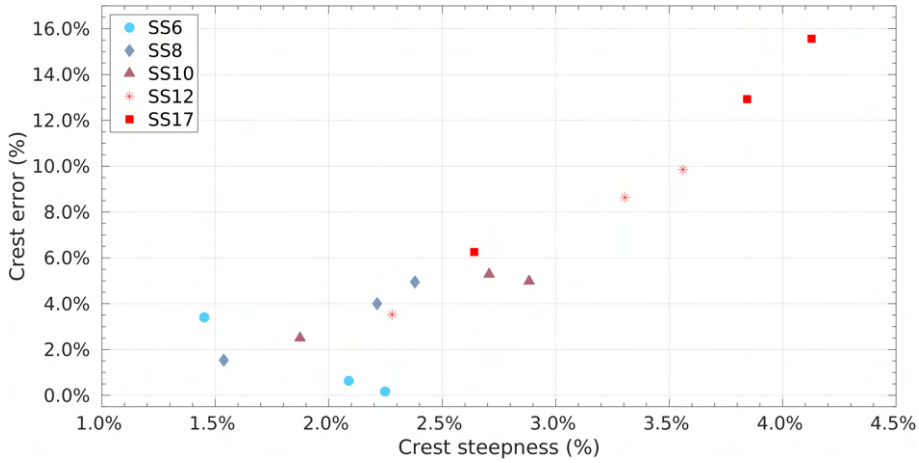

Figure 4.8 – Crest error $(1-C_{target}/C_{ensemble})$ from the FORM estimation and corresponding crest steepness C_{target}/λ_p for different sea states and POE levels

Since the EDW approach measures and analyzes the response of interest through only one short irregular wave packet, the reality of the calculated EDW remains in question and needs to be sufficiently analyzed. Therefore, to check the practicality of the EDW approach, one of the most important objectives is to check whether the time series of FORM-based EDW provides the most probable scenario among the waves having a certain crest in a given irregular wave condition. To confirm this, a geometrical similarity review is carried out between the EDW time series and the wave signals of similar magnitude generated in the long-time irregular wave time series.

Each graph in Figures 4.9 to 4.13 shows a plot of three FORM-based EDW time

Table 4.5 – Crest error and corresponding crest steepness summary table for different sea states and POE levels

Case		Crest steepness (%) C_{target}/λ_p	Crest error (%) $1 - C_{target}/C_{ensemble}$
SS6	**SS6-1**	1.5	3.4
	SS6-2	2.1	0.6
	SS6-3	2.2	0.2
SS8	**SS8-1**	1.5	1.5
	SS8-2	2.2	4.0
	SS8-3	2.4	5.0
SS10	**SS10-1**	1.9	2.5
	SS10-2	2.7	5.3
	SS10-3	2.9	5.0
SS12	**SS12-1**	2.3	3.5
	SS12-2	**3.3**	**8.6**
	SS12-3	**3.6**	**9.9**
SS17	**SS17-1**	2.6	6.3
	SS17-2	**3.8**	**12.9**
	SS17-3	**4.1**	**15.6**

series, along with irregular wave time series containing the target crest of each corresponding EDW case with 2 % tolerance. The number of irregular wave events extracted is presented in each graph for reference. The average of all the extracted irregular waves is additionally plotted on each graph to figure out the most probable shape of the irregular time series.

In the case of irregular wave time series extraction, a zero-crossing analysis is performed on 35 realizations for each sea state to list crest events and their occurrence times first. From the list of all events, crests corresponding to the ± 2 % range of the EDW target crest C_{target} and corresponding time of occurrence are extracted. Based on the crest occurrence time, data covering 1.8 s before and after are finally extracted and plotted. For reference, a period of 3.6 s has been selected based on the SS17-3, which has the longest period.

In the meantime, for reference, the linear NewWave inducing the corresponding C_{target} is calculated and presented together based on Eq. (1.10). Looking at the NewWave results first, we can observe that it has a less sharp crest and a deeper through in its overall shape at the focusing point. The larger the target crest, the more pronounced the difference in shape from the average profile of the extracted irregular waves. This emphasizes the importance of considering the nonlinear wave description again.

Looking at the irregular wave results for each sea state, it is visually observed that various irregular waves are extracted in terms of period and steepness in the case with

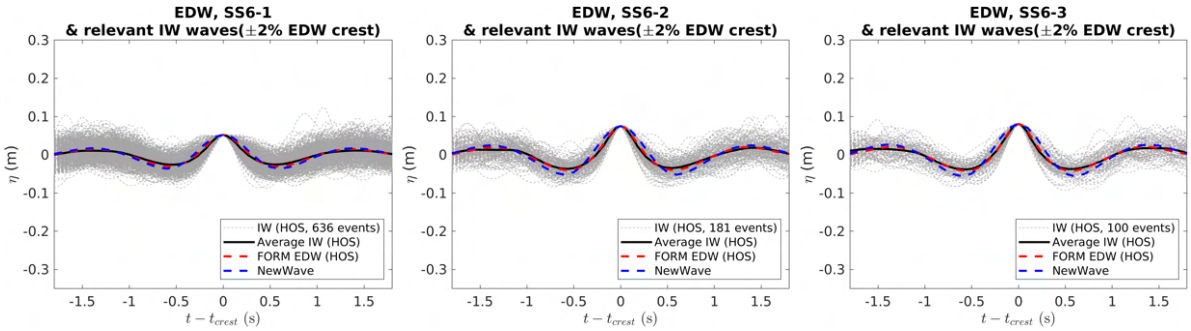

Figure 4.9 – EDW time signal shape comparison with all corresponding waves from irregular sea state, SS6 (model scale)

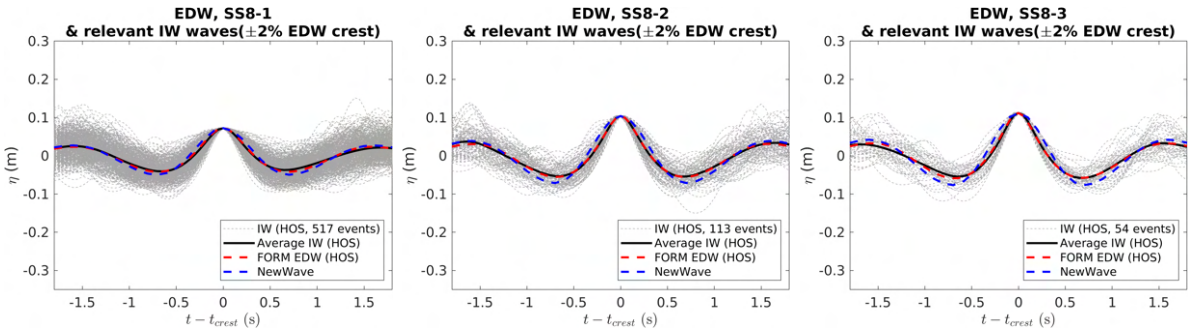

Figure 4.10 – EDW time signal shape comparison with all corresponding waves from irregular sea state, SS8 (model scale)

a high POE level (SS-1 cases in each sea state), and irregular waves similar to the EDW wave time series are extracted as the POE level is lowered from SS-1 to SS-3 in each sea state. Although this may appear relatively similar because the number of events corresponding to the target is quantitatively small as the POE level is lowered, it can be seen that from a qualitative point of view the individual waves extracted are basically similar in shape to the FORM-based EDW.

It is noteworthy that the average wave profile of the irregular wave has a very similar shape to the FORM-based EDW wave profile in all cases regardless of the POE level, while some discrepancies are found in the size of the trough and crest around the focusing point in the EDW case of SS17, the most severe case. Nevertheless, it can be said that the FORM-based EDW calculation process applying the HOS-NWT provides the most probable nonlinear wave shape considering that the overall shape does not deviate significantly from the qualitative aspects compared to the average shape of extracted nonlinear irregular waves.

A similar result was observed in previous research by Fedele et al. (2017) [30]. They conducted a long-time simulation of a particular storm-generated sea state with a Higher-Order Spectral (HOS) method and compared its crest statistics with results

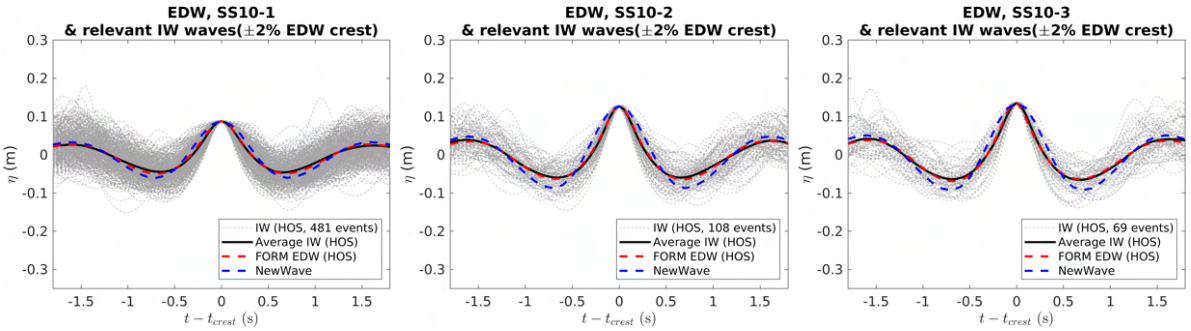

Figure 4.11 – EDW time signal shape comparison with all corresponding waves from irregular sea state, SS10 (model scale)

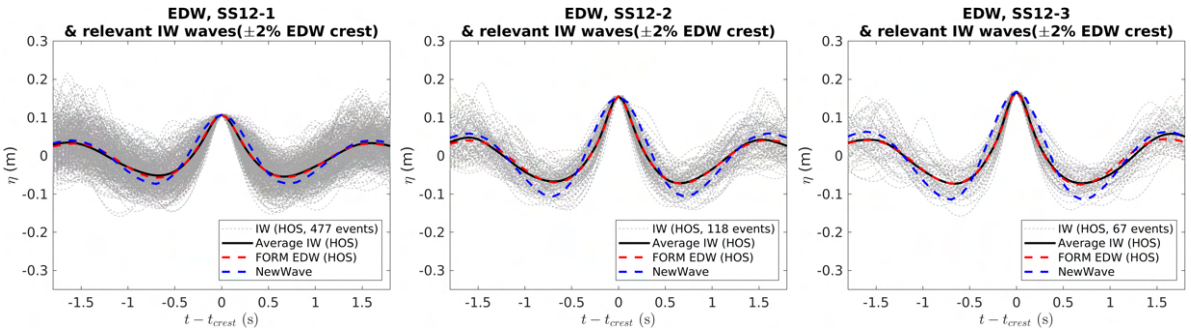

Figure 4.12 – EDW time signal shape comparison with all corresponding waves from irregular sea state, SS12 (model scale)

from analytical probability models. They found that a model called Fedele's Space-Time stochastic (FST) considering the wave effect up to a third-order had a good match with the HOS result. They also investigated a rogue wave of $crest/H_s = 1.6$ in terms of shape and occurrence probability in a given sea state and found that the shape is fairly similar to those observed in different storm seas namely Andrea, Draupner, and Killard, meaning that rogue waves are generated with a similar mechanism.

Previous research by Klein et al. (2021) [54] investigated the applicability of envelope soliton (ES) for the analysis of wave-structure interaction. ES was generated and compared with a standard MLRW profile using a simple linear model for wave and response descriptions. They found that the shape of ES is fairly similar to the MLRW profile. Following this research, we compared the FORM-based EDW with an ES exhibiting the same amplitude and frequency, see Figure 4.14. We observe that the FORM-based EDW results in a wave packet at the target location, which can only be approximated roughly by an ES. In addition, this wave packet experiences highly unsteady features between its generation and the target location. On this ground, in our specific application, the ES does not seem adequate to replace the EDW procedure.

The work of Klein et al. (2021) [54] calculated the ES and EDW yielding a specified

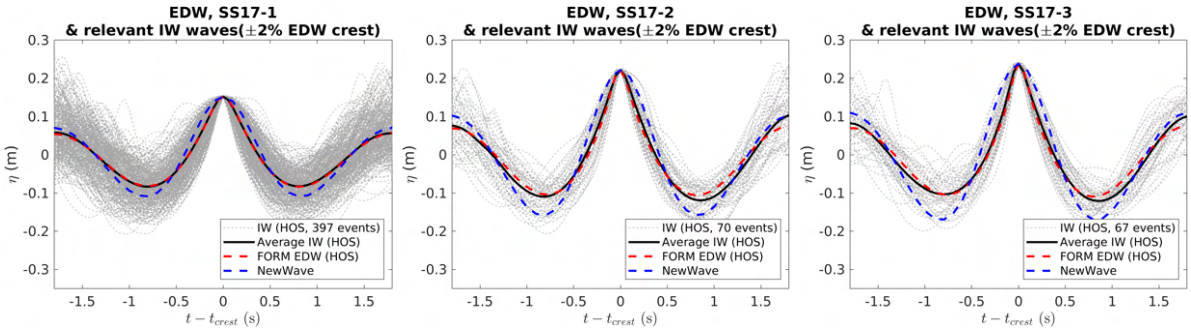

Figure 4.13 – EDW time signal shape comparison with all corresponding waves from irregular sea state, SS17 (model scale)

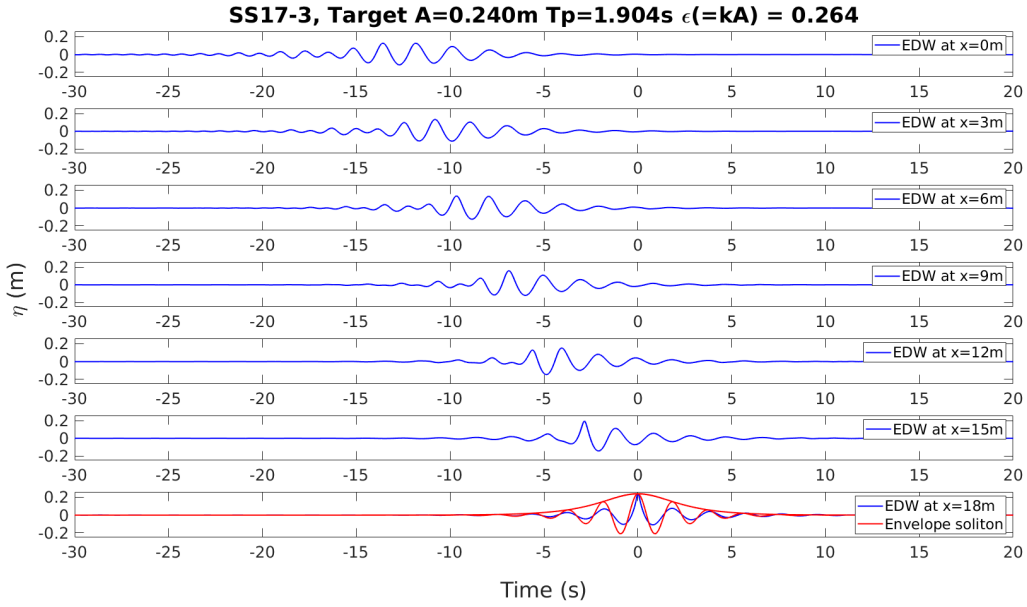

Figure 4.14 – Evolution of the EDW profile from the wavemaker (0 m) to the target location (18 m) having a desired profile with a specified target amplitude (blue curve) and envelope soliton (red curve). Both were calculated with the same input parameters of SS17-3: $A = 0.240$ m, $T_p = 1.904$ s, and $\epsilon = kA = 0.264$)

vertical bending moment (VBM), while this study considers crest amplitude as a target value for the calculation of ES and EDW. Their method was limited to a linear model, while the present FORM-based procedure considers a fully nonlinear wave model in the EDW calculation. Those elements may explain the different conclusions on the possible use of the ES as a design wave.

Another argument for the use of the ES in Klein et al. (2021) [54] is that it is almost impossible to reproduce the linear wave-based EDW in a wave tank because of the wave nonlinearities. However, in this study, we were able to overcome this limitation by using a nonlinear Numerical Wave Tank (HOS-NWT) in the EDW calculation algorithm.

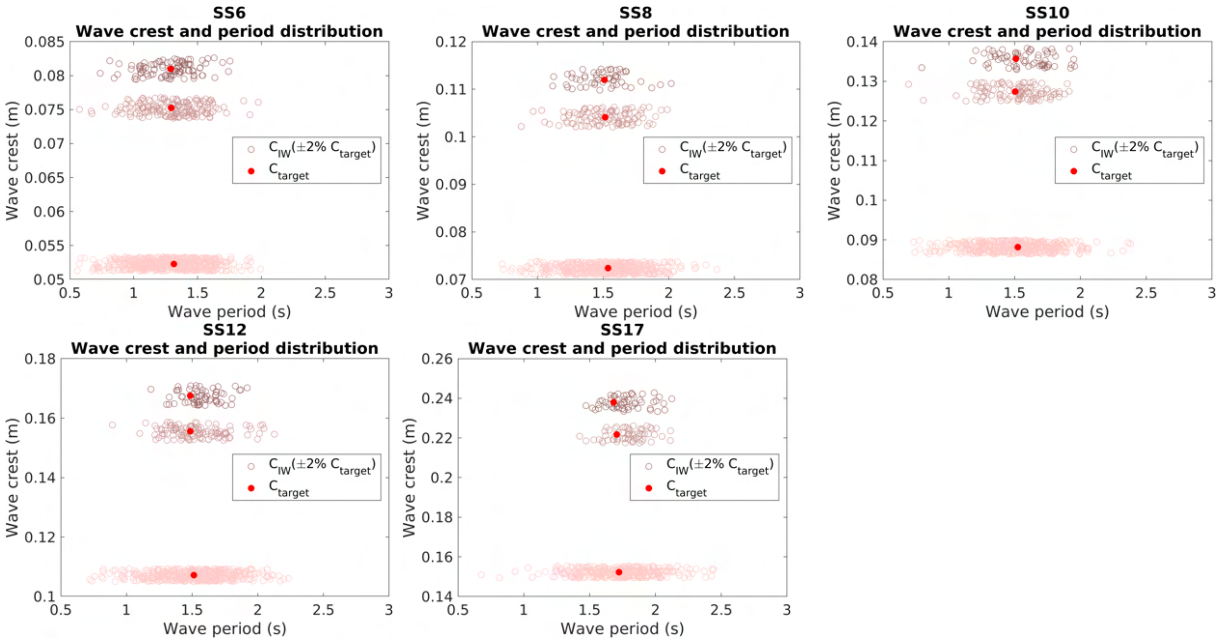

Figure 4.15 – Wave crest and period distribution (model scale)

Figure 4.15 shows the overall distribution of wave crest and period pair for all waves including EDW. Each graph corresponds to a different sea state result, and the three separate groups of points in each graph represent the extracted waves based on three different C_{target}. As pointed out earlier, a large dispersion can be observed for the crest and period group having the highest POE level in all sea states, and the degree of dispersion in the period obviously diminishes as the POE level decreases. Although it is difficult to draw a definitive conclusion due to the small number of events, from a physical point of view, it may be a reasonable way to think that the larger the crest the more limited the natural wave profile shape would be. Therefore, it can be expected to have a relatively similar shape between events in lower POE cases.

No noticeable change in the trend of the distribution is observed as the sea state condition changes. In most cases, the crest and period pair of EDW (red points) are located almost at the center of the irregular wave group, implying that the EDW calculated by the FORM method represents the most probable wave profile for a given sea state.

Meanwhile, as observed from the time signal results, the EDW cases with a relatively large discrepancy in a shape corresponding to SS17-2 and SS17-3 are located further from the center of the extracted wave group. From the time signal results in Figure 4.13, in both cases, the difference in a period seems to be mainly caused by the shape of the trough that occurred after the focusing crest, and the shape of the signals generated before the focusing crest is very comparable to the average shape

of the irregular waves. Given the above results, it can be considered that the numerical simulation of nonlinear wave elevation with the HOS-NWT and the calibration procedure successfully validate the generation of the target sea state and target EDW at the desired location of the numerical wave tank.

4.5 Experimental study

In this section, the wave qualification process is checked by comparing the irregular sea state results in the experiment with those generated in the numerical wave tank. Thus the same wave spectrum data including wave phase information used in the numerical simulation are applied as an input in order to perform cross-validation and to figure out uncertainties in the experimental setup (wavemaker, wave gauge, and absorbing beach). Note that the experimental study is performed with a reduced number of realizations for the irregular wave cases as listed in Table 4.1, and thus the same number of realizations is considered in the numerical simulation presented in this section.

4.5.1 Setup and test cases

All the waves are generated on a scale of 1/65 in the ocean engineering basin (see Section 3.1) with the experimental configuration shown in Figure 4.16. Several wave gauges are positioned in the tank and the reference location is (18.2 m, 15 m) expressed in the basin coordinate system, where wave gauge No.2 (WG2) is positioned. Five wave conditions identical to the numerical simulation are tested. Each sea state consists of at least 8 (maximum 12) realizations of 2h 30min full scale wave time series. In each irregular wave case, as mentioned above, the aim of the experimental study is to validate the numerical simulation, thus exactly the same EDW input data are used to generate the calculated EDW elevation at $x_0 = 18.2$ m and $t_0 = 45$ s (see Table 4.2).

4.5.2 Irregular wave results

The power spectral density of each sea state is estimated using Welch's overlapped segment averaging estimator following numerical simulation. Data measurement is done with a sampling rate of 100 Hz, and post-processing is carried out with the data of wave gauge No.2 installed 18.2 m from the wavemaker which corresponds to the target location x_0 (see Figure 4.16). As the spectral densities of all considered irregular sea

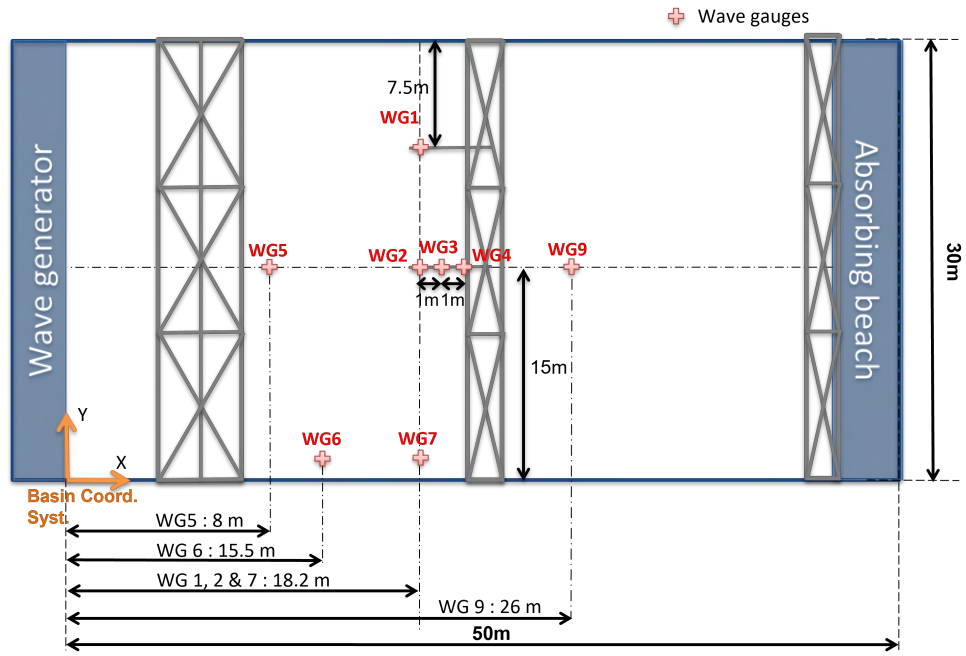

Figure 4.16 – Experimental setup

states are mostly within frequencies below 3 Hz, the sampling rate of 100 Hz can be considered sufficient to measure wave signals.

Figures 4.17-4.21 show the estimated average wave spectrum of the specified realizations for each sea state and ensemble probability distribution of wave crest at the target location.

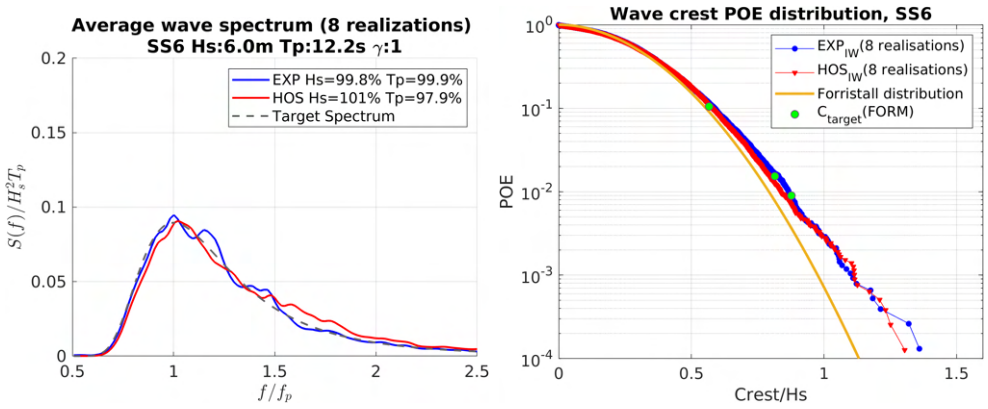

Figure 4.17 – SS6, Comparison of measured and calculated average wave spectrum of 8 realizations and corresponding wave crest probability distributions

As shown in the figures, the spectrum results of the experiment and the numerical simulation are overall consistent, but we observe that there are some differences in size and change patterns of the spectrum curve in specific frequency ranges. The experimental wave spectrum tends to have a larger energy density in the higher frequency

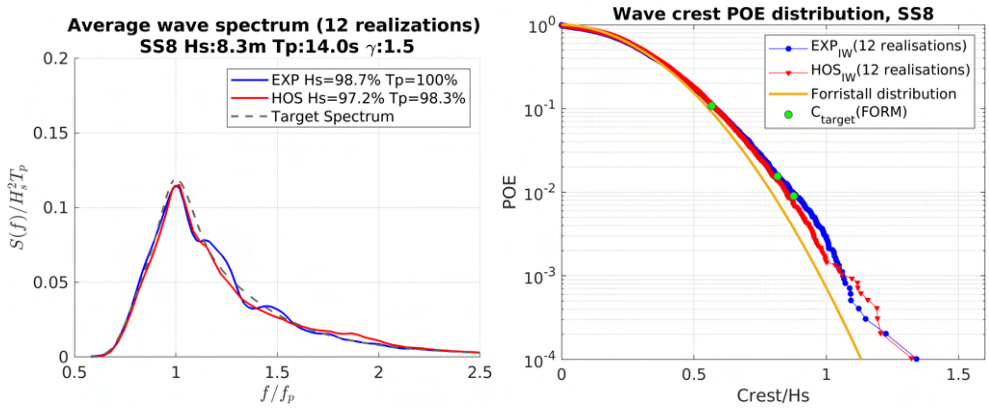

Figure 4.18 – SS8, Comparison of measured and calculated average wave spectrum of 12 realizations and corresponding wave crest probability distributions

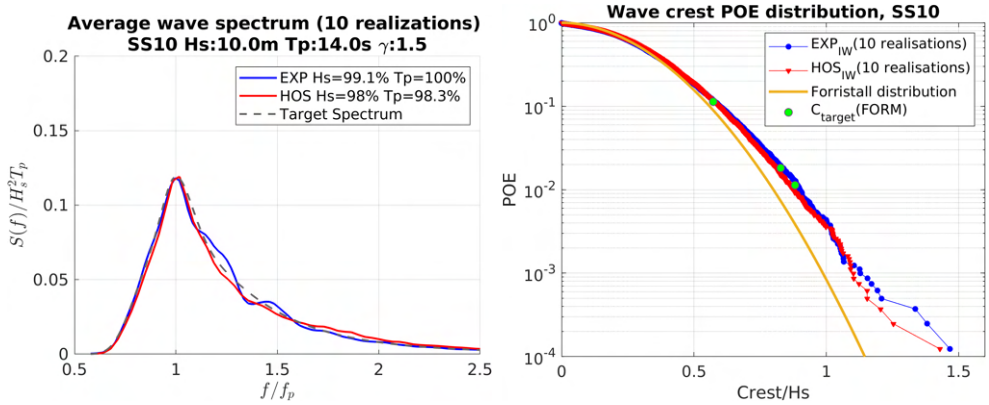

Figure 4.19 – SS10, Comparison of measured and calculated average wave spectrum of 10 realizations and corresponding wave crest probability distributions

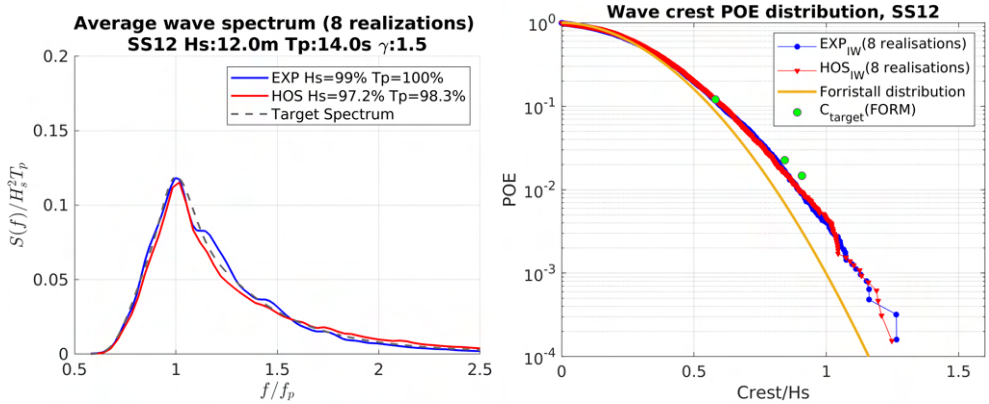

Figure 4.20 – SS12, Comparison of measured and calculated average wave spectrum of 8 realizations and corresponding wave crest probability distributions

range than the numerical results. Most of the discrepancies appear to come from frequency components higher than f/f_p = 1.0. The local variation of the numerical results is relatively small compared to the experiment, and the overall shape is found to be

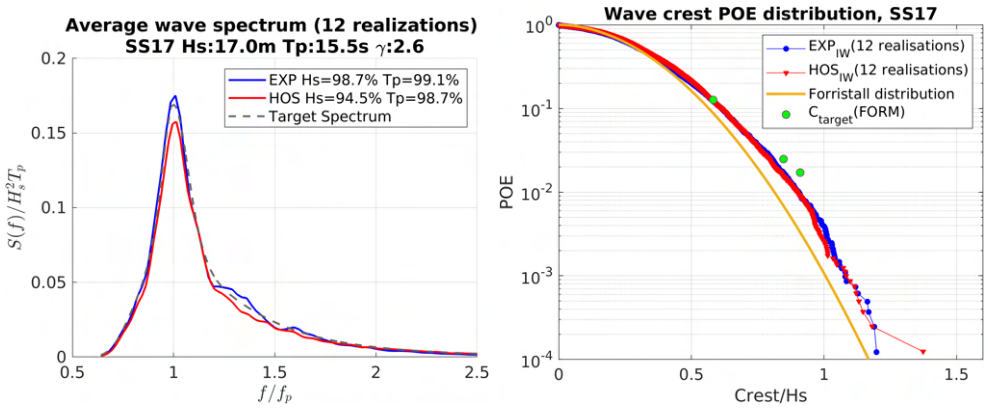

Figure 4.21 – SS17, Comparison of measured and calculated average wave spectrum of 12 realizations and corresponding wave crest probability distributions

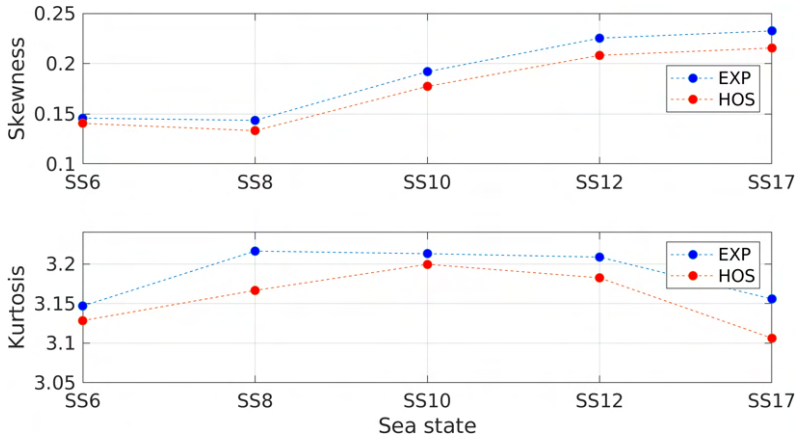

Figure 4.22 – Changes in Skewness and Kurtosis by sea state

more convergent to the target spectrum. The estimated spectrum parameters H_s and T_p both show good agreement with the target values, and as expected, SS17 has the largest difference in H_s with respect to the target in both experiment (1.3 %) and numerical simulation (5.5 %). Regarding the difference in T_p, no significant discrepancy is found over all cases. The estimated T_p of both the experiment and numerical result is over 97.9 % of the target T_p.

The aforementioned discrepancy between experiment and calculation in wave spectrum also naturally affects the POE curve as well. As the estimated spectrum of the experiment has larger energy in the high-frequency range, this results in a higher crest distribution, reducing the experimental slope in the POE curve. As compared with the numerically calculated wave crest POE curve with 35 realizations (Figures 4.3-4.7), which can be considered more statistically converged, a slight difference is observed in each sea state. Nevertheless, overall, the two measured and calculated POE curves up to $Crest/Hs = 1$, which corresponds to around the POE of 4×10^{-3} in each sea state, appear to agree fairly well with each other. As mentioned in the numerical anal-

ysis results in section 4.4.2, the theoretical Forristall distribution has a slightly different trend in slope, showing that the curve is always steeper than the other empirical POE distributions in all sea states as the higher-order effects above second-order are omitted. In other words, at the same POE level, the Forristall distribution estimates a less conservative value in crest size compared to the actual measurement result. This implies that higher-order terms more than a third order affect the magnitude of crests and the resulting POE curve. In the SS17 case which shows the greatest difference with the target spectrum, it is found that the lower the POE level, the closer the ensemble distribution is to the Forristall distribution.

The C_{target} plotted on the estimated POE with Eq. (2.34) and (2.35) is placed nearly on the ensemble POE distribution in the relatively moderate sea states. As the sea state becomes severe (SS12 and SS17 cases), the POE estimated by the FORM tends to give a conservative value. Jensen (2009) [46] likewise found that the FORM calculated a smaller β_{FORM} than brute force wave simulations. Although the POE analytically estimated by the FORM tends to move vertically upward in the severe wave cases, each result can be viewed as a possible scenario as it is still within the range of the single realization distribution group (see Figures 4.3-4.7, showing the same POE estimates by the FORM method compared with the numerical crest distribution by single realization).

Figure 4.22 shows the skewness and kurtosis of experiments and numerical analysis for each sea state. The skewness, which represents the asymmetry of the free surface profile corresponding to (not only, but mainly) the second-order effect, increases as the sea state became severe. This confirms that steep waves occur more frequently in severe conditions as expected. The largest difference in skewness is found in the most severe sea state, SS17. The kurtosis of most sea state cases is in the range from 3.1 to 3.2 (Gaussian process=3), and a tendency for kurtosis to gradually decrease in severe conditions is observed. It seems that breaking prevents having too strong tails of the POE distribution and results in the observed crest POE and kurtosis.

In the meantime, SS17 shows the largest difference between numerical and experimental results. Given that SS17 has the highest skewness, strong nonlinear effects and energy dissipation mechanisms may induce a large discrepancy in the spectrum results, which in turn leads to the largest differences in skewness and kurtosis.

Considering that the same input is used in the two environments, the numerical and the physical wave tank, there are some factors that affect the wave quality in each condition. From an experimental point of view, the most probable reasons for this variability are: i) the decrease in measurement accuracy of the resistive wave gauge due to temperature change and impurity adhesion, ii) three-dimensional effects of the wave tank such as the occurrence of transverse modes related to the discontinuous wavemaker

flaps, iii) reflected wave due to the imperfection of the absorbing beach, and iv) residual waves from the previous test case. However, as the wave quality varies depending on the condition of the reference tank, and wave evolution at various locations along the tank is also significantly different, further studies on the wave tank are needed to quantify the factors mentioned in this regard.

In the case of the numerical wave tank, since the wave breaking model is applied to most of the sea states except the mildest one (SS6), on top of all, the modeling of sea states including wave breaking phenomena is likely to mainly cause such discrepancies. In most of the sea conditions, it is observed that the breaking model is able to reproduce correctly the loss of energy as well as the corresponding crest POE. The discrepancy issue comes with the strongest sea state, SS17, showing that the breaking model overestimates the energy dissipated. Wave spectrum results in Figure 4.21 can be a good example of this issue, showing the discrepancy intuitively. In the range of $f/f_p = 1$ or more, a relatively large difference between the experiment and the numerical value is found. This numerical overestimation in energy dissipation by the wave breaking, in turn, influences a large difference in kurtosis and the corresponding crest POE distribution.

According to the previous research by Seiffert and Ducrozet (2018) [82], who carried out a comparative study of measured and calculated breaking waves, energy loss induced by wave breaking phenomena is mostly observed in the higher frequency range over f/f_p = 1, while little energy loss is seen in the lower frequency range. The study also focused on the possible causes of the discrepancy between measured and calculated breaking waves and mentioned that the process of gradually reducing the energy before the wave overturns for numerical stability is one possible reason why the calculated wave may produce less energy than the measured in the breaking region.

As the numerical wave tank considers only the main characteristics of the physical wave tank in a large framework excluding the uncertain factors mentioned, some local differences in wave spectrum results are attributed to the causes. However, the overall trends agree well with each other. In addition, based on the POE distribution results and the changing trend of the parameters (kurtosis and skewness) of all the cases, it can be said that the HOS-NWT is capable of accurately generating strong nonlinear wave elevations.

4.5.3 EDW time signal comparison

To check the EDW wave quality, the EDW time signals measured in the experiment are compared with the numerical simulation results. In Figures 4.23-4.27, three EDW

time signals corresponding to 3 different C_{target} in a given sea state are presented in each figure. The overall shape of the measured EDW time signal matches very well with the numerically calculated time signal in most cases. A slight time shift and differences in magnitude are observed at surrounding waves, but it seems insignificant. The average difference in crest appears to be less than 3 % at the focusing point corresponding to $t = 45$ s. Target crest C_{target} at $t = 45$ s tends to far exceed the neighbor peaks and this trend becomes even clearer as the target POE level decreases from SS-1 to SS-3 in each sea state, see H/λ of all EDW cases in Table 4.6.

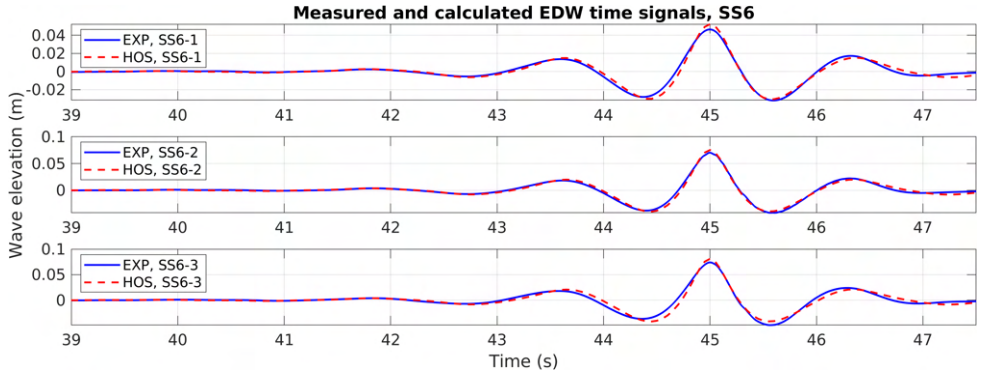

Figure 4.23 – Measured and calculated EDW profile at $x_0 = 18.2$ m, SS6 (model scale)

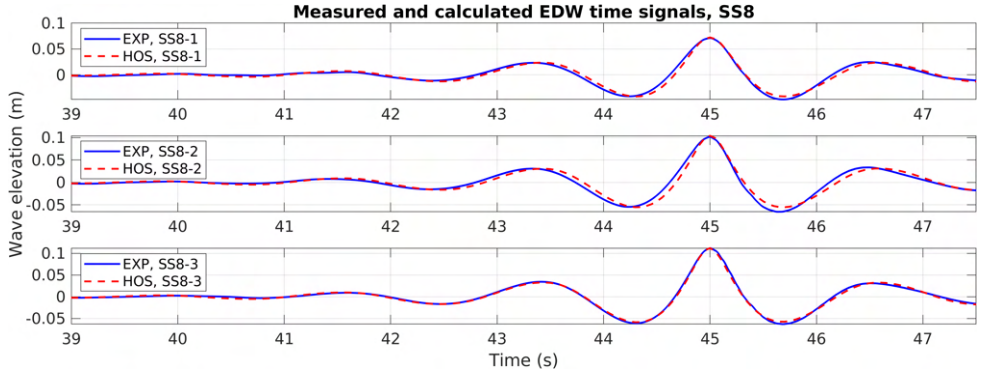

Figure 4.24 – Measured and calculated EDW profile at $x_0 = 18.2$ m, SS8 (model scale)

The difference between the C_{target} of each EDW case and the measured crest C_{EXP} is listed in Table 4.6 for all cases. For the case of the numerical EDW, it is confirmed that the calculated crest for all the cases has a very small error of 0.24 % on average with a maximum of 0.8 % compared to C_{target}. The steepness and period listed in the table are the values calculated with wave height and period of the EDW at $t_0 = 45$ s to characterize each EDW case.

In general, the higher the wave slope and the shorter the wave period, the greater the nonlinearity of waves, which tends to increase the difference between the peak

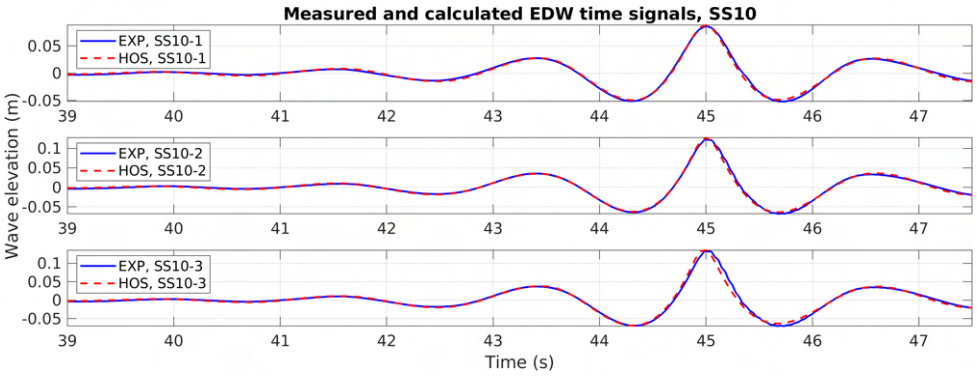

Figure 4.25 – Measured and calculated EDW profile at $x_0 = 18.2$ m, SS10 (model scale)

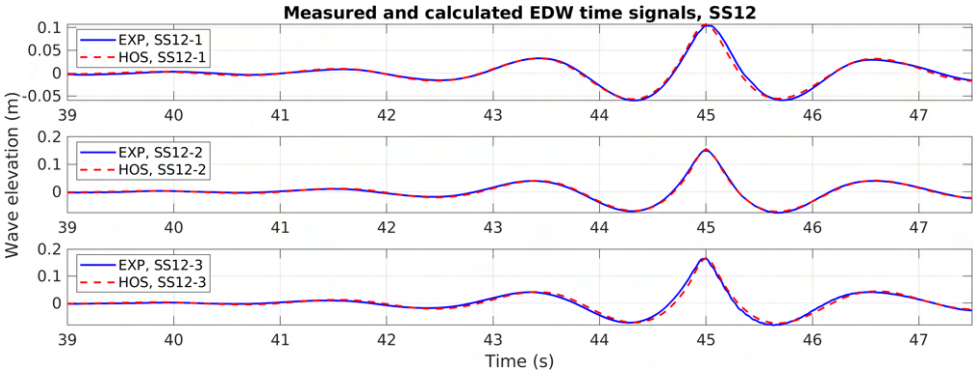

Figure 4.26 – Measured and calculated EDW profile at $x_0 = 18.2$ m, SS12 (model scale)

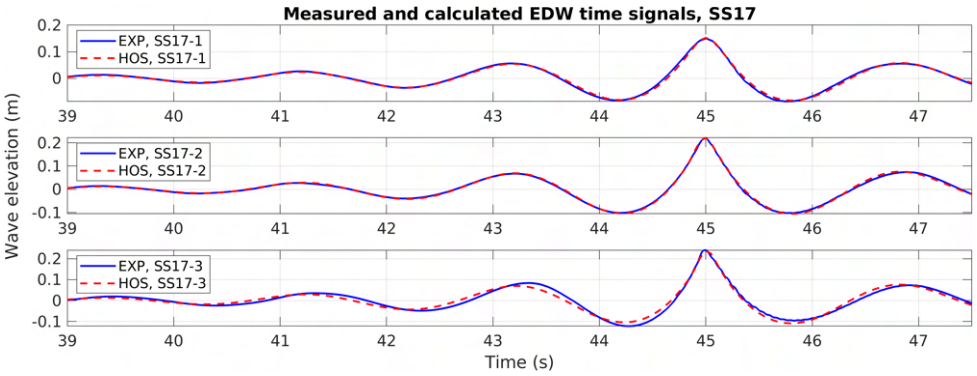

Figure 4.27 – Measured and calculated EDW profile at $x_0 = 18.2$ m, SS17 (model scale)

generated by the actual wavemaker and the theoretical value. An interesting point observed in the EDW case is that the largest difference up to 11.0 % between C_{target} and C_{EXP} is mostly observed in the SS6 sea state, the mildest sea state. Looking at the characteristics of EDW waves of the SS6 condition, the wave steepness of the three cases is the lowest compared to the other EDW cases, while the wave periods of the three cases are around 1.3 seconds, which are relatively short compared to the other cases. However, the period of these cases is not short enough to significantly affect

Table 4.6 – Difference between C_{target} and C_{EXP} of all EDW cases (model scale)

Case		$(H/\lambda)_{EDW}$ (%)	$Period_{EDW}$ (s)	C_{EXP} (m)	C_{target} (m)	C_{EXP}/C_{target}
SS6	**SS6-1**	3.06	**1.32**	0.0465	0.0523	**0.890**
	SS6-2	4.40	**1.30**	0.0704	0.0752	**0.936**
	SS6-3	4.72	**1.29**	0.0740	0.0810	**0.914**
SS8	**SS8-1**	3.10	1.54	0.0712	0.0724	0.983
	SS8-2	4.44	1.52	0.1017	0.1041	0.976
	SS8-3	4.77	1.51	0.1119	0.1120	0.999
SS10	**SS10-1**	3.77	1.52	0.0862	0.0881	0.978
	SS10-2	5.42	1.50	0.1233	0.1274	0.968
	SS10-3	5.58	1.51	0.1329	0.1357	0.979
SS12	**SS12-1**	4.56	1.51	0.1041	0.1072	0.971
	SS12-2	6.63	1.48	0.1492	0.1555	0.959
	SS12-3	7.03	1.49	0.1643	0.1675	0.980
SS17	**SS17-1**	**5.09**	1.72	0.1497	0.1523	0.983
	SS17-2	**7.21**	1.71	0.2207	0.2217	0.995
	SS17-3	**7.85**	1.68	0.2414	0.2380	1.014

the wave quality when considering the wavemaker's performance. Considering that the wave parameter range of the tank that the wavemaker guarantees a good quality wave is 0.5 s - 5 s in wave period, and with a maximum H_s estimated of around 0.8 m, the cause of the discrepancy in the SS6 cases having moderate steepness from 3 % to 4.7 % cannot be regarded as simply due to the influence of the wave period. In the case of SS17, which has the steepest EDW with H/λ of up to about 7.9 % and the longest periods of about 1.72 s, the measured C_{EXP} is almost identical to the C_{target}, showing that the wave generation is accurate even for very steep wave fields. From an experimental point of view, given that the largest discrepancy is observed in the EDW having relatively small focusing waves in size, the experimental uncertainties are likely to affect the wave quality the most. In the SS8, SS10, and SS12 cases, which have similar wave periods, no clear trend is found in the relation between steepness and the difference in wave amplitude. In most cases, the measured crest C_{EXP} is smaller than C_{target} with an average difference of 3.2 %.

4.5.4 Geometrical reviews on EDW wave

Geometrical reviews of the calculated EDW time signal with all the relevant irregular wave signals measured in the experiment are carried out. In the same way as the numerical analysis, irregular waves measured in each sea state with ± 2 % tolerance of C_{target} are extracted and plotted together with the numerically calculated EDW time signal. In addition, the average shape of the irregular waves extracted from the experiment and numerical simulation are presented to see how similar they are to each other and

EDW. It has to be noted that, in the case of the EDW profile, the numerical EDW profile calculated from the HOS is plotted, not the experimental measurement that showed a difference from the target value.

Figures 4.28-4.32 show the corresponding results for each sea state. As expected, in all cases without exception, the same trend as that observed in the numerical simulation is confirmed. The shape of the EDW time signal is observed to be very similar to the average time signal of all the extracted irregular waves, while in the SS17-3 case, the EDW wave signal has a relatively different shape in pre- and post-crest at $t = 45$ s compared to the mean wave signal. When all the individual irregular waves extracted with a ± 2 % tolerance of C_{target} are considered, results show a reasonable trend in terms of the overall shape. Considering the irregular wave itself consisting of numerous harmonic functions, in the case with a high probability of occurrence (SS-1 cases) in each sea state, it is observed that the irregular waves extracted from a sea state have various steepness and wave periods. And as the magnitude of C_{target} increases, the degree of dispersion in wave period and steepness decreases, and thus irregular wave signals which are geometrically more similar to the EDW were extracted.

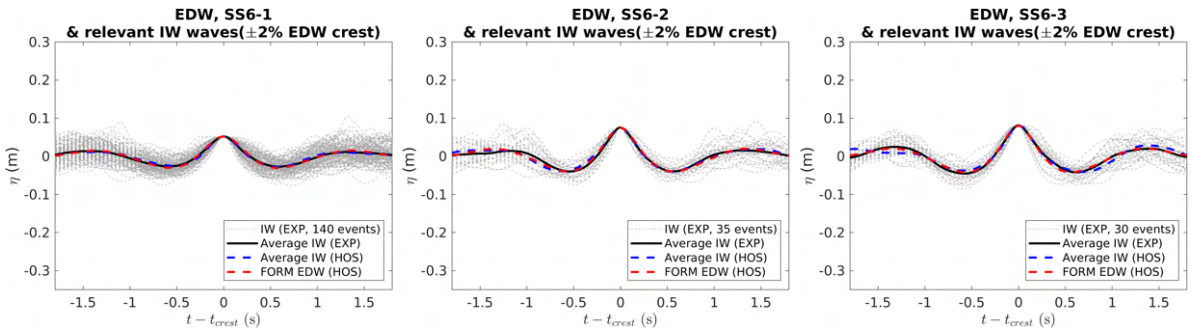

Figure 4.28 – EDW time signal shape comparison with all corresponding waves from irregular sea state, SS6 (model scale)

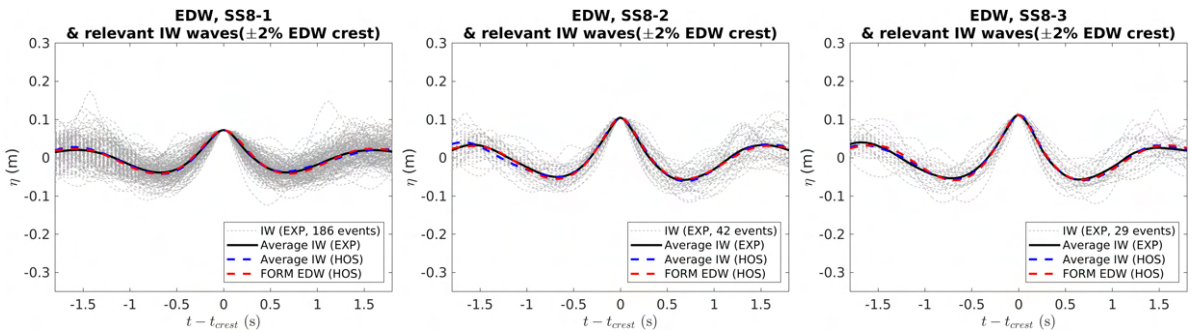

Figure 4.29 – EDW time signal shape comparison with all corresponding waves from irregular sea state, SS8 (model scale)

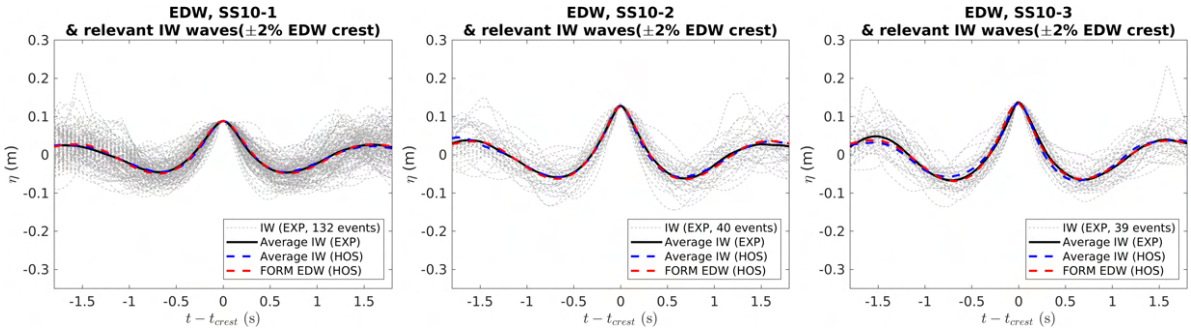

Figure 4.30 – EDW time signal shape comparison with all corresponding waves from irregular sea state, SS10 (model scale)

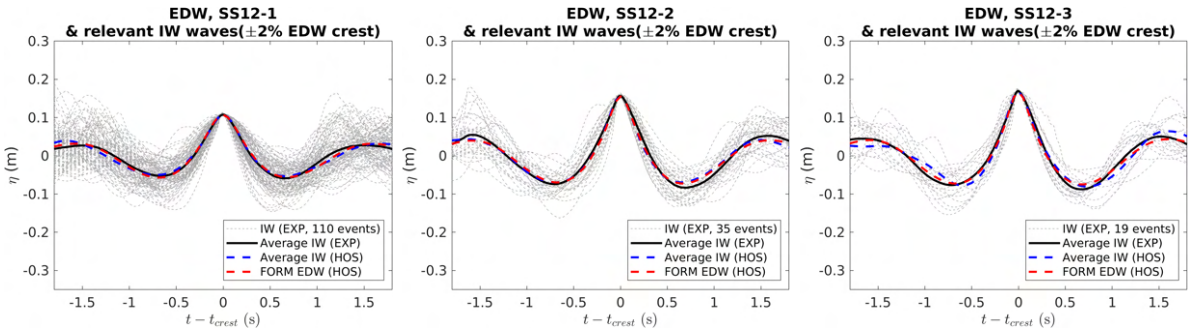

Figure 4.31 – EDW time signal shape comparison with all corresponding waves from irregular sea state, SS12 (model scale)

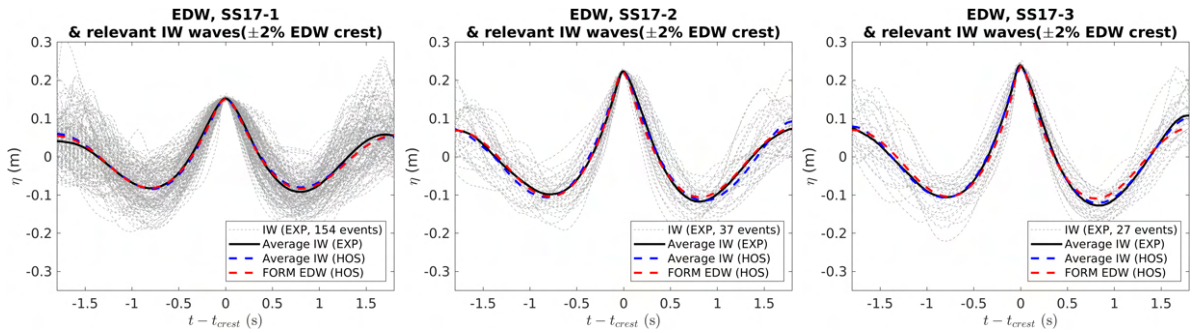

Figure 4.32 – EDW time signal shape comparison with all corresponding waves from irregular sea state, SS17 (model scale)

The corresponding wave crest and period distributions for the measured irregular waves extracted and the EDW are presented in Figure 4.33. The results are expressed in the same way as the numerical analysis results in section 4.4.2. Although some deviation of wave events is found in each case, the crest and period pairs of most waves are in a specific range. As the number of realizations decreases, the waves are distributed in a relatively reduced range compared to the numerical analysis which considered 35 realizations for each sea state, and it is found that the EDW is still in a position corresponding to the average in each distribution group. This confirms that the

FORM-based EDW wave profile generates a given target crest with the most probable shape. Thus it can be said that the FORM algorithm coupled with the HOS-NWT is clearly able to produce the nonlinear focusing wave profile which can occur in a given nonlinear irregular sea state.

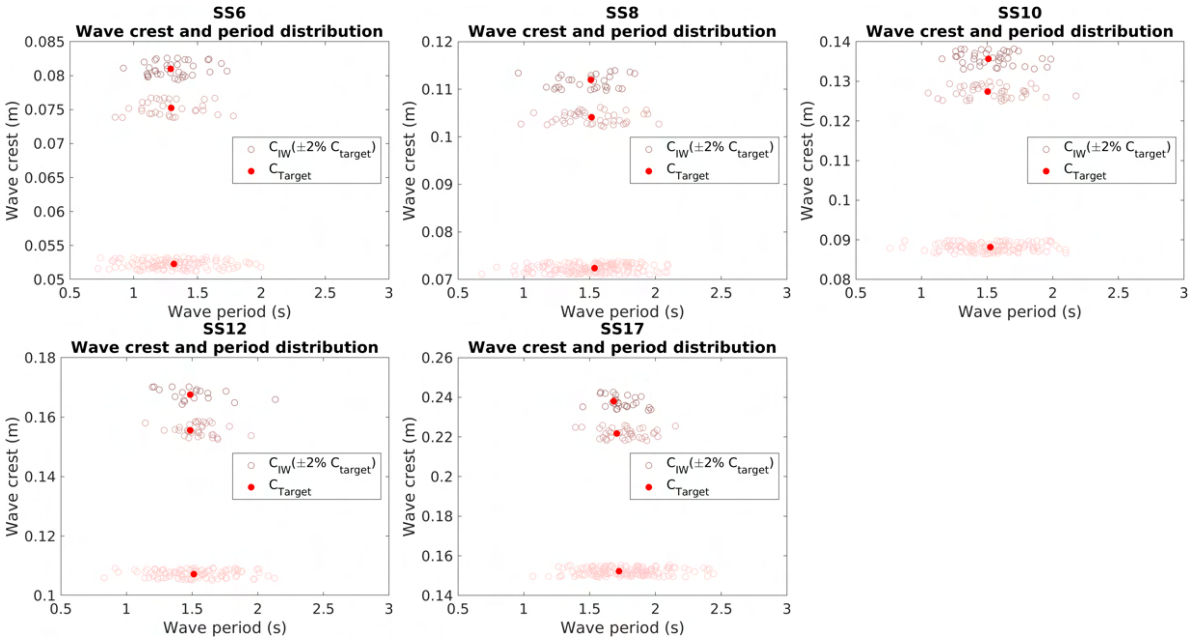

Figure 4.33 – Wave crest and period distribution (model scale)

4.6 Summary

Overall, through the numerical simulation itself as well as the comparison with experimental results for irregular wave sea states, this study has validated that the HOS-NWT successfully implemented the key features of the physical wave tank. The solver generated target irregular wave conditions with sufficient accuracy, containing strong nonlinear wave-wave interactions and complex energy dissipation by breaking waves. It has been confirmed that the shape of the wave spectrum and POE distribution curve are qualitatively and quantitatively comparable to the numerical calculation results.

Nevertheless, the solver was shown to overestimate the breaking phenomena in the most severe sea states, as identified by comparison with the experimental results applying the same wave data. Other reasons for the slight difference could be the physical limitations of the experimental settings.

Additionally, from a short-term statistical point of view, it was found that 8 to 12 realizations of a 2h 30min wave spectrum for each sea state provided fairly similar wave crest POE distributions up to $Crest/H_s = 1$ corresponding to the POE of around

4×10^{-3}. The Forristall distribution was always steeper than the numerically (or experimentally) estimated ensemble POE curve due to the absence of higher-order above second-order wave effects.

In the case of the FORM-based EDW, its elevation and corresponding wave components were calculated by applying the HOS-NWT to the FORM method. The algorithm used for the FORM optimization was the Hasofer and Lind (HL) based algorithm called MHLGA, which applies the merit function to increase its robustness and requires no gradient evaluation of the limit state function to increase the computational efficiency. The numerical and experimental validation of the practicality of the EDW calculation process applying the HOS-NWT was performed. All numerically calculated EDWs were generated in the experiment and compared with the measurements. Also, in both the numerical simulation and the experiment, EDW signals were compared with irregular waves that occurred in a given sea state in terms of the overall shape of wave elevation.

A review of the geometrical similarity with the irregular wave signals extracted from several realizations for each sea state confirmed that the FORM-based algorithm provides an EDW profile that is very similar to the average (or most probable) shape of the extracted waves in most cases. Even though some discrepancies in neighboring waves were found for the low POE level cases in severe sea conditions, the overall shape is still comparable. Accordingly, the crest and period distribution of all extracted irregular waves and EDW show that EDW is located almost in the middle of the irregular wave group. The POE value of the target crest C_{target} estimated by the analytical FORM expression agrees very well with the Monte Carlo reference result in moderate sea states. However, for EDW cases with low POE levels in severe sea states, the estimated POE by the FORM method is overestimated. The ratio of C_{target}/λ_p is found to be related to the POE estimation result by the FORM method. However, further studies seem to be needed to accurately figure out influencing parameters for the conservative POE estimation by the FORM.

To summarize, by applying the HOS-NWT to the FORM method, and considering higher-order wave contributions, the nonlinear focusing wave was calculated for all EDW cases, and we confirm that the calculated EDW is very comparable to the average of nonlinear irregular waves in terms of shape. It can therefore be said that the FORM-based EDW calculation procedure applying the HOS-NWT produces a wave scenario that is highly likely to occur in an actual sea state. From a structural response point of view, of course, taking higher-order contributions into consideration in the EDW calculation will also play an important role in predicting accurate structural responses for such abnormal waves.

Chapter 5

VBM INDUCED BY 3 DIFFERENT WAVE APPROACHES

5.1 Introduction

This Chapter 5 deals with the practicality of the EDW approach in the estimation of the VBM of a rigid container model with a 1/65 model scale. The new FORM algorithm applying the HOS-NWT for the EDW calculation introduced in Chapter 2 is applied as well to check its validity on the VBM. Validation is done through a comparative study with the Monte Carlo results obtained in a given sea state. The same five sea states considered in Chapter 4 are applied, but with a different number of realizations. The results of this new EDW approach are compared to the results obtained with the regular design wave approach.

Regarding the EDW case selection, 4 EDW profiles yielding 4 EDW profiles corresponding to 4 different POE levels are considered. The procedure is applied to both hogging and sagging for each probability level, including the most probable short-term extreme VBM response corresponding to a probability level of 10^{-3} for each sea state. This enables the comparative study with the Monte Carlo reference results at the same probability level in terms of geometrical point of view, and to identify the difference in the overall shape of each POE distribution.

A methodology to utilize the EDW approach from a practical point of view is presented by using a linear VBM RAO in the EDW calculation following Section 2.3.3. To be specific, the target VBM selected from the VBM POE curve of a given sea state is calculated by applying the HOS-NWT and the linear RAO, thus it is not purely linear due to the nonlinear wave description. However, here it is referred to as a linear target VBM to clearly distinguish it from the nonlinear VBM measured in the experiment.

Through the experiment, the nonlinear factor defined as the ratio between the linear VBM and the VBM measured by the reproduced EDW is analyzed in association with the given wave-related variables. It is intended to discuss how well the FORM-based EDW approach can evaluate the load for a given probability based on the statistics of the Monte Carlo reference results of a given sea state.

As the model is set to be rigid, the nonlinearity of the VBM measured in the experiment should be mostly influenced by the wave's nonlinear effect and the hull geometry. And it is found that the nonlinear factor, defined as a ratio between the VBM measured to the corresponding linear VBM at the same POE level in each VBM POE curve, is largely dependent on the amplitude of a given wave.

The overall distribution of the nonlinear factor in the hogging response induced by EDW appears to match very well with the Monte Carlo reference result, while the sagging response results show a relatively visible discrepancy compared to the hogging results. The EDW profile consisting of only one irregular wave packet, which would provide a less realistic memory effect of the system, and the statistically non-converged probability curves of the irregular wave case due to the limited number of realizations seem to be the main causes of such differences. In the same context, the most severe sea state (SS17) with 34 realizations shows a good agreement between the EDW and the Monte Carlo results, even though the strong nonlinear effects were expected to occur most actively among the five sea states. Possibly, as observed in the previous chapter, the SS17 case is relatively less severe than the other sea states in terms of wave crest distribution and kurtosis due to the intense energy dissipation by the wave breaking, which may have influenced the results.

5.2 Numerical models

5.2.1 Problem addressed/Configuration

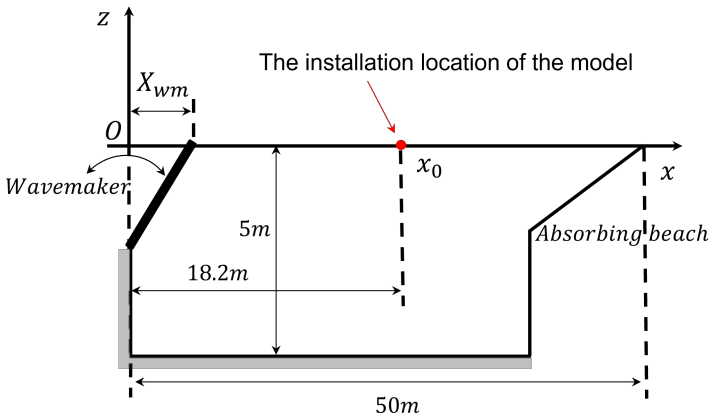

Figure 5.1 – 2D schematic view of test configuration with a model at a target location $x_0 = 18.2$ m

Figure 5.1 shows the side view of 50 m $\times$ 5 m (length $\times$ depth) EWT consisting of the wavemaker on the left side and the absorbing beach on the opposite side. This is

the configuration applied with the target location $x_0 = 18.2$ m away from the wavemaker, where the model is installed. Considering that the wave is being propagated with the wavemaker motion $X_{wm}(t)$ which is a wave input process at $x = 0$ m, it can be expected that the physical characteristics of the wave tank and the wave-wave interaction will affect the quality of the wave and consequently it does not give the desired quality of the wave elevation at x_0, $\eta(x_0, t)$. To consider such effects and provide a wave input process accordingly, the HOS-NWT and relevant wave calibration process are applied (see Section 2.2.2 and 2.2.3).

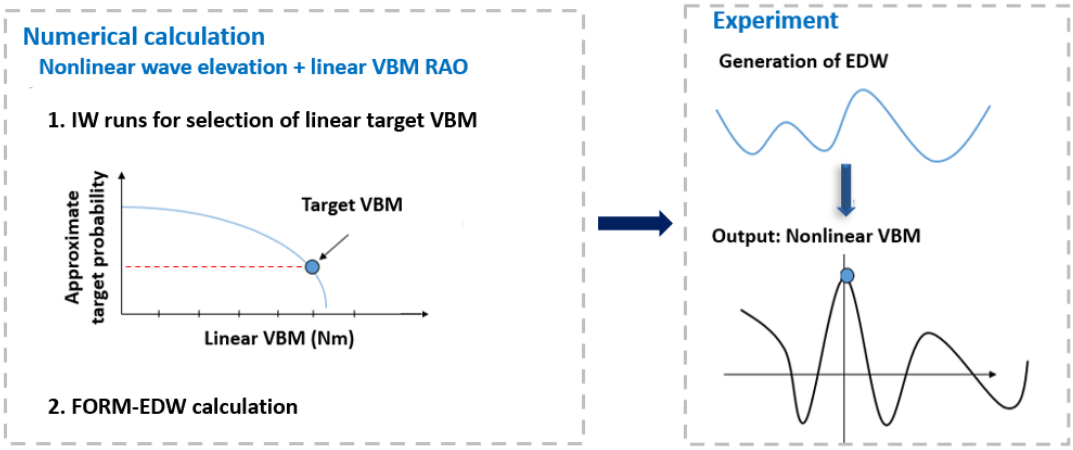

Figure 5.2 – General procedure of the EDW experiment, from target VBM selection to measurement

Figure 5.2 outlines the overall FORM-based EDW calculation procedure from the calculation of the EDW inducing a specific VBM to the experimental measurement of the actual VBM induced by the EDW. In practice, only the linear RAO is available for the VBM in absence of specific experiments or CFD computations. In this practical aspect, in the numerical part of the procedure given in Figure 5.2, the VBM time series are calculated by applying the linear VBM RAO calculated by BV Hydrostar [93] to the HOS-NWT nonlinear wave, without defining a nonlinear VBM hydrodynamic model. Therefore, the linear VBM RAO-based calculation procedure is partially nonlinear.

The overall procedure of the numerical part is as follows: i) building the reference long-time (Monte Carlo simulation) data with a full scale 9-hour wave elevation using the HOS-NWT and the linear RAO, ii) calculation of the corresponding approximate exceedance probability (POE) curve of hogging and sagging responses, iii) selection of a VBM corresponding to a specific POE level from the curve as a linear target VBM, and finally iv) the calculation of the EDW inducing the selected linear target VBM based on the FORM approach (see Figure 5.3).

The numerically calculated EDW is then reproduced in the experimental wave tank

(EWT) to measure the corresponding nonlinear VBM responses. Through a calculation of the nonlinear factor for each EDW case defined as a ratio of the VBM measured to the linear target VBM, $\text{VBM}^{NL}/\text{VBM}^{L} - 1$, the wave's nonlinear effect on the VBM response can be evaluated.

5.2.2 Linear VBM time signal computation

The zero-speed model is located at the target location x_0 and the wave elevation that encounters at the target location $\eta^{HOS}(x_0, t)$ is computed with the HOS-NWT with Eq. (5.1). The corresponding linear VBM time history is thus simply obtained with the linear VBM RAO as expressed in Eq (5.2).

$$\eta^{HOS}(x_0, t) = \sum_{i=0}^{N-1} A_i e^{i(2\pi f_i t + \epsilon_i)} \tag{5.1}$$

$$\text{VBM}^{\text{HOS}}(x_0, t) = \sum_{i=0}^{N-1} |RAO|_i A_i e^{i(2\pi f_i t + \epsilon_i + \psi_i)} \tag{5.2}$$

where N is the number of frequency components, A_i and $|RAO|_i$ are the wave amplitude and the linear VBM RAO amplitude of i^{th} frequency component, and ϵ_i and ψ_i are their respective phases. Once it is done, a linear VBM POE curve corresponding to a 9-hour duration is obtained, allowing us to select an approximate target value at the desired POE level. Then, the VBM-targeted FORM can be estimated.

5.2.3 VBM-targeted FORM calculation with HOS-NWT

The realizations of wave-related variables, u_i and $\bar{u}_i$ yielding the selected target VBM with a certain POE level (P_{tar}) in a given sea state, $\text{VBM}_{\text{IW}}(P_{tar})$, at a target time t_0 and the target location x_0 can be estimated with the limit state function as expressed below:

$$G(\mathbf{u}) = \text{VBM}_{\text{IW}}(P_{tar}) - \text{VBM}_{\text{EDW}}(x_0, t_0|\mathbf{u}) = 0 \tag{5.3}$$

where **u** corresponds to a set of uncorrelated normal distributed vectors, $\{u_i, \bar{u}_i\} = \{u_1, \bar{u}_1, u_2, \bar{u}_2, ..., u_N, \bar{u}_N\}$. $\text{VBM}_{\text{EDW}}(x_0, t_0|\mathbf{u})$ corresponds to the magnitude of the VBM time signal induced by the EDW consisting of **u** at x_0 and t_0.

As shown in Figure 2.11, the limit state surface (blue color) in u-space is defined with realizations $\{u_i, \bar{u}_i\}$ where $G(\mathbf{u})$ is less than or equal to 0. Among the realizations, the point with $\mathbf{u}^*$ having the shortest distance to the origin of the u-space is sought with the FORM linear optimization, providing the β_{FORM} (see Eq. (2.33)).

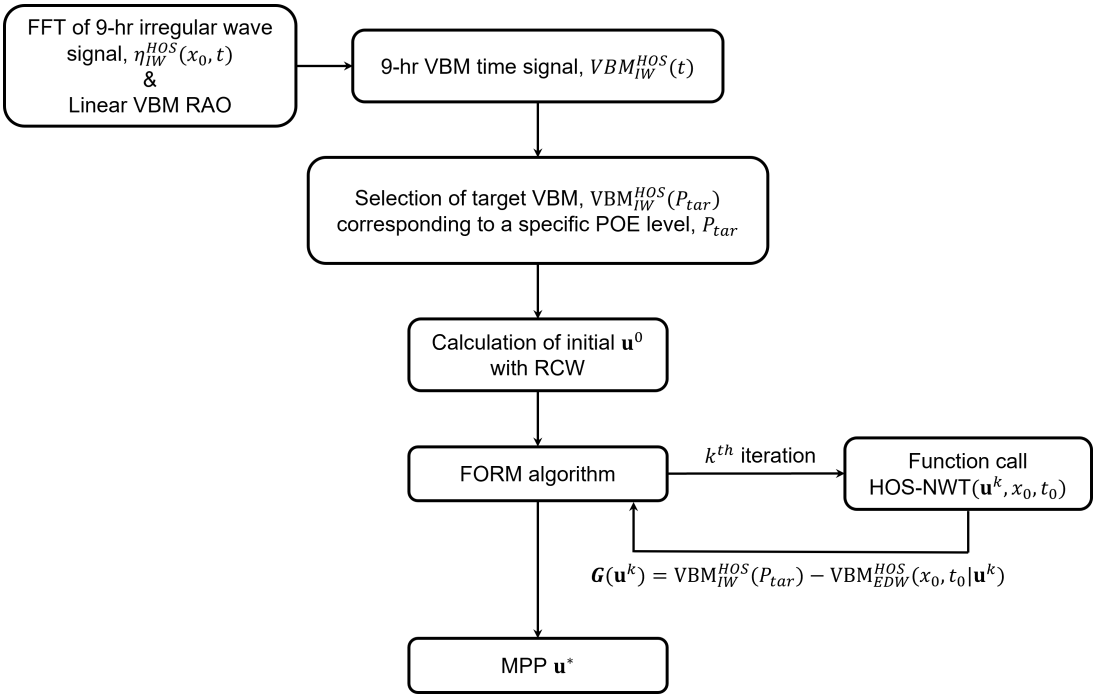

Figure 5.3 – HOS-NWT-coupled numerical calculation procedure for the FORM-based EDW with most probable point $\mathbf{u}^*$

Figure 5.3 shows the calculation procedure of the VBM-targeted EDW. As a first step, a VBM corresponding to a specific POE level (P_{tar}) on the VBM POE curve calculated based on the linear VBM RAO and 9-hour HOS-NWT wave elevation of a given sea state at the target location x_0 is selected as a target response, $\mathrm{VBM}_{\mathrm{IW}}^{\mathrm{HOS}}(P_{tar})$. Then, the definition of an initial $\mathbf{u}^0$ is performed for the initial wavemaker motion based on the RCW method applying the linear description of the wave as well as linear transfer function (see Section 1.2.2).

The initial wave amplitude A_i and phase ϵ_i of all the frequency components are calculated based on Eq. (1.16). Then, the corresponding initial set of $\{u_i, \bar{u}_i\}^0$ (=$\mathbf{u}^0$) and other relevant parameters for the initial wavemaker motion can be defined with Eq. (2.29) and (2.30). Starting with the initial wavemaker motion for $\mathbf{u}^0$, the iterative optimization process applying the successive HOS-NWT simulations is performed to find the most probable point (MPP) $\mathbf{u}^*$. A criterion applied in β is the same as the one considered for the crest-targeted FORM EDW in Chapter 4. The initial β (=β^0) is set to 0, and the newly calculated $\mathbf{u}^k$ at k^{th} iteration is applied to calculated β^k.

$$G(\mathbf{u}^k) = \mathrm{VBM}_{\mathrm{IW}}^{\mathrm{HOS}}(P_{tar}) - \mathrm{VBM}_{\mathrm{EDW}}^{\mathrm{HOS}}(x_0, t_0|\mathbf{u}^k) \tag{5.4}$$

At every iteration step of the process, the estimation of modal amplitudes for the calculated $\eta^{HOS}(x_0,t|\mathbf{u}^k)$ is carried out to compute the corresponding VBM time signal

$\text{VBM}^{\text{HOS}}_{\text{EDW}}(x_0, t|\mathbf{u}^k)$ with the linear VBM RAO and to estimate $G(\mathbf{u}^k)$ with Eq. (5.4).

In the numerical algorithm to find the MPP, here also applies the specific class of the FORM optimization algorithm called the Modified Hasofer and Lind with Goldstein-Armijo search (MHLGA), as explained in Chapter 2. MHLGA algorithm is based on Hasofer and Lind (HL) algorithm introduced by Hasofer and Lind (1974) [37], and has improved the HL algorithm in terms of its robustness as well as CPU cost, see Section 2.3.

The proposed procedure allows for the identification of the EDW considering wave nonlinearity. In the procedure, in particular, the numerically calculated EDW will be validated through dedicated experiments. The reproduced EDW in the EWT should always refer to a wave profile obtained numerically with the FORM procedure described previously.

From a geometrical perspective, it will also be validated whether the procedure provides the most probable wave episode for a specific level of VBM response through the comparative analysis with the experimental Monte Carlo reference results. Consequently focus is attributed to the analysis of experimental nonlinear VBM induced by the reproduced EDW compared to the linear target VBM.

5.3 Test cases

5.3.1 Environmental conditions

As summarized in Table 5.1, five sea states, mostly breaking sea states except for the mildest one, were defined with the JONSWAP spectrum. These are the same sea conditions with the same wave phase sets applied in Chapter 4. For each condition, the Monte Carlo approach is used to obtain the reference VBM data. Note that the experimental Monte Carlo reference results are used for comparative studies with i) the experimental nonlinear VBM responses induced by the experimentally reproduced EDWs that are numerically calculated based on the procedure in Section 5.2.3 and ii) the linear VBM RAO-based numerical Monte Carlo reference results.

Table 5.1 – Description of 5 different environmental conditions (full scale)

Case	H_s **(m)**	T_p **(s)**	γ	**Remark**
SS6	6	12.25	1	No breaking wave
SS8	8.3	14	1.5	Breaking wave
SS10	10	14	1.5	Breaking wave
SS12	12	14	1.5	Breaking wave
SS17	17	15.5	2.6	Breaking wave

5.3.2 Experimental Monte Carlo reference

To obtain the experimental Monte Carlo reference results, at least 8 (maximum 34) realizations of full scale 2h 30min measurements with different wave phase sets are considered for each sea state (see Table 5.2). In the case of the most severe sea state, namely SS17, 34 realizations have been considered to obtain a statistically more converged reference result. The measurement time for a single realization is about 1200 s (about 2h 40min in full scale). The time window used for the data analysis corresponds to 1080 s equivalent to about 2h 30min in full scale. The data in the selected time window correspond to signals sufficiently out of the transient period of the initial wave generation.

Table 5.2 – Number of experimental realizations for each sea state

Case	Number of realizations
SS6	8
SS8	12
SS10	10
SS12	8
SS17	34

5.3.3 EDW

In order to experimentally validate the procedure (see Section 5.2.3), several EDW cases have been applied to describe the corresponding experimental VBM responses (hogging and sagging respectively) at different levels of probability for each sea state case (SS6 to SS17). In this regard, as shown in Table 5.3, VBM responses at 4 specific POE levels corresponding to $10^{-1}, 10^{-2}, 5 \times 10^{-3}$, and 10^{-3} were selected as the target responses, $\mathrm{VBM}_{\mathrm{IW}}^{\mathrm{HOS}}(P_{tar})$. As mentioned in Section 5.2.3, the target VBM selection in a given sea state was carried out with the linear VBM RAO-based 9-hour VBM time signal, $\mathrm{VBM}_{\mathrm{IW}_{9hr}}^{\mathrm{HOS}}(t)$.

4 EDW cases corresponding to both hogging and sagging were taken into account for each sea state. Following the crest-targeted FORM EDW described in Chapter 4, all EDW cases were set to induce the corresponding VBMs at the target time $t_0 = 45$ s and at the target location $x_0 = 18.2$ m that coincides with the location of the 6-DOF load sensor (ATI). The range of the EDW frequency components is from 0.35 Hz to 1.6 Hz with N=78 equidistant frequency components ($df = 0.016$ Hz). Therefore, the repeat period of the EDW is larger than $t_0 = 45$ s, meaning that no memory effect by repeated waves affects the system. The model stays in calm water until the first EDW wave packet arrives at x_0. The EDW is always a wave profile obtained numerically by

FORM. In experiments, we compared the VBM response induced by the experimentally reproduced EDW to the experimental Monte Carlo reference results.

Table 5.3 – Description of EDW cases (model scale)

Type	Case	Target POE $P_{tar}(\mathrm{VBM}^{\mathrm{HOS}}_{\mathrm{IW}_{9hr}}(t))$	SS6	SS8	SS10	SS12	SS17
			$\mathrm{VBM}^{\mathrm{HOS}}_{\mathrm{IW}}(P_{tar})$ (Nm)				
Hogging	**Hog1**	10^{-1}	63.0	100.7	120.8	142.2	203.1
	Hog2	10^{-2}	91.3	144.0	169.9	200.1	282.9
	Hog3	5×10^{-3}	95.5	153.2	181.8	213.5	305.7
	Hog4	10^{-3}	108.0	170.6	199.1	240.2	335.4
Sagging	**Sag1**	10^{-1}	-63.0	-101.5	-120.5	-140.8	-202.4
	Sag2	10^{-2}	-90.1	-141.9	-167.5	-194.9	-275.6
	Sag3	5×10^{-3}	-95.4	-147.7	-187.0	-212.6	-301.2
	Sag4	10^{-3}	-106.9	-173.8	-201.3	-239.9	-350.6

The VBM RAO considered in the target VBM selection as well as the EDW calculation is a linear transfer function calculated by BV Hydrostar [93]. Thus, the experimental VBM response induced by the reproduced EDW in the experiment will differ from the linear target VBM, $\mathrm{VBM}^{\mathrm{HOS}}_{\mathrm{IW}}(P_{tar})$. Based on this fact, finding the trend between target VBM, $\mathrm{VBM}^{\mathrm{HOS}}_{\mathrm{IW}}(P_{tar})$, and the experimental nonlinear VBM, $\mathrm{VBM}^{\mathrm{EXP}}_{\mathrm{EDW}}(x_0, t_0)$, in terms of sea state and wave characteristics of each EDW case has been one of the main objectives in this study (see Figure 5.2). In addition, it has to be noted that the POE curve of the 9-hour VBM time series data used to select the target VBM is not long enough to statistically represent a given sea state. Depending on the wave phase configuration, the slope of the POE curve of 9-hour VBM data can be expected to be highly variable, and therefore, the value of VBM corresponding to a specific target POE will vary for each VBM POE curve. Thus, the specified target POE values used in the initial stage of the procedure only serve as indicators for estimating the approximate size of the target VBMs. Details are given in Section 5.5.4 for VBM statistics.

5.4 Experimental setup and methods

5.4.1 Setup

The experimental configuration is presented in Figure 5.4. As mentioned earlier in Chapter 3, the 6750-TEU containership was considered a target ship for the experimental study with a scale ratio of 1/65. Note that in the case of VBM responses, only the values directly measured by the ATI were used in the result analysis.

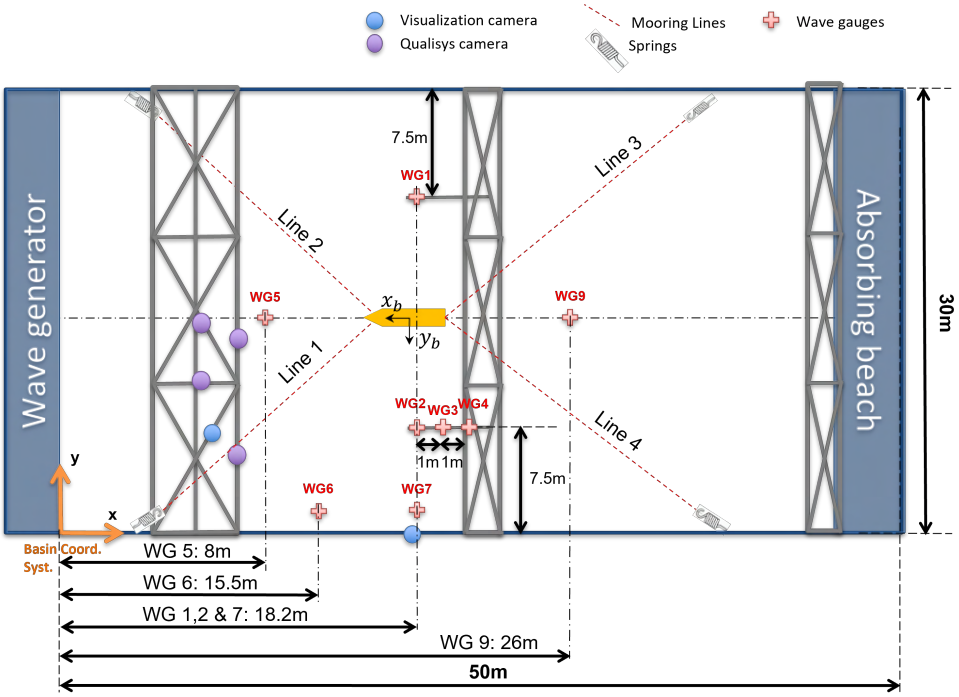

Figure 5.4 – Experimental setting for heading wave condition

As shown in Figure 5.4, 8 resistive wave gauges have been installed on both sides and the front and rear of the model. In particular, wave gauge No. 2, which was installed at the same longitudinal distance from the wavemaker as the ATI sensor, was considered a reference gauge for the data analysis.

5.4.2 Wave spectrum estimation

The average wave spectrum of all realizations for each sea state is shown in Figure 5.5. Note that there was an 8-month interval from the wave experiment presented in Chapter 4. Additional uncertainties due to sensor calibration, temperature, spurious waves, etc. could influence the wave measurement data. For this reason, the measurement data of wave gauge No.2 located 7 m away on the y-axis from the model is considered in the VBM experiment. Spectrum results are displayed as dimensionless quantities with their corresponding target values. Spectrum estimation was performed using the Welch method [98], and the time window used is 50 s long with 50 % overlap.

As can be seen from the results, overall, H_s of the estimated spectrum is slightly larger than the target value in most cases, and in the case of T_p, the result is in good agreement with the target value except for SS6. In the SS6 case, it can be seen that the shape of the estimated spectrum as compared to the target spectrum shows the largest difference visually, and the corresponding H_s and T_p show the largest error by

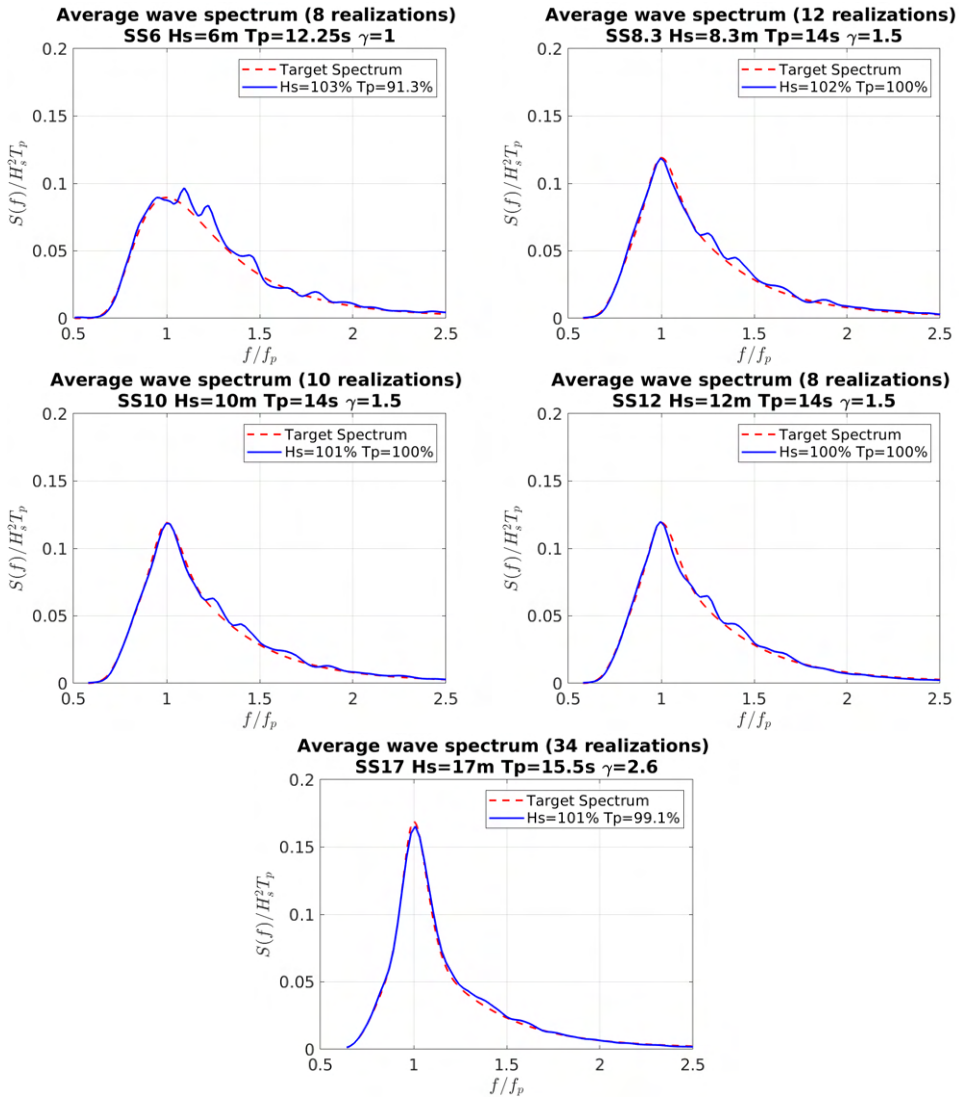

Figure 5.5 – Average wave spectrum of each sea state

$+3$ % and -8.7 %, respectively, as compared to the target values. Relatively similar overall spectrum results, including local fluctuations in the curve (blue), are found in SS8, SS10, and SS12 having the same T_p of 14.0 s. The maximum discrepancy in H_s and T_p in the three cases is 2 % and 0 % showing comparable results with respect to the target values. As shown in Figure 5.5, it can be said that the wave spectrum estimated has less smoothness with fewer realizations.

Considering that based on the $f/f_p = 1$, the estimated spectrum of lower-frequency components almost coincides with the target one, one can expect that higher-frequency components, more than $f/f_p = 1$, contribute to the such discrepancy in the estimation of the main parameters. In the case of SS17, which is the average of 34 realizations, a slight difference is observed as compared to the target spectrum in high-frequency components. However, the overall result seems comparable to the target as compared

to other cases.

The wave spectrum results in Figure 5.5 are compared with the calibration results presented in Section 4.5 for reference. Given that the wave-only tests were carried out 8 months prior to testing the model, it can be said that the aforementioned uncertainties may have influenced the wave quality: Some discrepancies are observed in the mildest sea state as compared to the wave-only test in terms of H_s (3.2 %) and T_p (8.7 %) presented in Chapter 4. Considering that T_p is calculated with the moments of the wave spectrum and the result is quite sensitive, it can be said that fairly comparable waves representing a given sea state are provided in all sea states.

The factors affecting the wave quality in experiments are related to the sensitivity of the measuring equipment, spurious waves such as transverse mode waves excited by the gaps between flaps and reflected waves by the physical limit of the absorbing beach, and the residual waves remaining from the previous run. Considering that the same wave was generated in the same experimental configuration, that would have similar spurious waves, above all, the difference between the two experimental results with a long time gap seems to be mainly due to the uncertainty in the sensitive wave gauge. The measurement of wave elevation via the resistive wave gauges is dependent on water conductivity, thus significantly different results for the same wave can be observed depending on temperature. According to Canard et al. (2022) [10], through a repeatability test, it was confirmed that the uncertainty of the wave calibration factor could account for up to about 3 %. In addition, the different residual wave conditions, which cannot be the same for each experiment, also seem to have contributed to the generation of these different wave qualities.

5.4.3 Sensitivity of VBM to the installation location

In the experiment, manual installation of the model at the target location using the four mooring lines was required, and therefore unavoidable human errors could occur in the installation procedure. This makes it very difficult to position the ATI sensor at the target location exactly coincident with the wave gauge No.2. In fact, the ATI sensor of the model was located at a distance of about 0.05 m in the upstream direction from the wave gauge ($x = 18.2$ m), and it was observed that the VBM response by the EDW occurred before $t = 45$ s. Due to the inconsistency in the installation location, it can be said that the VBM measured is the one induced by the waveform just before the full development of the target wave profile.

To determine how sensitive the model installation location is to the VBM response, the same EDW target value computed with two different target locations (x_0) of 18.2 m

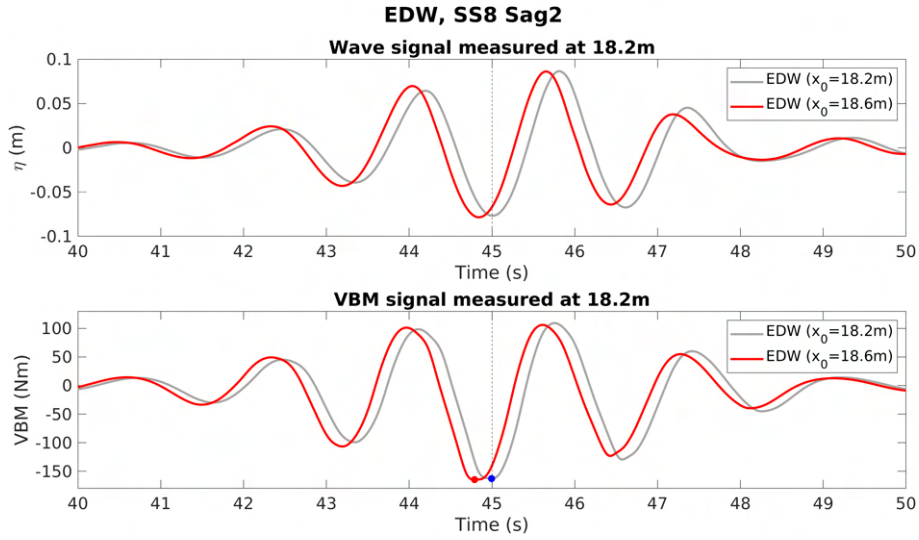

Figure 5.6 – Sensitivity of the EDW-induced VBM to the model installation location (model scale)

and 18.6 m were generated and the resulting VBM was measured with the ATI sensor at $x_0 = 18.2$ m. In the upper graph of Figure 5.6, the gray curve is the original wave profile where the focusing wave occurs at 18.2 m, and the red curve corresponds to the case where the target EDW profile occurs 0.4 m downstream of the x_0. The bottom graph shows the corresponding VBM responses induced by the EDWs above, showing that little difference is found in the magnitude of VBM with each other despite the 0.4m installation location difference. The difference in VBM magnitude is observed to be 0.9 %, so it can be considered that the model installation location sensitivity to the VBM is insignificant.

5.5 Experimental validation of EDW procedure

5.5.1 Generation of EDW in EWT

To qualitatively confirm the uncertainty factors affecting the wave quality in the actual experimental environment, the results of all EDW cases measured through wave gauge No.2 in the experiment with the model have been compared against those calculated in the HOS-NWT. Figure 5.7 shows the ratio of measured and calculated $\eta(x_0, t_0)$, height H, and period T of 8 individual EDWs for each sea state. H is a zero down-crossing wave height from a trough just before the target time t_0 to a crest at t_0, and T is a corresponding zero-crossing period as described in Figure 5.8.

The average(max/min) ratios in $\eta(x_0, t_0)$, H, and T of all EDW cases are observed to be 1.028(1.067/0.978), 1.018(1.045/0.965), and 0.999(1.006/0.993), and it can be

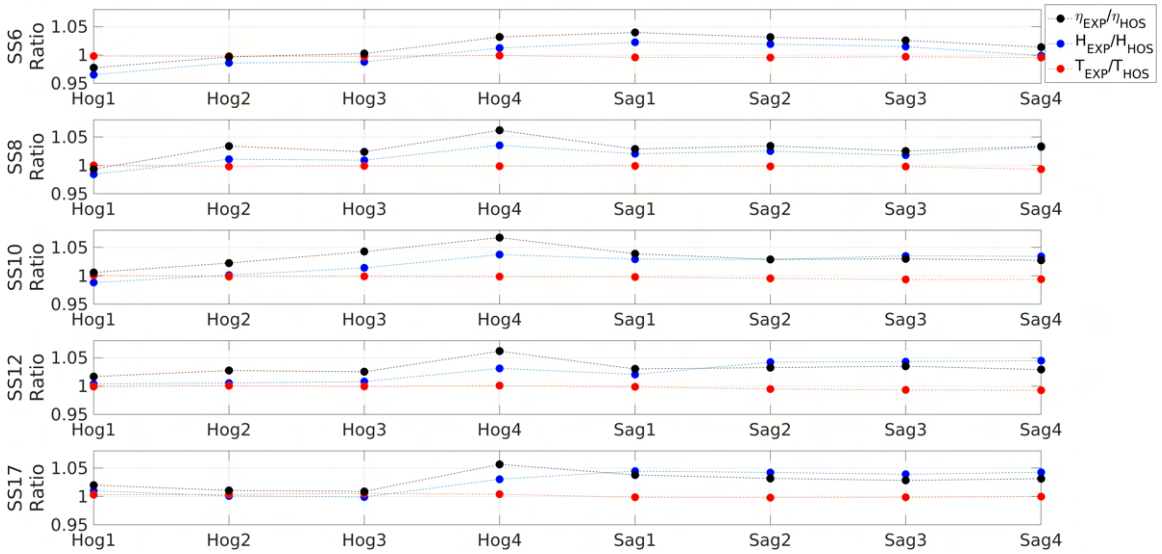

Figure 5.7 – The ratio of the measured EDW to the calculated EDW for main variables

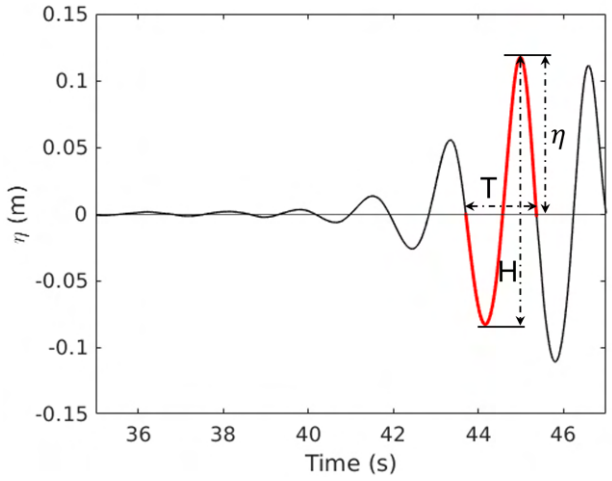

Figure 5.8 – Definition of the EDW η, height H, and period T

seen that the period is almost consistent with the HOS-NWT calculation result in all the cases. In each sea state, the maximum difference is observed in the Hog4 case, while the other cases show a very good agreement with the calculation, implying that the experimental setup including wave calibration was accurately performed.

Figures 5.9 for hogging and 5.10 for sagging show the time series of all EDW cases for SS10 that has a relatively large difference in measurements compared to the calculated variables (see Figure 5.8). As seen in Figures 5.9 and 5.10, the time series of the measured EDW including the zero-crossing period shows overall very good agreement with the numerically calculated EDW profile. Compared to the sagging-EDW (Figure 5.10), a large difference with a maximum of 7 % in $\eta(x_0, t_0)$ is observed in the hogging-EDW results (Figure 5.9). In the 4 sagging-EDW results, a noticeable discrepancy is

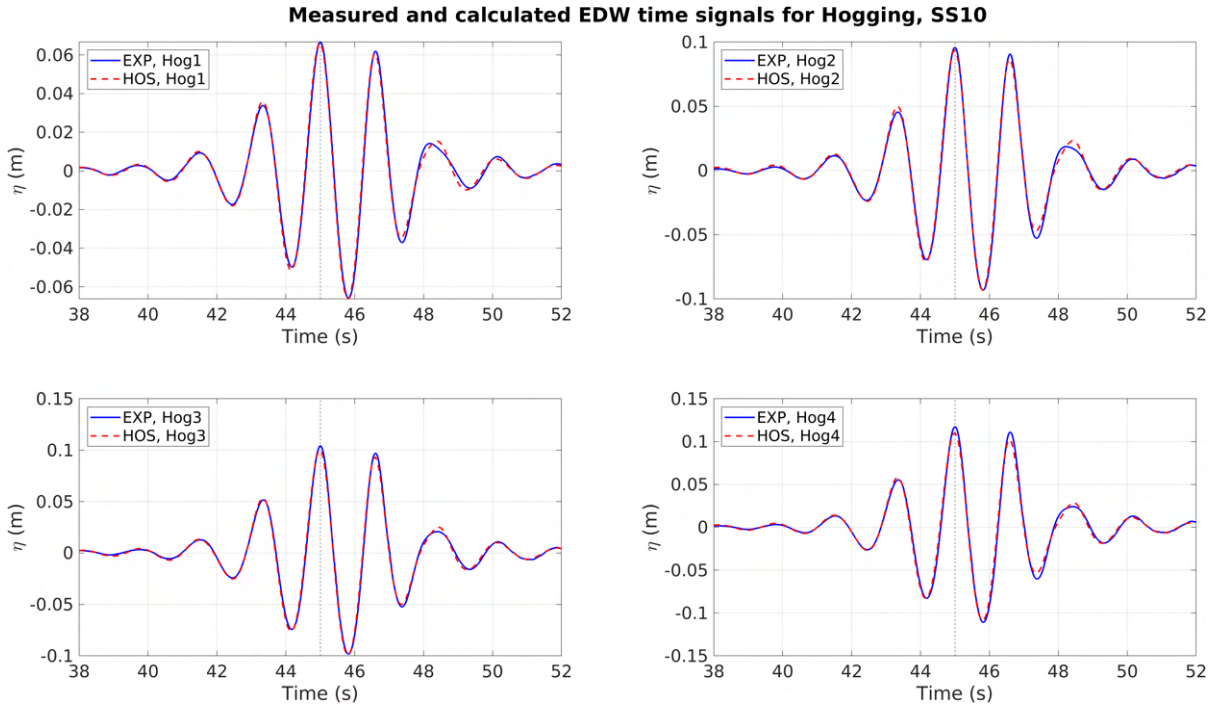

Figure 5.9 – SS10, Measured and calculated hogging-based EDW time signal (model scale)

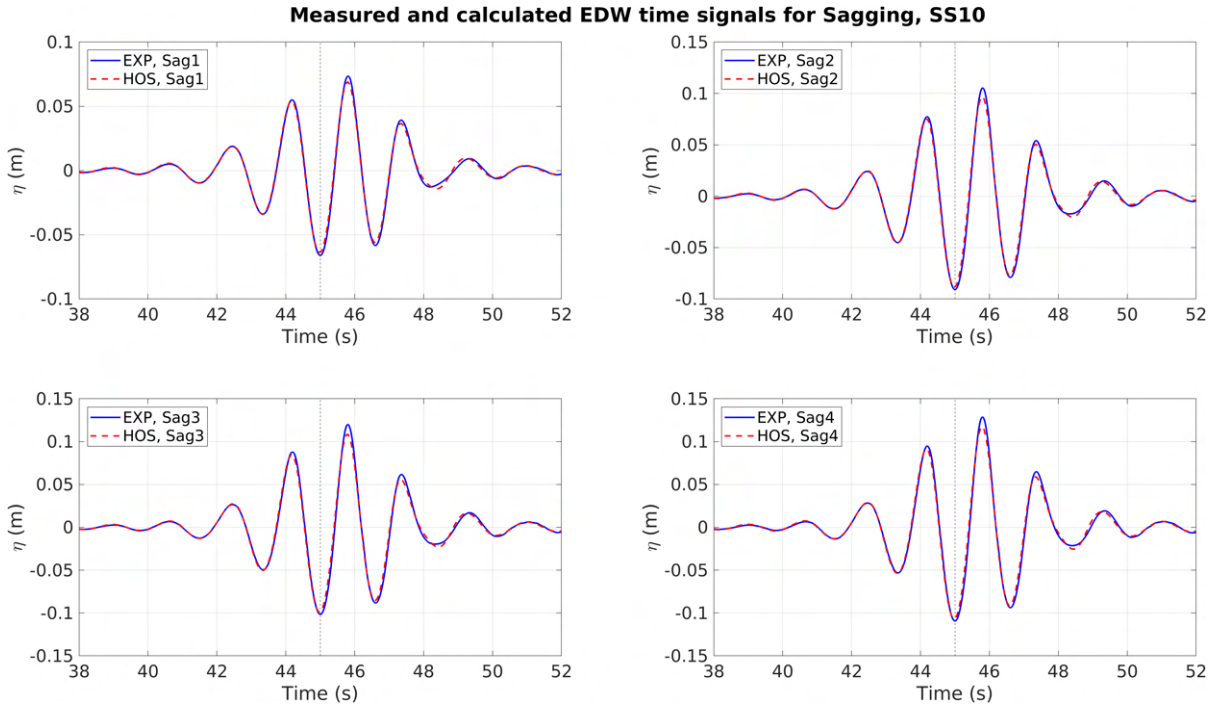

Figure 5.10 – SS10, Measured and calculated sagging-based EDW time signal (model scale)

observed in the following crest ($t =$ around 45.7 s) right after the trough at $t = 45$ s. On the other hand, the wave quality before $t = 45$ s, corresponding to the time interval of interest for the VBM response shows very good agreement with the numerical results.

5.5.2 Geometrical reviews on EDW and VBM response

A key aspect that we want to assess is whether the calculated nonlinear EDW has the most probable shape as compared to the actual irregular wave that generates a VBM response of similar magnitude. To check that, a review of the geometrical characteristics of EDW and measured VBM is carried out with all relevant irregular waves and their corresponding VBM signals for each sea state. First of all, VBM responses (VBM_{IW}^{EXP}) with ± 5 % tolerance to the EDW-induced VBM measured ($VBM_{EDW}^{EXP}(x_0, t_0)$) are extracted from all realizations for a given sea state. Then, the corresponding waves that occurred in the same time instant are extracted as well to compare with the EDW signal. As all the VBM responses and the corresponding wave signals are selected based only on the magnitude of EDW-induced VBM with $\pm 5\%$ tolerance, the extracted irregular wave signals can be various in shape. Thus, it can be figured out to what extent the geometrical shape of the EDW profile matches these random waves.

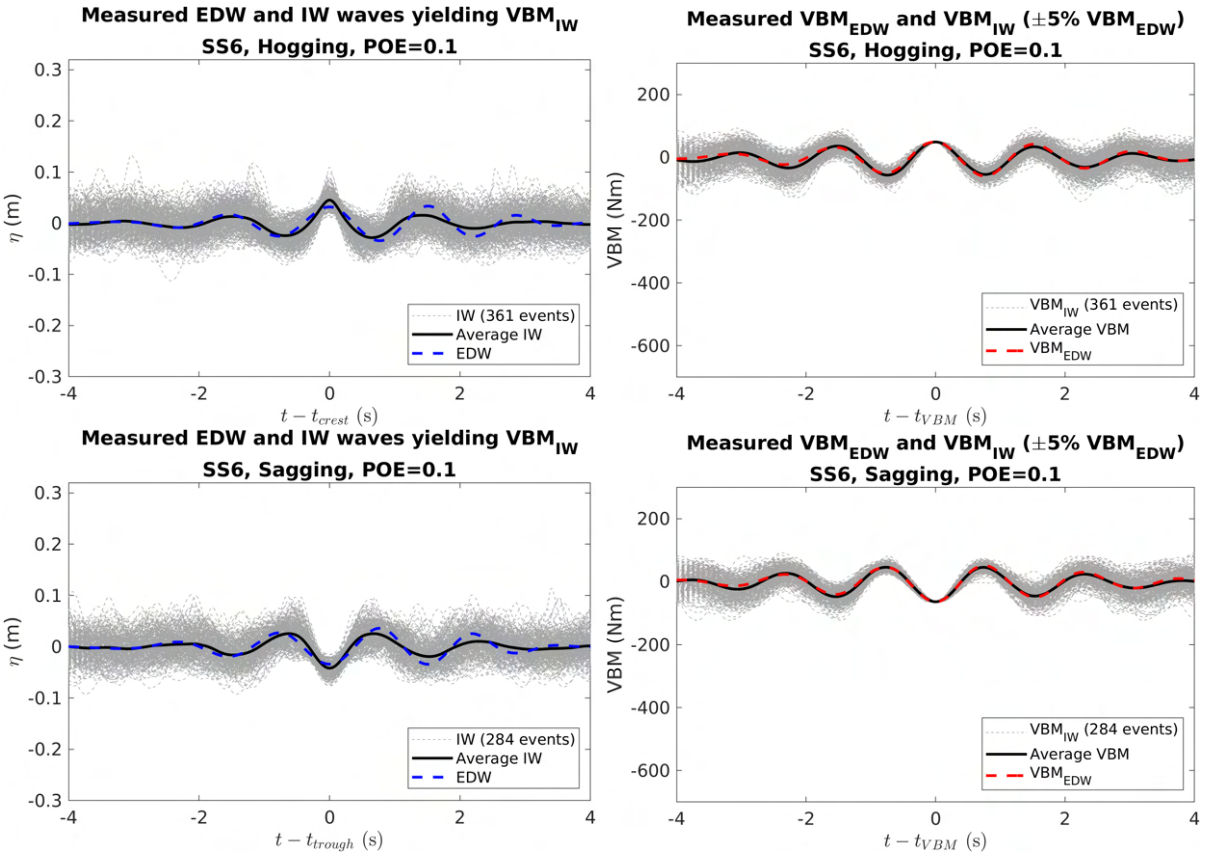

Figure 5.11 – SS6, target POE 0.1, EDW and extracted irregular waves (right side), and corresponding hogging and sagging responses (left side) (model scale)

Figures 5.11 to 5.18 show the extracted VBM (hogging and sagging) and corresponding wave time signals of SS6 and SS17, the mildest and the most severe sea state. For reference, the results of the other sea states (having similar trends of re-

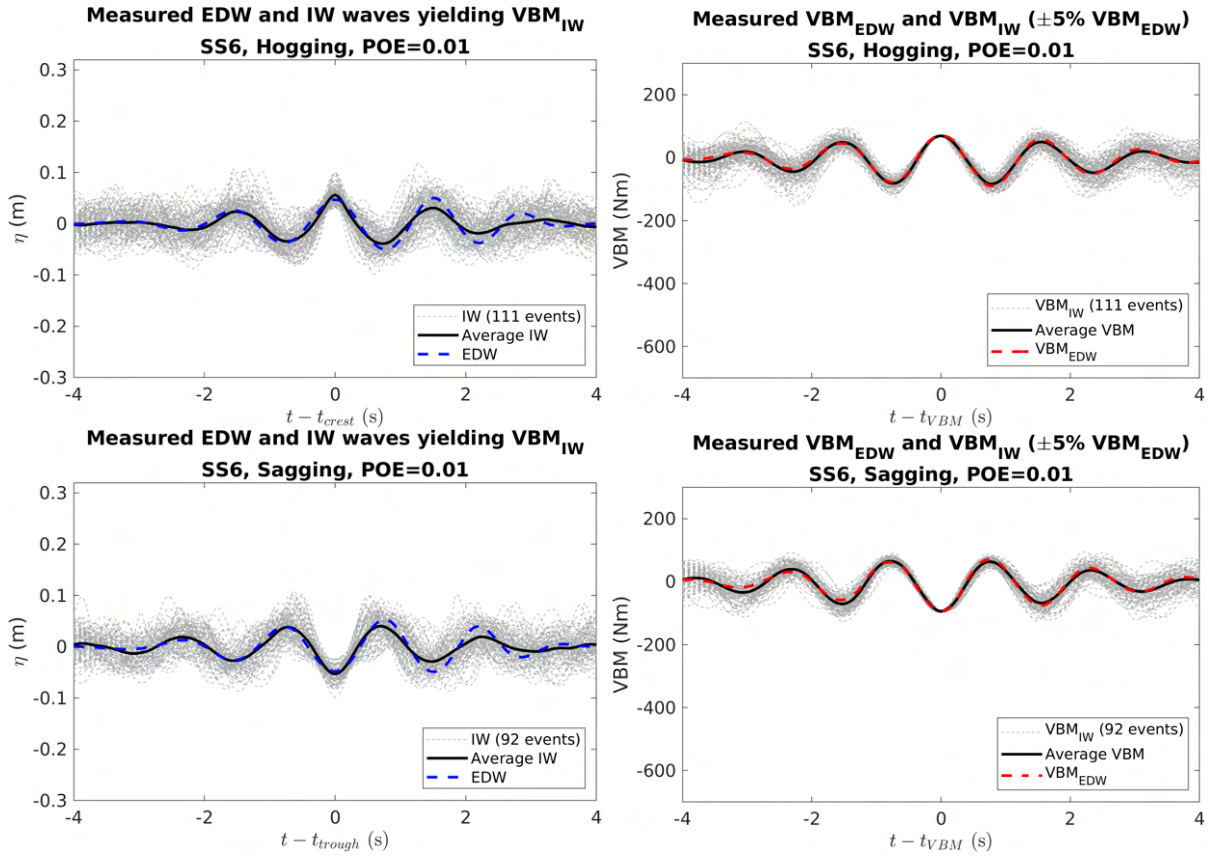

Figure 5.12 – SS6, target POE 0.01, EDW and extracted irregular waves (right side), and corresponding hogging and sagging responses (left side) (model scale)

sults) are presented separately in Appendix B. The graph of the wave signals that induced the VBMs is shown on the left and the corresponding VBM response signals are shown on the right. In the case of all the VBM signals (± 5 % tolerance of the VBM by EDW) extracted, the shape of all are very comparable with the VBM induced by EDW in all sea states in terms of peak value and period. It is observed that the hogging and sagging signals induced by EDW (red curve) are in very good agreement with an average of all irregular VBM signals. The periods of most VBM signals extracted with 5 % tolerance in VBM magnitude are also very similar to the VBM by EDW with no appreciable local fluctuations.

In the case of corresponding wave signals, a relatively large range of fluctuation with respect to the wave peak and period is found. In addition, as compared to the shape of hogging and sagging-related waves, the dispersion degrees of the peak of the irregular waves, inducing the hogging response is clearly larger than that of the sagging waves. This dispersion, however, only holds on the wave signals, while the VBM signals are far less scattered. Asymmetric wave shape with a high crest and less deep trough, which are the characteristics of the nonlinear wave, seems to be naturally

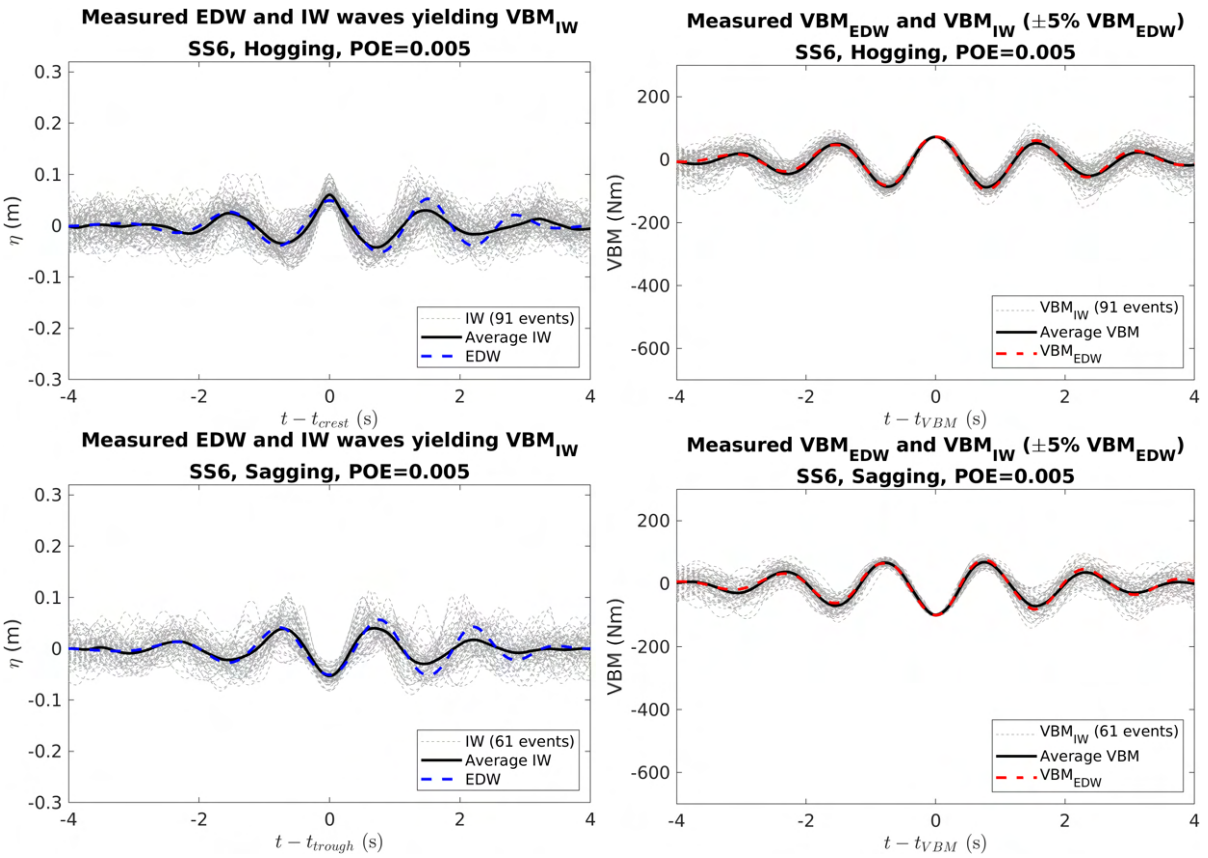

Figure 5.13 – SS6, target POE 0.005, EDW and extracted irregular waves (right side), and corresponding hogging and sagging responses (left side) (model scale)

reflected in the results.

The EDW and the average shape of irregular waves are more similar in sagging than hogging in all cases. The difference between the two wave shapes is noticeable, especially in the case where the target VBM is large for each sea state. Contrary to this, the shape difference is small as the target VBM decreases. Overall, the wave shape before t=0 matches the average shape of the irregular wave very well, whereas the discrepancy of the two signals after $t = 0$ is noticeably different. Nevertheless, the VBM response signal by the corresponding EDW shows overall good agreement with the average of irregular VBM responses.

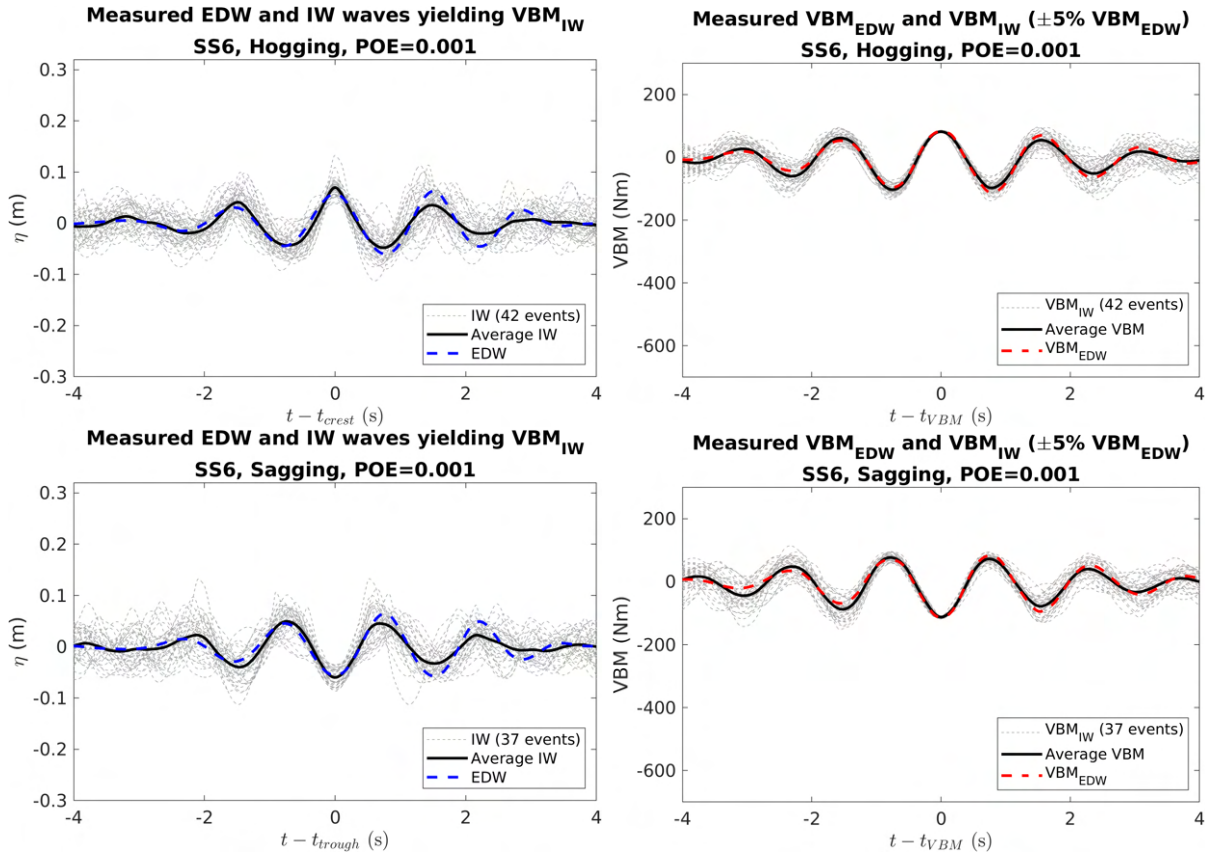

Figure 5.14 – SS6, target POE 0.001, EDW and extracted irregular waves (right side), and corresponding hogging and sagging responses (left side) (model scale)

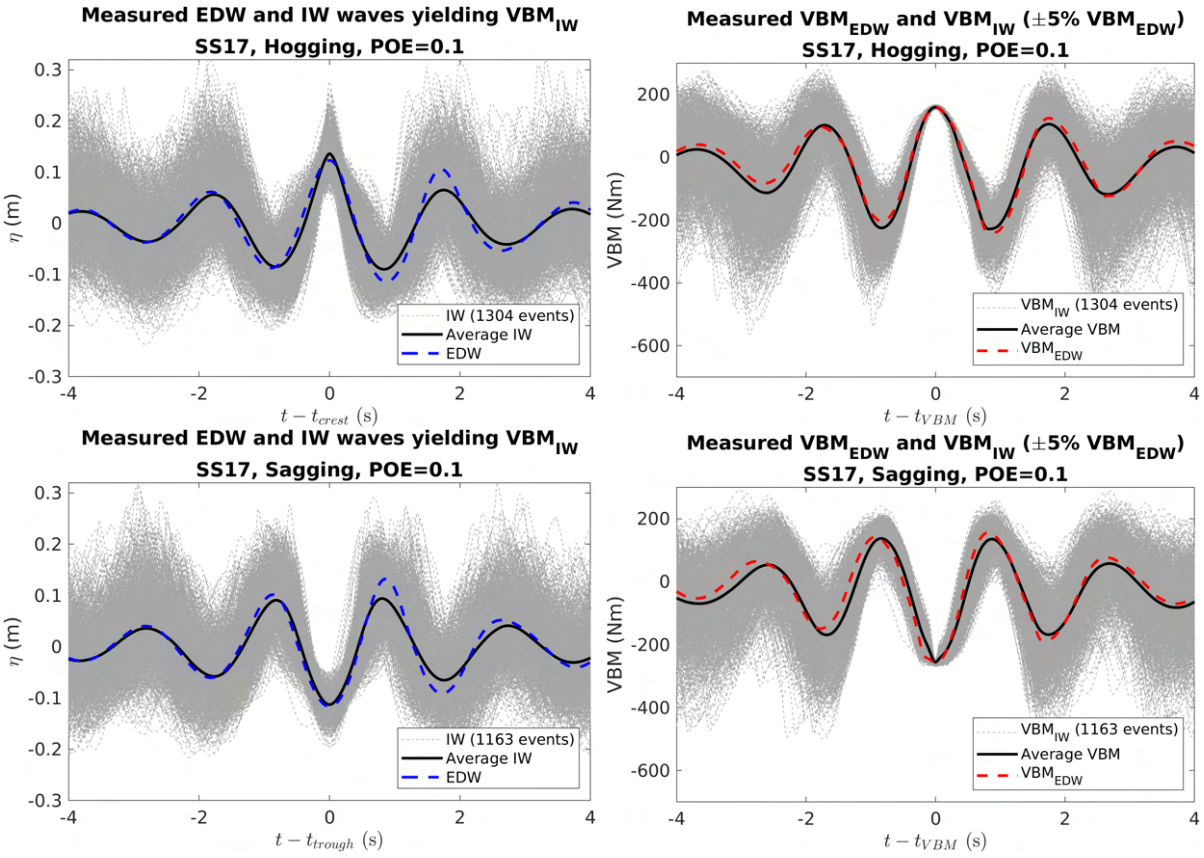

Figure 5.15 – SS17, target POE 0.1, EDW and extracted irregular waves (right side), and corresponding hogging and sagging responses (left side) (model scale)

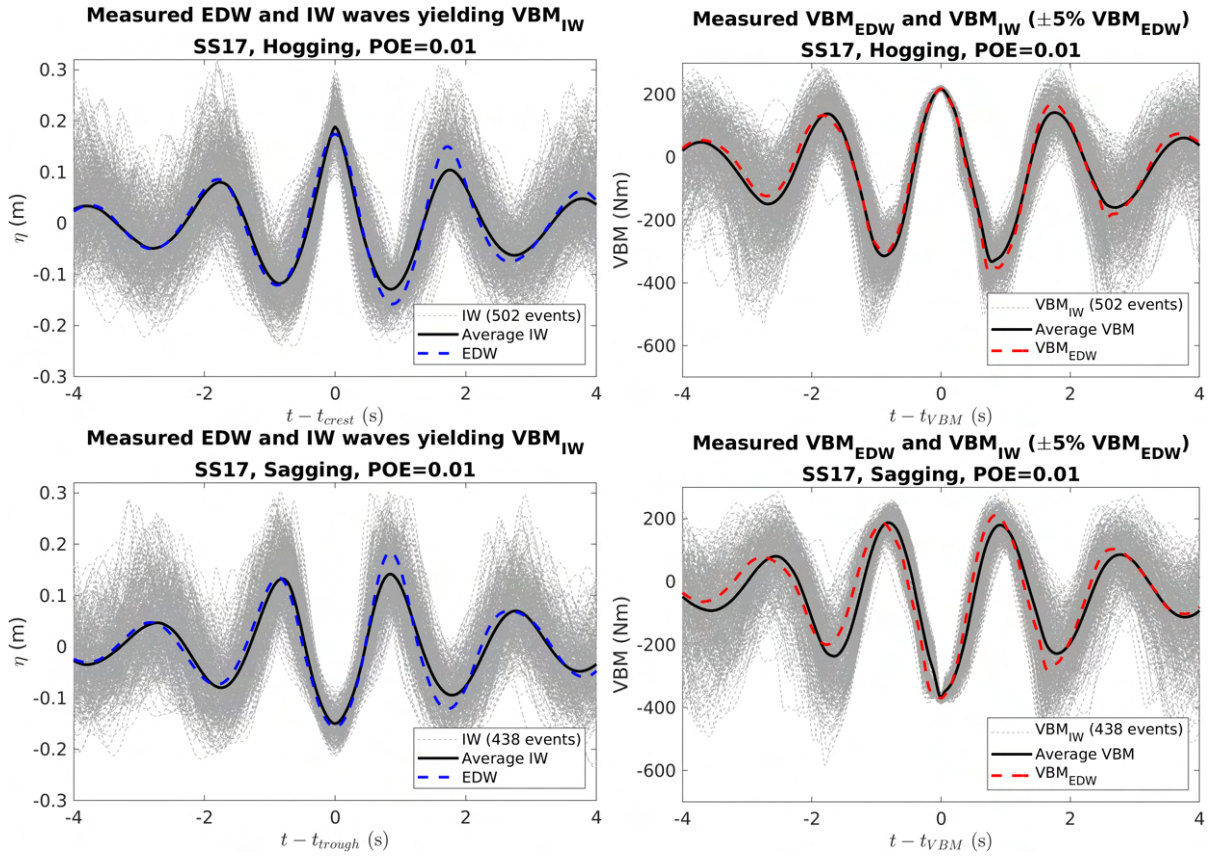

Figure 5.16 – SS17, target POE 0.01, EDW and extracted irregular waves (right side) and corresponding hogging and sagging responses (left side) (model scale)

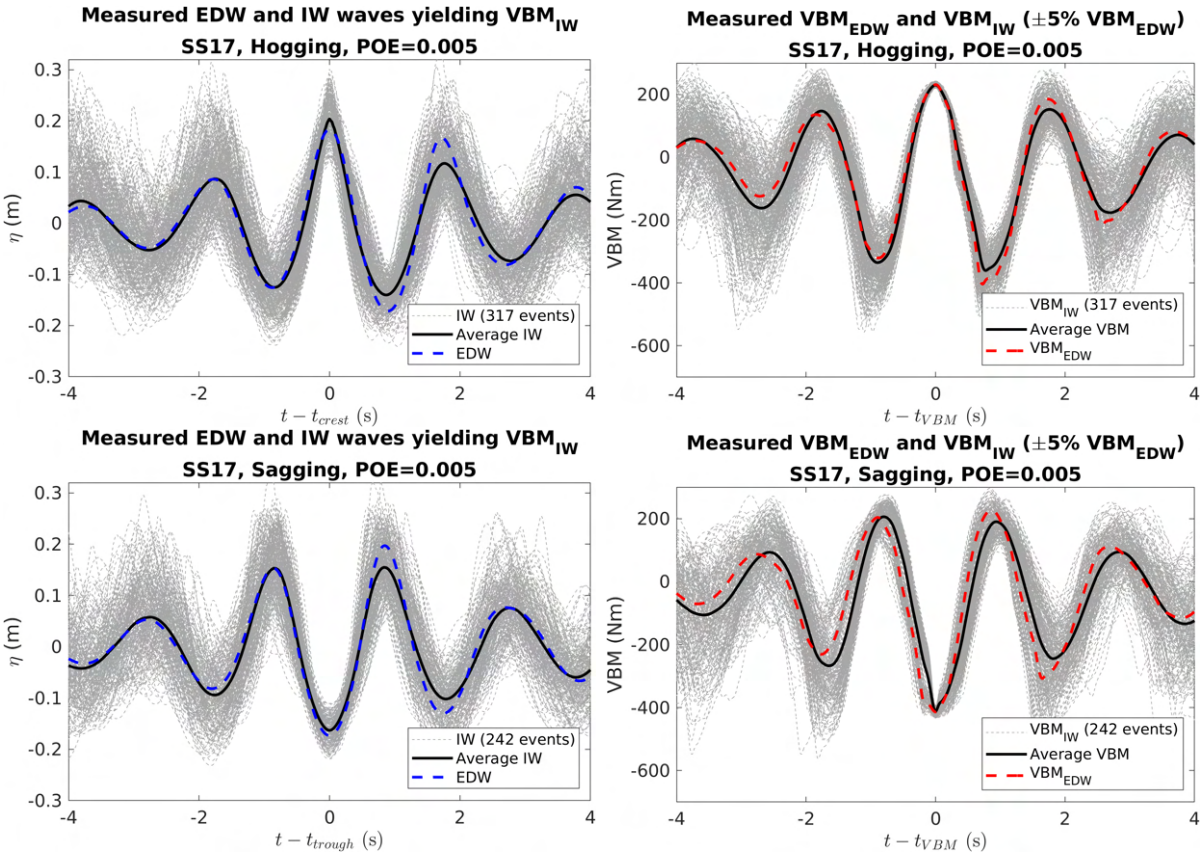

Figure 5.17 – SS17, target POE 0.005, EDW and extracted irregular waves (right side), and corresponding hogging and sagging responses (left side) (model scale)

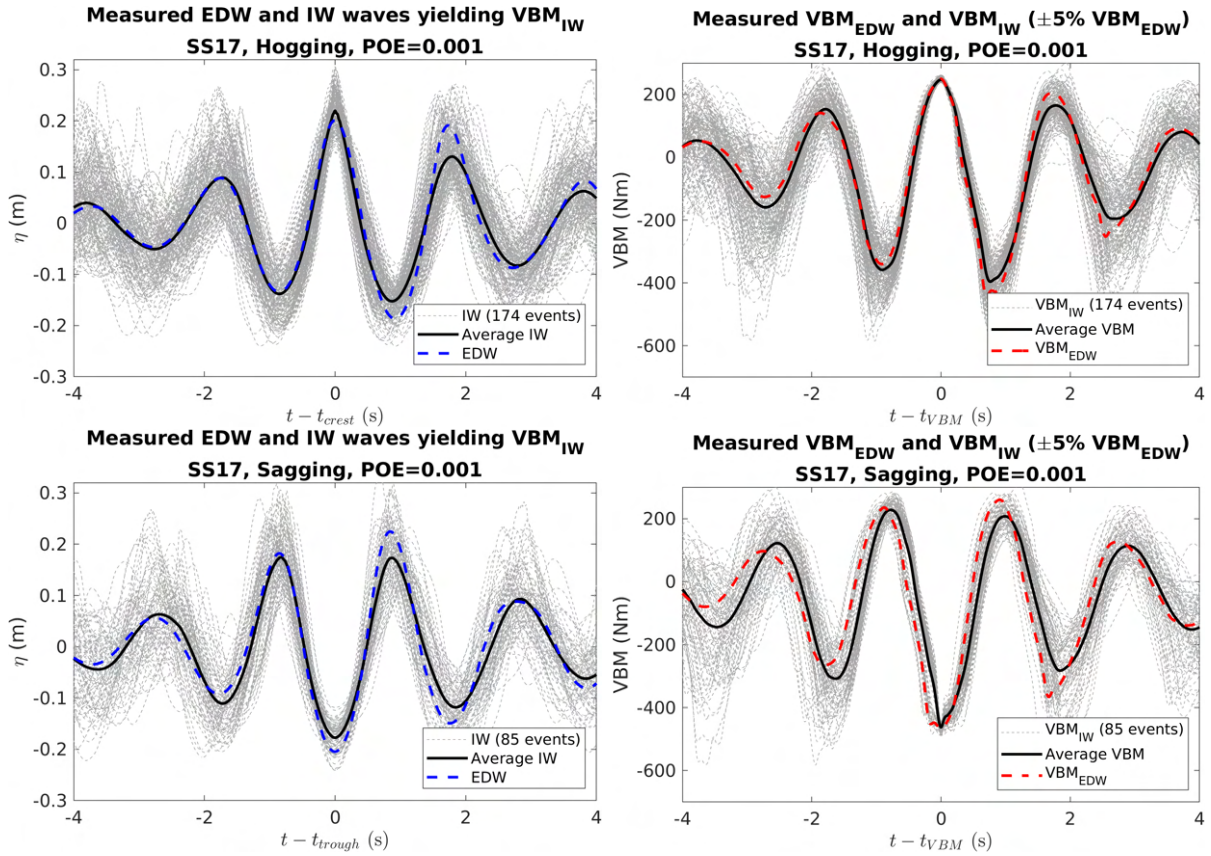

Figure 5.18 – SS17, target POE 0.001, EDW and extracted irregular waves (right side), and corresponding hogging and sagging responses (left side) (model scale)

5.5.3 Distribution of wave peak and period

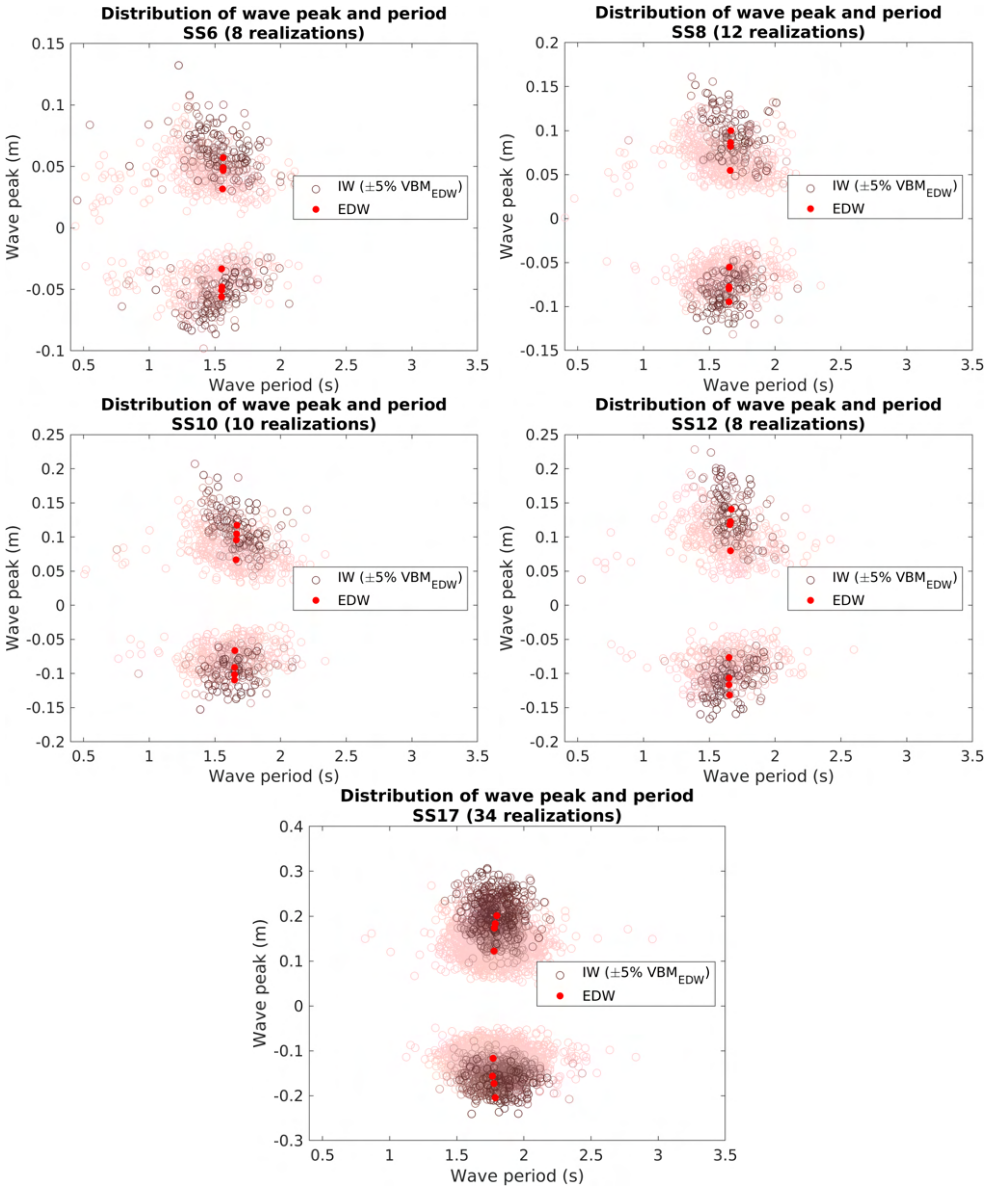

Figure 5.19 – Distribution of all EDW relevant waves extracted in each irregular sea state

The extracted irregular waves and corresponding EDW shown in the previous section are plotted with wave peak and period pairs in Figure 5.19 to clearly figure out the overall distribution of both EDW and irregular waves. In each graph, the points over and under the y=0 horizontal plane symmetry line denote hogging-based waves and sagging-based waves respectively.

The 8 red points in each graph correspond to 8 EDW cases. The lower the probability of exceedance, the further the red point from y=0. A variation is given to the colors of the surrounding points which correspond to the relevant irregular wave events extracted from all realizations. Darker colors indicate irregular waves associated with

the EDW of lower POE levels. In each graph, in the case of irregular wave distribution, there are some points that deviate from the main region, but most of the points are located in a certain range surrounding the EDW points. As observed in the wave time series, most EDW cases appear to have a peak and period pair close to the center of the irregular wave distribution.

In terms of the probability of occurrence, EDW can be seen as belonging to the wave range with the highest occurrence probability among the waves that induce a VBM of a similar target value. The latter confirms that the result is consistent with the objective of the FORM method. Given the overall shape of the EDW signal, and the peak and period distribution results, it can be seen that the nonlinear EDW profile calculated through the new FORM algorithm while applying the HOS-NWT is comparable with the most probable wave profile.

5.5.4 VBM probability of exceedance

Target VBM's POE correction with a 85-hour wave signal

It should be noted again that obtaining a POE curve with statistical convergence up to a specific level of probability depends on the length of the response signal. In order to obtain a POE curve converged up to a 10^{-3} probability level which corresponds to the level of an extreme event in the 3-hour short-term sea state, a sufficiently long time signal is required. In this regard, for the comparison of the calculated linear VBM RAO-based VBM POE curve with the VBM POE curve of the experimental Monte Carlo reference results, each case should be sufficiently long and similar.

The wave time signals taken into account when calculating the linear VBM POE curve and selecting the target VBM correspond to only 9 hours in full scale. From a probabilistic point of view, the 9-hour-based VBM POE curve cannot be a representative result for a given sea state. For example, Figure 5.20 shows the wave peak POE curves of measurement and calculation with various wave seed configurations for the same sea state. It can be seen that the POE curve of the 9-hour wave changes significantly as the wave seed configuration changes.

The curve (blue color) used when selecting the initial target VBM is literally one of them. In the same vein, the target POE value of the target VBM chosen for each EDW case is also highly dependent on it. To solve the issue, the full scale 85 hours of wave elevation time series (35 realizations of 2h 30min wave elevation) of a given sea state and corresponding linear VBM RAO-based VBM response time series were re-calculated, and we applied the re-calculated VBM results $\mathrm{VBM}^{\mathrm{HOS}}_{\mathrm{IW}_{85hr}}(t)$ as the numerical Monte Carlo reference for the comparative study with the experimental results.

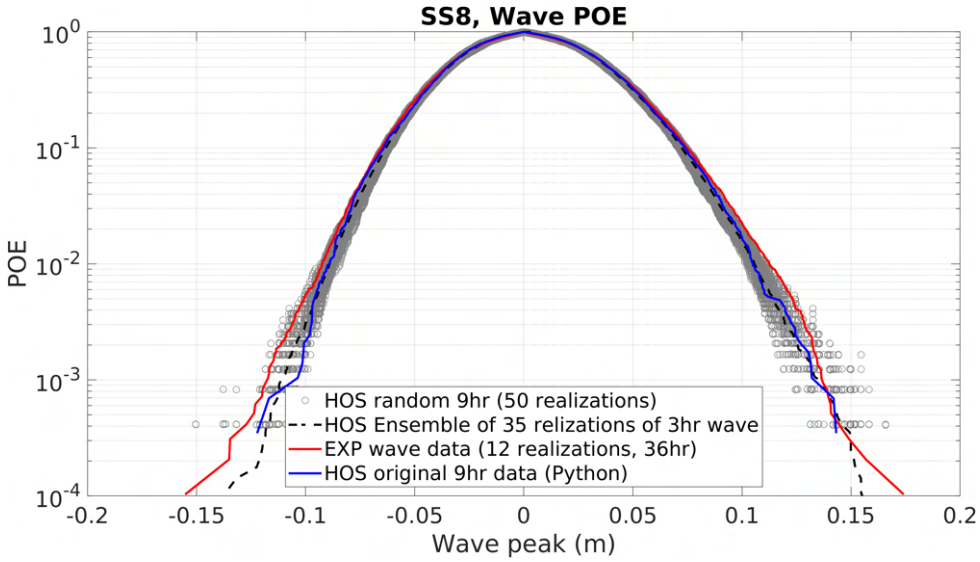

Figure 5.20 – Variability of 9-hour wave POE curve with various wave phase sets (model scale)

The corresponding VBM POE curve was then used for the final comparison with the experimental results.

Accordingly, for the 4 target VBMs of each sea state that were initially selected based on the POE curve of a 9-hour VBM time signal ($\text{VBM}^{\text{HOS}}_{\text{IW}_{9hr}}(t)$), their POE values corresponding to 0.1, 0.01, 0.005, and 0.001 (same for all sea states) were replaced with the statistically converged POE values by referring to the 85-hour VBM signal. In detail, the initial target VBM can be found in the POE curve of the 85-hour numerical Monte Carlo reference ($\text{VBM}^{\text{HOS}}_{\text{IW}_{85hr}}(t)$), and the POE value at that position was finally taken as the POE of each target VBM. It can be said the changed POE is statistically reliable. Table. 5.5.4 shows the detailed results for the replaced POEs $\mathbf{P}_{tar}(\text{VBM}^{\text{HOS}}_{\text{IW}_{85hr}}(t))$ for all the target VBMs. Also, the POE of each target VBM estimated by the FORM method using Eq. (4.2) is presented in the table for reference. The results show that the FORM gives fairly comparable estimates for most cases, while it tends to overestimate the POE for the relatively large target responses with a maximum difference of 100 % as compared to the $\mathbf{P}_{tar}(\text{VBM}^{\text{HOS}}_{\text{IW}_{85hr}}(t))$ in each sea state. A similar trend was observed in the numerical study of the vertical bending moment of a ship by Jensen (2009) [46].

VBM POE curve correction with estimated H_s

Considering that the numerical assumptions for wave generation in the NWT and the uncertainty factors in the EWT affect the wave quality, as a result, the waves in the two environments cannot be exactly the same. From a quantitative point of view, an

Table 5.4 – Replacement of the POE value for the selected target VBM to the statistically converged value and the POE estimated by the FORM method

	$\mathbf{P}_{tar}(\mathrm{VBM}^{\mathrm{HOS}}_{\mathrm{IW}_{9hr}}(t))$	$\mathbf{P}_{tar}(\mathrm{VBM}^{\mathrm{HOS}}_{\mathrm{IW}_{85hr}}(t))$		FORM estimation	
	HOG and SAG	HOG	SAG	HOG	SAG
SS6	0.1	0.1060	0.1075	0.0959 (-9.5 %)	0.0968 (-9.9 %)
	0.01	0.0095	0.0109	0.0093 (-3.0 %)	0.0106 (-2.2 %)
	0.005	0.0061	0.0062	0.0061 (-0.6 %)	0.0063 (1.1 %)
	0.001	0.0010	0.0015	**0.0015 (48.8 %)**	**0.0018 (22.3 %)**
SS8	0.1	0.1115	0.1055	0.0959 (-14.0 %)	0.0933 (-11.5 %)
	0.01	0.0109	0.0127	0.0096 (-12.0 %)	0.0112 (-11.6 %)
	0.005	0.0058	0.0087	0.0053 (-9.6 %)	0.0078 (-10.5 %)
	0.001	0.0015	0.0015	0.0015 (5.4 %)	0.0013 (-16.9 %)
SS10	0.1	0.1101	0.1111	0.0973 (-11.7 %)	0.0995 (-10.5 %)
	0.01	0.0114	0.0134	0.0114 (-0.8 %)	0.0132 (-1.6 %)
	0.005	0.0060	0.0044	0.006 (-0.2 %)	0.0046 (5.0 %)
	0.001	0.0023	0.0020	0.0022 (-3.2 %)	0.0020 (-2.6 %)
SS12	0.1	0.1158	0.1224	0.1049 (-9.4 %)	0.1107 (-9.6 %)
	0.01	0.0097	0.0148	0.0112 (15.4 %)	0.0166 (11.9 %)
	0.005	0.0055	0.0061	**0.0071 (30.1 %)**	**0.0077 (26.5 %)**
	0.001	0.0011	0.0011	**0.0019 (79.9 %)**	**0.0020 (78.4 %)**
SS17	0.1	0.1300	0.1350	0.1164 (-10.5 %)	0.1189 (-12.0 %)
	0.01	0.0142	0.0184	0.0160 (12.6 %)	0.0205 (11.3 %)
	0.005	0.0059	0.0065	**0.0078 (33.5 %)**	**0.0095 (45.7 %)**
	0.001	0.0019	0.0009	**0.0034 (78.1 %)**	**0.0017 (100.7 %)**

accurate comparison is possible only when numerical and experimental Monte Carlo references are the results in the same sea condition with the same spectral characteristics, in particular H_s. To check this, the significant H_s of a given sea state in each environment was first compared.

Table 5.5 – Estimated H_s and correcting factor (full scale)

	${H_s}^{target}$	${H_s}^{9hr}$	${H_s}^{85hr}$	${H_s}^{exp}$	$\frac{{H_s}^{target}}{{H_s}^{9hr}}$	$\frac{{H_s}^{target}}{{H_s}^{85hr}}$	$\frac{{H_s}^{target}}{{H_s}^{exp}}$
SS6	6	5.88	6.10	6.18	1.020	0.983	0.971
SS8	8.3	8.18	8.10	8.44	1.015	1.024	0.983
SS10	10	9.72	9.74	10.10	1.029	1.026	0.991
SS12	12	11.40	11.61	12.03	1.053	1.034	0.997
SS17	17	15.95	16.05	17.26	1.069	1.059	0.985

As summarized in Table 5.5, the results of experiments and numerical calculations for each sea state show a difference from the target sea in terms of the significant wave height H_s. From a quantitative point of view, to compare the experimental Monte Carlo reference with the linear VBM responses of a given sea state with at least the same

H_s, the ratio of the target H_s to the estimated H_s (H_s^{exp} for the experimental result and H_s^{85hr} for the numerical result) is considered as a correction factor, and equivalent VBM POE curves for H_s considering the correction factor are calculated respectively with Eq. (5.5). Note that all analysis results after this section are the results considering the H_s correction factor.

$$\begin{aligned} \text{equivalent VBM}_{\text{IW}}^{\text{EXP}}(t) &= \text{VBM}_{\text{IW}}^{\text{EXP}}(t) \times \frac{H_s^{target}}{H_s^{exp}} \qquad \text{for experimental Monte Carlo results} \\ \text{equivalent VBM}_{\text{IW}}^{\text{HOS}}(t) &= \text{VBM}_{\text{IW}_{85hr}}^{\text{HOS}}(t) \times \frac{H_s^{target}}{H_s^{85hr}} \qquad \text{for numerical Monte Carlo results} \end{aligned} \tag{5.5}$$

Equivalent VBM POE distribution

Figures 5.21 to 5.23 show the results from the POE distribution of the VBM response measured and calculated for each sea state. As mentioned earlier, the numerical and experimental Monte Carlo results and all experimental single realization results in each figure correspond to the equivalent VBM POE curves considering the correction factor in H_s. The linear VBM response calculated with 35 realizations of 2h 30min wave elevation has been used as a reference (green curve). Accordingly, the POE of the target VBMs selected based on the initial 9-hour HOS wave data is replaced with the POE value corresponding to each target VBM ($\text{VBM}_{\text{IW}}^{\text{HOS}}(P_{tar})$) on the green curve (blue points). The measured nonlinear VBMs ($\text{VBM}_{\text{EDW}}^{\text{EXP}}(x_0, t_0)$) induced by the reproduced EDWs in the EWT are also plotted at the same corrected POE levels (yellow points).

In the case of experimental results, not only the ensemble POE of all realizations (Experimental Monte Carlo result displayed in a blue curve) but also the POE of individual realizations (gray points) corresponding to about full scale 2h 30min is displayed to figure out the variability of the POE curve with random wave phase sets. A Jeffrey 95 % confidence interval is taken into account as well for each value of the experimental Monte Carlo POE result (blue curve) to check the statistical variability [7].

As expected, the estimated statistical uncertainty through the Jeffrey 95 % confidence interval appears to be very large at the tail part of the experimental Monte Carlo POE curve of all sea states. It is worth noting that for SS17, the result of 34 realizations, the height of the confidence interval corresponding to the difference between the upper and lower bound is significantly reduced at lower POE levels as compared to the rest of the sea state results.

Looking at the POE results of individual realizations, it can be seen that the range

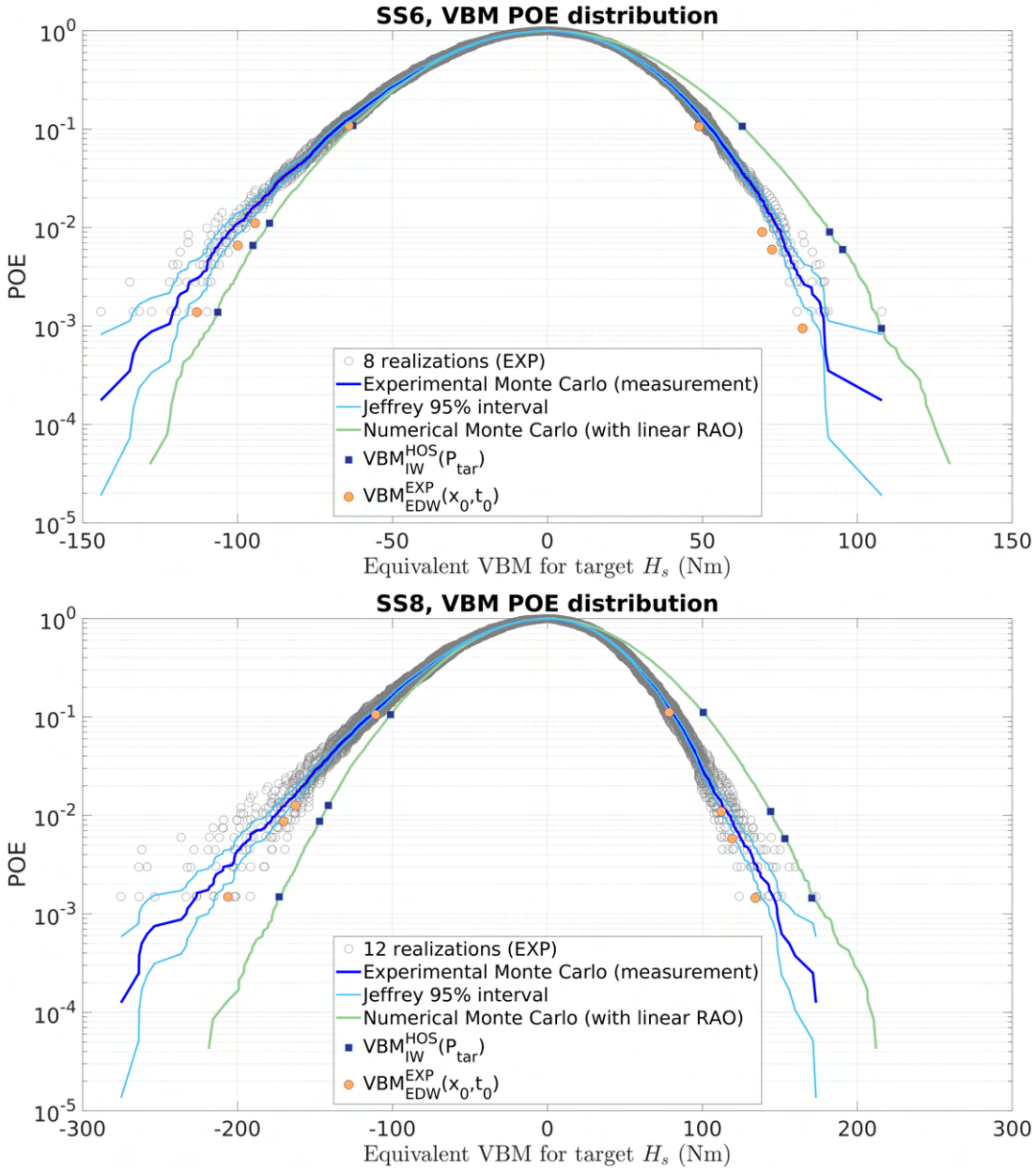

Figure 5.21 – Empirical VBM POE distribution for SS6 and SS8 (model scale)

of the sagging POE distributions is noticeably larger as compared to the hogging results in all sea states. The latter indicates that the sagging responses contain stronger nonlinear wave and the corresponding nonlinear motion effects than the hogging responses. It is likely that the nonlinear wave-structure interaction occurs more intensely in the sagging response from a viewpoint of structural response characteristics, resulting in a large range of the POE distribution. In the same vein, the slope increase rate of the nonlinear sagging POE curve with respect to the linear VBM RAO-based numerical Monte Carlo reference (green curve) increases significantly as the sea state became more severe. Whereas, in the hogging response, it is observed that the difference in

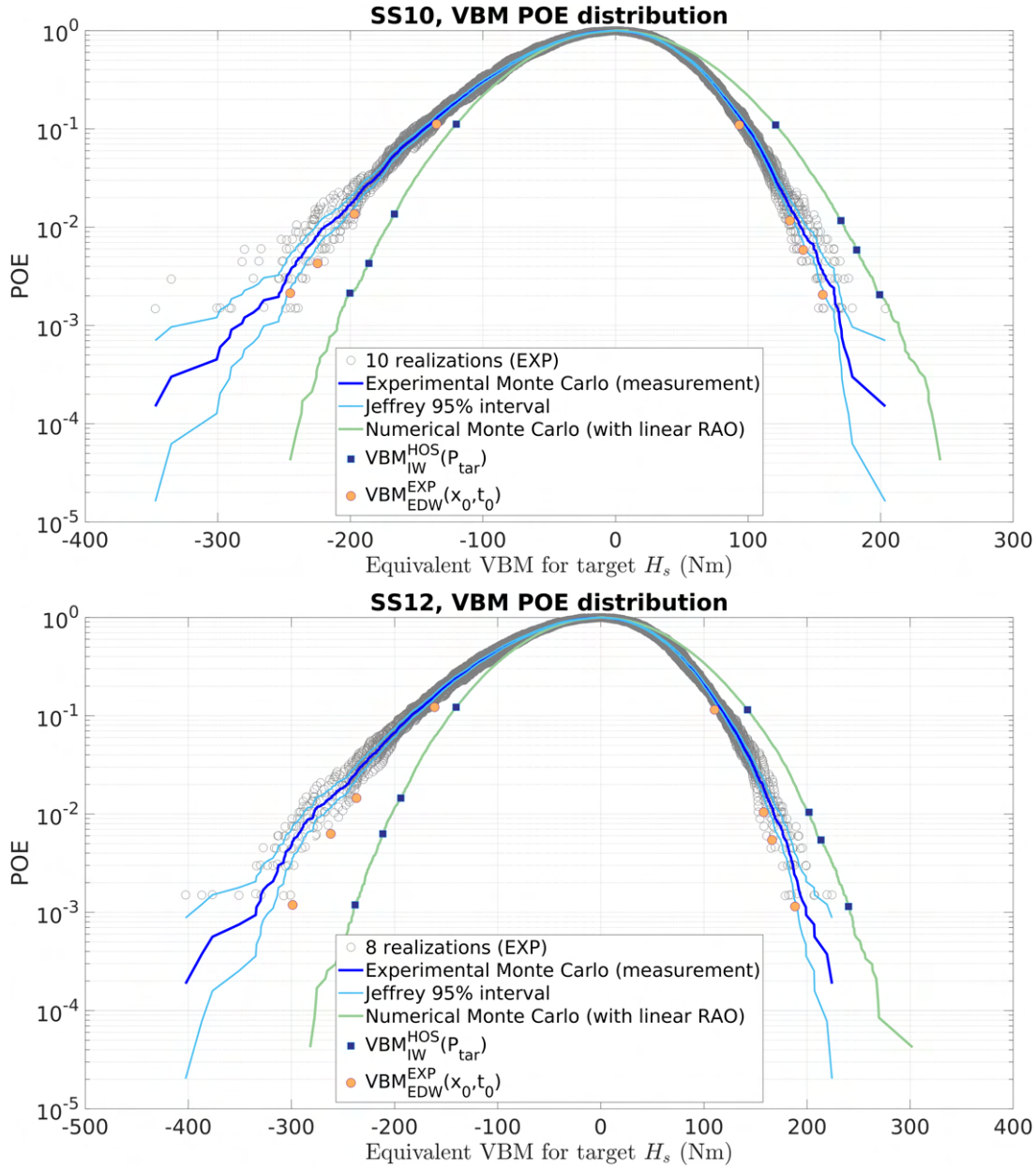

Figure 5.22 – Empirical VBM POE distribution for SS10 and SS12 (model scale)

the nonlinear response to the linear response is qualitatively similar overall.

The EDW-induced nonlinear hogging responses (yellow points) are in very good agreement with the experimental Monte Carlo reference results. The sagging responses by EDW are also similar in magnitude to the irregular wave result in most sea states. However, in all cases, the response by the EDW is always lower than the response by the irregular wave of the same POE level. The EDW-induced sagging responses of the SS6 and SS12 cases in which a relatively small number of realizations (8 runs) were performed show a relatively large difference from the irregular wave result compared to the other sea state case. As expected, the difference becomes larger as the POE

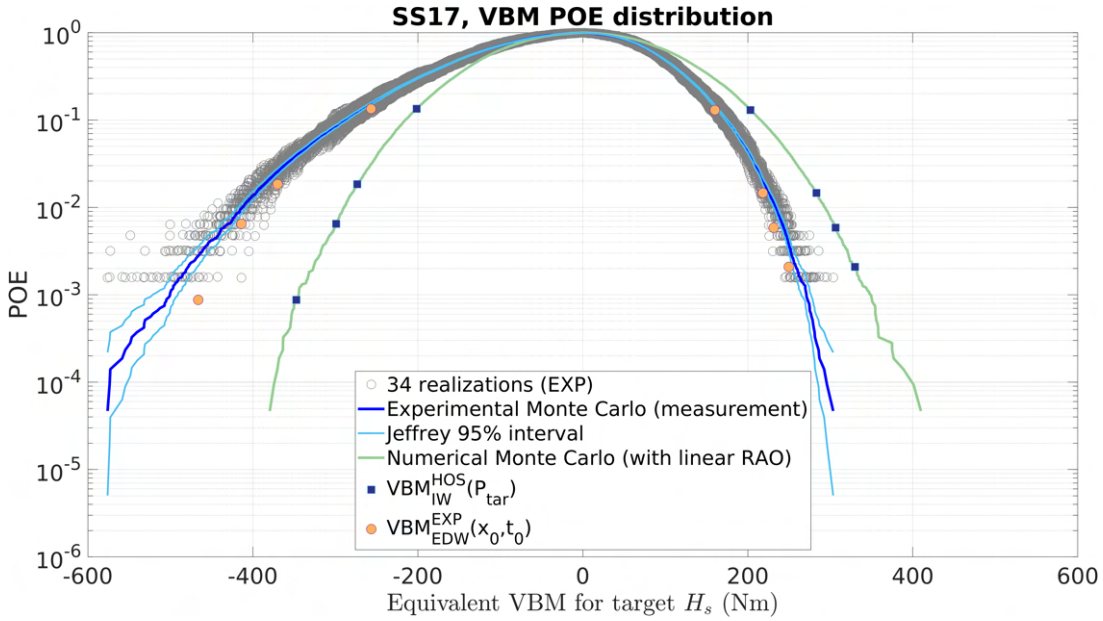

Figure 5.23 – Empirical VBM POE distribution for SS17 (model scale)

level decreases, and a noticeable difference is observed especially in SS12, where the sea conditions are more severe. In the case of SS17, which has been implemented 34 times, the ensemble curve of the nonlinear VBM also seems sufficiently converged up to the POE level of 10^{-3}, with little fluctuation in the tail part of the curve. In all EDW cases of SS17, EDW-induced both the hogging and sagging responses are in overall good agreement with the irregular wave result (blue curve).

5.6 Nonlinear effects in the VBM

5.6.1 VBM RAO sensitivity to the EDW calculation

One thing to note again is that the EDW is calculated by applying the linear VBM RAO for the practical use of the EDW approach. However, depending on the sea conditions, one may arise that the vessel will behave differently, which is likely to result in a different RAO.

From a statistical perspective, if it is significantly different from the nonlinear response, the EDW calculated based on the linear RAO basis corresponding to a given POE level will possibly exhibit large discrepancies in comparison to the 'exact' EDW. The nonlinear effects on the VBM responses are further discussed with the concept of nonlinear RAO (Appendix A). The linear and the estimated nonlinear RAO for each sea state are compared in terms of their time signals and POE curve.

The amplitude of the target VBM selected at a given POE level will be different.

However, if the VBM response spectra are similar to each other, then the EDWs that induce each VBM should also be similar. To check this and also to experimentally validate the estimation process of the nonlinear hogging and sagging RAO, further tests were performed with the EDW calculated based on the experimental nonlinear VBM RAO for the SS17 sea state. Note that the EDW calculation procedure applied is exactly the same as mentioned in Section 5.2.3, but with the experimental nonlinear VBM RAO instead of the linear RAO. The detailed estimation procedure for the nonlinear RAO is introduced in Appendix A.

Table 5.6 – Difference between $\mathrm{VBM}_{\mathrm{IW}}^{\mathrm{HOS}}(P_{tar})$ and $\mathrm{VBM}_{\mathrm{EDW}}^{\mathrm{EXP}}(x_0, t_0)$ for nonlinear VBM RAO-based EDW cases (model scale)

P_{tar}	$\mathbf{HOG}_{\mathbf{IW}}^{\mathbf{HOS}}(P_{tar})/\mathbf{HOG}_{\mathbf{EDW}}^{\mathbf{EXP}}$ **(Diff. %)**	$\mathbf{SAG}_{\mathbf{IW}}^{\mathbf{HOS}}(P_{tar})/\mathbf{SAG}_{\mathbf{EDW}}^{\mathbf{EXP}}$ **(Diff. %)**
10^{-1}	156.0 / 158.2 (-1.39 %)	-264.2 / -254.3 (-3.89 %)
10^{-2}	216.0 / 217.3 (-0.60 %)	-366.4 / -370.5 (-1.10 %)
5×10^{-3}	233.0 / 230.5 (1.08 %)	-399.0 / -405.1 (-1.51 %)
10^{-3}	258.3 / 252.1 (2.45 %)	-457.1 / -465.0 (-1.69 %)

The results are summarized in Table 5.6. It is observed that the maximum difference between the nonlinear RAO-based $\mathrm{VBM}_{\mathrm{IW}}^{\mathrm{HOS}}(P_{tar})$ and $\mathrm{VBM}_{\mathrm{EDW}}^{\mathrm{EXP}}(x_0, t_0)$ is about 3.9 % and the average difference is about 1.7 %. It means that the nonlinear VBM RAO estimation is correctly performed and represents fairly well the actual VBM response of the rigid model. Nevertheless, a discrepancy exists. Appendix A discusses the possible causes of this discrepancy by comparing the full scale 2h 30min VBM signal calculated from the estimated RAO and the measured irregular waves with the actual measured VBM.

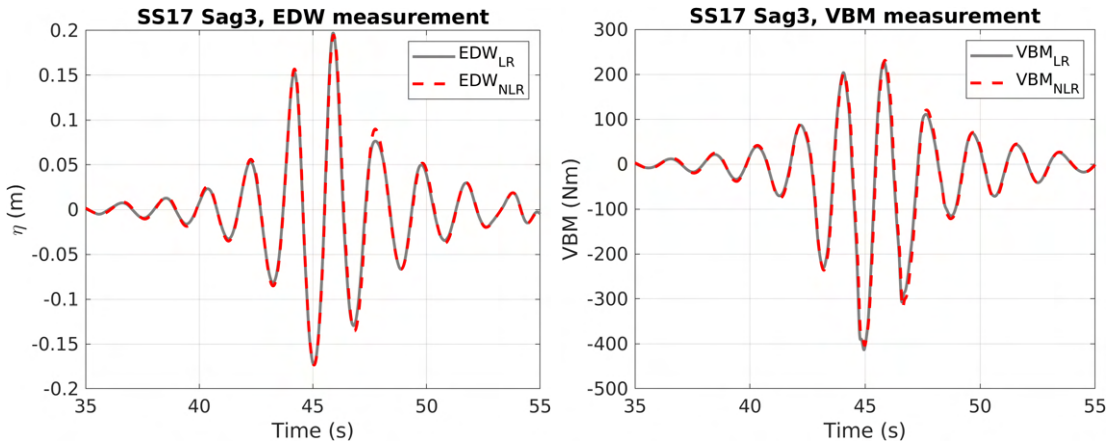

Figure 5.24 – Linear and nonlinear VBM RAO based EDW and corresponding measured VBM in the experiment

As a next step, to confirm the VBM RAO sensitivity to the EDW wave profile, two

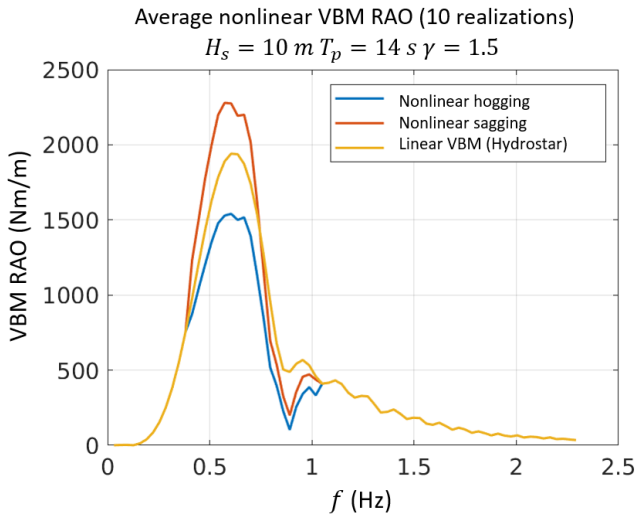

Figure 5.25 – Example of linear VBM RAO from BV Hydrostar and nonlinear VBM RAO estimated with the experimental measurement for SS10

sagging EDW signals calculated based on the linear and nonlinear RAO are compared. Figure 5.24 is an example of the comparison, showing the two EDW elevations and their corresponding sagging responses. At the trough at $t = 45$ s, the two values are almost the same, and there is a slight difference in the other neighboring peaks. This means that the difference between linear and nonlinear VBM RAO only makes a difference in determining the magnitude of $\text{VBM}_{\text{IW}}^{\text{HOS}}(P_{tar})$, and the corresponding EDWs based on the linear or the nonlinear RAO inducing the two different $\text{VBM}_{\text{IW}}^{\text{HOS}}(P_{tar})$ are almost identical (see Figure 5.25 as an example of linear and nonlinear VBM RAO). For this specific case, the significant difference in the amplitude of the nonlinear VBM RAO as compared to the linear one does not induce a significant change in the EDW. Accordingly, the two VBM time signals are also almost identical as shown in Figure 5.24.

More specifically, the comparison between the two EDWs can be performed through the reliability index β_{FORM} associated with the exceedance probability of the process of interest in Eq (2.33). Thus, the POE estimation can be done as well by applying the FORM method in Eqs. (2.34) and (2.35) with β_{FORM} and its component $\mathbf{u}^*$. The estimated POEs of the linear and nonlinear VBM RAO-based EDWs are summarized in Figures 5.26-5.27 for each sea state.

In the graph, the x value of each EDW case corresponds to the 85-hour simulation-based POE value of the target VBM, $\mathbf{P}_{tar}(\text{VBM}_{\text{IW}_{85hr}}^{\text{HOS}}(t))$. The diagonal dotted line in each graph corresponds to the $\mathbf{P}_{tar}(\text{VBM}_{\text{IW}_{85hr}}^{\text{HOS}}(t))$, providing an intuitive comparison with the POE values estimated by the FORM for each sea state.

Compared with the EDW time signal, a relatively noticeable difference is observed

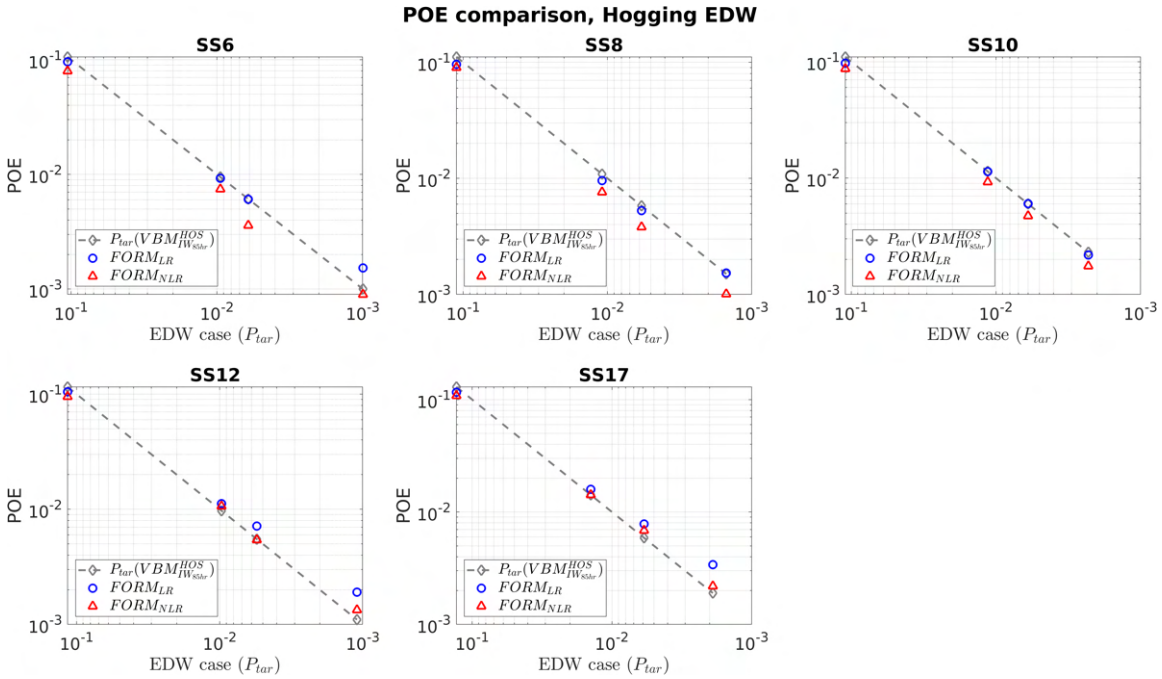

Figure 5.26 – Linear and nonlinear VBM RAO-based FORM POE estimation for hogging EDW cases

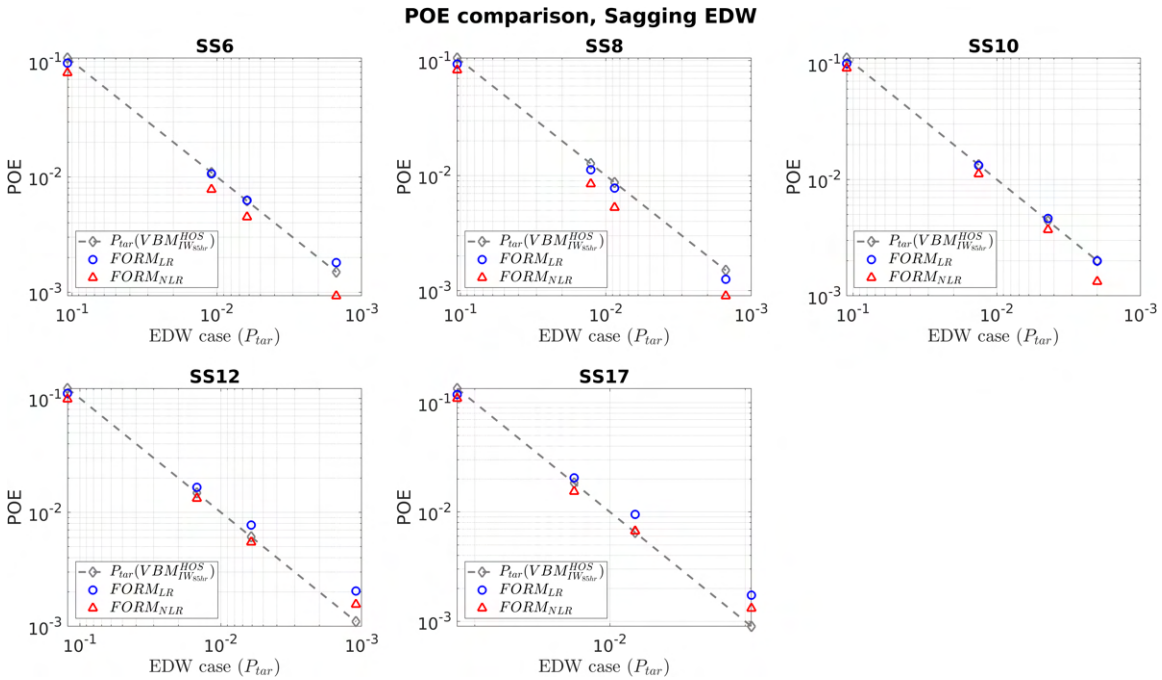

Figure 5.27 – Linear and nonlinear VBM RAO-based FORM POE estimation for sagging EDW cases

in the estimated POE value of each EDW case. Although the target peak is almost similar, there is a difference in the surrounding peaks, and it seems that the difference in the wave components constituting the two EDW wave profiles based on the linear

and nonlinear RAO sensitively affects the magnitude of β_{FORM}.

This eventually leads to a visible difference in the estimated POE results. As compared with $\mathbf{P}_{tar}(\text{VBM}^{\text{HOS}}_{\text{IW}_{85hr}}(t))$, in relatively mild sea conditions (SS6, SS8, and SS10), the nonlinear RAO-based POE results for both hogging and sagging tend to be underestimated, and the linear RAO-based POE estimates show fairly good agreement with $\mathbf{P}_{tar}(\text{VBM}^{\text{HOS}}_{\text{IW}_{85hr}}(t))$. The POE estimate of the linear RAO-based EDW is found to be overestimated as the sea state becomes severe. In all cases, the linear VBM RAO-based EDW gives a more conservative value (higher POE) than the nonlinear VBM RAO-based EDW.

5.6.2 Estimation of wave nonlinear effect on VBM

Throughout the whole process, the wave approaches considered, namely the Monte Carlo reference and the EDW method, will have both the calculated linear VBM denoted as VBM^{L} (based on the linear VBM RAO and the HOS-NWT) and the measured nonlinear VBM denoted as VBM^{NL} in experiments. Then, the VBM's nonlinear factor defined as $\text{VBM}^{NL}/\text{VBM}^{L}$-1 can be estimated in each wave approach. Nonlinear factor results estimated from numerical and experimental Monte Carlo references can be expressed according to the POE level, and based on this, the feasibility of the EDW approach can be evaluated from a statistical point of view.

Assuming that the VBM's nonlinear factor mainly depends on the amplitude of the linear VBM, the nonlinear factor of a specific linear target VBM having low exceedance probability can be obtained with a reduced number of simulations in more severe sea states than in mild sea states. This is reasonable if the peak period T_p of sea states considered is the same, i.e. different T_p is expected to influence this process and should consequently be reflected in the nonlinear factor results.

To check this assumption, the nonlinear factor corresponding to the difference between the nonlinear VBM (blue curve) and the linear VBM (green curve) on the same POE level for each sea state shown in Figures 5.21 to 5.23 is presented with respect to the linear value in Figure 5.28.

Figure 5.28 shows encouraging results that the nonlinear factors of a given linear VBM level for each sea state exhibit similar behaviors to each other, implying that the nonlinear factor is largely dependent on the magnitude of the linear VBM. However, due to the various environmental conditions (H_s and T_p), some discrepancies are observed between curves. The additional nonlinear effects of each different sea condition including the wave breaking seem to influence the response of the system. Nevertheless, as shown in the results, the overall trend seems comparable.

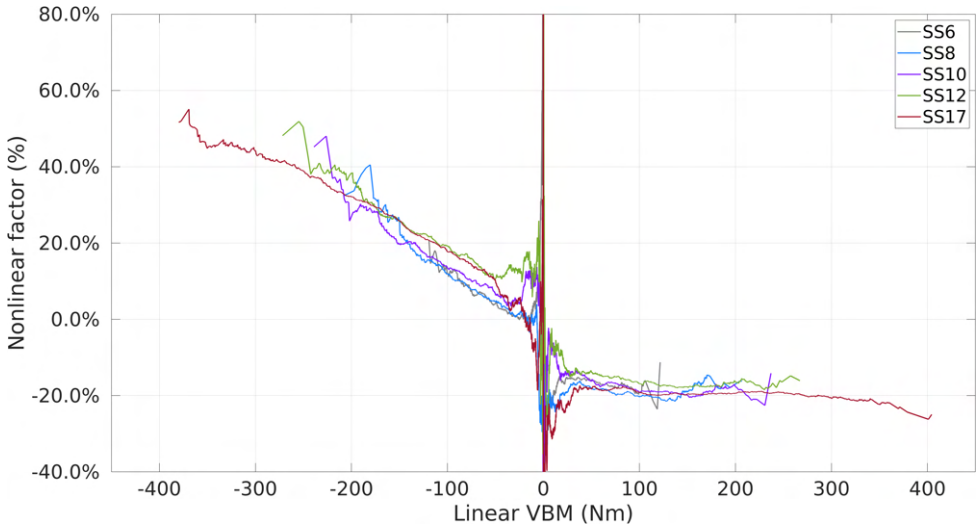

Figure 5.28 – Nonlinear effects of various irregular wave conditions on VBM (model scale)

Table 5.7 – Description of regular wave cases of $\lambda/L_{pp} = 1$ (model scale)

Case	H (m)	T (s)	$H/\lambda(\%)$	Linear target VBM, $\mathbf{VBM^L_{RW}}$
RW1	0.0938	1.677	2.1	90.4
RW2	0.1677	1.669	3.8	162.0
RW3	0.2308	1.658	5.2	223.6
RW4	0.3077	1.641	7.0	298.5
RW5	0.3846	1.619	8.7	372.9
RW6	0.4615	1.592	10.5	447.2

Complementary to the quantification of nonlinear effects in irregular sea states, it is also possible to evaluate those effects in regular waves. The nonlinear effects measured in the regular wave experiment with the same model [6] are presented together with the experimental Monte Carlo reference results in Figure 5.30. The corresponding regular wave test cases are shown in Table 5.7. Note that based on the POE curve and the corresponding Jeffrey 95 % confidence interval results presented in Figures 5.21 to 5.23, the last ten points of the ensemble VBM POE curve of each sea state were excluded from the plot as they are expected to have high stochastic variability. In turn, this could give an incorrect interpretation of the results displayed in Figure 5.28. For reference, the error bar based on the Jeffrey 95 % confidence interval of the SS17 case is presented to show the variability at the end of both hogging and sagging nonlinear factor curves. In addition, the nonlinear factor of the VBM ranging from -40 Nm to 40 Nm induced by too small waves in all sea states was also excluded from the plot as it is not the region of interest and is not physically meaningful (showing the maximum 80 % in nonlinear factor).

As shown in Table 5.7, the regular waves with the same $\lambda = L_{pp}$ but various wave steepness from 2 % to 10.5 % are considered. For the nonlinear effect estimation, the target linear VBM, $\text{VBM}^{L}_{\text{RW}}$, is simply calculated for each case by multiplying the wave amplitude A_{RW} corresponding to half the regular wave height $H/2$ by the linear VBM RAO of a corresponding wave frequency as expressed in Eq. (5.6). The wave frequency is determined by the stream function with given λ and H.

$$\text{VBM}^{L}_{\text{RW}}(f) = |RAO|(f) \times A_{RW}(f) \tag{5.6}$$

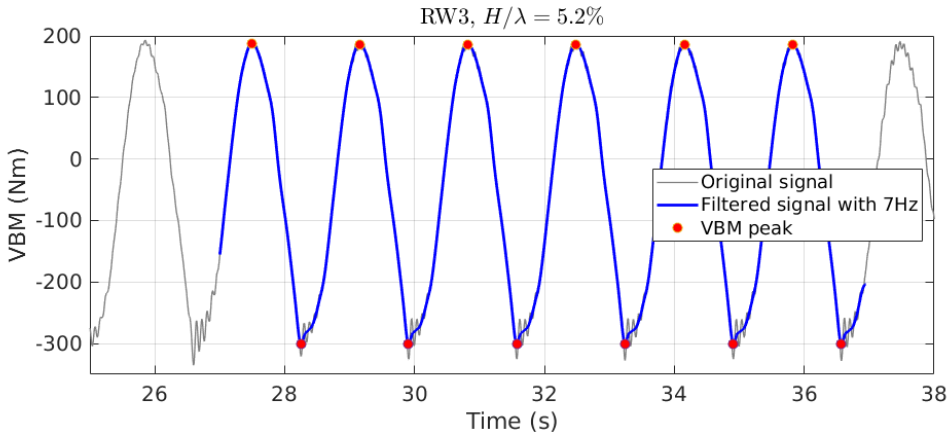

Figure 5.29 – VBM time signal in regular wave (model scale)

In the case of the experimental VBM response, $\text{VBM}^{\text{EXP}}_{\text{RW}}$, induced by the given regular waves, the average of the peak values of six or more responses is taken as shown in Figure 5.29. The same filtering frequency of 7 Hz is applied for the regular case. In Figure 5.30, the nonlinear factor in hogging shows slightly conservative results in the range where the size of the target VBM is small, but the regular wave results are in very good agreement with the experimental Monte Carlo results across the entire VBM range. Although the regular wave approach is simple, as it induces conservative responses with continuous sinusoidal waves providing unrealistic system memory effects, the approach is regarded as a method that contains a less realistic physical sense. However, the point is that the regular design wave approach works well in this specific case.

The nonlinear factor of the target VBM to the EDW case corresponding to the difference between the linear target VBM $\text{VBM}^{\text{HOS}}_{\text{IW}}(P_{tar})$ on the linear numerical Monte Carlo reference curve and the nonlinear VBM measured $\text{VBM}^{\text{EXP}}_{\text{EDW}}(x_0, t_0)$ on the experimental Monte Carlo reference curve are also presented in Figure 5.30. Overall, the EDW gives a less conservative nonlinear factor compared to the regular wave results.

The nonlinear effect induced by the EDW agrees quite well with the experimen-

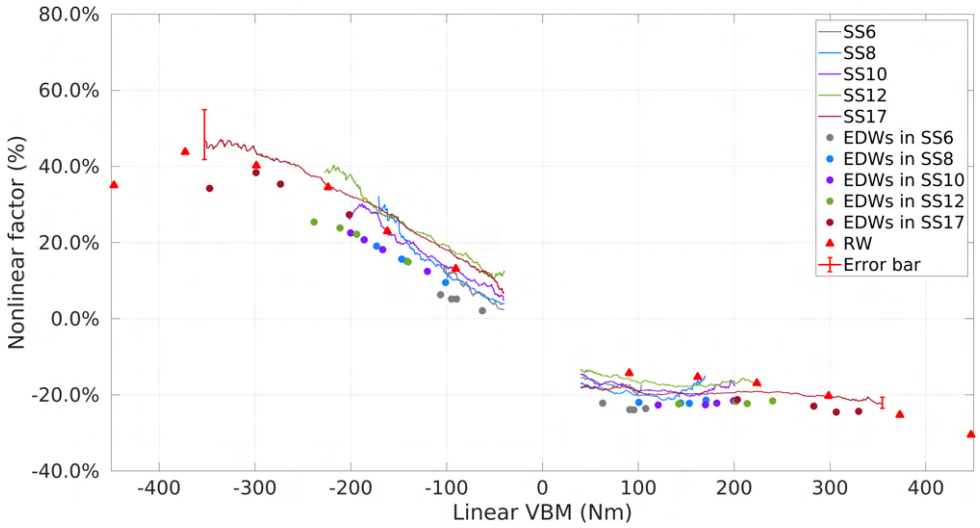

Figure 5.30 – Nonlinear effects of various RW and EDW cases on VBM (model scale)

tal Monte Carlo results in hogging. In sagging, although the overall trend of the EDW results is similar to the Monte Carlo results, the difference is relatively large. The maximum difference is found to be around 18 % for the EDW case with $\text{VBM}_{\text{IW}}^{\text{HOS}}(P_{tar}) = -212.6$ Nm in SS12 (green color) (see Figure 5.30).

Considering that the sagging response itself is larger than hogging under the same wave condition and that high-frequency responses are observed, it can be expected that a relatively stronger wave-structure interaction occurs in sagging. The overestimated wave energy dissipation mechanism in numerical simulations as compared to the experiment may affect the numerical Monte Carlo reference result, which consequently may cause less accurate POE estimation for the selected target VBMs. In addition, given that the EDW induces the VBM response with one wave packet, the system's memory effect can be a possible reason for such a relatively large discrepancy with the experimental Monte Carlo results as well as the regular wave results in the sagging compared to the hogging.

According to Jensen (2009) [46], the memory of the wave bending moments is less than 50 s, which corresponds to about 6.2 s in the model scale of this study. This means that the VBM responses up to about 6.2 s before the target time can affect the VBM response. Compared with the Monte Carlo reference results which contain various wave scenarios, the EDW profile was found to be close to the mean wave profile of the Monte Carlo results and the previous response was relatively less conservative (see Figures 5.11 to 5.18). As a result, it can be considered that the underestimated VBM's memory effect by the EDW may affect a such difference.

In addition, in the case of the experimental Monte Carlo results (apart from SS17), each case is the result of a limited number of realizations (8 to 12 runs), which is not

sufficiently long for obtaining statistical convergence up to a 10^{-3} probability level according to Korean Register (2017) [55]. As shown in Figures 5.11 to 5.18, the Jeffrey 95 % confidence interval for most sea states except SS17 explains that the nonlinear VBM POE curve has a less converged (less reliable) shape in the low POE level range. Therefore, we focused on the qualitative comparison rather than the quantitative comparison with the irregular wave result, and it is confirmed that the EDW result shows a similar trend to the irregular wave result. The EDW results appear to be less affected (less dependent) on sea conditions. The nonlinear factors are not noticeably differentiated sea state by sea state and show a smooth change trend with respect to the linear VBM size. That is, the amplitude of the linear target VBM appears to be the main variable of the nonlinear factor.

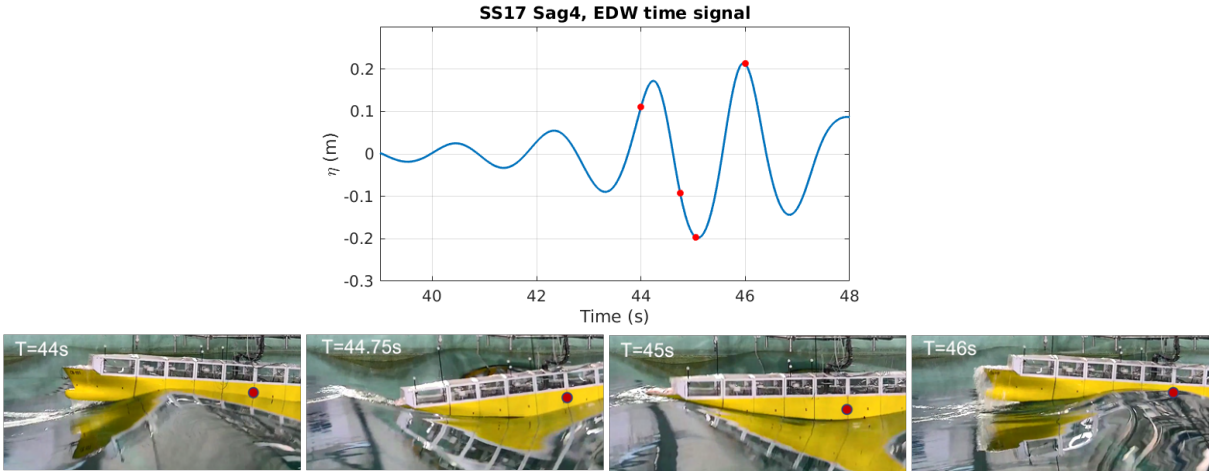

Figure 5.31 – Green water observed in the most severe EDW case (Sag4) in SS17. The corresponding EDW time signal(top). 4 snapshots (from left to right) corresponds to 4 points from left to right in the graph (model scale)

In SS17, a decreased sagging nonlinear factor compared to the previous case is found in the most severe EDW case with the wave steepness of 7.2 % and λ/L_{pp} close to 1. Figure 5.31 shows the corresponding sagging EDW time signal. Snapshots of certain time instants indicated by 4 red points including the target time instant are plotted below the EDW time signal in Figure 5.31. The bow part of the model is fully immersed just before (44.75 s) the target trough for the sagging reached the target location (18.2 m from the wavemaker) corresponding to the red point on the model at 45 s. Right after that, green water on the deck at 45 s is observed. The crest at the bow part seems to have energy loss due to the interaction with the model. Therefore, the vertical upward force by the wave at the bow part acts with reduced magnitude, making the sagging response at the COG less developed.

It may be expected that the gravity of the green water in the bow part is applied in

a vertically downward direction at 45 s. Due to this additional nonlinear wave-structure interaction, maximization of the sagging response at the ATI position appears to be suppressed. As a result, the most severe EDW case in SS17 has decreased the sagging response more than expected, leading to a decreasing trend in the nonlinear factor shown in Figure 5.30.

As shown in Figure 5.30, in hogging results, the measured hogging $\mathrm{HOG}_{\mathrm{EDW}}^{\mathrm{EXP}}(x_0, t_0)$ induced by each EDW case is always smaller than the target hogging $\mathrm{HOG}_{\mathrm{IW}}^{\mathrm{HOS}}(P_{tar})$ with an average difference of -22 %. On the other hand, $\mathrm{SAG}_{\mathrm{EDW}}^{\mathrm{EXP}}(x_0, t_0)$ is always larger than $\mathrm{SAG}_{\mathrm{IW}}^{\mathrm{HOS}}(P_{tar})$, showing a fairly clear increasing trend in the nonlinear effect from 3 % to 38.5 % as the magnitude of target sagging increases. The trend is very comparable with the nonlinear RAO estimation result (see Figure A.4). Given that similar results were observed in previous studies with rigid models [22, 19], that showed larger sagging and smaller hogging than linear estimates, it can be seen as a general result that appears in the rigid model. Considering that the model is set as rigid, the parameters that affect the nonlinear effects in the VBM response are most likely wave-related properties.

As mentioned earlier, nonlinear effects are largely dependent on the value of the target VBM. Thus, it can be said that the characteristics of individual EDWs are the main variables that can determine the magnitude of the nonlinear effects. Among various wave-related parameters, the focus has been on wave steepness (H/λ) and the variance of the wave spectrum (m_0). The EDW spectrum corresponds to a specific spectrum for a defined target response. Thus, the m_0 of each EDW can be used as an indicator for the individual EDW cases.

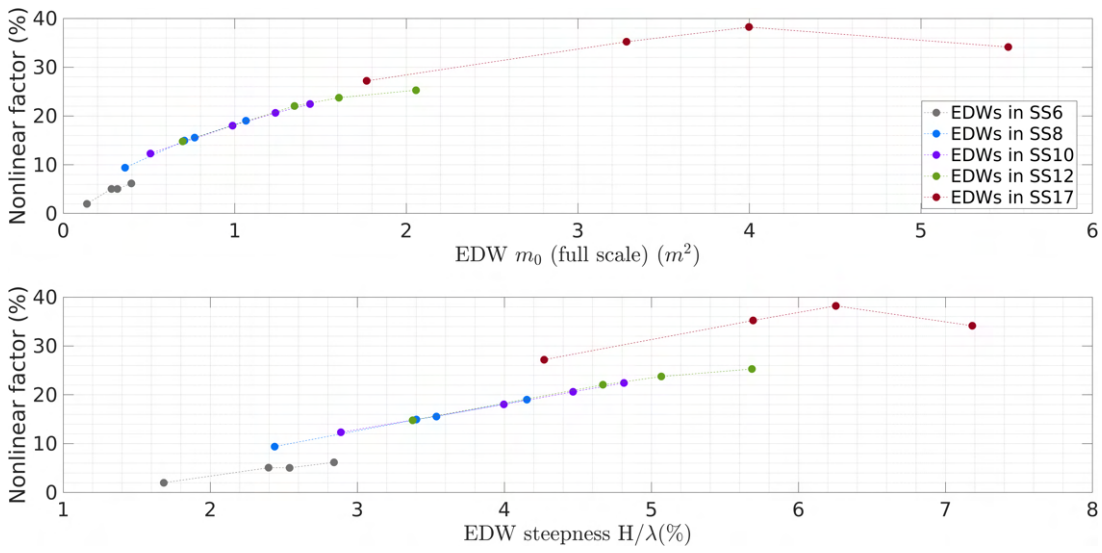

Figure 5.32 – Relationship between the sagging nonlinear factor and the main characteristics of the corresponding EDW case

Figure 5.32 shows the nonlinear effect of all EDW cases for the variance of EDW spectrum and steepness. H and T are the zero down-crossing wave height and period as defined in Figure 5.8, and λ is a value obtained through linear dispersion relation with T. Overall, as m_0 and steepness increase, the sagging nonlinear factor also increases. This implies that the individual wave has a main influence on the sagging nonlinear factor. In cases SS6 and SS17, which have different T_p, results are distinguished from the other three cases with the same T_p. This demonstrates that the VBM response also depends on the sea condition.

This indicates that it is important to perform the VBM study for each peak period of the sea state. It may also explain the differences observed with the regular design wave, in which λ is chosen as $L_{pp} = 4.409$ m, which is the condition maximizing the response. The wave period of all EDWs in each sea state is found to be within a similar range. Therefore, the λ/L_{pp} ratios correspond to around 0.86 for EDWs in SS6, 0.95 for EDWs in SS8, SS10, SS12, and 1.15 for EDWs in SS17. Not only this but also the different wave steepness can affect having different VBM responses. As an example, in the case of Sag4 in SS17 near VBM $= -350$ Nm, which showed the largest difference from the adjacent RW in the similar VBM range (see Figure. 5.30), its wave steepness is found to be smaller ($H/\lambda = 7.2$ %) as compared to the adjacent RW with $H/\lambda = 8.7$ %. In other words, it can be seen that the wave variables of EDW are found to be less conservative than in RW and may consequently affect inducing a lower VBM response.

As expected, both m_0 and H_s/λ_p increase as the sea condition becomes severe (see Figure 5.33). The sea condition is also responsible for the nonlinear sagging response and has to be considered as one of the factors for the estimation of the relationship between the linear and nonlinear sagging response.

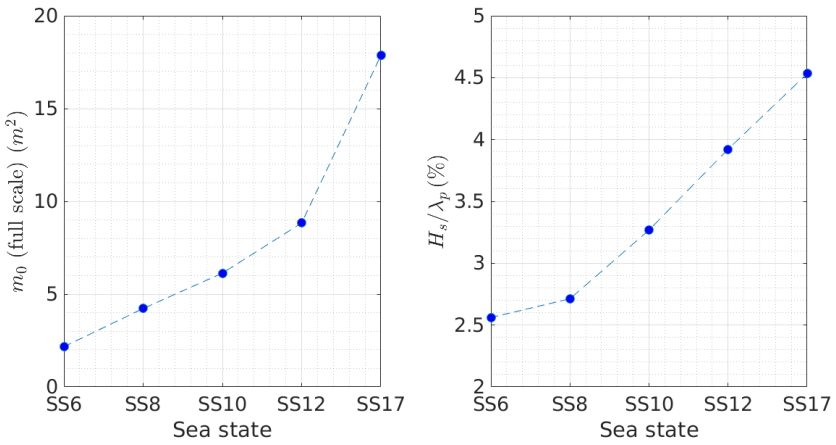

Figure 5.33 – Variance (left) and representative wave steepness (right) of a given sea state

Through the relationship between the parameters mentioned and the linear tar-

get sagging, SAG^{tar}_{EDW}, an empirical formula for the estimation of nonlinear sagging, SAG^{est}_{EDW} is derived according to Eq. (5.7). This enables us to practically estimate the nonlinear sagging response through the linear target sagging. However, since this formula only considers the dynamics of a rigid ship in a limited number of sea states with specific peak periods, more studies are needed to validate its broad application.

$$SAG^{est}_{EDW} = SAG^{tar}_{EDW}(1 + \frac{(H_s/\lambda_p)^2}{0.01}) \times e^{(\frac{m_{0EDW}}{m_{0IW}})^2} \times (1 + (\frac{H}{\lambda})_{EDW}) \tag{5.7}$$

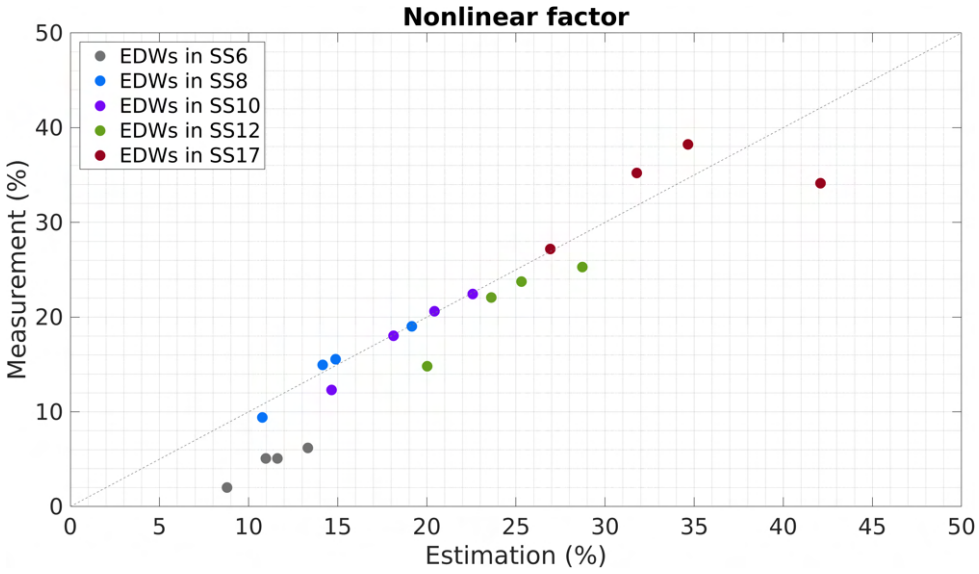

Figure 5.34 – Empirical formula for the estimation of nonlinear sagging from linear target sagging response

Figure 5.34 shows the estimated coefficients except SAG^{tar}_{EDW} in the right term of Eq. (5.7) in percentage format. The results for each EDW case are presented in Figure 5.34 as a scatter plot with respect to the corresponding sagging nonlinear factors. The estimated coefficients follow the trends of the sagging nonlinear factors fairly well. Of all EDW cases, the estimated SAG^{est}_{EDW} of the most severe EDW case in the SS17 sea state is 8 % higher than that of SAG^{exp}_{EDW}. In addition, the estimated SAG^{est}_{EDW} of the most mild EDW case in SS6 is also a bit higher than that of SAG^{exp}_{EDW} with 7 %, while the other cases have a fairly good agreement with an average difference of around 4 % between SAG^{est}_{EDW} and SAG^{exp}_{EDW}. Overall, the empirical formula tends to give conservative estimates compared to the measured nonlinear sagging responses but is quite similar.

5.7 Summary

The nonlinear VBM response of a rigid model was studied by three different methods namely, i) the stochastic (Monte Carlo) approach with a number of realizations of a given sea state and deterministic (EDW), ii) the regular design wave and iii) the FORM-based EDW. More emphasis was placed on confirming the practicality of the EDW approach, and the Monte Carlo results were used as reference data. Five sea states were considered. At least eight measurements were performed for each sea state case corresponding to full scale 2h 30min measurements with different random phase sets. From a practical point of view, the EDW was calculated by considering the linear VBM RAO instead of considering the exact nonlinear response of the structure. The changing trend between the linear target VBM and the measured nonlinear VBM was estimated in relation to the given wave characteristics.

To verify the FORM process applying the modified HLGA algorithm (MHLGA) and the HOS-NWT nonlinear wave solver, and to determine whether the process provides the most probable wave scenario and comparable VBM response, an overall comparative study with the Monte Carlo reference results in a given sea state was carried out. The results showed that, in each sea state, the EDW and the corresponding VBM measured were sufficiently similar to the average shape of all the irregular waves and the corresponding VBM responses extracted in a given sea state. This confirmed that the FORM-based EDW applying the HOS-NWT successfully generates the most probable nonlinear wave profile.

In the VBM POE curve results, it was observed that the degree of variability of the 2h 30min irregular wave-based VBM response to the random wave phases was significantly greater in sagging than in hogging, showing that the nonlinear effect due to the wave-structure interaction was much more pronounced in the sagging response. Nonlinear VBM response induced by the FORM-based EDW followed the overall trend of experimental Monte Carlo results and regular wave results, but in most cases, the VBM induced by the EDW showed relatively lower values than others.

The wave energy dissipation mechanism in a numerical wave tank which can not exactly be the same as the experiment and the system's memory effect generated by a short wave packet cannot be excluded as possible reasons for the less conservative results. From an experimental point of view, a smaller discrepancy with the irregular results was observed in SS17, which is the result of the 34 realizations. This emphasizes the need for sufficiently long time series data for the quantitative comparison with the other wave approaches.

The nonlinear factor, defined by the ratio of the measured VBM and the linear VBM showed that the hogging results of all wave types did not change significantly depend-

ing on the size of the linear VBM and had values in the range of about 22 %. On the other hand, the nonlinear factor in the sagging result showed a clear increasing trend as the magnitude of linear VBM increased. In particular, it was confirmed that the sagging result was highly dependent on the magnitude of the linear VBM (wave amplitude). Note that this only holds for when the T_p of the sea states considered are the same or at least close to each other. The nonlinear factors were found to be distinguished with respect to the peak period of the sea state, and thus it was confirmed that the sea state is also one of the influencing parameters to be considered in estimating the relationship between the nonlinear response and the linear response.

Given that the corresponding nonlinear VBM RAO estimation and VBM difference are the results of a 'rigid model', it can be said that such nonlinear VBM responses are closely related to the sea state and the characteristics of individual EDW waves. Based on that, an empirical formula for estimating the nonlinear sagging response was defined by considering the wave steepness H/λ and variance of the wave spectrum m_0, which are the representative variables among wave-related variables. In most cases, the nonlinear sagging response estimated through the empirical formula had a size similar to the measured nonlinear sagging response.

For the most severe EDW case in SS17, where the linear target VBM is -351 Nm, an additional nonlinear wave-structure interaction such as green water on the bow part which reduced the sagging was observed. In this case, the empirical formula gave a relatively overestimated value of 8 % higher than the measured as it does not consider such an effect. Nevertheless, the estimation results were similar enough to measurements in most cases. The current empirical formula can be said to be suitable for estimating the sagging response to the short-term sea state. However, since this is a result derived from one specific zero-speed rigid model, additional research considering parameters such as the model's flexibility, size, and speed are needed.

Chapter 6

Ship responses in -120 degree oblique regular waves

6.1 Introduction

The VBM response in head seas has been studied in detail with various wave conditions covering from mild to severe sea conditions but changing the wave heading angle lead to additional bending moments. This specific chapter deals with this problem for a zero-speed rigid model in regular waves to understand accurately the physical mechanisms involved in the resulting responses and to provide reference data for future benchmark studies.

Over the last decade, the effect of hull flexibility on wave-induced loads has received much attention and has been one of key concerns in ship design. Therefore, many experimental studies have been conducted highlighting the significant contribution of hydroelasticity on structural response [41, 67, 61, 13].

Numerical investigations of the wave-induced motions and loads of flexible bodies have been conducted for several decades and have provided good estimates. However, converged numerical results based on several numerical theories for various environmental and operating conditions have been an issue to address. A benchmark study of the vessel's VBM response found that the VBM responses estimated through various nonlinear numerical tools showed large discrepancies in severe head sea conditions [53]. In a previous experimental study with a flexible model by Zhu et al. (2011) [102], numerical models based on 2D strip theory and 3D potential theory predicted quite similar results in the horizontal bending moment (HBM) in oblique seas. Whereas the numerical results showed significant differences in the vertical shear force (VSF) and vertical bending moment (VBM) compared to the experimental results.

To overcome the limitations of the numerical solvers mentioned above, wave-induced bending moments have been studied using Computational Fluid Dynamics (CFD), especially for extreme wave conditions. The hydroelastic effects of a flexible ship have been studied with an approach based on a two-way coupling between the CFD and a structural analysis solver [28]. In this case, experimental results with a sufficiently

rigid model can be an appropriate reference that may be used to validate the coupling approach. Experimental data available for reference, however, are relatively rare.

Taking the above into account, it is intended to identify the response characteristics of a zero-speed rigid containership model to the wave nonlinearity under a -120 degree oblique regular wave condition. Therefore, the experiment is conducted considering 7 wave steepnesses with H/λ series ranging from 1 % to 10.5 %, and each series consists of various λ/L_{pp}.

From the experimental results, it is found that the importance of the wave's nonlinear effects on the motions and loads increases as the wave becomes steeper. In addition, the contribution of the additional bending moment by the mooring system is qualitatively evaluated through a comparative study with linear numerical calculation results from BV Hydrostar [93] with and without the mooring system.

6.2 Experimental setup

6.2.1 Test configuration

For the same containership model considered in the previous chapter, model tests in -120 degree oblique wave conditions were conducted in the ocean engineering basin (see Section 3.1). As presented in Figure 6.1, four soft mooring lines with stiffness of 58 N/m installed with α_i of 45, -45, -135, and 135 degree (from line No.1 to 4) based on the x_b of the body-fixed reference frame were applied to maintain the heading of the model while minimizing its influence on the global performance of the model. The spring applied in each mooring line is longer and heavier than that used for the previous experiment in heading wave conditions in Chapter 5 and in Bouscasse et al. (2022) [6]. Thus, its contribution to an increase in overall mass may be expected. BV Hydrostar [93] estimates the surge natural period of the model as 10.4 s on a model scale with consideration of the additional mooring stiffness matrix in Eq. (6.2), and it is observed to be 10.1 s in the free decay test.

The stiffness matrix of the moored model is attributed to the restoring force term of the model $\mathbf{K}$ (see Appendix C) and mooring system stiffness $\mathbf{K_m}$.

$$\mathbf{K_{total}} = \mathbf{K} + \mathbf{K_m} \tag{6.1}$$

The following 6-by-6 mooring stiffness matrix $\mathbf{K_m}$ of n mooring lines was applied based on Al-Solihat and Nahon (2016) [86]. The applied stiffness matrix only holds for the linear spring mooring system.

$$\mathbf{K_m} = \begin{pmatrix} K_{11_m} & 0 & 0 & 0 & K_{15_m} & 0 \\ 0 & K_{22_m} & 0 & K_{24_m} & 0 & 0 \\ 0 & 0 & K_{33_m} & 0 & 0 & 0 \\ 0 & K_{42_m} & 0 & K_{44_m} & 0 & 0 \\ K_{51_m} & 0 & 0 & 0 & K_{55_m} & 0 \\ 0 & 0 & 0 & 0 & 0 & K_{66_m} \end{pmatrix} \tag{6.2}$$

Considering the n horizontal mooring lines, each term of the matrix can be expressed as:

$$\begin{aligned} K_{11_m} &= 0.5n[(T/L) + k_{moor}], \\ K_{33_m} &= n(T/L), \\ K_{24_m} &= 0.5n[(T/L)D + k_{moor}D], \\ K_{44_m} &= n[0.5y_RT + 0.5(T/L)(y_R^2 + D^2) + 0.5k_{moor}D^2], \\ K_{55_m} &= n[0.5x_RT + 0.5(T/L)(x_R^2 + D^2) + 0.5k_{moor}D^2], \\ K_{66_m} &= n(TR/L)(R + L), \\ K_{22_m} &= K_{11_m},\ K_{42_m} = K_{24_m} = -K_{15_m} = -K_{51_m} \end{aligned} \tag{6.3}$$

where k_{moor} and T denote spring stiffness and pretension of each mooring line, and L and D are the stretched length of each line and vertical distance from the COG of the model to the fairlead respectively. $R = (x_R, y_R)$ corresponds to the radius of a circle by the fairlead point of each line based on the z-axis of the COG. As all mooring lines were positioned at the centerline of the model (see Figure 6.1), $y_R = 0$ was applied for all mooring lines.

6.2.2 Horizontal restoring moment by a mooring system

The experiment was carried out at zero speed with no other appendage controlling the model, thus, the only possibility to perform the test is by using the mooring lines. As mentioned in Chapter 5, the mooring lines are not expected to affect the VBM in head sea conditions. However, in oblique seas, the mooring system may contribute to the HBM and the motions. This means that we cannot directly remove the mooring contribution. In this chapter, the contribution of the mooring to the measured HBM and its effect on the motions are thoroughly discussed.

Based on Eq. (2.2), the horizontal bending moment (M_z^A) at a position $\mathbf{A}$ can be

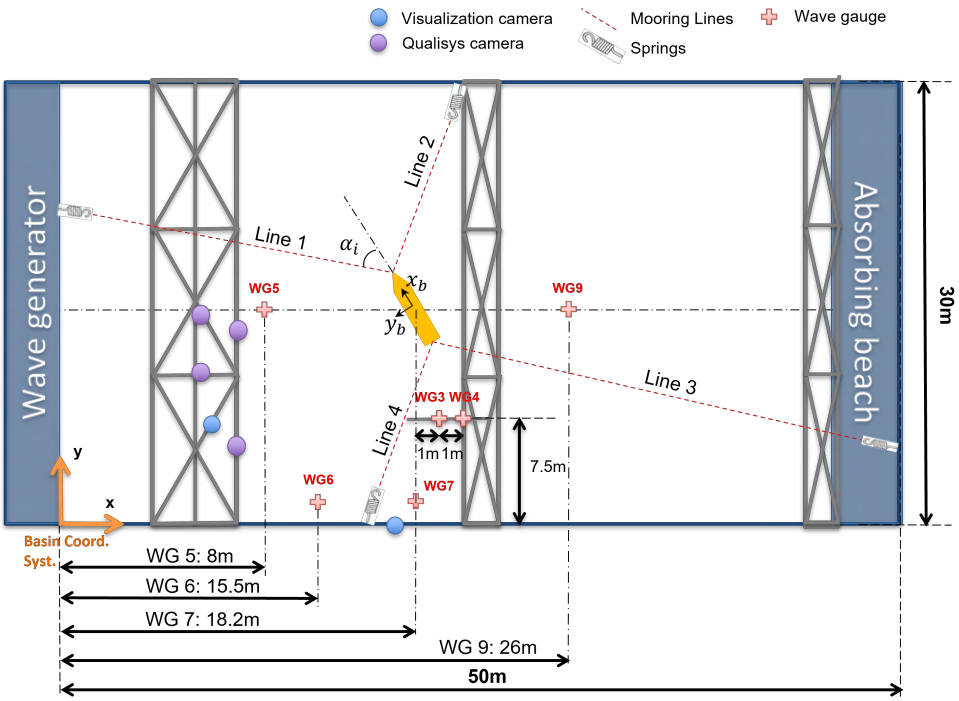

Figure 6.1 – Experimental configuration for a -120 degree oblique wave condition

calculated by solving the simplified standard Euler law in the x-y plane of the body-fixed reference frame as expressed below:

$$M_z^A = \left(-M_{extz}^A + I_z\,\dot{r} + m\,(x_G - x_A)\,(\dot{v} + ru)\right)^{x<x_A} \tag{6.4}$$

with

$$M_{extz}^A = \sum_{i=1}^{j-1}(M_{hydro_z/h_i} + \mathbf{r}_A^{G_i} \times F_{hydro_y/h_i})^{x<x_A} + M_{z\ moor}^A \tag{6.5}$$

where j-1 corresponds to the number of segments in $x < x_A$ range. F_{hydro_y/h_i} and M_{hydro_z/h_i} denote fluid force and moment acting on the i^{th} segment, and $M_{z\ moor}^A$ is restoring moment a position $\mathbf{A}$ by the mooring line tension.

Note that, as the 3-DOF load sensors in each segment only measure F_z, M_x, and M_y, the M_{hydro_z/h_i} and F_{hydro_y/h_i} cannot be obtained. Therefore, the reconstruction of M_z^A at any intersegment is limited, and M_z^A can be obtained only at the intersegment No.4 through the direct measurement of the ATI sensor (see Figure 3.4). Considering that the model is moored with four spring lines, the M_z^A measured by the ATI corresponds to the wave-induced moment containing the additional restoring moment by the mooring system as one component of M_{extz}^A. Quantification of the mooring system's contribution to the horizontal bending moment at x_A can be estimated with mooring line tension data.

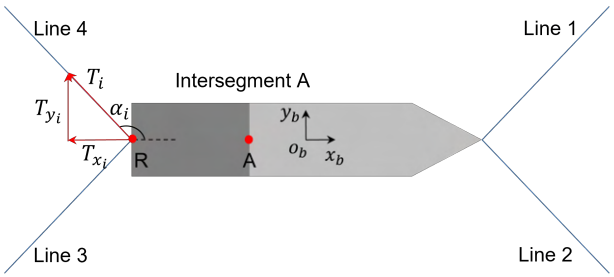

Figure 6.2 – Schematic view of mooring lines in the x-y plane and decomposition of line tension components

The mooring tension-induced bending moment in the z-axis at a position x_A, $M^A_{z\,moor}$, can be obtained by the cross product of the distance vector, $\mathbf{r}$ and the tension vector, $\mathbf{T_i}$ of i^{th} mooring line as follows (see Figure 6.2):

$$\begin{aligned} M_{z_i} &= (-r_{y_i} T_{x_i} + r_{x_i} T_{y_i}) z_b \\ &= (r_{x_i} T_{y_i}) z_b \qquad (\because r_{y_i} = 0) \\ &= (r_{x_i} \|\mathbf{T}_i\| \sin\alpha_i) z_b \end{aligned} \tag{6.6}$$

With this in mind, the bending moment by the mooring line tension at the intersegment No.4 can be estimated with the two lines located at the bow or stern respectively. With the two lines located $x < x_4$, for example, $M^4_{z\,moor}$ can be calculated as:

$$M^4_{z\,moor} = \sum_{i=1}^{2} (r^R_A \|\mathbf{T}_i\| \sin\alpha_i)^{x<x_4} \tag{6.7}$$

This allows identifying the contribution of the mooring system to M^4_z at the intersegment No.4 with the direct measurement from the ATI. It is important to note that the model geometry is y-axis asymmetric, and the ATI position is not the center of the moment of the two mooring line sets at the bow and stern (i.e. COG of the model), thus each mooring set may induce different moments in magnitude. In addition, as the wave heading is in a -120 degree oblique condition, generating yaw motion, the phase of each signal is expected to be different.

6.2.3 Test cases

To check the effect of wave nonlinearity in detail, a test matrix consisting of several cases in H/λ from 1 % to 10.5 % is considered [6]. In each wave steepness case, a number of cases corresponding to λ/L_{pp} varying from minimum 0.25 to maximum 2.0 are considered. This enables a comparison of the RAO curves of the responses of interest with respect to the wave steepness (see Table 6.2.3). That is, with the fixed

λ/L_{pp} ratio and steepness series, the corresponding wave height H and nonlinear wave period T are calculated based on the stream function theory (see Appendix D) and reproduced in the ocean wave tank. To check and correct the wave height with respect to the corresponding target values of a given wave, experimental wave calibration was first performed at the target location ($x = 18.2$ m) before the model installation (see Section 2.2.3).

Table 6.1 – Description of regular wave cases (model scale)

Case in $H/\lambda(\%)$	λ/L_{pp}	$T(s)$	$H(m)$
1.0	$0.313 \sim 2.0$	$1.03 \sim 2.67$	$0.017 \sim 0.115$
2.1	$0.25 \sim 2.0$	$0.84 \sim 2.37$	$0.023 \sim 0.188$
3.8	$0.25 \sim 1.5$	$0.83 \sim 2.04$	$0.042 \sim 0.252$
5.2	$0.25 \sim 1.5$	$0.83 \sim 2.03$	$0.058 \sim 0.346$
7.0	$0.25 \sim 1.125$	$0.82 \sim 1.74$	$0.077 \sim 0.346$
8.7	$0.25 \sim 1.125$	$0.81 \sim 1.72$	$0.096 \sim 0.433$
10.5	$0.25 \sim 0.875$	$0.80 \sim 1.49$	$0.115 \sim 0.404$

6.3 Experiments

6.3.1 Hydrostatic VSF and VBM distributions in calm water

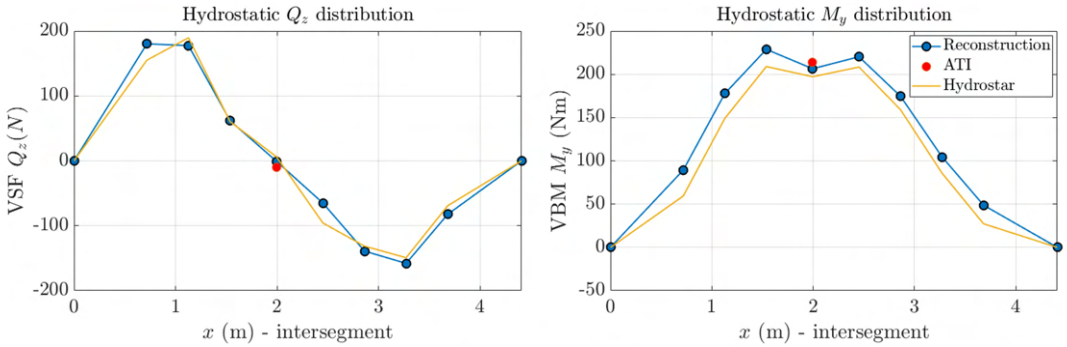

Figure 6.3 – Comparison of reconstructed hydrostatic VSF (Q_z) and VBM (M_y) distribution with Hydrostar result and direct measurement (model scale)

Note that the reconstruction of VSF and VBM at every intersegment was first performed by following the method outlined in Section 2.1. This ensured that the experimental setup is properly set. Figure 6.3 shows the hydrostatic distribution of the reconstructed VSF and VBM in calm waters calculated by equations (3.1) to (3.4). BV Hydrostar results and direct measurements were compared. Overall, it can be seen that the VSF distributions show good agreement. However, as shown in Figure 6.3,

small discrepancies are observed against the BV Hydrostar results in the VSF (Q_z) distributions, especially at intersegments No.1 (0.719 m from stern) and 5 (2.453 m from stern). The difference appears to be more visible in the VBM (M_y) distributions.

Considering that the heading wave experiments [6] which applied a lighter spring with the same stiffness ($k = 58$ N/m) as the spring stiffness of the corresponding oblique experiments agreed very well with the BV Hydrostar results, the use of longer and heavier springs on the mooring line to cover the large drift expected in the oblique wave condition appears to have contributed to the change in the overall weight of the model. That is, the increase of the system's displacement involves the change of buoyancy as a result of the draft change, which eventually affects the hydrostatic load distribution of the model. While, as mentioned before, the mooring system is considered in the BV Hydrostar only through a stiffness matrix (refer to Section 6.2.1).

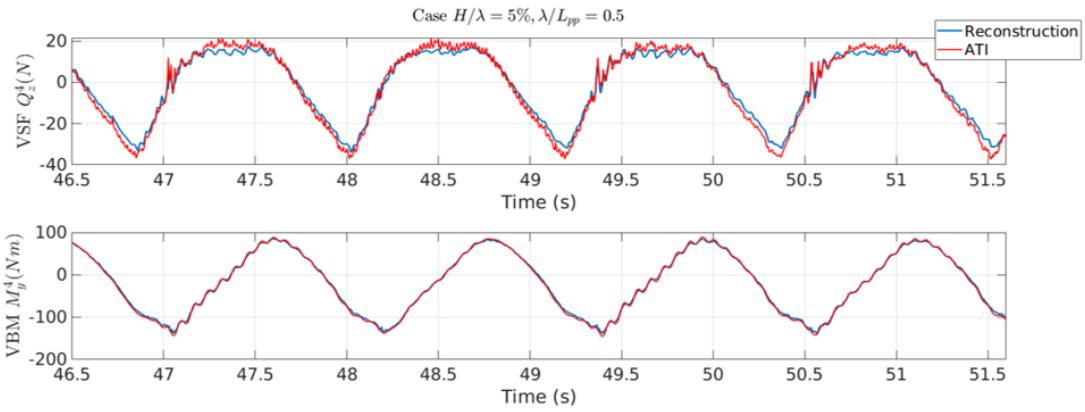

Figure 6.4 – Time signal of hydrodynamic VSF and VBM (model scale)

Reconstructed VSF and VBM at the intersegment No.4 (blue point at $x = 2$ m in Figure 6.3) calculated with the 9 3-DOF load cells are very comparable to measurements (red point). This means that the variables considered in the simplified equations of the reconstruction process represent sufficiently well the motion and load response characteristics of the model. The hydrodynamic time series of the reconstructed and directly measured VSF and VBM presented in Figure 6.4 show that the reconstructed result can even capture local oscillations with very similar periodic responses in terms of shape and magnitude.

6.3.2 Response time series of the cases near the peak period

The nonlinear response characteristics of 7 cases in H/λ corresponding to configuration close to the peak period of the HBM response ($\lambda/L_{pp} = 0.4375$) are first discussed. For clarity, Figures 6.5 and 6.6 present only the results for $H/\lambda = 1$ %,

5.2 %, and 10.5 %. Note that the presented time series responses correspond to 7 Hz filtered (blue line) and unfiltered (red line) measurements. This allowed to estimate the potential influence of the high-frequency vibration due to impact that may occur in the most severe conditions on the wave bending moments. The time range presented corresponds to the selected time window for the data analysis.

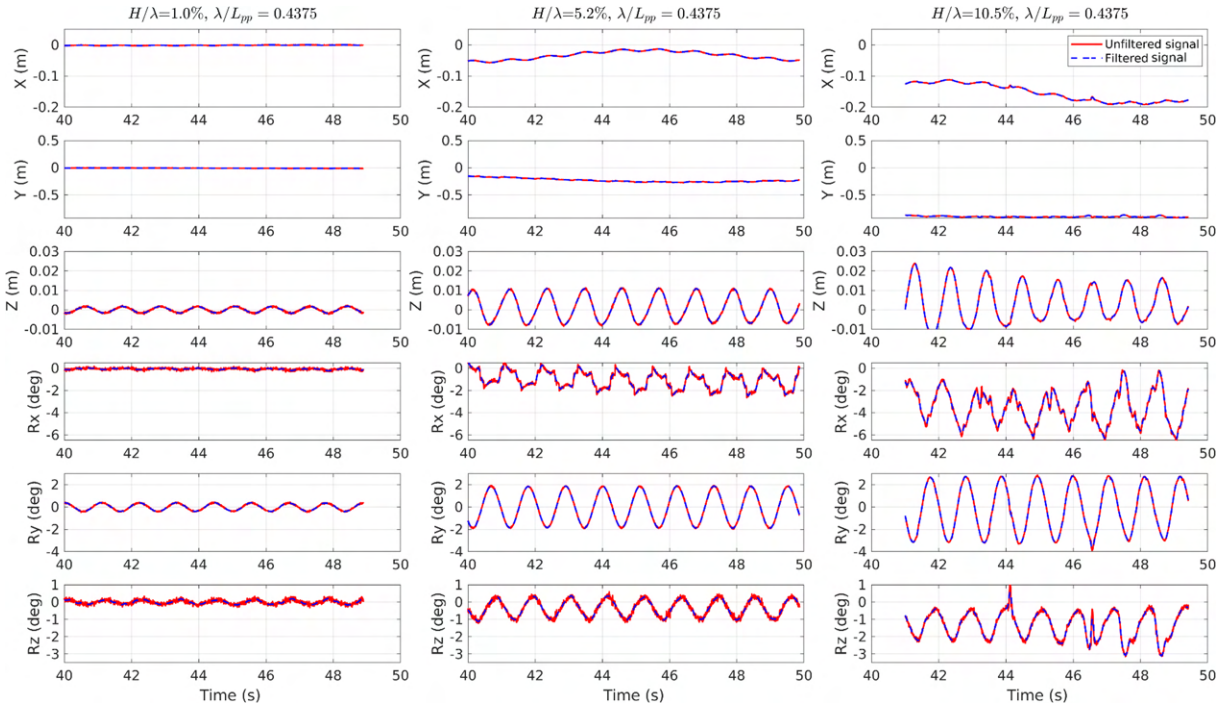

Figure 6.5 – 6-DOF motion time signals of the cases with $H/\lambda = 1$ %, 5.2 %, and 10.5 % having the same λ/L_{pp} of 0.4375 (model scale)

Looking at the surge motion, a low-frequency response corresponding to the natural period measured in the free decay test (10 s) was observed when H/λ is more than 5 %. In the sway, the mean drift motion steadily increases, reaching up to about 0.9 m when $H/\lambda = 10$ %. A typical periodic response is observed in the heave and rotational motions, while the roll motion exhibits a relatively unstable response with local oscillations. The average value of the yaw motion gradually moves away from 0 as the H/λ becomes steeper. This explains the increase in the asymmetry of the HBM response in Figure 6.6.

In the case of VBM (M_y^4) and HBM (M_z^4) measured by the ATI sensor at the intersegment No.4, the most sinusoidal response in which the first harmonic component seems to be dominant is observed in both signals when the $H/\lambda = 1$ %. As the steepness increases, both responses are found to have an asymmetric shape based on $y = 0$, and the high-frequency components are clearly observed in the time signals for $H/\lambda = 10$ %. The picture of each test case is presented in Figure 6.6 for clear understanding. In

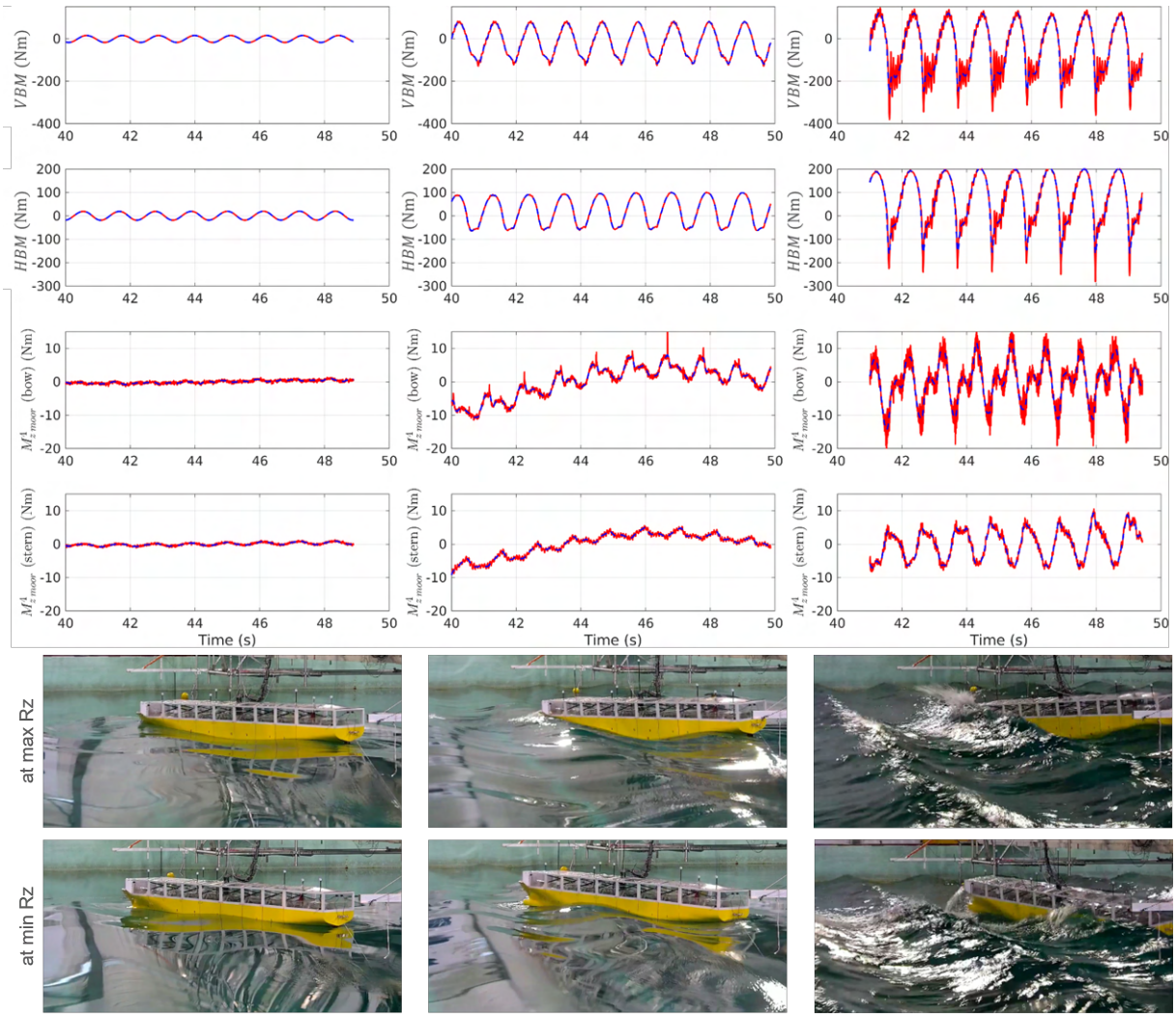

Figure 6.6 – Moment time signals of the cases with $H/\lambda = 1$ %, 5.2 %, and 10.5 % having the same λ/L_{pp} of 0.4375 (model scale)

short, in the $H/\lambda = 10$ % case, the slamming response occurs very strongly at the bow part of the model, and the effect is measured as a high-frequency impact in the VBM and HBM. The VBM reaches a magnitude similar to the head wave case. However, the magnitude of the filtered response applied in the RAO calculation has a significant difference of about 35 % in VBM and 45 % in HBM, respectively, as compared with their unfiltered response. This leads to questioning the validity of the rigid model assumption in the oblique case and should be further investigated.

The change in the yaw motion can be related to the moment $M^4_{z\,moor}$ induced by the two mooring line sets at the bow and stern. To be specific, looking at the moment time series induced by each mooring line set at the bow and stern in Figure 6.6, it can be seen that the steeper the wave, the clearer the results of opposite phases are shown. However, the moment induced by the lines of the bow is, on average, greater

than the moment due to the stern lines. The overall response demonstrates that the mooring lines play a role in balancing out the dynamics (heading angle of the model). The negative sign-biased response is related to the asymmetric HBM and the gradual shift of the average model's heading to the negative yaw direction. It is observed that the magnitude of $M^4_{z\,moor}$ is observed to account for about 10 % in HBM in the most severe cases (see Figure 6.6).

6.3.3 Response amplitude operator (RAO) estimation

The calculation of motion and bending moment RAO is performed according to the method explained in Section 3.5. All the variables applied to the denominator are theoretical values including half the wave height, $H/2$. In the numerator, the physical quantity takes the 1^{st} and 0^{th} harmonic components from the Fourier decomposition or the average of maximum/minimum values measured in the selected time window. For reference, the latter applied filtered data, and measurements in calm water conditions are intentionally excluded to consider only the hydrodynamic response.

6-DOF motions

The estimated 1^{st} harmonic 6-DOF motion RAOs at the COG of the model for each H/λ series are presented in Figure 6.7 together with the linear BV Hydrostar results with and without the mooring system for comparison.

Overall, it can be said that the experimental results are in very good agreement with the linear RAO results considering the mooring stiffness matrix in most motions. However, some discrepancies appear in sway for short-wave cases. Such dynamics induce large drift motions. The experimental roll RAO follows very well the linear result in relatively less steep cases and shows a large changing rate as the wave steepness increases. A similar trend is found in heave, pitch, and yaw results, but with a relatively small magnitude in the changing rate of each curve. In the yaw motion, the BV Hydrostar results with and without the mooring system show relatively noticeable discrepancies for the long-wave cases of wave period $T = 1.5$ s or more. Given that the horizontal mooring setup applied in this study generates additional resilience in surge, sway, and yaw motions, inconsistently. The mooring system effects are particularly evident in yaw motion for large periods.

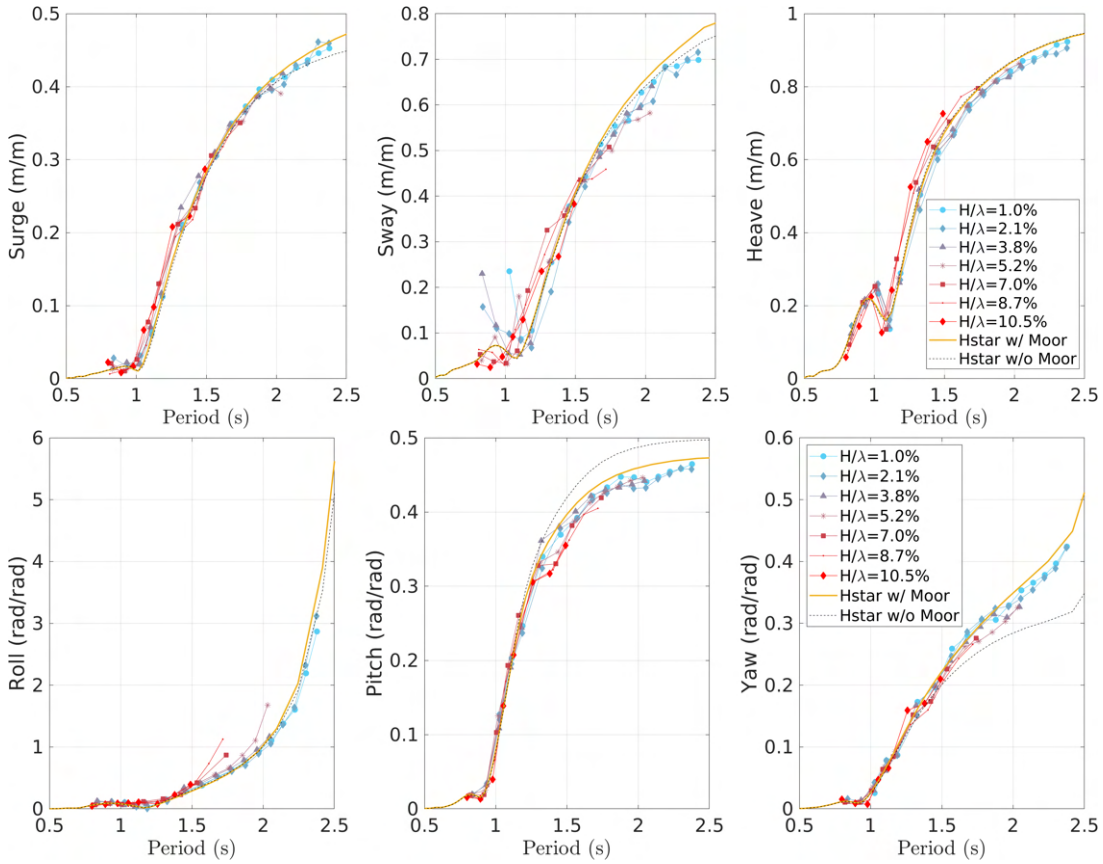

Figure 6.7 – 1^{st} harmonic 6-DOF motion RAOs at the COG of the model for each H/λ series

VBM and HBM

1^{st} and 0^{th} harmonic VBM RAOs at the intersegment No.4 were estimated using the ATI data for each H/λ case (see Figure 6.8). The wave's nonlinear effect can be clearly observed near the peak period range of the 1^{st} harmonic. The $H/\lambda = 1$ % case contains very small nonlinearities. This demonstrates results that are comparable to BV Hydrostar in most wave period ranges. Some discrepancies near the peak period imply that the VBM induced by $H/\lambda = 1$ % wave contains nonlinearities as observed in the previous experimental study by Bouscasse et al. (2022) [6].

The magnitude of the peak of the curve was expected to increase in proportion to the wave steepness of the series. However, the maximum value of the curve is observed in $H/\lambda = 5$ %. Then the curve gradually decreases as it goes higher than $H/\lambda = 5$ %.

Meanwhile, a clear increasing trend is confirmed in the 0^{th} harmonic VBM RAO. One thing to note here is, that for very steep wave cases ($H/\lambda = 10.5$ %) near the peak period, the 0^{th} harmonic contribution is almost 35 % of the $1st$ harmonic. The 0^{th} and 1^{st} harmonic VBM components are found to account for the majority part of the total

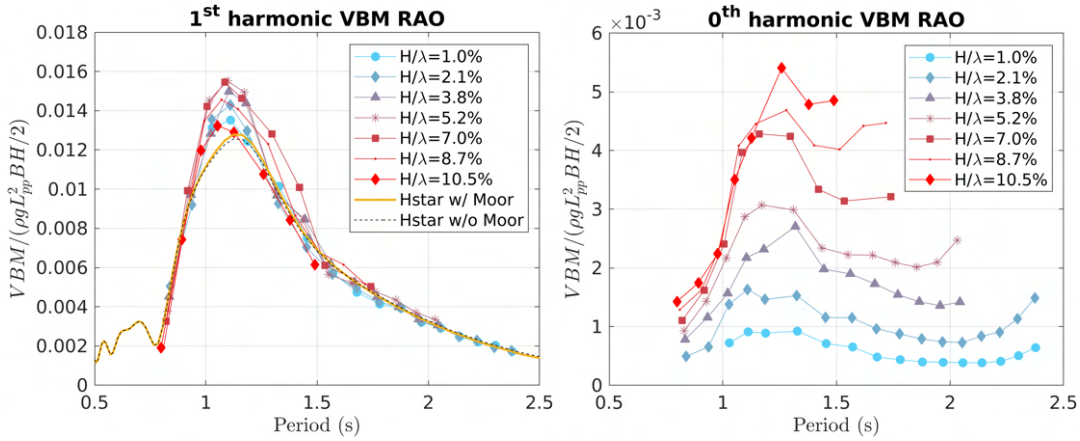

Figure 6.8 – 1^{st} and 0^{th} harmonic VBM RAO at the intersegment No.4 for each H/λ case

VBM RAO presented in Figure 6.9 where the RAO was calculated with filtered data.

In Figure 6.9, the overall increasing and decreasing trend in sagging and hogging, correspond to the average of maxima and minima respectively in the selected time window. Considering that the sagging RAO of each H/λ series is always higher than its hogging RAO (see Figure 6.9), it may be concluded that the 0^{th} harmonic component (mean VBM) is biased to the negative sign based on VBM $= 0$ Nm. One thing to note is that the sagging result has a tendency to increase clearly in proportion to the H/λ. On the other hand, the hogging RAO near the pear period increases up to $H/\lambda = 5$ % with a maximum value and starts to decrease when the case is $H/\lambda > 5$ %. The peak in both RAO results tends to shift gradually as the H/λ changes.

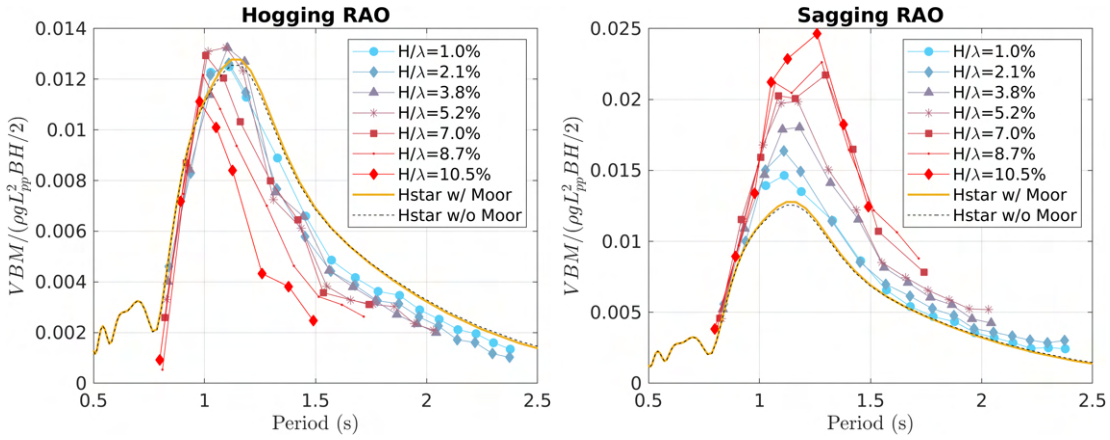

Figure 6.9 – Hogging (average of maxima measured) and sagging (average of minima measured) RAO estimated with the direct measurement (ATI) for each H/λ case

In the case of the HBM results presented in Figure 6.10, the 1^{st} harmonic HBM RAO for $H/\lambda = 1$ % has the same tendency that the one observed in VBM results, showing a magnitude larger than the linear prediction near the peak period. The influence of

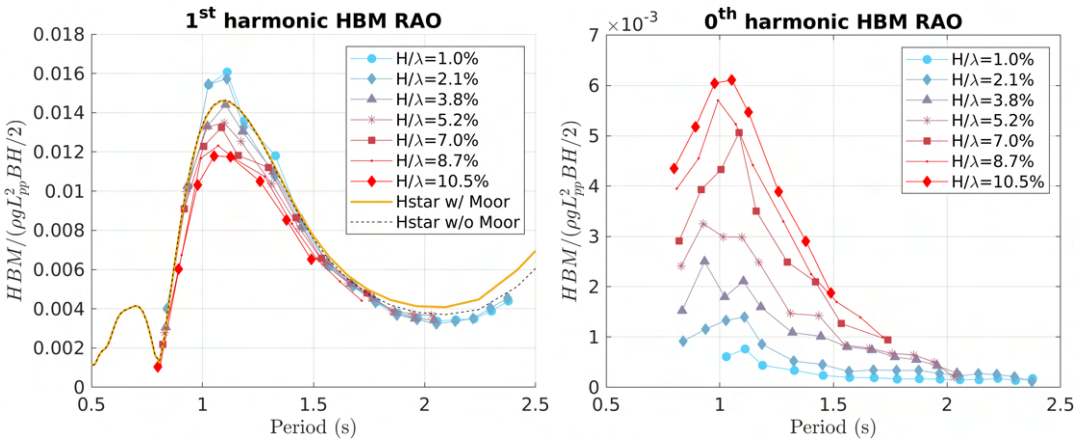

Figure 6.10 – 1^{st} and 0^{th} harmonic HBM RAO for each H/λ case

the disturbed waves such as waves that propagate from the bow to the stern by the diagonally arranged model and wave configuration sensitively affects the responses in mild conditions. On the other hand, the overall shape of the curve is in good agreement with the linear results, and the RAO curve continuously decreases with the increase of H/λ. The 0^{th} harmonic RAO shows the opposite trend to the 1^{st} harmonic result, a distinct increasing trend to the H/λ as that observed in the VBM result (see Figure 6.10).

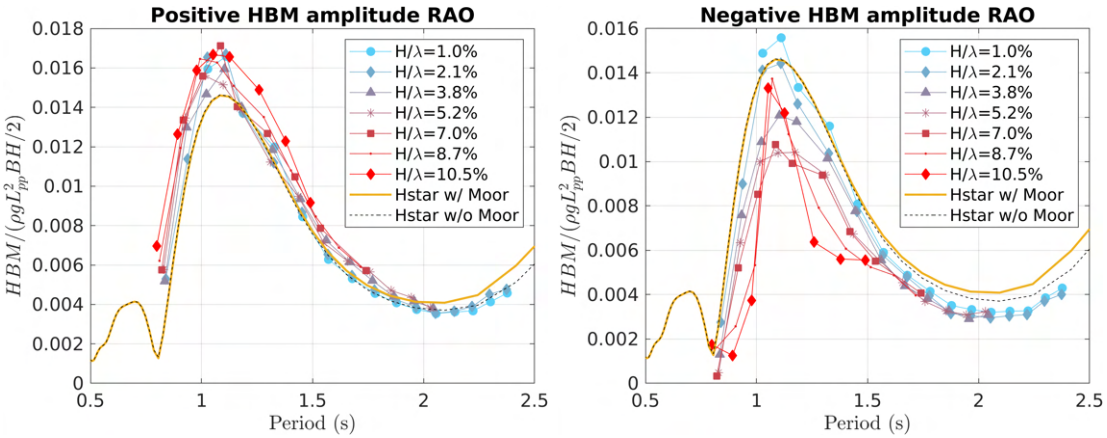

Figure 6.11 – Positive HBM (average of maxima measured) and negative HBM (average of minima measured) RAO estimated with the direct measurement (ATI) for each H/λ case

The positive and negative HBM, which correspond to the average of maxima and minima containing all frequency components, show different patterns of curve fluctuations near the peak period in Figure 6.11. This explains that not only the 1^{st} and the 0^{th} harmonics but also the higher harmonic components (e.g. slamming impact) need to be identified. Figure 6.12 shows the hogging (positive) and sagging (negative) VBM (HBM) RAO of $\lambda/L_{pp} = 0.4375$ corresponding to the near peak period of 1.116 s for all

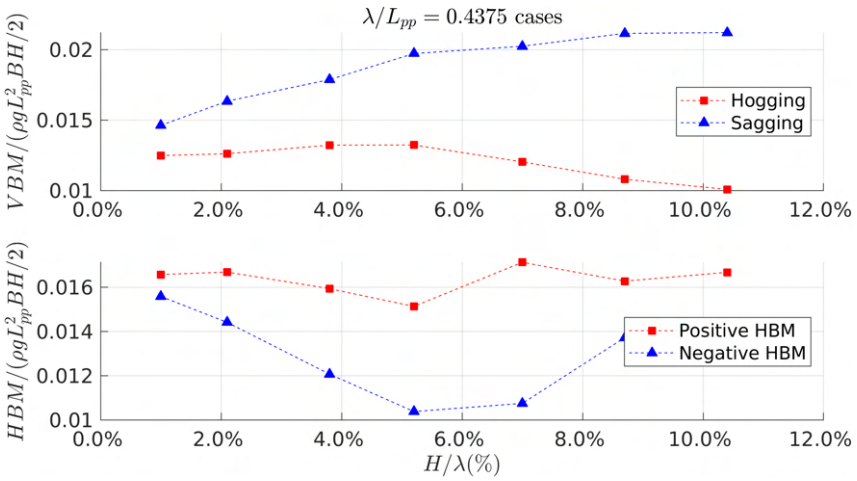

Figure 6.12 – Hogging and sagging RAO (top) and positive HBM and negative HBM RAO (bottom) for $\lambda/L_{pp} = 0.4375$ case

H/λ series. An interesting point is that except for the sagging RAO, the other remaining three responses reach maximum or minimum RAO value when $H/\lambda = 5$ %, and the RAO curve increases or decreases based on this.

Given that the model is rigid, the changes in the RAOs near the peak period with respect to the H/λ can be related to the wave and/or response nonlinear effects. Those can be defined as a ratio of measurements to linear values, $\text{HBM}_{NL}/\text{HBM}_L - 1$. The same applies to the VBM responses. To check this, linear values are first calculated by considering the linear RAO from Hydrostar. The linear indicator of both responses for a given wave frequency (f) is defined as:

$$\begin{aligned} \text{VBM}_L(f) &= |\text{RAO}^{VBM}(f)| \times A(f) \\ \text{HBM}_L(f) &= |\text{RAO}^{HBM}(f)| \times A(f) \end{aligned} \tag{6.8}$$

where A is the amplitude of a given wave and RAO represents linear responses calculated by BV Hydrostar [93]. The nonlinear effect of the wave on the magnitude of VBM and HBM including all harmonic components are then evaluated. The overall calculation procedure is shown in Figure 6.13, and the results are presented in Figure 6.14.

Looking at the VBM RAO presented in Figure 6.14 first, the ratio of the nonlinear sagging response to the linear value shows a continuous increase. On the other hand, hogging shows a slight increase until it reaches $H/\lambda = 5$ %, and thereafter steady decreasing trend is observed until $H/\lambda = 10$ %. A sagging response greater than 80 % compared to the linear value is observed in the most severe condition ($H/\lambda = 10$ %), and hogging appears to be 20 % less in comparison to the linear case. Nonlinear HBM also shows a large difference from the linear value in the negative response, showing

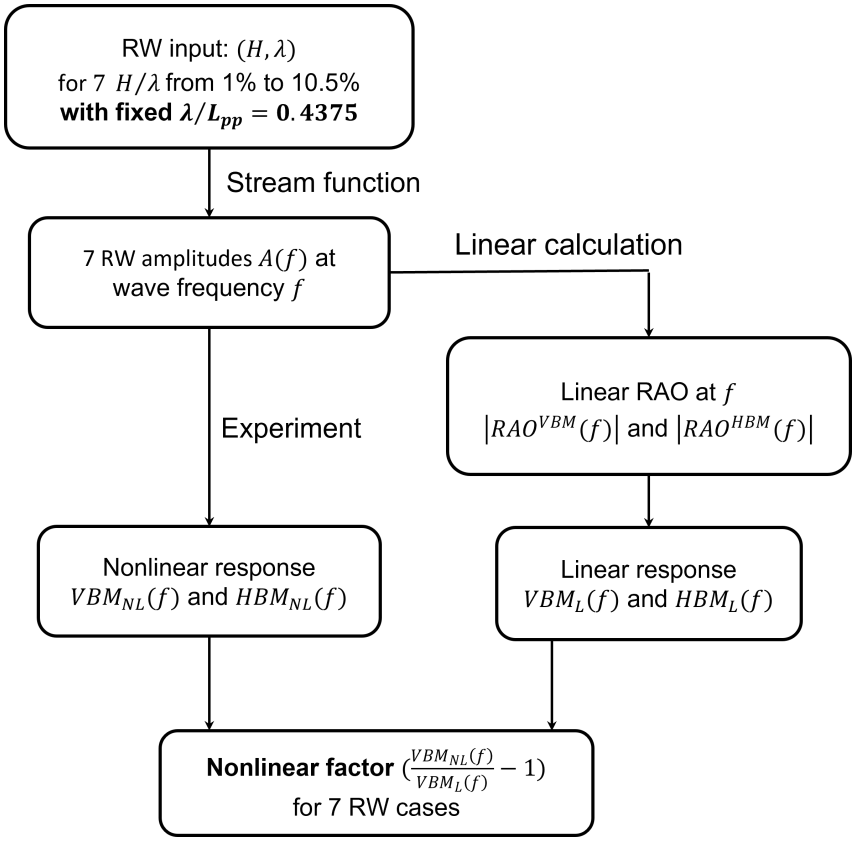

Figure 6.13 – Nonlinear factor calculation procedure for the 7 RW cases in H/λ with $\lambda/L_{pp} = 0.4375$

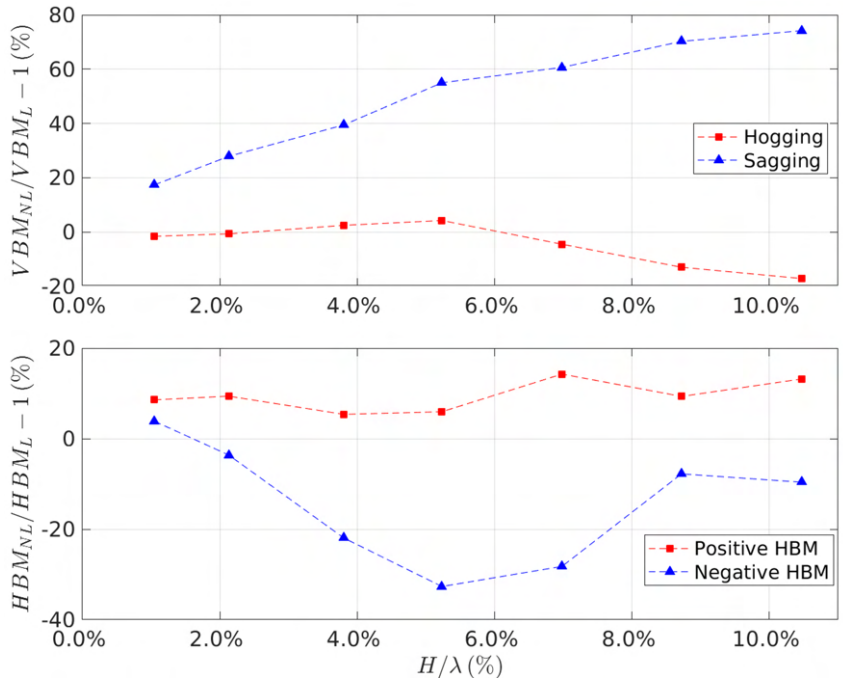

Figure 6.14 – Nonlinear factor for the 7 cases in H/λ with $\lambda/L_{pp} = 0.4375$

an increase or decrease in nonlinear effects based on $H/\lambda = 5$ %. The response tends to decrease by up to 40 % as compared to the linear value.

As shown in Figure 6.15, to check the contribution of harmonic components in 7 wave steepness cases with $\lambda/L_{pp} = 0.4375$, component decomposition was carried out for both VBM and HBM obtained from experiments. Interestingly, as for the relationship between the 1^{st} harmonic and other harmonics of HBM, it is confirmed that their relative contribution in the response tends to change overall in the opposite way to each other with the increase of wave steepness. In the VBM results, it is observed that the 1^{st} harmonic increases up to $H/\lambda = 5$ % and then decreases, while the remaining harmonic components are found to gradually increase overall with the increase of wave steepness. In addition, for the case that H/λ is more than 7 %, the higher harmonic components more than third-order are found to account for a significant part of the overall response. This is a result of the wave-structure interaction, showing that the more severe the given wave condition, the stronger the nonlinearity of the interaction.

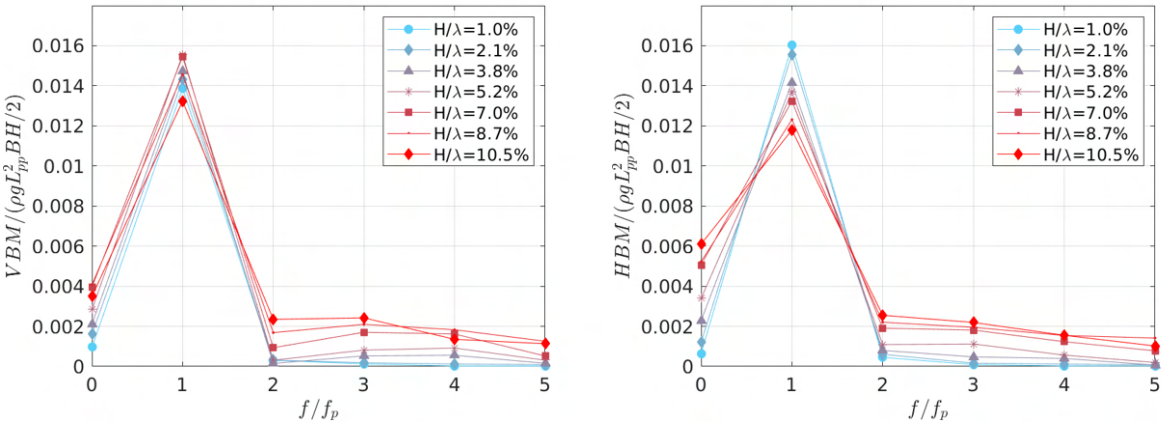

Figure 6.15 – Harmonic components of VBM and HBM of all H/λ series with $\lambda/L_{pp} = 0.4375$

Given the results about the harmonic components and the nonlinear factor for the 7 wave cases near the peak period, it can be said that when a given wave's steepness is greater than $H/\lambda = 5$ %, a more intense wave-structure interaction occurs, resulting in a response with strong nonlinearity. The nonlinearity of the response could become stronger if the high-frequency slamming impact is considered in the analysis as observed in the very steep wave case ($H/\lambda = 10.5$ %). The response of the resulting wave bending moments in the peak period varies greatly depending on the wave steepness.

6.3.4 Contribution of mooring system to HBM

As mentioned earlier, the HBM (M_z^4) measured by the ATI includes the additional effect induced by the mooring line, and the corresponding internal moment $M_{z\,moor}^4$ at the ATI position can be estimated using the tension data of the two lines of the bow or stern. To qualitatively evaluate the contribution of the mooring system to the HBM, the z-axis moment by mooring lines was calculated. Note that only the hydrodynamic tension by a given wave is considered by excluding the mean tension of the selected time window, and the corresponding results are presented in Figure 6.16.

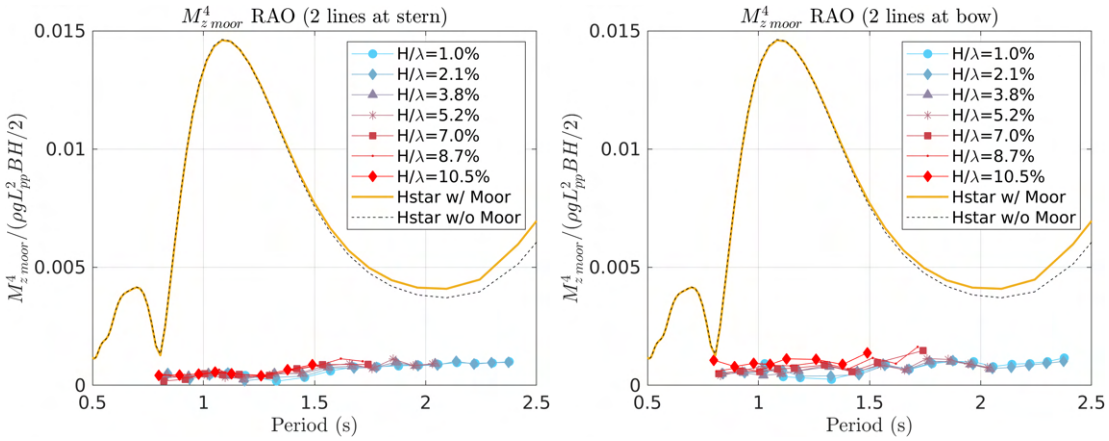

Figure 6.16 – z-axis bending moment RAO at the intersegment No.4, estimated with the mooring tension data of the stern (left) and bow (right)

Overall, the $M_{z\,moor}^4$ RAO of the stern and bow lines are similar to each other, but in the case where H/λ is relatively steep, it is observed that the mooring lines at the bow, which encounter the undisturbed wave first, relate with the estimation of more conservative RAOs in particular for the cases with $T < 1.7$ s. Considering that each mooring line set at the bow and the stern acts as a counterbalance to maintain the heading angle of the model, the result showing a larger magnitude of the moment by mooring lines of the bow possibly contributes to making the HBM signal asymmetric, and consequently, the average heading angle of the model is likely to be changed in those cases. The distribution of the mean yaw and the difference between the average $M_{z\,moor}^4$ of the bow and stern lines for all cases is presented in Figure 6.17.

In Figure 6.17, it is observed that the mean yaw of each case corresponding to 'the measured mean yaw - the target yaw (-120 degree)' stays around 0 degree in relatively mild conditions (up to $H/\lambda = 3.8$ %). $M_{z\,moor}^4$ difference shows the same trends as well. When the H/λ increases more than 5.2 %, both the mean yaw and $M_{z\,moor}^4$ difference starts to change. It is found to be -2 degree when $M_{z\,moor}^4$ difference is around 15 Nm in $H/\lambda = 10.5$ %. This implies that the difference between the two $M_{z\,moor}^4$ of the

two mooring line sets at stern and bow at the ATI position may relate to the changes in average yaw angle. Overall, the more the mean yaw motion of a given wave case differs from the initial -120 degree, the greater the $M^4_{z\,moor}$ difference, showing that there is a correlation.

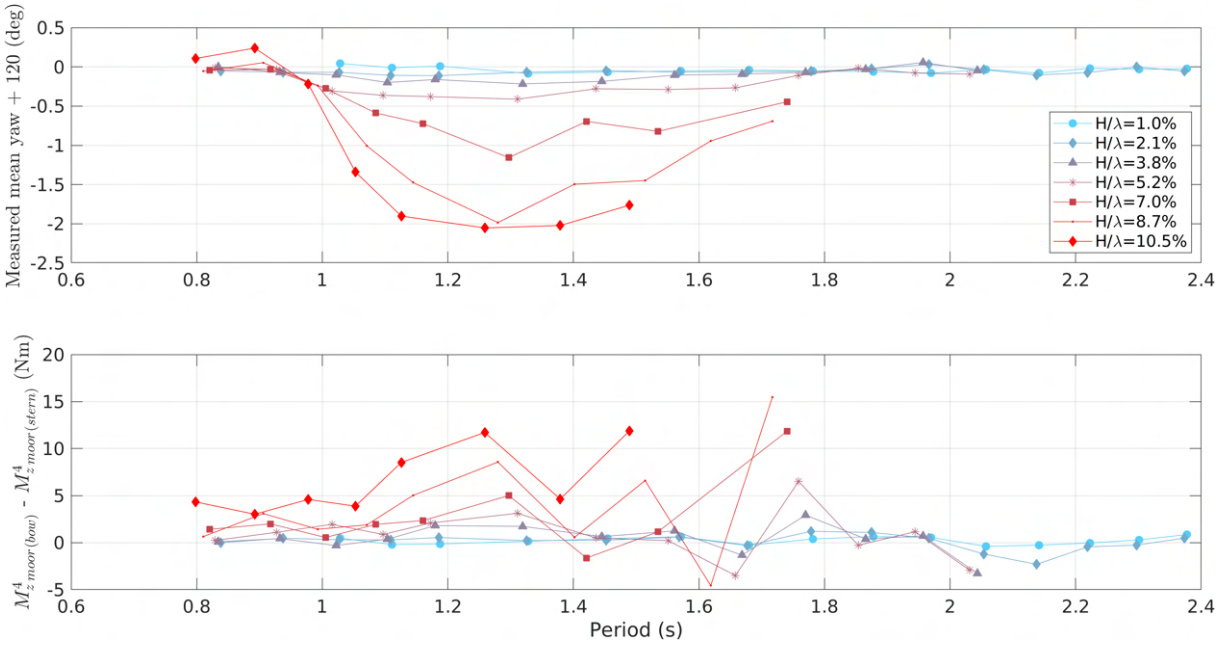

Figure 6.17 – Measured mean yaw - target yaw (-120 degree) for all RW cases (top) and difference of $M^4_{z\,moor}$ of the bow and stern mooring lines (bottom)

Comparisons of model tests with and without mooring

The presence or absence of the mooring system contributes to the HBM, but it is not the only factor having an influence. The intersegment No.4, is close to the COG of the model but does not coincide with it, and the model geometry is y-axis asymmetric. That is, the interaction between the mooring system and the model results in different wave quality at the bow and stern, and the position of interest to evaluate may take some part in the HBM results.

A more intuitive way to compare the effects of a mooring system is to compare test results with and without mooring lines. However, in reality, an accurate comparison between the response of the unconstrained model which drifts because of waves and changes in way of the bow angle and the response of the moored model is impossible. However, if the motion changes between the two configurations are within an acceptable range, it will be likely that the comparative analysis of the HBM response time series includes meaningful results.

To confirm the above a special test was carried out for a wave period of 1.116 s, which is the same as the peak period of the HBM, and a wave slope of 3.1 % corresponding to a case for which the drift effect is not excessive. In the case where the steepness is more than 5 % with the same period, excessive drift occurs from the beginning. Since this affects the motions, it is impossible to compare results.

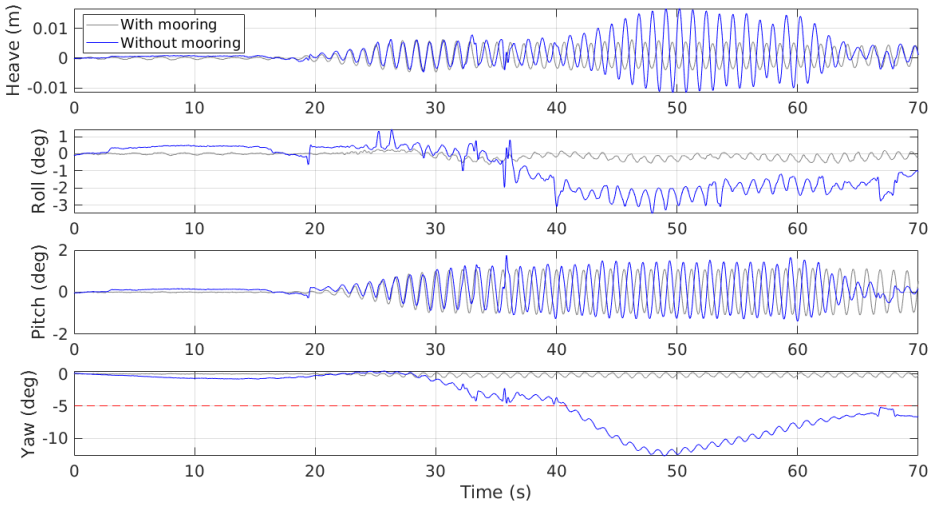

Figure 6.18 – Test case with $H = 0.062$ m $T = 1.116$ s $H/\lambda = 3.1$ %. 4-DOF motion time signals measured with/without mooring system

The comparative analysis of motions with and without accounting for the mooring system is presented in Figure 6.18. For the comparison of physically reasonable responses, a criterion was set for yaw motion at 5 degrees based on the designated heading angle of -120 degrees. Responses thereafter were excluded from the analysis. Regarding a yaw criterion, it was hard to find previous studies that dealt with this topic in detail, covering a criterion for the analysis. Therefore, the transient range of the 6-DOF motions of the two tests with and without accounting for the mooring system was referred to first, and a criterion was set based on particularly sensitive responses. It was found to be yaw motion, and the magnitude of the yaw criterion was determined by referring to the time range before when the yaw changes excessively ($t = 40$ s).

As shown in Figure 6.18, from around 20 s, when the wave generated by the wavemaker reaches the model to around 40 s, the heave and pitch motions show similar results to responses from the moored model. On the other hand, in the case of roll and yaw, which are more affected by model drift, it can be observed that they lag behind the responses of the model including with the mooring system.

The top two graphs in Figure 6.19 show the result of the wave bending moments (VBM and HBM) measured by the ATI sensor, and the last graph shows the horizontal

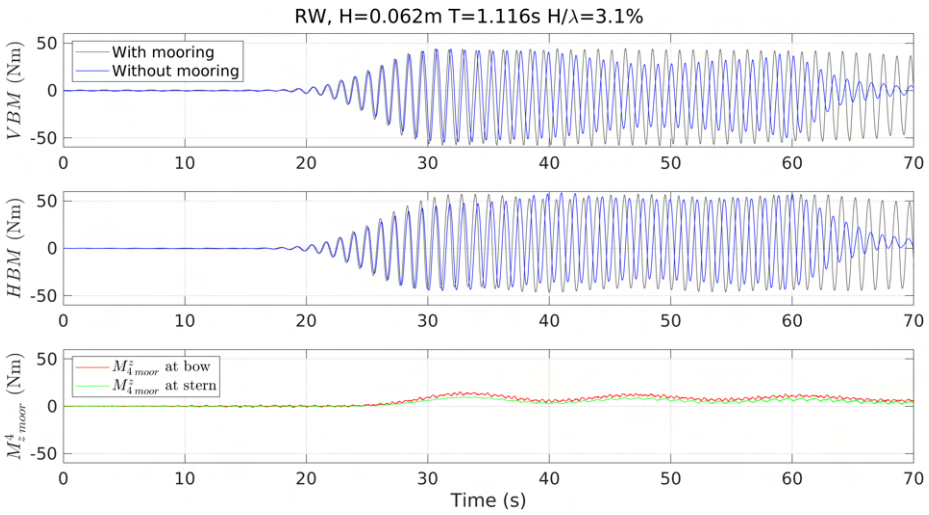

Figure 6.19 – Time signals measured with/without mooring system: VBM, HBM, and $M^4_{z\,moor}$ at stern and bow

moment at the ATI position by the mooring lines' tension at the same moment.

In the case of the wave bending moments, the results without mooring lines are observed to be generally low. Considering that the model is continuously drifting without restoration by the mooring system, the zero-crossing period is continuously longer over time, and its size is gradually reduced as compared to the result of the case with the mooring. However, the signal shows a response of a similar period and size at the start of the test. It can be seen that the long-period response of the moment time series due to the mooring may affect the HBM response (see the last graph in Figure 6.19).

Considering the above, it can be seen that the heading of the ship changed excessively after facing the first wave encounter. As a consequence, the responses show a completely different trend from the results of the moored model. Therefore, it was decided to consider the wave bending moment in the range from 35 s to 40.5 s.

The time interval selected for analysis is shown in Figure 6.20, and it can be roughly estimated that the difference between HBM results is comparable. The phase difference between the two signals corresponds to about 0.5 s, and it seems that the difference between the two HBM in magnitude (with and without the mooring lines) is similar to $M^4_{z\,moor}$ at intersegment No.4.

To demonstrate the influence of the presence or absence of mooring lines, Figure 6.21 is presented. The black points of each graph correspond to the difference between the peak values of the blue curve and the gray curve and the peak values of the moment generated by each mooring line set (red and green). It can be observed that the HBM (+)peak difference is directly related to the sign of the difference between the moment by the bow and stern mooring line sets. When both moments are equal, the

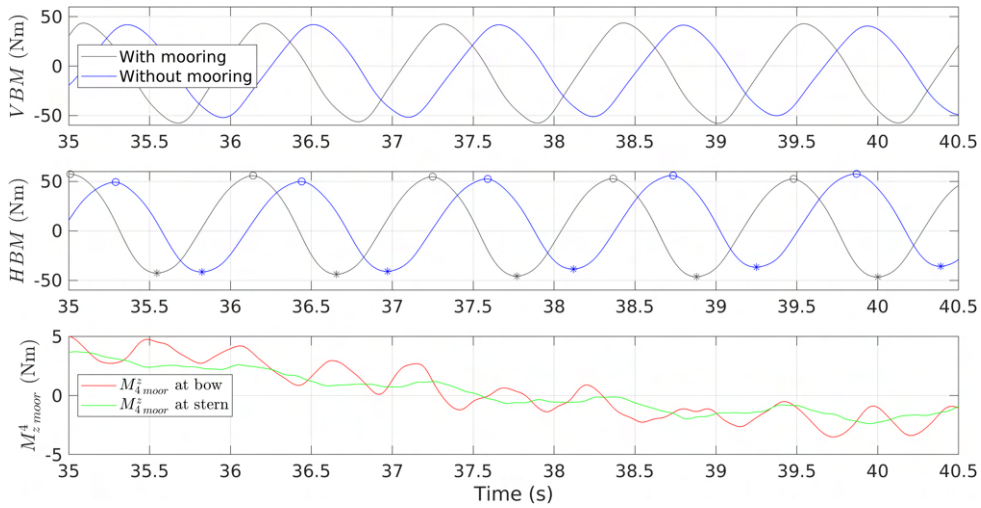

Figure 6.20 – The moment signals of the selected time interval for the comparative analysis: VBM (top), HBM (mid), and $M^4_{z\,moor}$ at stern and bow (bottom)

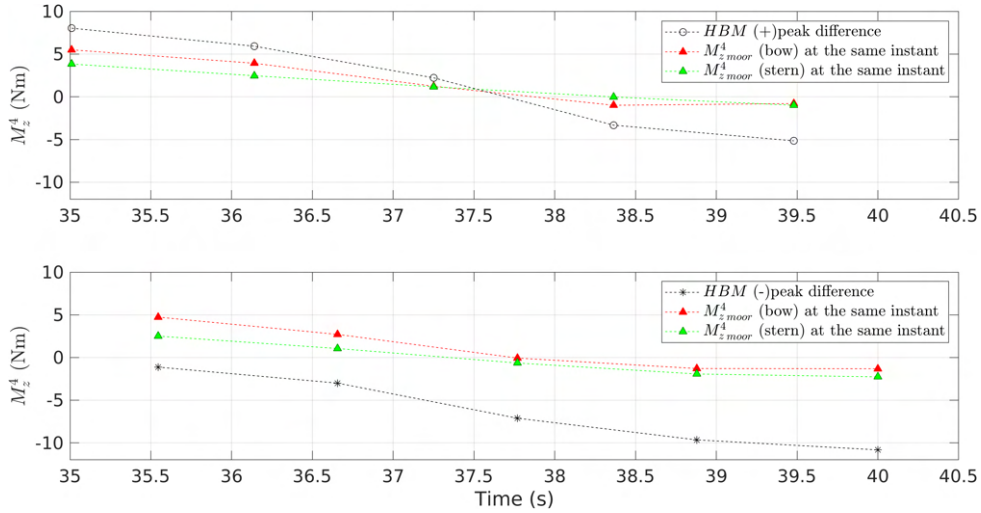

Figure 6.21 – Correlation between HBM difference by the presence and absence of mooring (black point) and $M^4_{z\,moor}$ of two mooring sets (red and green points).

HBM (+)peak difference is close to 0, and the change in sign is consistent with both results. For the HBM (-)peak results, the mean is not zero and the roll motion starts to deviate significantly after $t = 37.5$ s. Thus it is ambiguous to interpret the result in detail. The overall changing trend of the HBM (-)peak difference is similar compared to the moments by the bow and stern mooring line sets.

Given that the experimental conditions are not strictly identical, the possibility that other factors may affect the results cannot be excluded. The reason why the range of the maximum and minimum values of the additional moment by the mooring lines is relatively small is also likely to be influenced by several factors including the change in bow angle due to the drift.

6.4 Summary

The response characteristics of the horizontally moored rigid model in a -120 degree oblique regular wave condition were investigated with 7 different wave sets in terms of H/λ. The effect of the wave steepness caused an increase and(or) decrease of the estimated RAO curves of the 6-DOF motions, HBM and VBM, and as expected most responses showed the largest difference from the linear estimation when $H/\lambda = 10$ %. In particular, in the VBM and HBM responses of the cases corresponding to near the peak period of the HBM RAO, it was confirmed that strong nonlinear responses from the intense wave-structure interaction and in particular slamming were observed when H/λ was 7 % or higher containing a large proportion of higher harmonic components. For low wave steepness, the positive HBM was larger than the negative one, and slamming changed the trend for the larger steepness cases. For the same cases, the VBM reached similar values as the ones observed in head waves. The assumption of a rigid model was validated in head waves. For this case, the filtered data were shown to be very close to what would be the rigid solution. However, this should be carefully verified for the oblique case where slamming pronounces and structural vibrations are more visible.

The oblique condition was tested with a soft mooring system positioned in way of the bow and stern. The soft mooring system at the bow and stern provided different magnitudes of restoring moments from each other, which became more pronounced in steep wave conditions. In particular, under the wave condition of $H/\lambda = 10.5$ % with $\lambda/L_{pp} = 0.4375$ corresponding to the vicinity of the HBM peak period, it was observed that the magnitude of $M^4_{z\,moor}$ by the bow lines had a difference of -15 Nm compared to $M^4_{z\,moor}$ by the stern lines. The $M^4_{z\,moor}$ difference by the two mooring line sets at the bow and stern was approximately less than 10 % of the HBM response measured by the ATI sensor.

The time series response of $M^4_{z\,moor}$ by the bow line tension was in phase with the negative-biased HBM signal measured by the ATI sensor, and the corresponding mean yaw was found to decrease as the difference in $M^4_{z\,moor}$ increased. Although it cannot be concluded that the mooring system is the 'cause' of the asymmetric HBM and the yaw change, it has been shown that there is a correlation. The y-axis asymmetric model geometry may be one of the main influences as well and can be partially responsible for the asymmetric HBM response and changes in mean yaw motion.

Chapter 7

Conclusions

The application of a Monte Carlo method and equivalent design methods to determine the vertical bending moment (VBM), horizontal bending moment (HBM), and 6-DOF motions of a 9-segment containership model in head and -120 degree oblique seas has been studied.

The main achievements in head sea experiments are i) the validation of the HOS-NWT's ability in generating accurate (non-)breaking sea states and ii) the development of an irregular EDW calculation procedure for the VBM analysis. The developed EDW calculation procedure combines a fully nonlinear wave solver, HOS-NWT, and a linear VBM RAO. It takes advantage of existing numerical algorithms, making the procedure more efficient and reliable.

It has been shown that using a nonlinear numerical wave model can facilitate the generation of waves of a desired sea condition and increase the accuracy of hydrodynamic load analysis. This can be particularly important when the waves are used not only in experiments but also in future CFD studies.

Given that the existing EDW methods apply a simple linear wave model, the application of the HOS-NWT in the FORM-based irregular EDW calculation procedure has significantly improved the accuracy of the experimental reproduction of the computed EDW. The consideration of the linear VBM RAO in the EDW calculation has been shown to provide an EDW profile fairly similar to that obtained with a nonlinear RAO. This fact will contribute to increasing the practical application of the EDW procedure in design load analysis.

The detailed conclusions for the above-mentioned findings in head sea conditions are as follows.

• **Validation of the HOS-NWT solver** was carried out with a wave-only numerical campaign through the analysis of crest statistics and wave spectrum of non-breaking and breaking sea states. A comparison with the experimental results was performed to validate that the HOS-NWT successfully implemented the key features of the physical wave tank. The solver generated target irregular wave conditions with sufficient accuracy, containing strong nonlinear wave-wave interactions and complex energy dis-

sipation induced by breaking waves. The solver tended to overestimate the breaking phenomena in the most severe sea states. However, it has been confirmed that the shape of the wave spectrum and POE distribution curve obtained via experiments are qualitatively and quantitatively comparable to the numerical calculation results.

• **Verification of the nonlinear FORM-EDW calculation algorithm applying the modified HLGA algorithm (MHLGA) and the HOS-NWT nonlinear wave solver** was also carried out. The first target quantity was the crest height at a certain position and time in a wave-only case. A geometrical similarity review on the nonlinear EDW profile confirmed that the calculated EDW was a plausible most probable wave profile, showing that the algorithm applied was well formulated. The inclusion of nonlinear wave effects by the HOS-NWT model in the procedure represents an adequate manner to overcome the accuracy problems encountered in the classical EDW methods based on linear solvers.

• **Applicability of the regular and irregular EDW approaches for the VBM analysis** was confirmed. The focus was placed more on the irregular EDW approach. All EDW-induced VBMs tended to be smaller than Monte Carlo reference results for all sea states. The discrepancy was more prominent in severe sea conditions and for sagging responses, which have stronger nonlinear characteristics than hogging. The slope of the VBM POE curve is sensitive to the changes in time-series response. The fact that the numerical wave quality including the relatively overestimated energy dissipation mechanism due to wave breaking compared to the experimental waves may affect the numerical Monte Carlo reference result and consequently cause less accurate POE estimation for target VBMs. An additional cause can be that the system's memory effect generated by a short EDW wave packet may provide less intense VBM responses at given POE levels. However, the shape of the focusing waves and the resulting VBM responses generally showed a similar tendency to the Monte Carlo results at various POE levels of up to 10^{-3}, demonstrating its applicability to the VBM analysis.

• **The nonlinear factor defined as a ratio of the measured VBM and the linear VBM** was found to be greatly dependent on the magnitude of target response in sagging results. In addition, it was found to be dependent on the peak period of the sea state, and thus the sea state should be also taken into consideration in estimating the relationship between the nonlinear response and the linear response. As a result, an empirical formula for the nonlinear sagging response estimation of the rigid model was defined with the given variables of the EDW and the sea state. Overall, a very good

agreement was found between the empirical estimates and the actual measured EDW-sagging responses. The maximum difference of up to 8 % and the average difference of 4 % may be considered acceptable within the context of engineering approximation.

Note that this formula was only validated for one specific size model and λ/L_{pp} applied in this study. Therefore, for wider application of the formula, additional research considering other parameters that affect VBM response, such as ship size, speed, and flexibility, is required, and the empirical formula is expected to serve as a good basis.

Through regular wave experiments in a -120 degree oblique sea, nonlinear trends on motions and wave bending moments were observed with increasing wave steepness (7 wave steepnesses ranging from $H/\lambda = 1$ % and 11 %). These were observations whose results cannot be accurately predicted by linear theory.

The restoring moment of the soft mooring system was found to be correlated with the asymmetric HBM and the mean yaw motion. The effect was qualitatively identified, and it is expected to be used as useful data for either experimental studies of similar settings or numerical simulations.

• **At the HBM peak period, large slamming events occurred for $H/\lambda = 10.5$ %, the steepest wave case.**, which additionally affected the wave bending moments of the rigid body model. Results showed that the unfiltered signals of VBM and HBM containing slamming impacts could increase by 35 % and 45 % of the respective filtered signals. This led to the conclusion that the assumption of a rigid model in the oblique wave conditions should be further investigated perhaps with CFD computations and consequences attributed to hydrodynamic nonlinearities should be further discussed.

• **The increase in wave steepness changed the trend of the 1st harmonic and maximum/minimum response RAOs around the peak period.** The experimental results tended to contain nonlinearity even for $H/\lambda = 1$ %. First harmonic 6-DOF motions and HBM RAO results were found to display a continuously increasing or decreasing trend as the wave steepness increases from $H/\lambda = 1$ % to 11 %. On the other hand, the first harmonic VBM RAO kept increasing up to the $H/\lambda = 5$ % and then started decreasing. In the RAO results of the maximum and minimum VBM and HBM, different trends were observed from the first harmonic RAO results. Excluding sagging, the increase and decrease of RAO values were markedly observed in comparison with $H/\lambda = 5$ %. The strong nonlinear response in the extreme wave condition was prominent in the case of $H/\lambda = 5$ % or more, and the proportion of higher harmonic components increased significantly. This highlighted the importance of considering higher

harmonic responses for steep waves.

• **The effect of the restoring moment by the four soft mooring lines ($M^4_{z\,moor}$) on the responses of the model** was identified. Two different mooring sets at the bow and stern provided different magnitudes of restoring moments, which became more pronounced in steep wave conditions. The difference was approximately up to 15 Nm, which corresponds to less than about 10 % of the total HBM measured by the ATI sensor. The time series of $M^4_{z\,moor}$ by the bow line tension was in phase with the negative-biased HBM signal measured by the ATI sensor, and the corresponding mean yaw change was found to increase as the difference in $M^4_{z\,moor}$ increased. This revealed that, although the mooring system may not be a direct cause, it is at least a factor related to the asymmetric HBM and the change in mean yaw motion.

• **A specific additional test was performed without the mooring system to further understand the effects of the mooring lines.** It was possible for this case to estimate the magnitude of the mooring line effect from a qualitative point of view by comparing the HBM time series with and without mooring lines. As a result, it was confirmed that the nonlinearity of the wave affects the response characteristics of the internal load to a large proportion, and the response can be changed by the geometry of the ship and the influence of the mooring system. As the nonlinearity of the wave increased, the ratio of the higher-order harmonic components of the internal load increased significantly, which emphasized the importance of considering the nonlinear wave and setting up a sophisticated experiment.

Through the application and analysis of various design wave approaches, the advantages and disadvantages of different methods were identified. Regular design waves and irregular EDW may be insufficient as very accurate analysis methods for estimating wave loads, but they can be considered sufficiently efficient approaches in the initial design stage as they provided comparable and reliable estimates. The results presented in this thesis suggest that an improved method or direction for wave load analysis should be considered.

Further research on the nonlinear RAO estimation method for given sea states may facilitate the calculation of the numerical VBM response, allowing the accurate load analysis limited to short-term analysis in experiments to be extended to the long-term. Also, it would allow a detailed comparative analysis with the EDW calculated from the linear RAO.

Differences in linear and nonlinear wave loads and their change patterns were observed with limited models and wave cases. However, unless the hull shape changes

significantly, the trend of results is estimated to be similar for container ships. Further studies on the irregular EDW approach with additional variables such as vessel size, vessel speed, and flexibility are needed for a more robust correlation analysis of linear and nonlinear wave loads, to be able to generalize the conclusion mentioned.

Disturbed waves as a result of wave-structure interaction seem to have a relatively large influence on the structural responses in the oblique wave condition. Large slamming events were found and a dedicated study should be undertaken to shed light on this problem. In this regard, it seems that as future research, the application of the Monte Carlo and the EDW approach in oblique sea conditions may improve our understanding with respect to the characteristics of each approach and resulting wave loads.

Appendix A

Nonlinear VBM RAO estimation

A.1 Nonlinear VBM transfer function (TF)

Even if the model is set to be rigid, as the nonlinear wave propagation is considered an excitation, the VBM response for each frequency component basically contains nonlinearity and is dependent on the sea state. In addition, due to the ship's structural response characteristics and nonlinear waveform, the hogging (positive VBM peak) and sagging (negative VBM peak) responses are not exactly symmetric. In general, the sagging response tends to be much larger than the hogging response. One thing to note is that the VBM transfer function (TF) does not reflect the effects, but provides only the half the sum of the two responses, sagging and hogging for each frequency component. Here, a practical technique to calculate the asymmetric VBM response with nonlinear VBM transfer function estimated for a given sea state is presented, and the calculated VBM time signals are directly compared with the one measured for validation and further discussion.

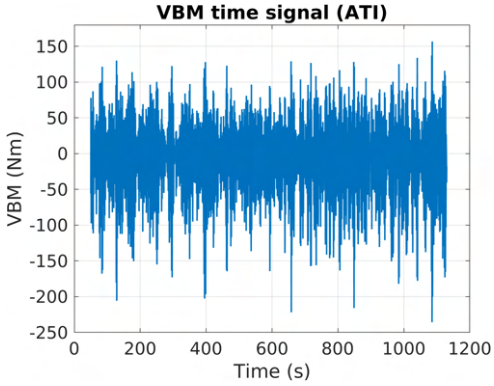

Figure A.1 – VBM time signal for sea state SS8 (model scale)

For the estimation of the VBM transfer function, FFT-based spectral estimation providing the amplitude and corresponding phase of each frequency component is first done for the wave and VBM response time signal measured in the experiment respectively (see Figure A.1). Power spectral density of the wave $S(f)$ and the VBM response $S_R(f)$ are estimated by the Welch's overlapped segment averaging estimator. The du-

ration of the window is 50 s long with 50 % overlap. Estimation of the nonlinear VBM transfer function is then performed using Eq. $(A.1)$, the ratio of the VBM response spectrum (output), $S_R(f)$ to the wave spectrum (input), $S(f)$.

$$|RAO_i|^2 = \frac{S_R(f_i)}{S(f_i)} \qquad (i = 0, ..., N-1) \tag{A.1}$$

The estimated VBM transfer function is expressed as a complex exponential form as follows:

$$\alpha_i = |RAO_i^{VBM}|e^{i\psi_i} \qquad (i = 0, ..., N-1) \tag{A.2}$$

where $|RAO_i^{VBM}|$ is VBM RAO amplitude of i^{th} frequency component and ψ_i is the corresponding phase. Further data processing is performed on the measured original VBM time signals to compute the transfer functions of sagging and hogging, respectively, for a given sea state.

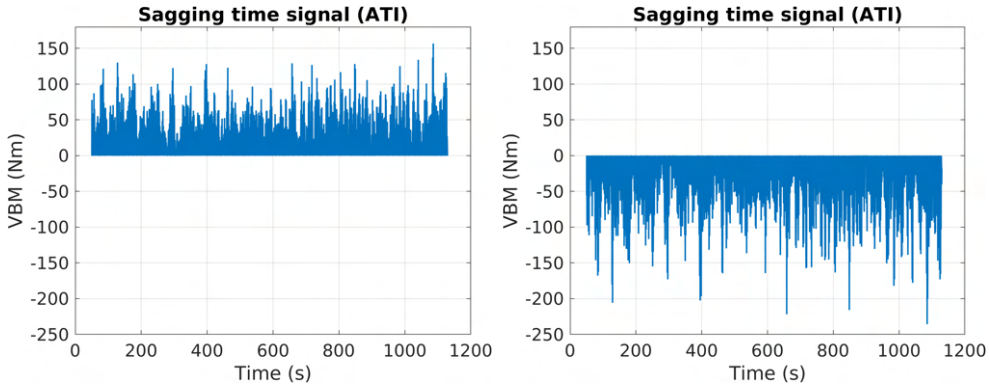

Figure A.2 – VBM time signals for hogging and sagging TF estimation (model scale)

As shown in Figure A.2, by leaving the response of interest as it is, and setting as 0 for the opposite signals based on VBM$= 0$ Nm, the time signal only for hogging or sagging can be obtained. Then, through the same TF estimation process applied for the original VBM signal, hogging and sagging transfer functions can be estimated separately. Expressed each result in the complex exponential form:

$$\begin{aligned} \beta_i &= |RAO_i^{hog}|e^{i\psi_i^{hog}} \\ \gamma_i &= |RAO_i^{sag}|e^{i\psi_i^{sag}} \qquad (i = 0, ..., N-1) \end{aligned} \tag{A.3}$$

where $|RAO_i^{hog}|$ and $|RAO_i^{sag}|$ are hogging and sagging RAO amplitudes of i^{th} frequency component respectively and ψ_i^{hog} and ψ_i^{sag} are corresponding phases. The $|RAO_i^{VBM}|$ in Eq. $(A.2)$ corresponds to half the sum of hogging and sagging of i^{th} component. In the same context, for $|RAO_i^{hog}|$ in β_i, since the negative signals are set

to 0 and the TF estimation is done only with the positive signals, the amplitude $|RAO_i^{hog}|$ corresponds to half the hogging. The same goes for $|RAO_i^{sag}|$ in γ_i, but calculated with the opposite signals. Thus, the following relation has to be satisfied:

$$|RAO_i^{VBM}| = |RAO_i^{hog}| + |RAO_i^{sag}| \qquad (i = 0, ..., N-1) \tag{A.4}$$

To check this, Figure A.3 is presented and show that both are exactly the same as each other in all frequency components.

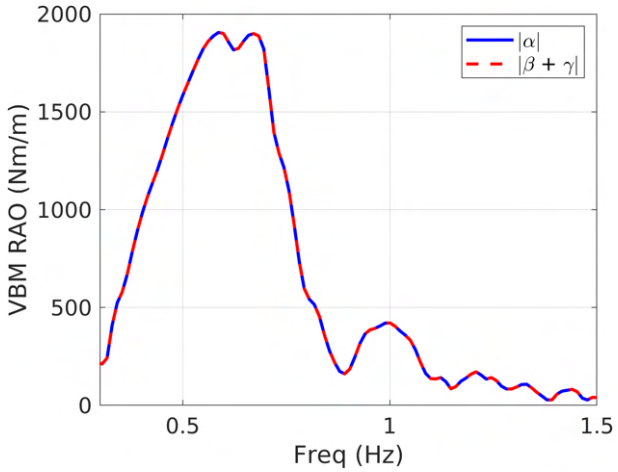

Figure A.3 – Comparison of two VBM RAO estimated with the original VBM time signal and the separated VBM time signals (model scale)

Figure A.4 shows the linear and experimental nonlinear VBM RAO for five different sea states where the experimental RAO (RAO_{NL}^{hog} and RAO_{NL}^{sag} respectively) corresponds to the average RAO of all 2h30 realizations of each sea state. For reference, coherence analysis is also performed to take only VBM RAO data having a coherence index of 0.8 or higher out of 1.0. As seen in Figure A.4, the VBM RAO satisfying the coherence criterion is found to be in the range around the peak of the RAO curve of each sea state, and the VBM RAO of frequency components with coherence indices less than the criterion is replaced with the existing linear VBM data.

An interesting point is that the hogging RAO (RAO_{NL}^{hog}) does not change much depending on the changes in sea state. Some visible differences are observed in the most severe case (SS17) near the peak frequency and $f = 1.0$ Hz, while the other cases have little change in the curve over the main frequency range. On the other hand, a clear increasing tendency in the sagging RAO (RAO_{NL}^{sag}) is observed as the sea state becomes severe. Given that the model is rigid, the difference between the target VBM and the measured VBM induced by the calculated EDW in the experiment is likely to have a similar trend to the relation between the linear VBM RAO and the estimated nonlinear VBM RAO for each sea state.

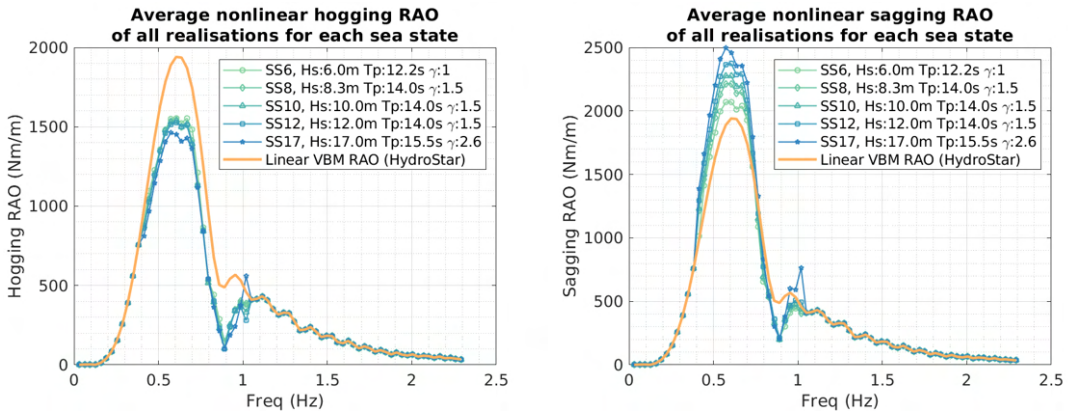

Figure A.4 – Nonlinear hogging (RAO_{NL}^{hog}) and sagging RAO (RAO_{NL}^{sag}) for each sea state (model scale)

A.2 Calculation of VBM signal with the estimated RAO

To verify the above nonlinear RAO estimation procedure, VBM time series is recalculated applying the RAO_{NL} and one specific 2h30 wave realization data for each sea state. The calculated VBM signal is then compared with the VBM time signal measured in the experiment. Figure A.5 shows the overal procedure applying the average nonlinear RAO (RAO_{NL}) and FFT of a specific wave realization among K realizations (i.e. $\eta^k(x_0,t)$ for k^{th} realization).

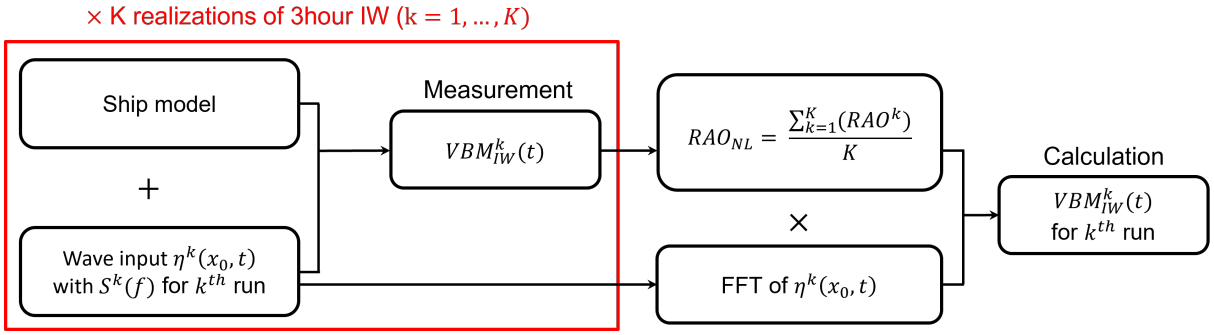

Figure A.5 – Calculation of nonlinear VBM response time series with average nonlinear VBM RAO

Given the fact that the number of wave components considered for the experimental generation of full scale 2h30 wave elevation corresponds to 10800 ranging from 0 to 100 Hz, the initially applied frequency range (0.03 to 2.3 Hz with N=72 equidistant frequency) of the VBM RAO is interpolated based on the wave frequency components. As a result, complex exponential form of sagging and hogging can be obtained as follows:

$$\begin{aligned} Hogging_i &= |RAO_i^{hog}|A_i e^{i(\psi_i+\epsilon_i)} \\ Sagging_i &= |RAO_i^{sag}|A_i e^{i(\psi_i+\epsilon_i)} \qquad (i=0,...,N-1) \end{aligned} \tag{A.5}$$

where A_i and ϵ_i denote wave amplitude and phase, and ψ is the VBM RAO phase. In Figure A.6, the frequency range presented corresponds to the range where the linear RAO data is replaced by the estimated nonlinear RAO. A slight difference is observed in the range from $f = 0.4$ to 0.8 Hz, while in the relatively higher frequency range around $f = 1.0$ Hz, quite noticeable discrepancy is observed compared to the result from the Hydrostar. The estimated phase results of each sea state are taken into consideration in the VBM time signal calculation.

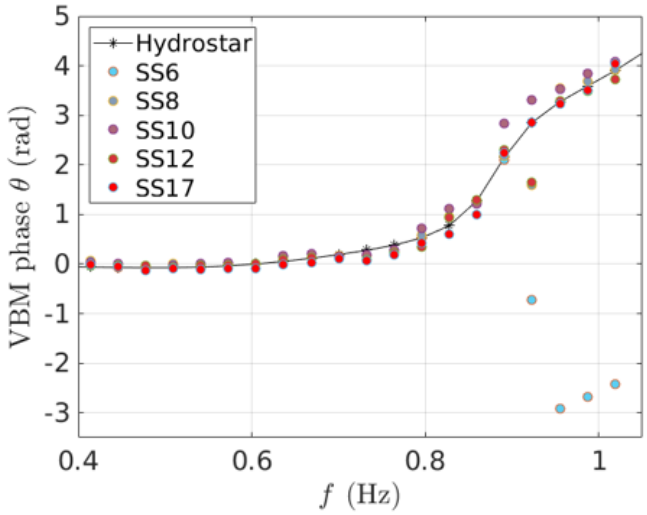

Figure A.6 – Nonlinear VBM RAO phase estimated for each sea state ranging from 0.4 Hz to 1.1 Hz

The inverse FFT of the VBM complex amplitude in $(A.5)$ provides symmetric hogging and symmetric sagging time series respectively. Therefore, to represent the asymmetry of the VBM response for a given sea state, a detailed procedure applied is presented following:

- First, nonlinear hogging and sagging RAO are separately applied, calculating symmetric hogging and sagging time signal respectively

- But, apply the same VBM phase ψ for the inverse FFT of both responses to synchronize them in time signal based on y=0). Then, symmetric hogging and sagging time signal based on y=0 with a slight asymmetry due to the wave nonlinearity is generated.

- To reproduce the asymmetric VBM response, we put 0 for all negative signals in hogging results (1) and 0 for all positive signals in sagging results (2).

- Finally, combine the two signals (1) and (2), making an asymmetric VBM signal. The result is directly compared to the VBM signal from the ATI.

A.3 Calculation results

In each Figure from A.7 to A.11, following three VBM responses are presented for comparison; i) measurement with ATI (black curve), ii) calculated result with nonlinear VBM RAO (red curve), and iii) calculated result with linear VBM RAO (blue curve). For a detailed comparison, the entire time-series data, as well as time-series data of a specific section are presented for each sea state.

As can be seen from the time series showing the overall response, the phase effect of each signal was expected to appear, but the difference due to the phase difference seems to be insignificant. When it comes to the VBM signal calculated with the linear RAO, it can be seen that the result using the linear TF shows a symmetrical response based on VBM$= 0$ Nm, that is, it does not reflect the characteristics of the actual response. While the nonlinear VBM RAO-based time signal shows a very good agreement with the actual response in terms of phase and magnitude in all sea states.

Although some notable differences in local peaks are observed, it can be said that the results are very satisfactory given that the applied nonlinear VBM RAO is the average one. For reference, when estimating the average nonlinear RAO of hogging in each sea state, the variability of each realization's RAO was not large. Due to that, looking at the zoomed-in time series in each Figure, it can be seen that the positive peak events in the red curve have values very comparable to those of the actual measurement by the ATI (black curve).

Conversely, in the case of sagging, the deviation of the nonlinear RAO estimated for each realization is relatively large. As a result, looking at the red curve to which the average nonlinear RAO is applied, it is observed that the larger the absolute size of the sagging event, the greater the difference with the ATI measurement result. This becomes more pronounced as the sea conditions become more severe. Taking SS17 in Figure A.11 as an example, in the three local time series graphs, it can be seen that large discrepancies with the ATI measurement (black curve) are mostly observed in relatively large responses.

This result is appeared to be reflected in the POE result of the VBM response calculated and measured for each sea state. When looking at the error near the tail part of

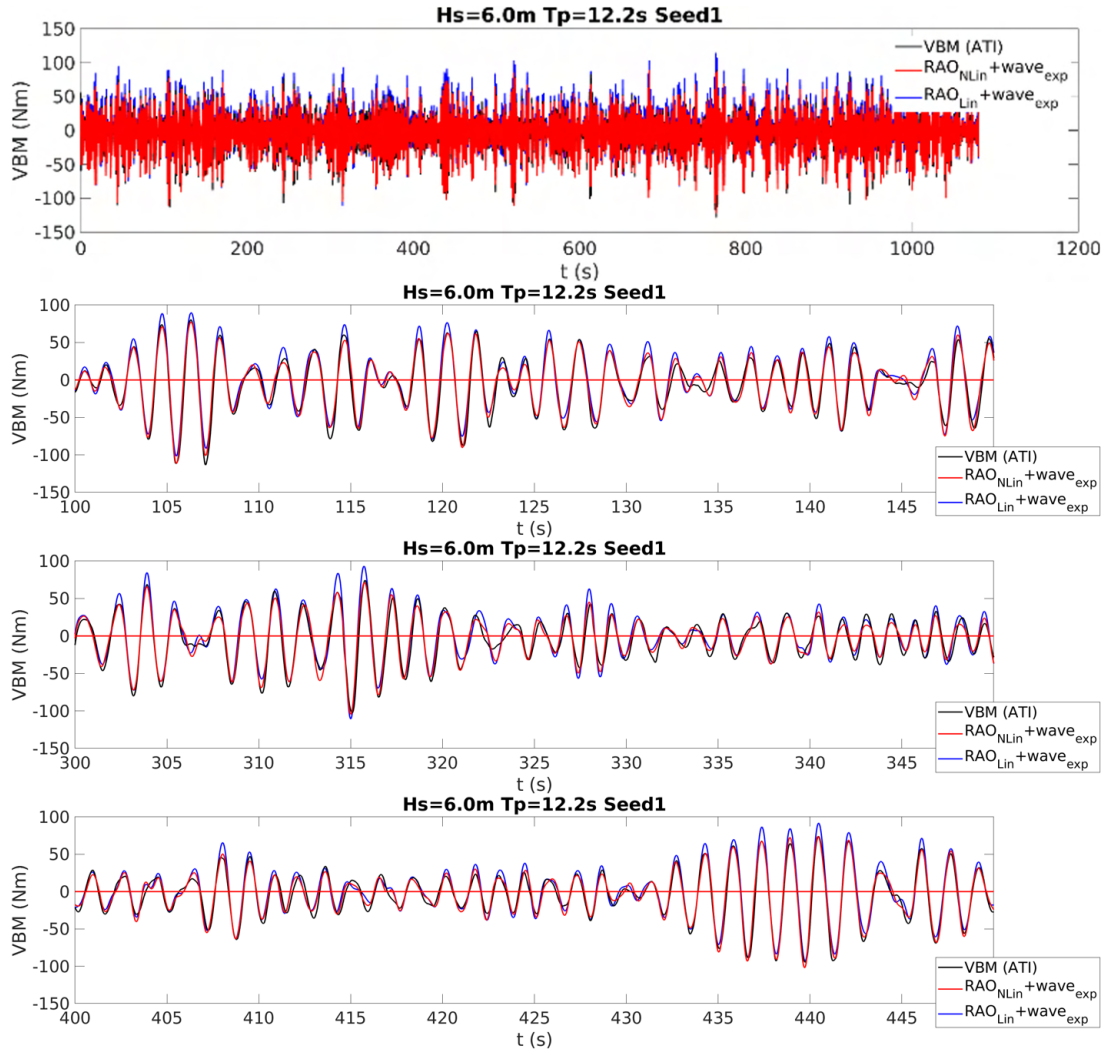

Figure A.7 – SS6, Comparison of VBM response; measurement (black), nonlinear RAO-based VBM (red), linear RAO-based VBM (blue)

the POE curve with respect to the ATI measurement in Figures A.12 and A.13, the discrepancy is clearly large in the sagging result compared to the hogging. The minimum and maximum errors are found to be around 6 % in SS6 and 13 % in SS10 respectively. One to note here is that, in the SS17 case in which 34 realizations were performed, the discrepancy is rather reduced by 8 %, showing that the number of realizations affects the RAO estimation. In the case of hogging, the actual measurement results show a very high degree of agreement with the error of up to 6 %, a minimum of 2 %, and an average of 3.6 %, and the shape of the POE curve can be said to be also almost identical.

In Figure A.14, the error at each POE level is presented with respect to the VBM POE of each sea state as the x-axis. As mentioned above, it can be seen that the difference from the actual measurement result becomes more pronounced as the POE

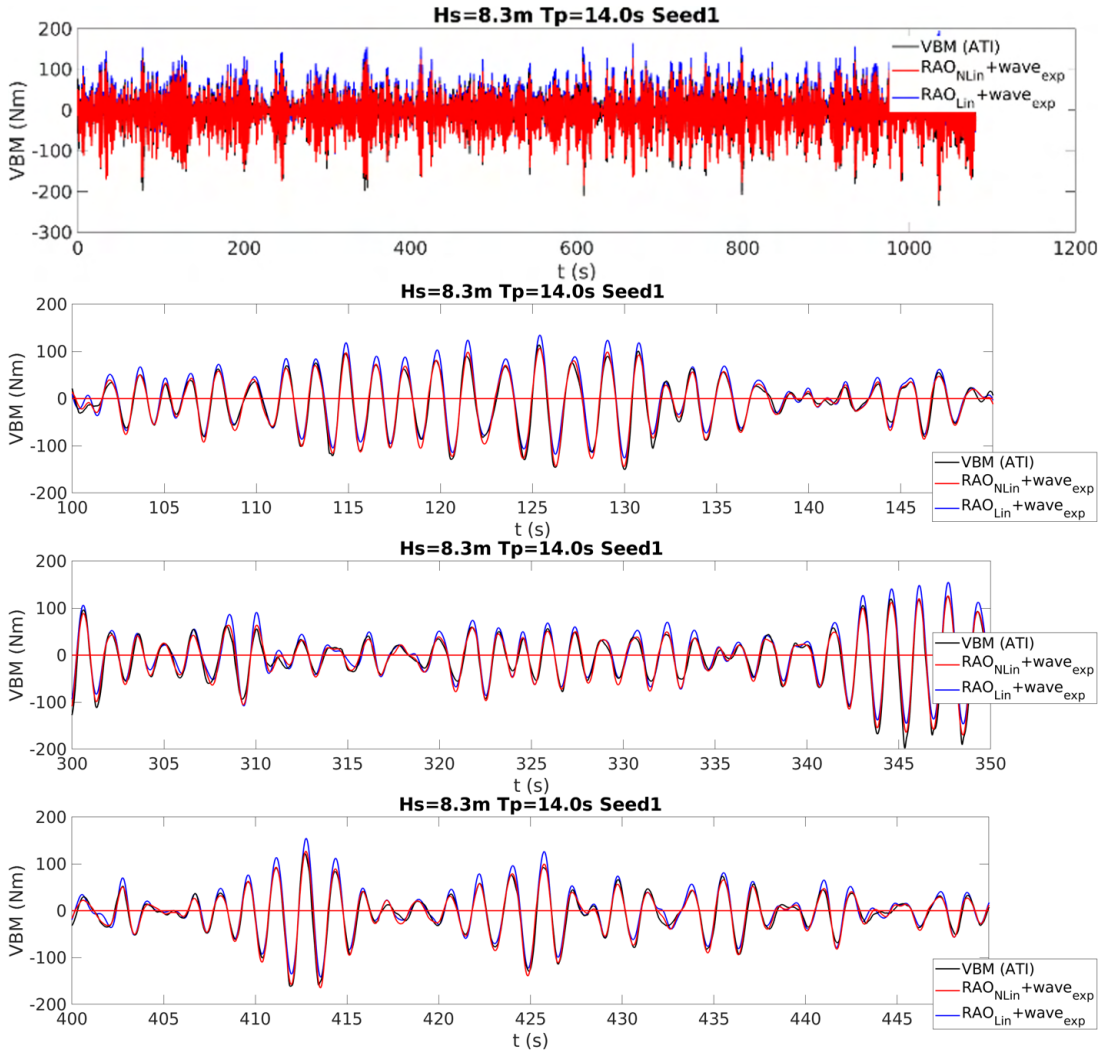

Figure A.8 – SS8, Comparison of VBM response; measurement (black), nonlinear RAO-based VBM (red), linear RAO-based VBM (blue)

level gets lower and as the sea state becomes more severe. The SS17 result from the 34 realizations shows good convergence with the actual measurement result. For the same wave input, sagging has a greater response variability than hogging, implying that it may contain relatively strong nonlinearity. Therefore, it is natural for the sagging response to have large dispersion for various wave scenarios.

To sum up, the asymmetric response characteristics of sagging and hogging were successfully calculated with the proposed technique, showing a good agreement with the direct measurement, and therefore, it can be said that the process for the nonlinear RAO estimation was found to be appropriate.

Given the comparison between the measurement and the calculation with the average RAO that tends to provide lower values in extreme events, one thing to mention is, from a conservative point of view, if the extreme value is of interest, it may be reason-

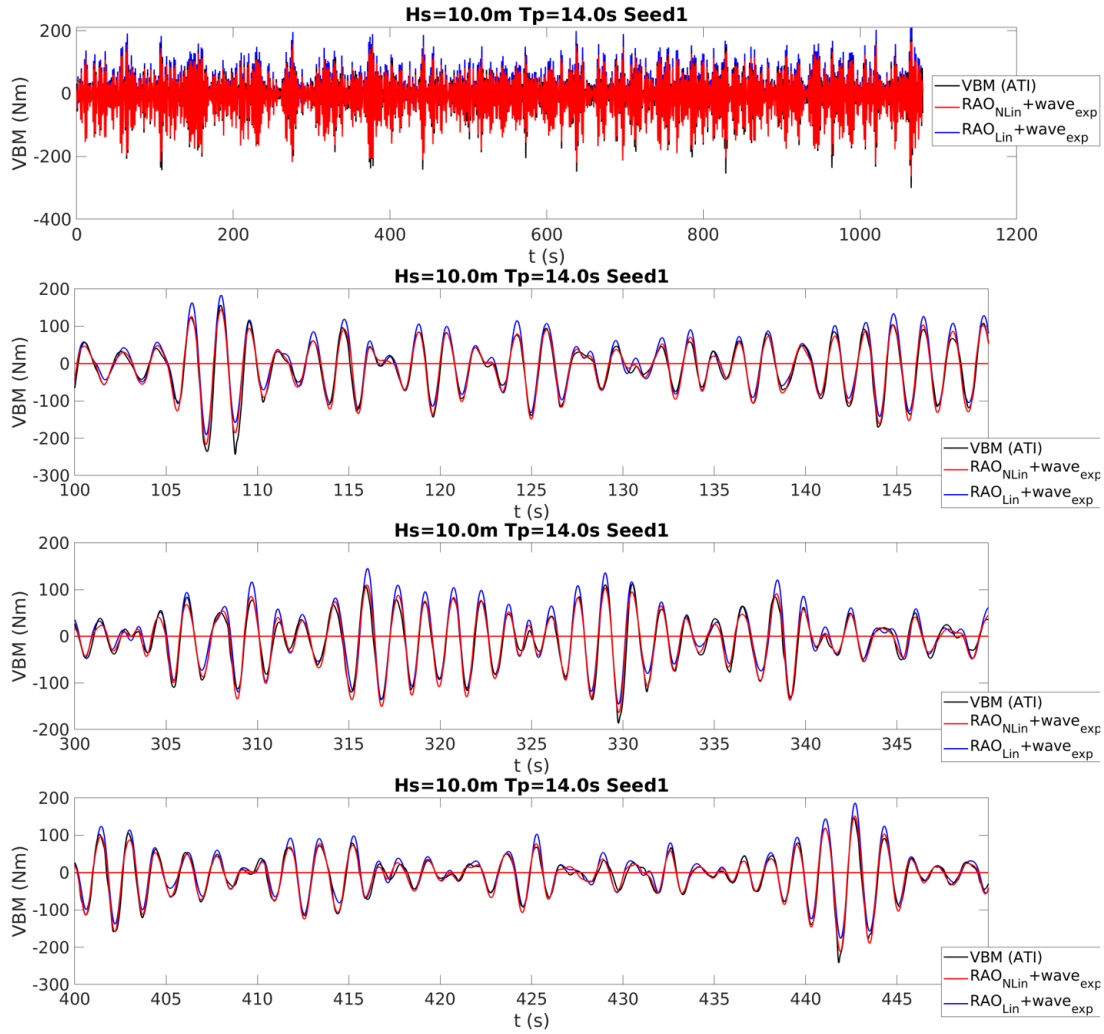

Figure A.9 – SS10, Comparison of VBM response; measurement (black), nonlinear RAO-based VBM (red), linear RAO-based VBM (blue)

able to consider the maximum RAO of a specific realization in the calculation of a VBM signal rather than the average RAO.

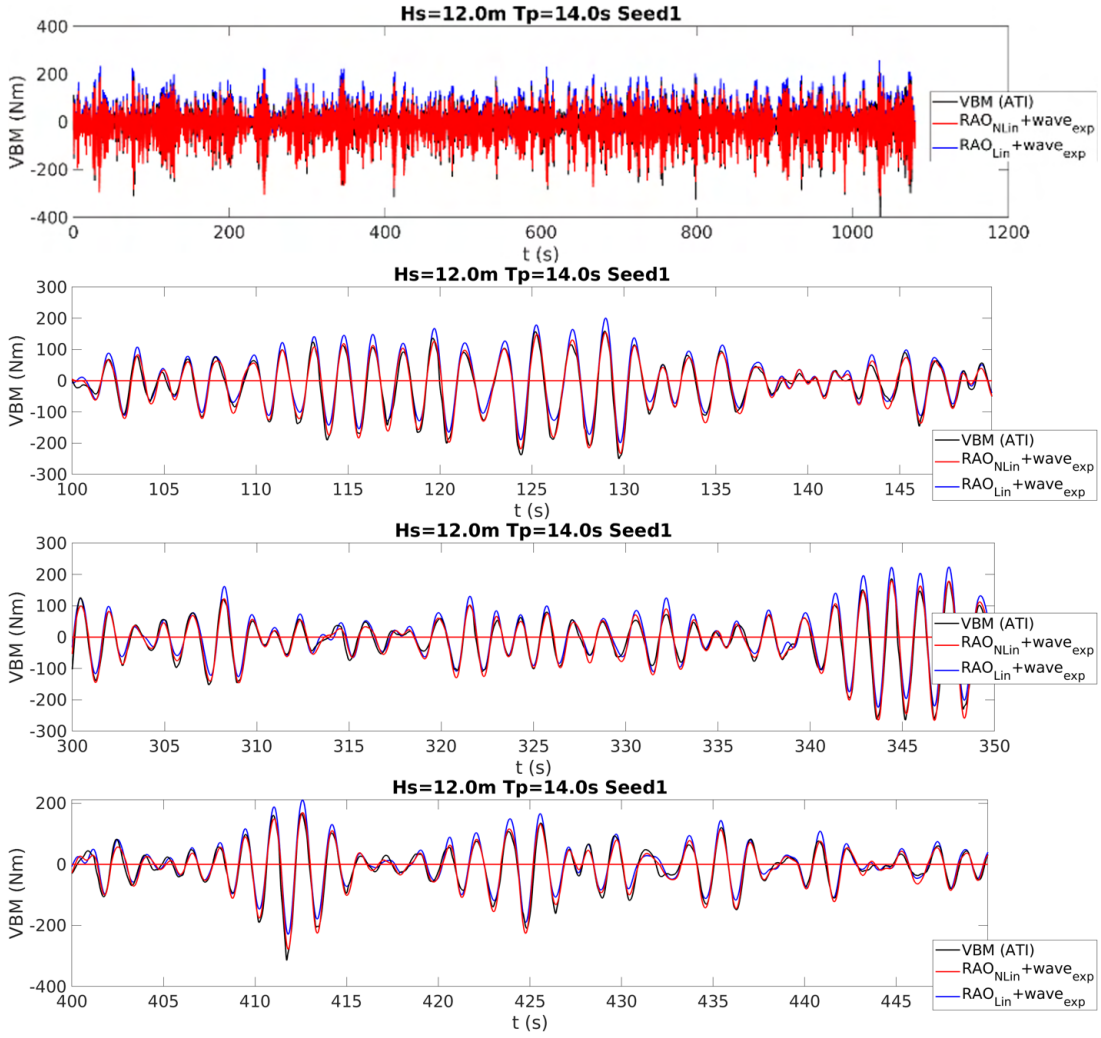

Figure A.10 – SS12, Comparison of VBM response; measurement (black), nonlinear RAO-based VBM (red), linear RAO-based VBM (blue)

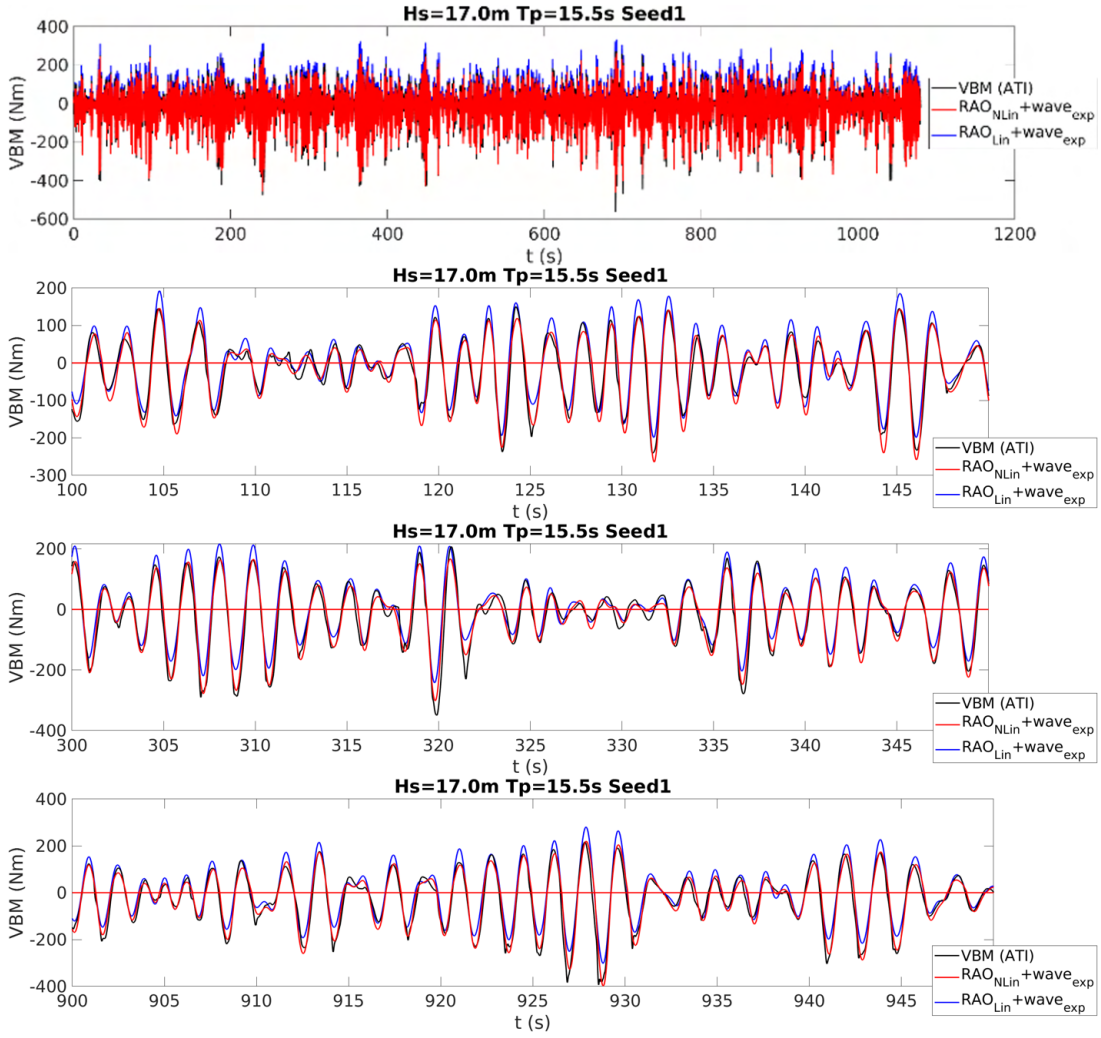

Figure A.11 – SS17, Comparison of VBM response; measurement (black), nonlinear RAO-based VBM (red), linear RAO-based VBM (blue)

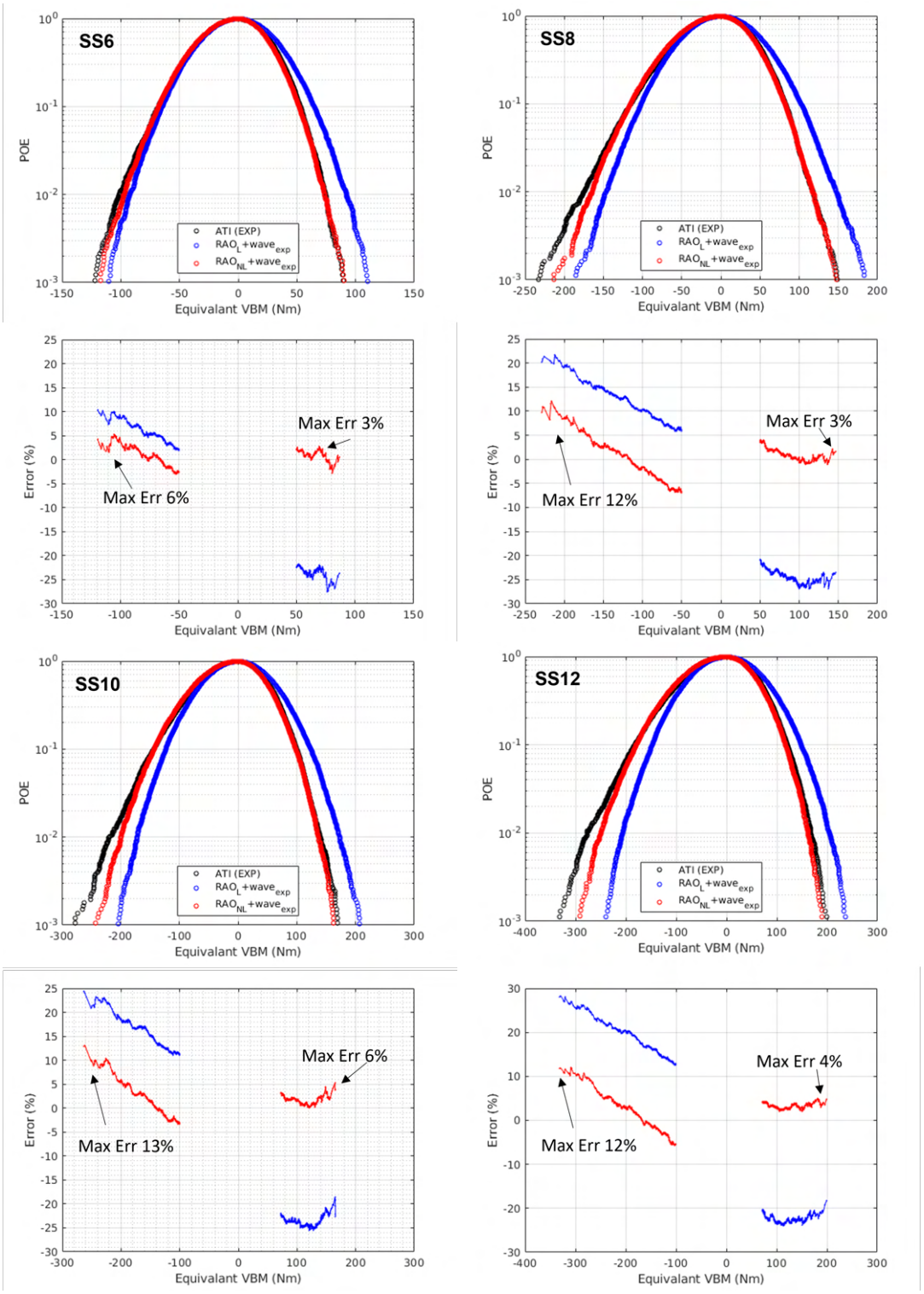

Figure A.12 – SS6, SS8, and SS10. VBM POE curve comparion; measurement (black), nonlinear RAO-based VBM (red), linear RAO-based VBM (blue)

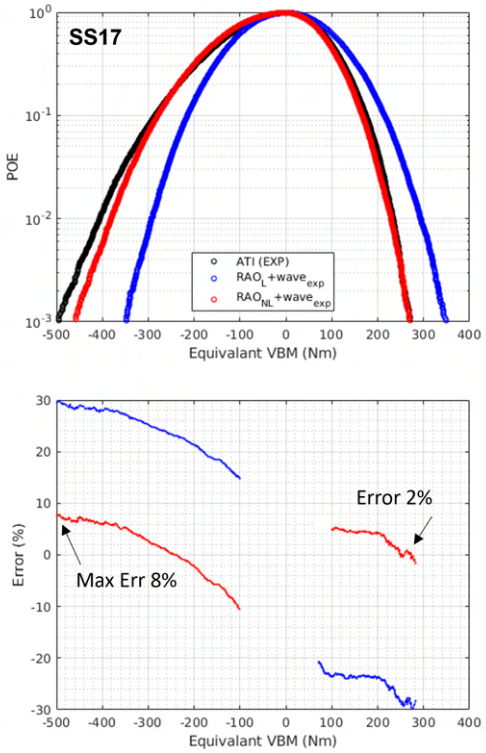

Figure A.13 – SS12 and SS17. VBM POE curve comparion; measurement (black), non-linear RAO-based VBM (red), linear RAO-based VBM (blue)

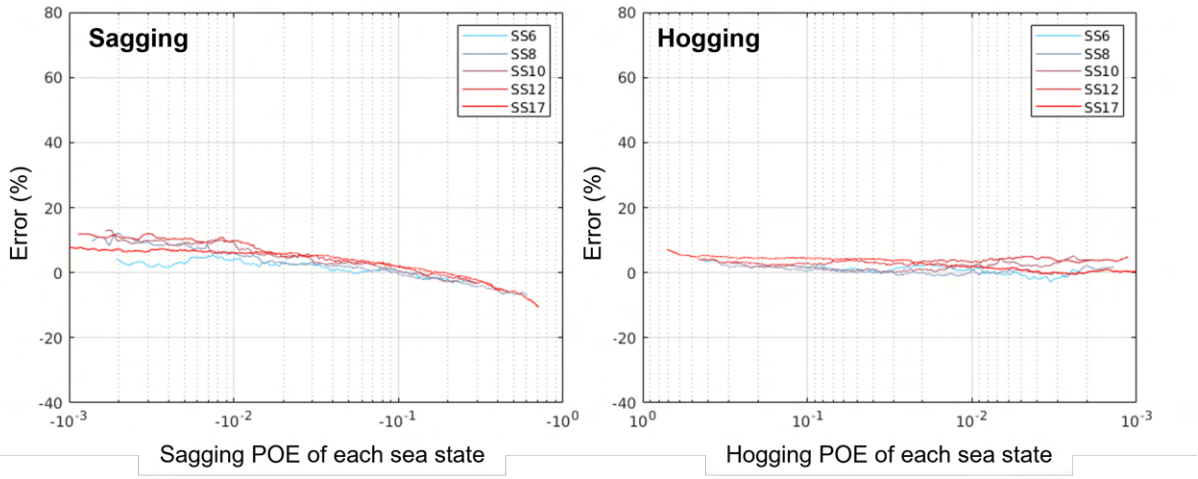

Figure A.14 – VBM POE curve error trend

Appendix B

Additional graphs of the geometrical similarity review for SS8, SS10, and SS12

Sea state $H_s = 8.3m$, $T_p = 14s$, $\gamma = 1.5$ (SS8) results

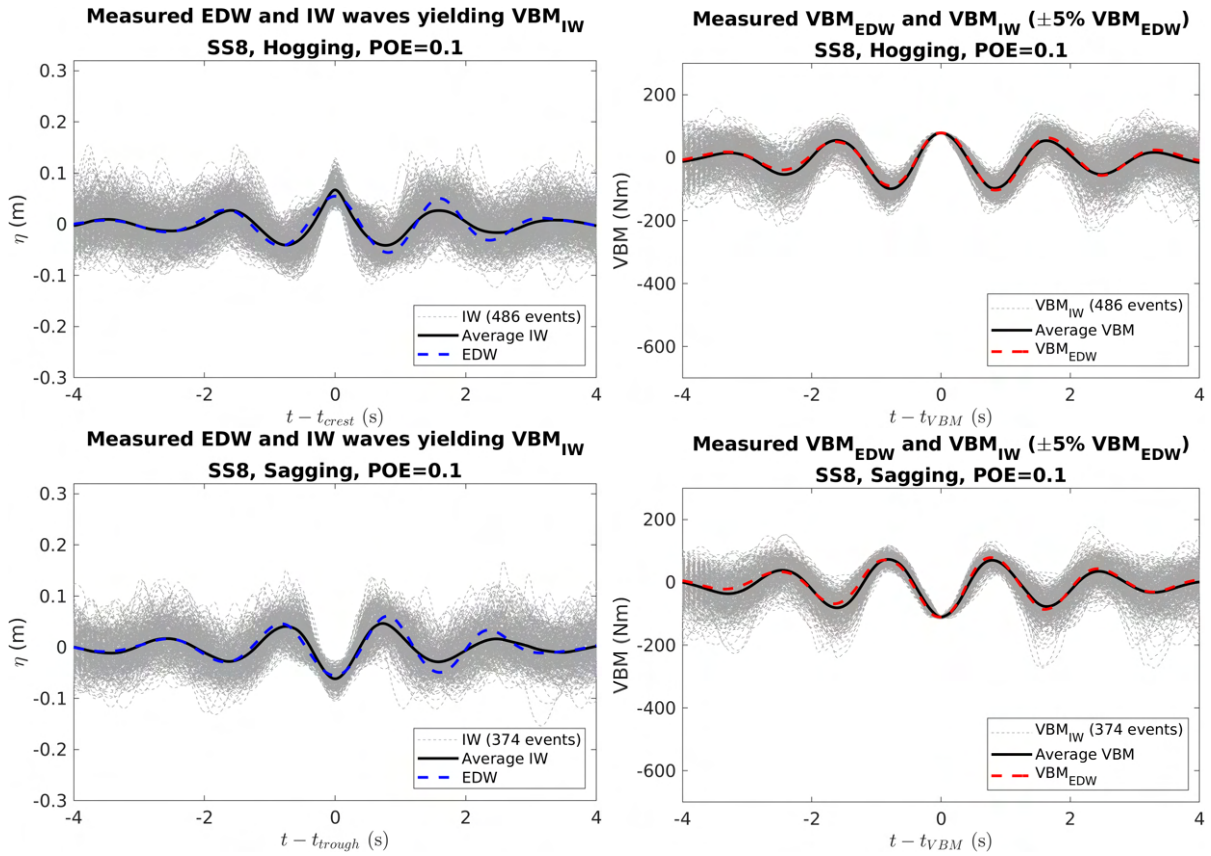

Figure B.1 – SS8, target POE 0.1, EDW and extracted irregular waves (right side), and corresponding hogging and sagging responses (left side) (model scale)

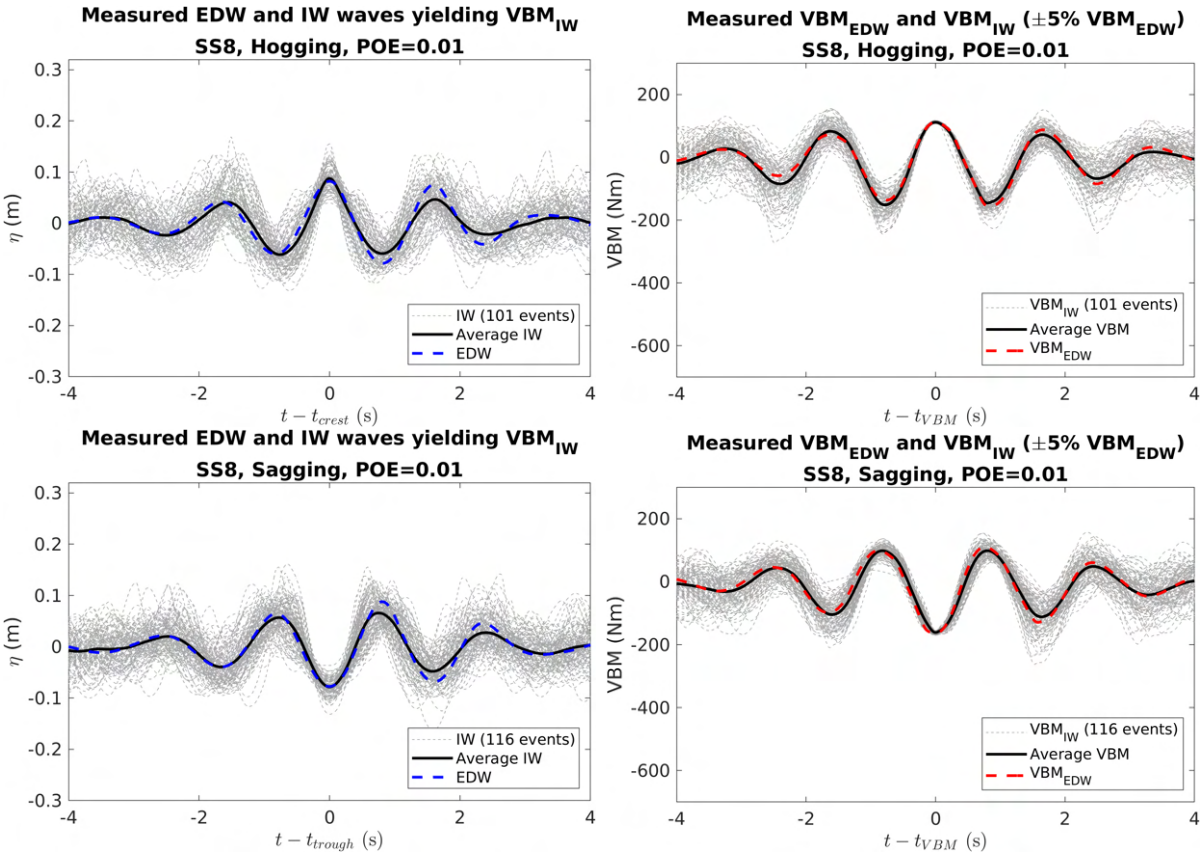

Figure B.2 – SS8, target POE 0.01, EDW and extracted irregular waves (right side), and corresponding hogging and sagging responses (left side) (model scale)

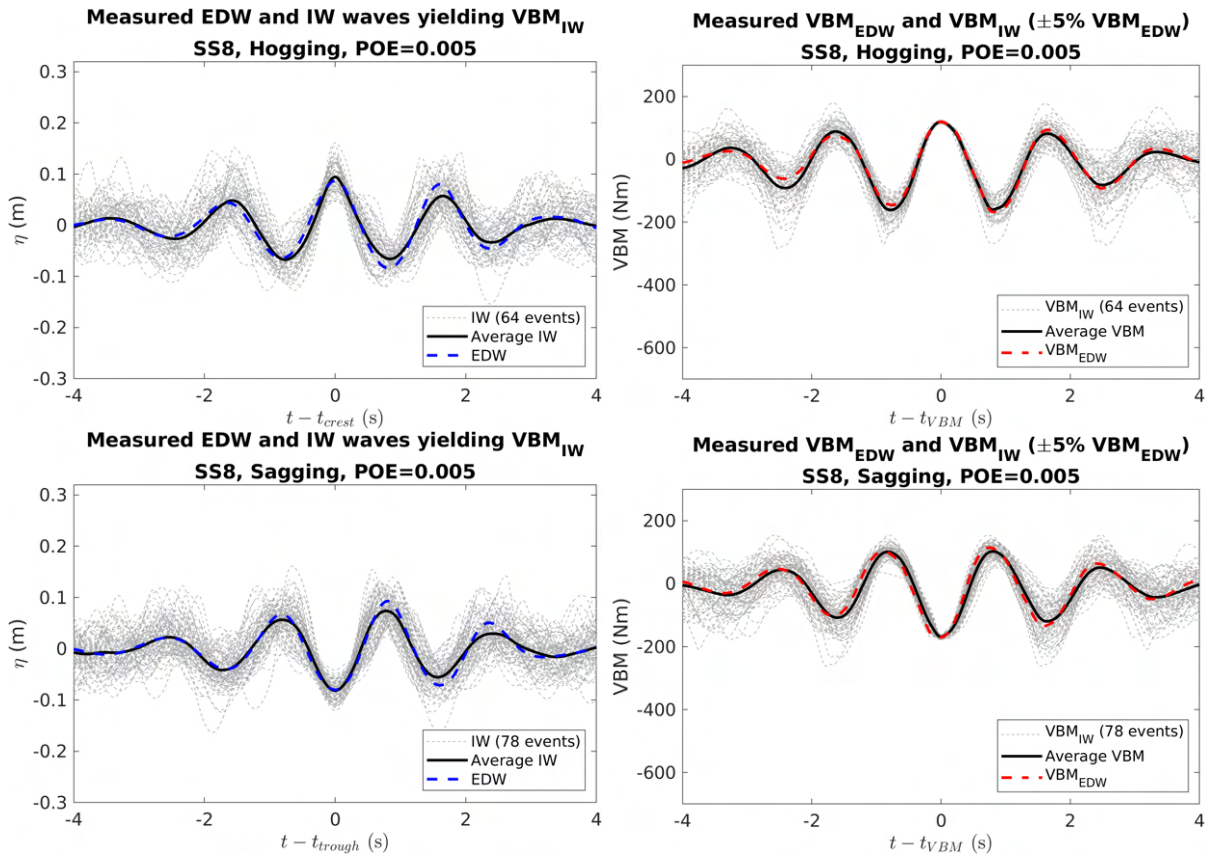

Figure B.3 – SS8, target POE 0.005, EDW and extracted irregular waves (right side), and corresponding hogging and sagging responses (left side) (model scale)

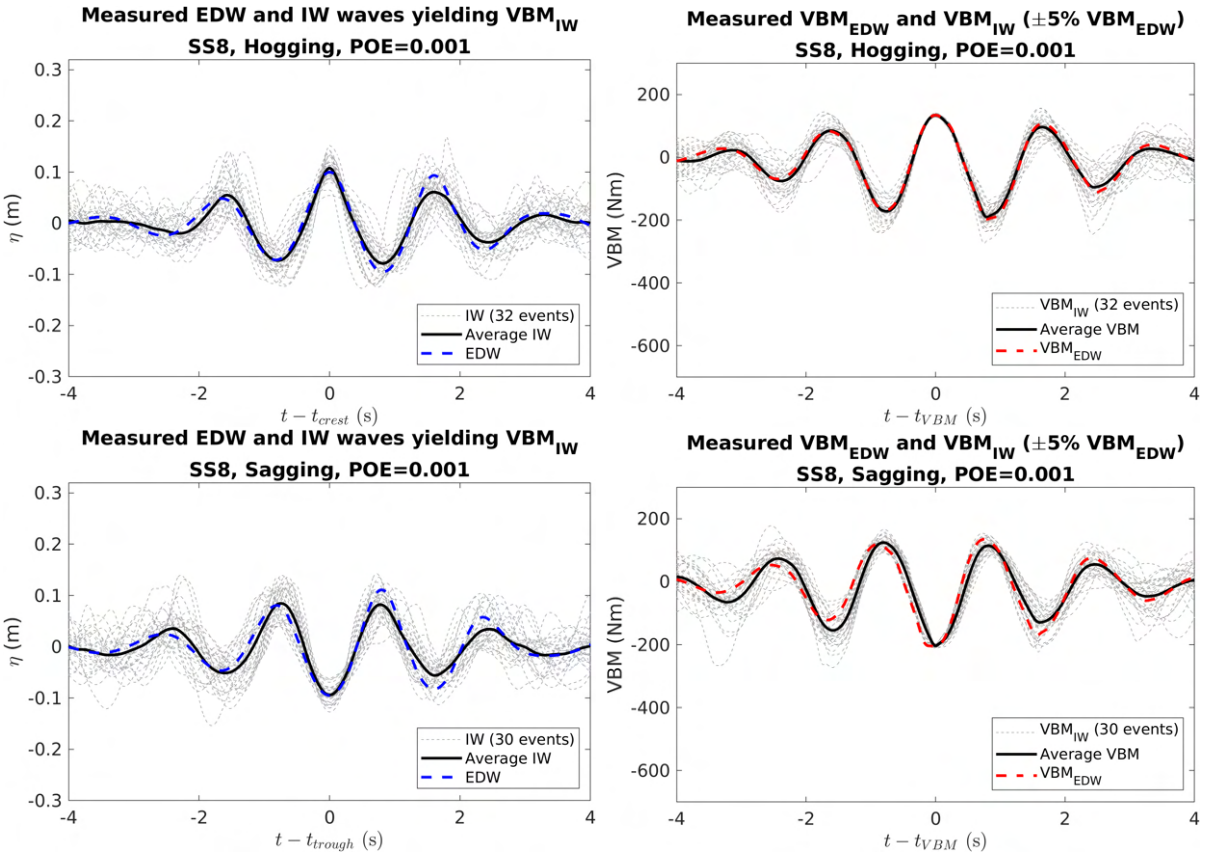

Figure B.4 – SS8, target POE 0.001, EDW and extracted irregular waves (right side), and corresponding hogging and sagging responses (left side) (model scale)

Sea state $H_s = 10m$, $T_p = 14s$, $\gamma = 1.5$ (SS10) results

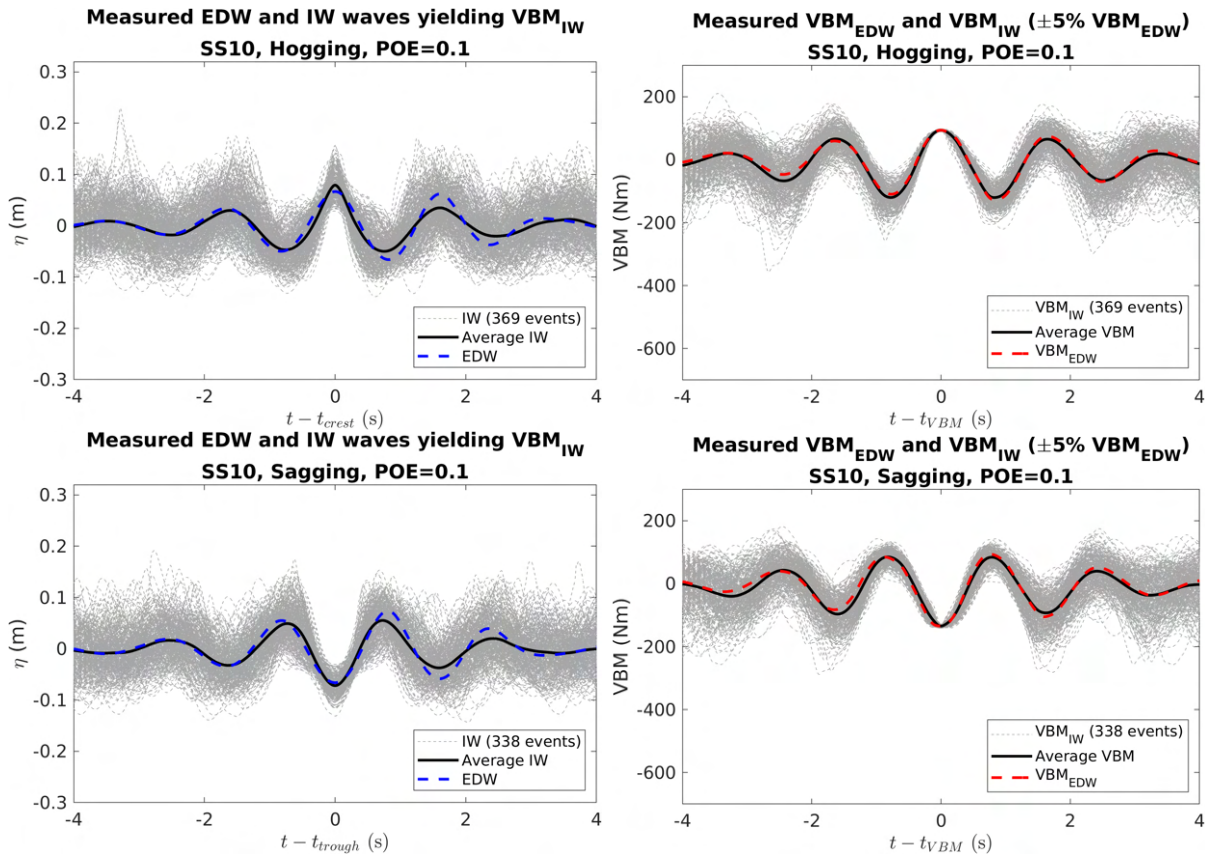

Figure B.5 – SS10, target POE 0.1, EDW and extracted irregular waves (right side), and corresponding hogging and sagging responses (left side) (model scale)

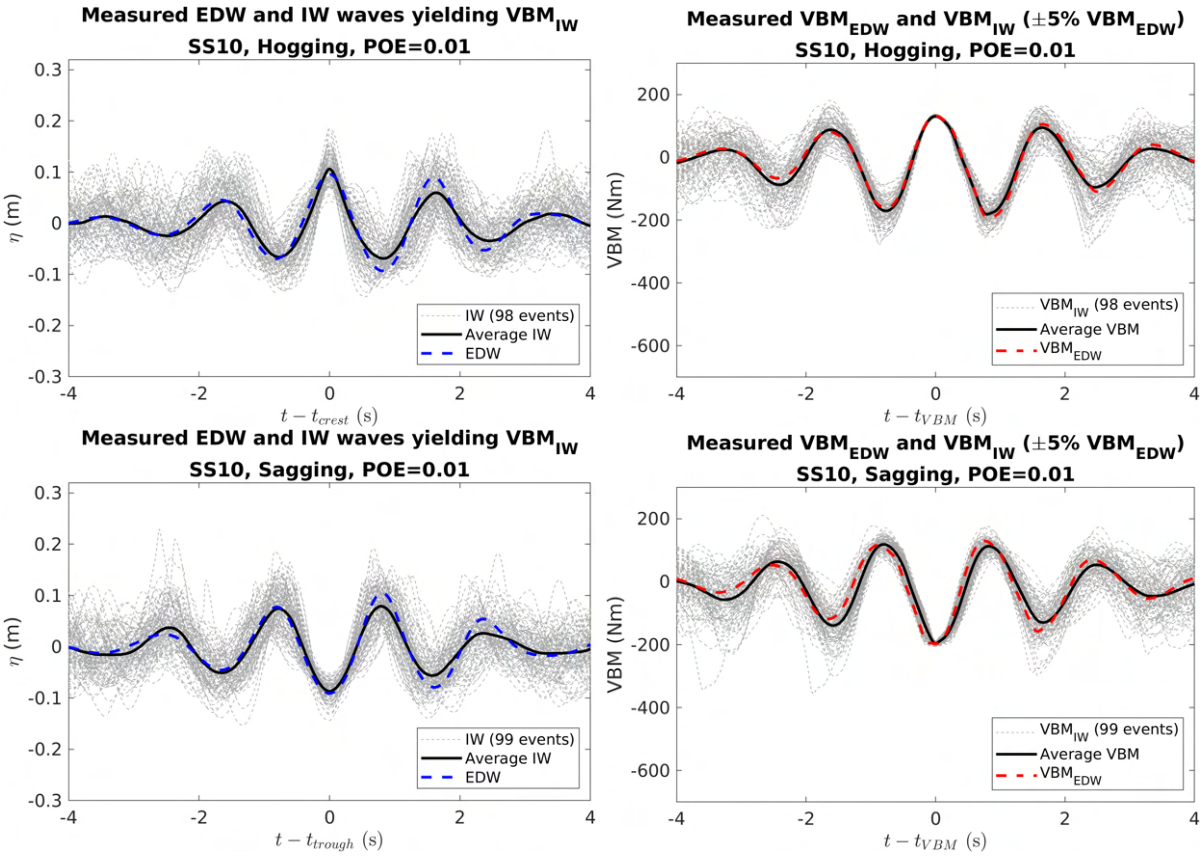

Figure B.6 – SS10, target POE 0.01, EDW and extracted irregular waves (right side), and corresponding hogging and sagging responses (left side) (model scale)

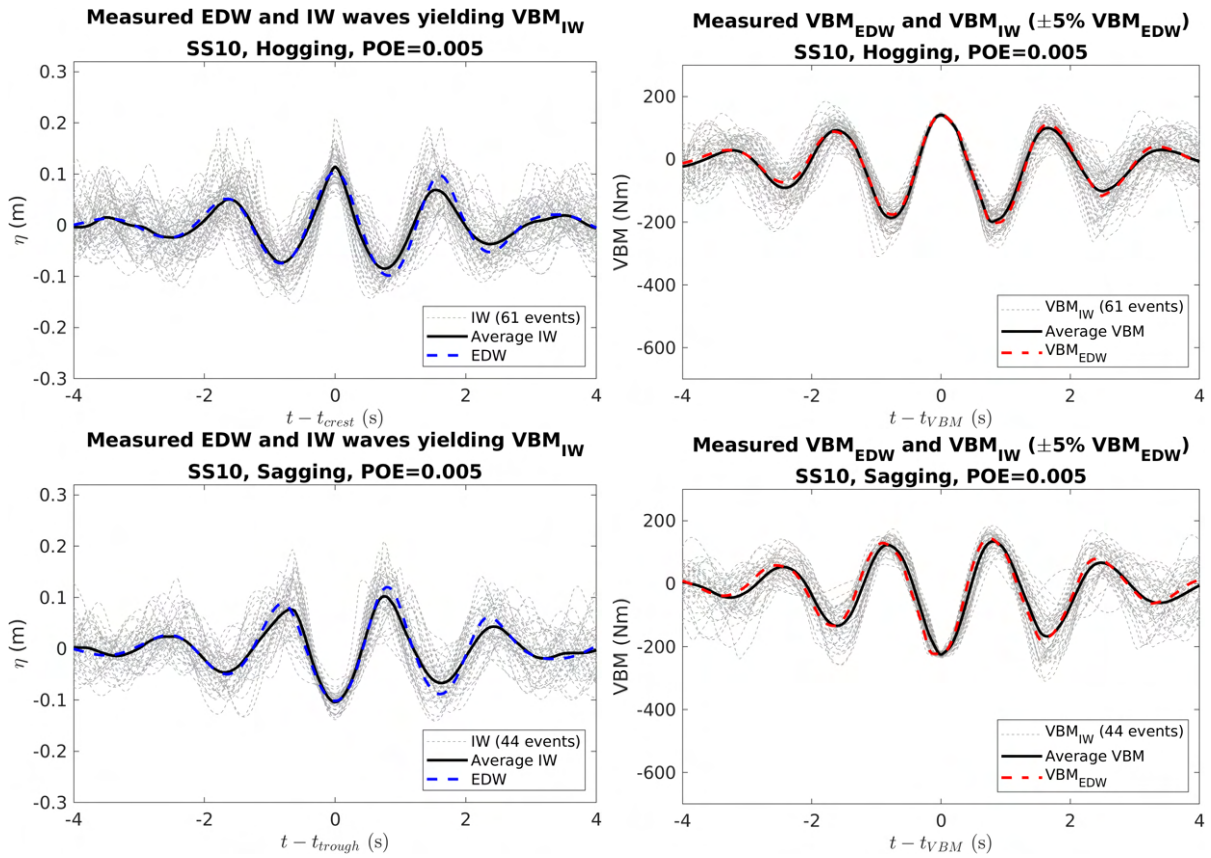

Figure B.7 – SS10, target POE 0.005, EDW and extracted irregular waves (right side), and corresponding hogging and sagging responses (left side) (model scale)

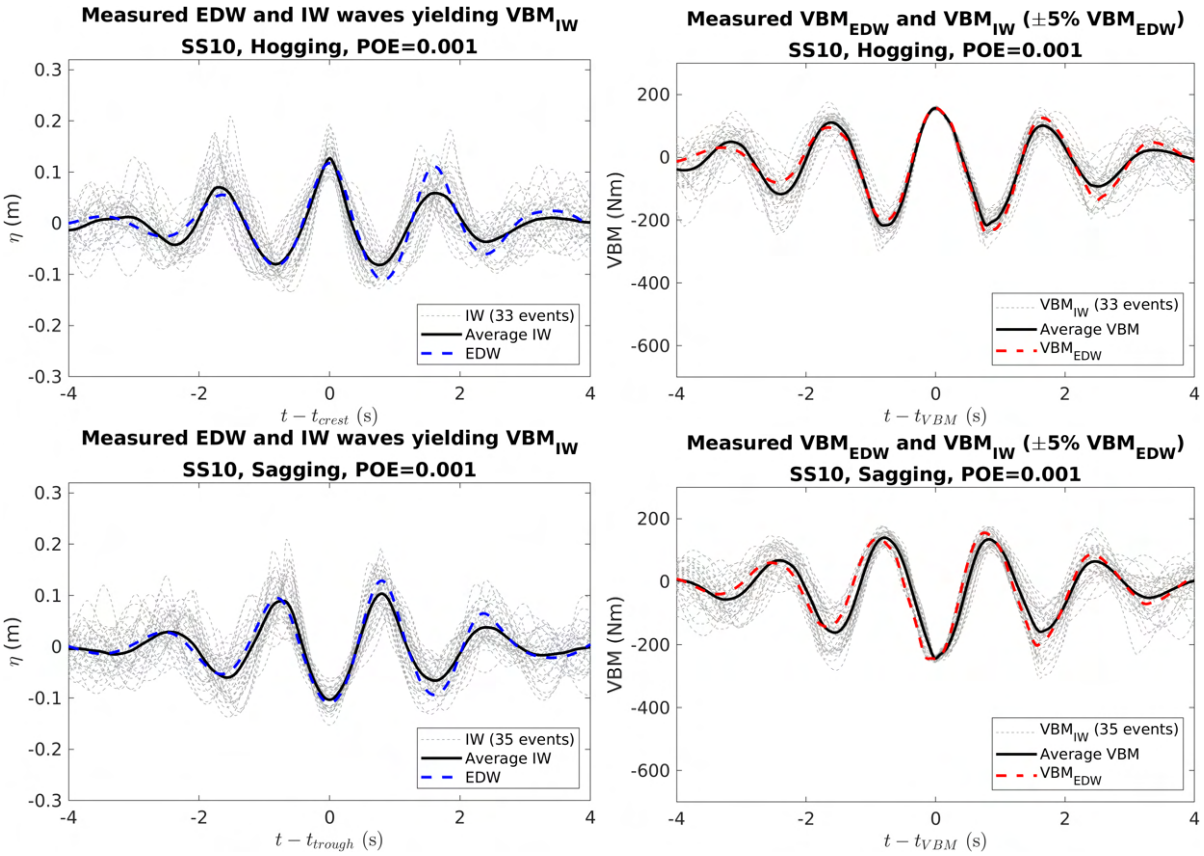

Figure B.8 – SS10, target POE 0.001, EDW and extracted irregular waves (right side), and corresponding hogging and sagging responses (left side) (model scale)

Sea state $H_s = 12m$, $T_p = 14s$, $\gamma = 1.5$ (SS12) results

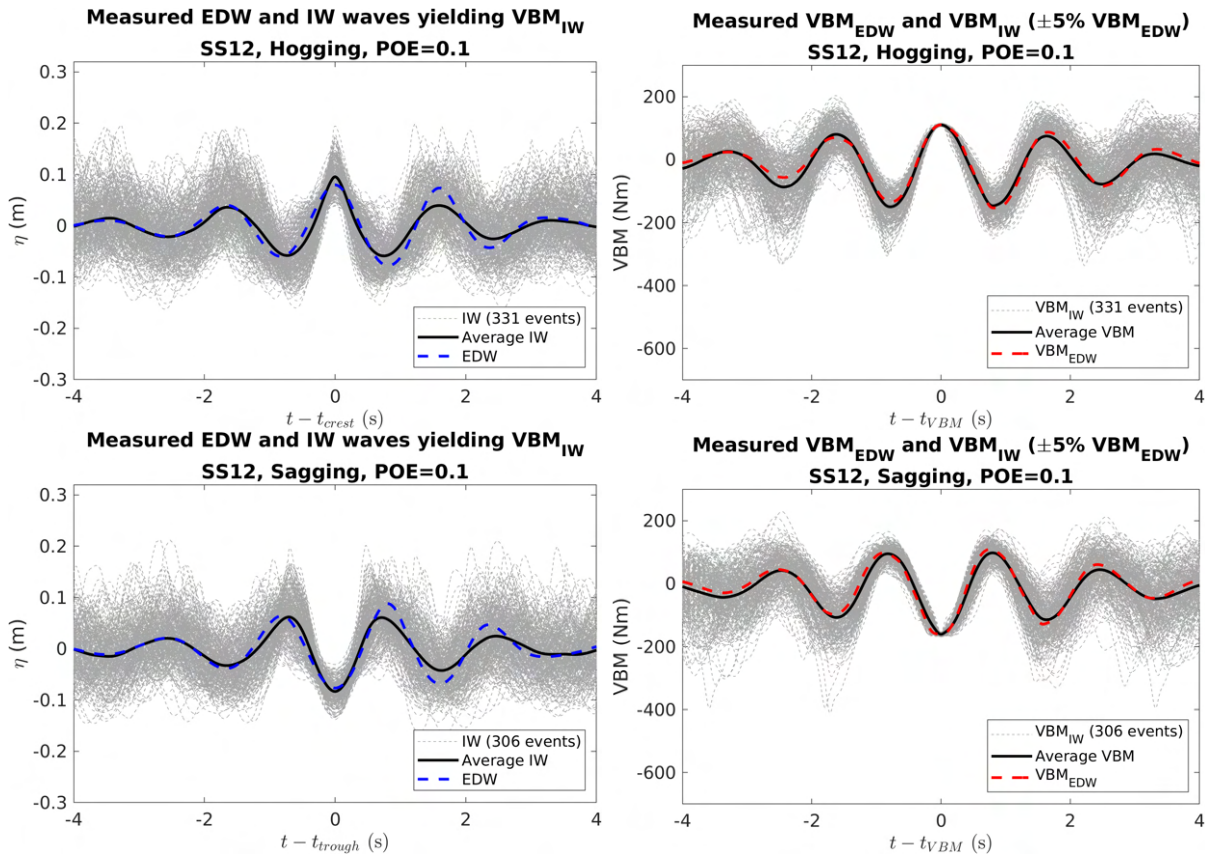

Figure B.9 – SS12, target POE 0.1, EDW and extracted irregular waves (right side), and corresponding hogging and sagging responses (left side) (model scale)

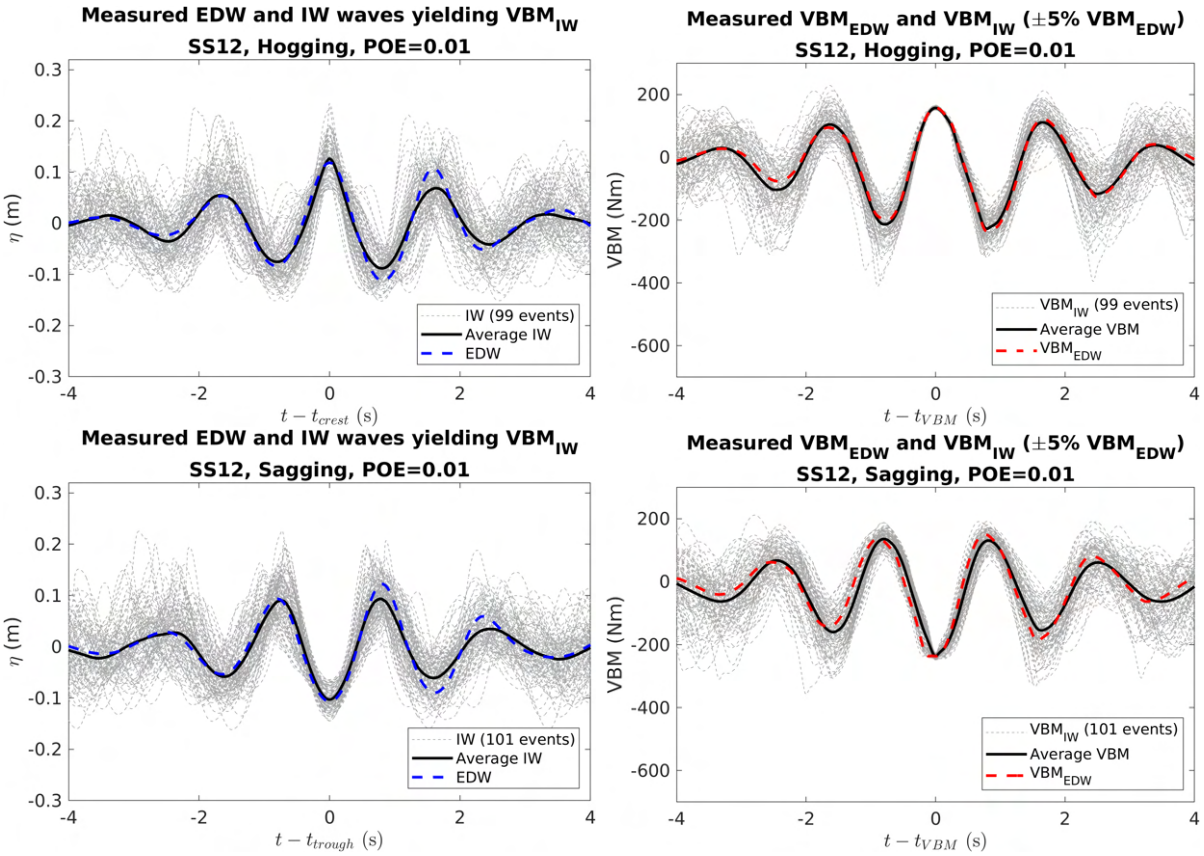

Figure B.10 – SS12, target POE 0.01, EDW and extracted irregular waves (right side), and corresponding hogging and sagging responses (left side) (model scale)

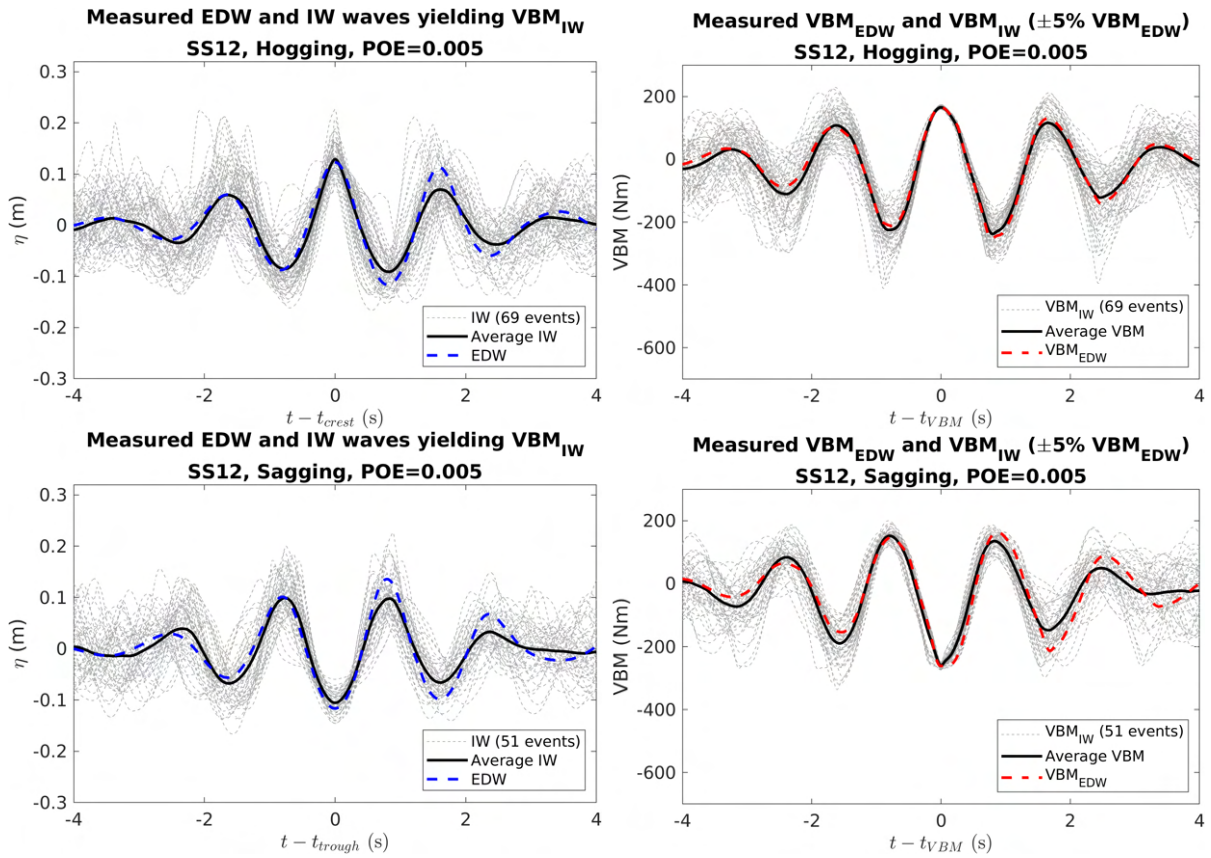

Figure B.11 – SS12, target POE 0.005, EDW and extracted irregular waves (right side), and corresponding hogging and sagging responses (left side) (model scale)

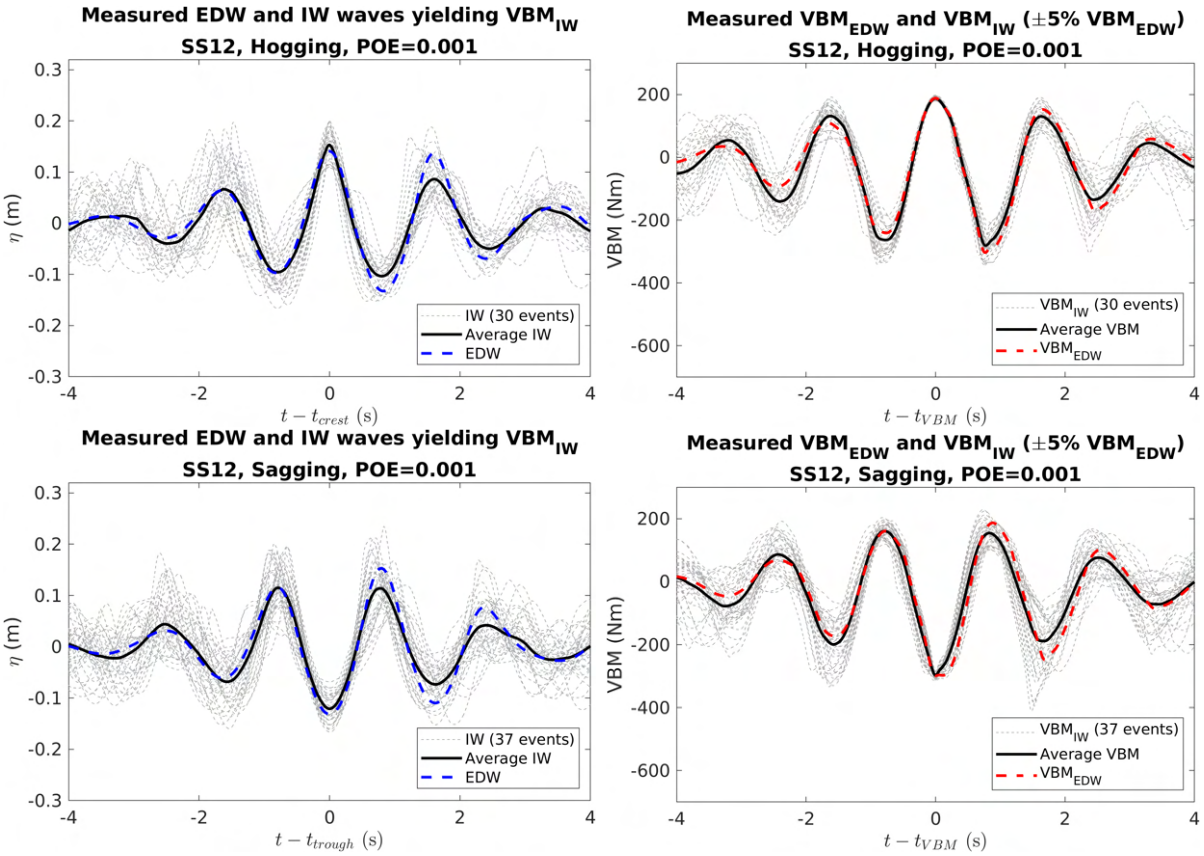

Figure B.12 – SS12, target POE 0.001, EDW and extracted irregular waves (right side), and corresponding hogging and sagging responses (left side) (model scale)

Appendix C

Linear seakeeping analysis

C.1 Rigid body kinetics

This section thus covers the analysis of linear responses of a rigid ship applying the potential flow theory. It is necessary to understand and solve the boundary value problems for the velocity potential, and when the boundary condition is properly linearized, it becomes possible to define and solve the problems in the frequency domain.

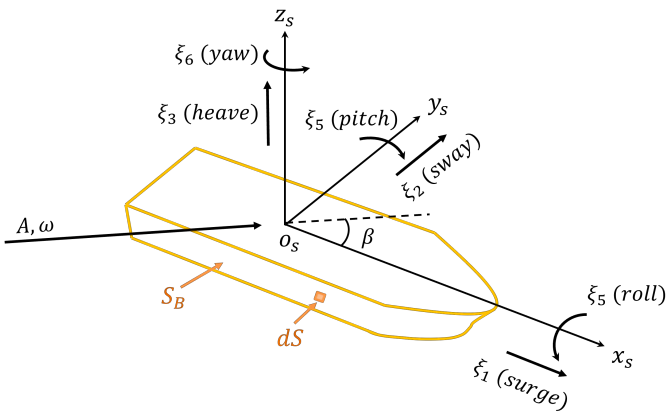

Figure C.1 – Definition of 6 degrees of freedom perturbations in a seakeeping frame $\{s\}$

To estimate the motions and loads of a vessel generated by a given specific wave, it is necessary to consider not only the undisturbed incident wave but also velocity potentials representing the mechanism of the interaction between the given wave and a vessel as one of the total velocity potentials. The linearization of the problem allows the decomposition of the total velocity potential [68]:

$$\phi(\mathbf{x}, t) = Re\left[\left(A(\phi_I(\mathbf{x}) + \phi_D(\mathbf{x})) + \sum_{j=1}^{6} \xi_j \phi_j(\mathbf{x})\right) e^{i\omega t}\right] \tag{C.1}$$

where $\mathbf{x} = (x, y, z)$, ϕ_I and ϕ_D are the unit-amplitude incident and diffraction velocity potential respectively, and ξ_j and ϕ_j are the complex rigid-body motions and unit-amplitude radiation potentials for six degrees of freedom. The ϕ_I and ϕ_D are considered to be independent of the floating body motion. A is a wave amplitude which is a first-

order quantity. For the zero speed case, the solutions can be obtained with the velocity potential satisfying the following boundary conditions [66]:

$$\begin{cases} \nabla^2\phi = 0 & \text{in the fluid} \\ -\omega^2\phi + g\dfrac{\partial\phi}{\partial z} = 0 & \text{on the free surface} \\ \dfrac{\partial\phi}{\partial n} = \mathbf{V}_n & \text{on } S_b \\ \dfrac{\partial\phi}{\partial z} = 0 & \text{at z=-h} \\ \lim\limits_{R_b\to\infty}[\sqrt{\dfrac{\omega^2}{g}R_b}(\dfrac{\partial\phi}{\partial R_b} - i\dfrac{\omega^2}{g}\phi)] = 0 & \text{For disturbed waves} \end{cases} \tag{C.2}$$

where R_b is radius around the oscillating body and $\mathbf{V}_n$ is the normal component which is dependent on the type of velocity potential considered. The incident potential has the following relation with diffraction potential:

$$\begin{aligned} \phi_I(\mathbf{x}) &= -\frac{g}{\omega}e^{-ik(x\cos\beta - y\sin\beta)e^{kz}} \\ \frac{\partial\phi_D}{\partial n} &= -\frac{\partial\phi_I}{\partial n} \qquad \text{on } S_B \end{aligned} \tag{C.3}$$

where β is wave heading angle corresponding to the propagation direction with respect to the positive direction of x-axis as shown in Figure C.1.

$$\frac{\partial\phi_D}{\partial n} = i\omega n_k \qquad \text{(k=1, ..., 6)} \tag{C.4}$$

where ωn_k corresponds to the normal velocity of the wetted surface S_B to the unit wave amplitude.

For an unrestrained rigid ship oscillating in waves, its kinetics can be expressed in a vectorial setting with an application of Newton's second law:

$$\mathbf{m}\ddot{\xi} = \sum \mathbf{F} \tag{C.5}$$

where $\ddot{\xi}$ is the second time derivative of the external forces-induced 6-DOF perturbations, $\xi = [\xi_1, \xi_2, \xi_3, \xi_4, \xi_5, \xi_6]$ corresponding to motions with respect to an equilibrium state of a ship. Figure C.1 shows a coordinate used for the seakeeping analysis so called seakeeping frame $\{s\} = (x_s, y_s, z_s)$. As it is fixed to the equilibrium state, not fixed to the body, the frame has a fixed orientation with the inertial reference frame. For the input process where the first-order component is expected to be dominant, as the

second-order effects obtainable by considering the body-fixed frame are regarded as negligible, the seakeeping frame can be applied. Considering the wave is the predominant force acting on the ship, the force vector will consist of the following components:

$$\mathbf{m}\ddot{\xi} = \mathbf{F}_{Res} + \mathbf{F}_{F.K} + \mathbf{F}_D + \mathbf{F}_R \tag{C.6}$$

where $\mathbf{F}_{F.K}$ denotes the force by incident wave called Froude-Krylov force, and $\mathbf{F}_D$ and $\mathbf{F}_R$ stand for the forces by diffracted and radiated waves respectively (disturbed waves). Restoring force $\mathbf{F}_{Res}$ of a freely floating body consists of a hydrostatic force and gravity of a ship with respect to a mean water surface:

$$\mathbf{F}_{Res} = \mathbf{F}_{Gravity} + \mathbf{F}_{Static} \approx -\mathbf{K}\xi \tag{C.7}$$

Expressed in a matrix form, it is,

$$F_{Res_k} = -K_{kj}\xi_j \tag{C.8}$$

which introduces the restoring coefficient K_{kj}. The subscript stands for the k-direction resulting component caused by the j-direction motion. Given that surge, sway and yaw have no resilience for x-z symmetry ship, the non-zero components can be derived as follows:

$$\begin{aligned}
K_{33} =& \rho g A_{WP} \\
K_{35} =& K_{53} = -\rho g \iint_{A_{WP}} x dA \\
K_{44} =& \rho g V(z_b - z_g) + \rho g \iint_{A_{WP}} y^2 dA \\
K_{55} =& \rho g V(z_b - z_g) + \rho g \iint_{A_{WP}} x^2 dA
\end{aligned} \tag{C.9}$$

where $r_g = (x_g, y_g, z_g)$ and $r_b = (x_b, y_b, z_b)$ denote the position of center of gravity and center of buoyancy of a ship, and A_{WP} is water plane area. In the linear analysis, as the assumption that the motion of a ship is small is made, the restoring force is estimated as a term proportional to the motion with a constant restoring coefficient.

The wave excitation force of k^{th} degree of freedom corresponding to the sum of the Froude-Krylov and diffraction force is expressed as follows with the Bernoulli's equation:

$$\begin{aligned}
\mathbf{F_{F.K}} + \mathbf{F_D} &= \iint_{S_B} (\mathbf{P}_{F.K} + \mathbf{P}_D)\mathbf{n} dS \\
F_{F.K_k} + F_{D_k} &= -A \iint_{S_B} (\rho \frac{\partial \phi_I}{\partial t} + \rho \frac{\partial \phi_D}{\partial t}) n_k dS \\
&= -A\rho \iint_{S_B} i\omega(\phi_I + \phi_D) e^{i\omega t} n_k dS
\end{aligned} \tag{C.10}$$

Given the diffraction and radiation potentials follows Green's theorem and the radiation boundary condition in (C.4), Eq. (C.10) can be written as:

$$F_{F.K_k} + F_{D_k} = -A\rho e^{i\omega t} \iint_{S_B} (\phi_I \frac{\partial \phi_k}{\partial n} + \phi_k \frac{\partial \phi_D}{\partial n}) dS \tag{C.11}$$

where ϕ_k denotes k^{th} radiation potential. Finally, applying the body boundary condition for the diffraction potential (C.3) to (C.11) leads to Haskind relation [36] evaluating the external force without the consideration of diffraction potential:

$$F_{F.K_k} + F_{D_k} = -A\rho e^{i\omega t} \iint_{S_B} (\phi_I \frac{\partial \phi_k}{\partial n} - \phi_k \frac{\partial \phi_I}{\partial n}) dS \tag{C.12}$$

In the case of the radiation force F_R, it is also calculated in the same Bernoulli pressure equation but with ϕ_R:

$$\begin{aligned}
\phi_R(\mathbf{x}) &= \sum_{j=1}^{6} \xi_j \phi_j(\mathbf{x}) \\
F_R &= \iint_{S_B} -\rho \frac{\partial \phi_R}{\partial t} \mathbf{n} e^{i\omega t} dS \\
F_{R_k} &= -\rho \iint_{S_B} \left(\sum_{j=1}^{6} \xi_j \phi_j \right) e^{i\omega t} i\omega n_k dS \qquad \text{(k=1, ..., 6)} \\
&= -\rho \sum_{j=1}^{6} \xi_j \iint_{S_B} \phi_j e^{i\omega t} \frac{\partial \phi_k}{\partial n} dS \qquad \left(\text{where } \frac{\partial \phi_k}{\partial n} = i\omega n_k\right) \\
&= \sum_{j=1}^{6} \xi_j e^{i\omega t} f_{kj} \qquad \left(\text{where } f_{kj} = -\rho \iint_{S_B} \phi_j \frac{\partial \phi_k}{\partial n} dS\right)
\end{aligned} \tag{C.13}$$

The force f_{kj} is complex term in k^{th} degree of freedom induced by a motion in j direction. Considering that it is a result of a sinusoidal wave, decomposition of the radiation force can be carried out, showing the following relation [68]:

$$f_{kj} = \omega^2 a_{kj} - i\omega b_{kj} \tag{C.14}$$

thus,

$$\begin{aligned}
F_{R_k} &= \sum_{j=1}^{6} (\omega^2 a_{kj} - i\omega b_{kj}) \xi_j e^{i\omega t} \qquad \text{(k=1, ..., 6)} \\
&= \sum_{j=1}^{6} (-\ddot{\xi}_j a_{kj} - \dot{\xi}_j b_{kj})
\end{aligned} \tag{C.15}$$

where a_{kj} and b_{kj} correspond to the k^{th} degree of freedom added mass and damping coefficient resulting from motion in the j^{th} degree of freedom. Both are frequency-

dependent, where the added mass coefficient is in-phase with the motion while the latter is 90 degrees out of phase with motion. Expressed a_{kj} and b_{kj} in matrix form, it is:

$$\mathbf{F}_R = -\mathbf{a}\ddot{\xi} - \mathbf{b}\dot{\xi} \tag{C.16}$$

C.2 Linear Response Amplitude Operator (RAO)

For a lateral-symmetry (about the x-z plane) floating structure, the generalized mass matrix follows as

$$\mathbf{m} = \begin{pmatrix} m & 0 & 0 & 0 & mz_g & 0 \\ 0 & m & 0 & -mz_g & 0 & 0 \\ 0 & 0 & m & 0 & 0 & 0 \\ 0 & -mz_g & 0 & I_x & 0 & -I_{xz} \\ mz_g & 0 & 0 & 0 & I_y & 0 \\ 0 & 0 & 0 & -I_{zx} & 0 & I_z \end{pmatrix} \tag{C.17}$$

By Green's second identity, symmetric matrix of the added mass and damping coefficients with $a_{kj} = a_{jk}$ and $b_{kj} = b_{jk}$ can be applied for a zero speed ship in no current. Further details regarding the components of each coefficient are given in Faltinsen (1993) [29].

$$\mathbf{a} = \begin{pmatrix} a_{11} & 0 & a_{13} & 0 & a_{15} & 0 \\ 0 & a_{22} & 0 & a_{24} & 0 & a_{26} \\ a_{31} & 0 & a_{33} & 0 & a_{35} & 0 \\ 0 & a_{42} & 0 & a_{44} & 0 & a_{46} \\ a_{51} & 0 & a_{53} & 0 & a_{55} & 0 \\ 0 & a_{62} & 0 & a_{64} & 0 & a_{66} \end{pmatrix} \mathbf{b} = \begin{pmatrix} b_{11} & 0 & b_{13} & 0 & b_{15} & 0 \\ 0 & b_{22} & 0 & b_{24} & 0 & b_{26} \\ b_{31} & 0 & b_{33} & 0 & b_{35} & 0 \\ 0 & b_{42} & 0 & b_{44} & 0 & b_{46} \\ b_{51} & 0 & b_{53} & 0 & b_{55} & 0 \\ 0 & b_{62} & 0 & b_{64} & 0 & b_{66} \end{pmatrix} \tag{C.18}$$

Restoring force coefficient matrix $\mathbf{K}$ is as follows:

$$\mathbf{K} = \begin{pmatrix} 0 & 0 & 0 & 0 & 0 & 0 \\ 0 & 0 & 0 & 0 & 0 & 0 \\ 0 & 0 & \rho g A_{wp} & 0 & -\rho g \iint_{A_{wp}} x dA & 0 \\ 0 & 0 & 0 & \rho g \nabla \overline{GM_T} & 0 & 0 \\ 0 & 0 & -\rho g \iint_{A_{wp}} x dA & 0 & \rho g \nabla \overline{GM_L} & 0 \\ 0 & 0 & 0 & 0 & 0 & 0 \end{pmatrix} \tag{C.19}$$

With the defined coefficients, the equations of rigid-body motions having steady-state sinusoidal responses is expressed in the following form:

$$\left(-\omega^2(\mathbf{m}+\mathbf{a})+i\omega\mathbf{b}+\mathbf{K}\right)\xi=\mathbf{F_{F.K}}+\mathbf{F_{D_k}} \tag{C.20}$$

where

$$\begin{aligned}\mathbf{D}&=\left(-\omega^2(\mathbf{m}+\mathbf{a})+i\omega\mathbf{b}+\mathbf{K}\right)\\ A\mathbf{F}_{ex}&=\mathbf{F_{F.K}}+\mathbf{F_{D_k}}\end{aligned} \tag{C.21}$$

Considering the response by a sinusoidal regular wave of the amplitude A, both parts of the equation can be rearranged as terms for $e^{i\omega t}$, corresponding to the amplitude of displacement ($\mathbf{D}$) and excitation force of unit wave ($\mathbf{F}_{ex}$), respectively. Therefore, for the linear solution, it allows the application of frequency domain analysis, and practical data such as motion Response Amplitude Operator (RAO) with a specified wave frequency range and various wave direction β can be obtained.

$$\mathbf{D}\xi e^{i\omega t}=A\mathbf{F}_{ex}e^{i\omega t} \tag{C.22}$$

thus, the motion RAO in a vector matrix form is,

$$\text{Motion RAO}=\frac{\xi}{A}=\frac{\mathbf{F}_{ex}}{\mathbf{D}} \tag{C.23}$$

Similarly, wave-induced internal loads such as shear force **Q** and bending moment **M** acting on a cross section at a position x_A have the following relationship:

$$\begin{aligned}\mathbf{Q}(x_A)&=\int_{AP}^{x_A}(\mathbf{m}(x)\ddot{\xi}-\sum\mathbf{F}(x))dx\\ \mathbf{M}(x_A)&=\int_{AP}^{x_A}\mathbf{Q}(x)dx\end{aligned} \tag{C.24}$$

Thus, the internal load RAO at position x_A is,

$$\begin{aligned}\text{Shear force RAO}&=\frac{\mathbf{Q}(x_A)}{A}\\ \text{Bending moment RAO}&=\frac{\mathbf{M}(x_A)}{A}\end{aligned} \tag{C.25}$$

Appendix D

STREAM FUNCTIONS FOR REGULAR WAVES

D.1 Formulations

Considering a reference frame that moves at the constant phase velocity c, the wave flow has a steady motion with respect to the moving reference frame of (x, z) where the orientation of x and z corresponds to the direction of wave propagation and vertical upward at the free surface at rest respectively. In two-dimensional flow, a stream function corresponds to a vector field $\psi(x, z)$ satisfying:

$$\frac{\partial \psi}{\partial x} = -w \qquad \text{and} \qquad \frac{\partial \psi}{\partial z} = u \tag{D.1}$$

In addition, assuming that the fluid is irrotational, the stream function, $\psi(x, z)$, satisfies the Laplace's equation and the dynamic free surface condition:

$$\nabla^2 \psi(x, z) = 0, \tag{D.2}$$

$$g\eta + \frac{1}{2}\left[\left(\frac{\partial \psi}{\partial x}\right)^2 + \left(\frac{\partial \psi}{\partial z}\right)^2\right] = R_c, \quad \text{on } z = \eta\,, \tag{D.3}$$

where R_c is the Bernoulli constant, η is the free-surface elevation. With the consideration of a free-slip condition on the bottom ($z = -h$) and on the free surface ($z = \eta$), a streamline on each location can be defined where the variation between the two lines corresponds to the flow rate (Q). Thus, the following boundary conditions at the bottom and the free surface can be written as follows:

$$\psi(x, z = -h) = 0, \quad \psi(x, z = \eta(x)) = -Q \tag{D.4}$$

In addition, considering periodic characteristics, the mean of the free surface for one cycle corresponding to the range of 0 to λ, the wave period, in the x-axis is zero:

$$\int_0^{\lambda} \eta(x)dx = 0 \tag{D.5}$$

With an application of Fourier decomposition, η and ψ satisfying $(\mathrm{D}.2)$ and $(\mathrm{D}.4)$ at $z = -h$ can be expressed as follows:

$$\eta(x) = \frac{A_0}{2} + \sum_{n=1}^{N_2} A_n \cos\left(k_n x\right) \tag{D.6}$$

$$\psi(x,z) = B_0 z + \sum_{n=1}^{N_1} B_n \frac{\sinh\left(k_n(z+h)\right)}{\cosh\left(k_n h\right)} \cos(k_n x) \tag{D.7}$$

where A_n, B_n, and k_n correspond to the modal amplitude of the free surface elevation, the stream function, and the wave number for the n^{th} Fourier series component, respectively.

In the open-source code algorithm, the N_1 and N_2 representing the total number of modes are automatically determined considering the convergence on the amplitude of the modes introduced by Ducrozet et al. (2019) [26]. The corresponding horizontal and vertical velocity u and w can be obtained by substituting $(\mathrm{D}.7)$ into $(\mathrm{D}.1)$:

$$u(x,z) = B_0 + \sum_{n=1}^{N_2} k_n B_n \frac{\cosh(k_n(z+h))}{\cosh(k_n h)} \cos(k_n x) \tag{D.8}$$

$$w(x,z) = \sum_{n=1}^{N_2} k_n B_n \frac{\sinh(k_n(z+h))}{\cosh(k_n h)} \sin(k_n x) \tag{D.9}$$

The wave pressure $p(x,z)$ can also be expressed with the velocity components as follows:

$$\frac{p(x,z)}{\rho} = R_c - gz - \frac{1}{2}\left[(u)^2 + (w)^2\right]. \tag{D.10}$$

In the equations addressed, there are $2N_2{+}5$ (when $N_1 = N_2$) unknown components to be solved containing B_n with $n = 0$ to N_1, the modal amplitude of the stream function, η_{x_m} with $m = 0$ to N_2, the free free surface elevation, R_c, Q, and the phase velocity c. Additionally, one another unknown, which could be the wave number k or the wave period T depending on the inputs of the solution is presented. To solve the problem, not only the N_2 number of equations for dynamic and kinematic boundary conditions each, but also four additional equations related to the zero mean free surface elevation, wave height, fluid velocity, and dispersion relation (in terms of k, c, and T) have to be defined.

BIBLIOGRAPHY

[1] L Adegeest, A Braathen, and T Vada. « Evaluation of methods for estimation of extreme nonlinear ship responses based on numerical simulations and model tests ». In: *Proc. 22nd Symposium on Naval Hydrodynamics, Washington DC*. Vol. 1. 1998, pp. 70–84.

[2] Allianz Global Corporate&Specialty SE AGCS. *Safety and shipping review 2021*. 2021.

[3] X Barthelemy et al. « On a unified breaking onset threshold for gravity waves in deep and intermediate depth water ». In: *Journal of Fluid Mechanics* 841 (2018), pp. 463–488.

[4] SS Bennett, DA Hudson, and P Temarel. « A comparison of abnormal wave generation techniques for experimental modelling of abnormal wave–vessel interactions ». In: *Ocean engineering* 51 (2012), pp. 34–48.

[5] Félicien Bonnefoy et al. « Time domain simulation of nonlinear water waves using spectral methods ». In: *Advances in Numerical Simulation of Nonlinear Water Waves*. World Scientific, 2010, pp. 129–164.

[6] B Bouscasse et al. « Experimental analysis of wave-induced vertical bending moment in steep regular waves ». In: *Journal of Fluids and Structures* 111 (2022), p. 103547.

[7] Lawrence D Brown, T Tony Cai, and Anirban DasGupta. « Interval estimation for a binomial proportion ». In: *Statistical science* 16.2 (2001), pp. 101–133.

[8] Bureau Veritas. « Structural Rules for Container Ships, Rule Note NR 625 ». In: *Paris. France* (2021).

[9] Maxime Canard, Guillaume Ducrozet, and Benjamin Bouscasse. « Generation of 3-hr Long-Crested Waves of Extreme Sea States With HOS-NWT Solver ». In: *International Conference on Offshore Mechanics and Arctic Engineering*. Vol. 84386. American Society of Mechanical Engineers. 2020, V06BT06A064.

[10] Maxime Canard, Guillaume Ducrozet, and Benjamin Bouscasse. « Varying ocean wave statistics emerging from a single energy spectrum in an experimental wave tank ». In: *Ocean Engineering* 246 (2022), p. 110375.

[11] John R Chaplin. « Developments of stream-function wave theory ». In: *Coastal Engineering* 3 (1979), pp. 179–205.

[12] John R Chaplin. « On frequency-focusing unidirectional waves ». In: *International Journal of Offshore and Polar Engineering* 6.02 (1996).

[13] Zhanyang Chen, Jialong Jiao, and Hui Li. « Time-domain numerical and segmented ship model experimental analyses of hydroelastic responses of a large container ship in oblique regular waves ». In: *Applied Ocean Research* 67 (2017), pp. 78–93.

[14] Zhanyang Chen et al. « Numerical and experimental analysis of hydroelastic responses of a high-speed trimaran in oblique irregular waves ». In: *International Journal of Naval Architecture and Ocean Engineering* 11.1 (2019), pp. 409–421.

[15] Ju-hyuck Choi et al. « Intact stability analysis of dead ship conditions using FORM ». In: *Journal of Ship Research* 61.03 (2017), pp. 167–176.

[16] Günther F Clauss and Christian E Schmittner. « Experimental optimization of extreme wave sequences for the deterministic analysis of wave/structure interaction ». In: (2007).

[17] Robert G Dean. « Stream function representation of nonlinear ocean waves ». In: *Journal of Geophysical Research* 70.18 (1965), pp. 4561–4572.

[18] A Der Kiureghian. « The geometry of random vibrations and solutions by FORM and SORM ». In: *Probabilistic Engineering Mechanics* 15.1 (2000), pp. 81–90.

[19] Jesper Skjoldager Dietz. *Application of conditional waves as critical wave episodes for extreme loads on marine structures*. Technical University of Denmark, 2005.

[20] Douglas G Dommermuth and Dick KP Yue. « A high-order spectral method for the study of nonlinear gravity waves ». In: *Journal of Fluid Mechanics* 184 (1987), pp. 267–288.

[21] Ingo Drummen, MingKang Wu, and Torgeir Moan. « Experimental and numerical study of containership responses in severe head seas ». In: *Marine Structures* 22.2 (2009), pp. 172–193.

[22] Ingo Drummen, MingKang Wu, and Torgeir Moan. « Numerical and experimental investigations into the application of response conditioned waves for long-term nonlinear analyses ». In: *Marine Structures* 22.3 (2009), pp. 576–593.

[23] Guillaume Ducrozet, Mathias Fink, and Amin Chabchoub. « Time-reversal of nonlinear waves: Applicability and limitations ». In: *Physical Review Fluids* 1.5 (2016), p. 054302.

[24] Guillaume Ducrozet et al. « A comparative study of two fast nonlinear free-surface water wave models ». In: *International Journal for Numerical Methods in Fluids* 69.11 (2012), pp. 1818–1834.

[25] Guillaume Ducrozet et al. « A modified high-order spectral method for wavemaker modeling in a numerical wave tank ». In: *European Journal of Mechanics-B/Fluids* 34 (2012), pp. 19–34.

[26] Guillaume Ducrozet et al. « CN-Stream: Open-source library for nonlinear regular waves using stream function theory ». In: *arXiv preprint arXiv:1901.10577* (2019).

[27] Guillaume Ducrozet et al. « Implementation and validation of nonlinear wavemaker models in a HOS numerical wave tank ». In: *International Journal of Offshore and Polar Engineering* 16.03 (2006).

[28] Ould El Moctar et al. « Nonlinear computational methods for hydroelastic effects of ships in extreme seas ». In: *Ocean Engineering* 130 (2017), pp. 659–673.

[29] Odd Faltinsen. *Sea loads on ships and offshore structures*. Vol. 1. Cambridge university press, 1993.

[30] Francesco Fedele, Claudio Lugni, and Arun Chawla. « The sinking of the El Faro: Predicting real world rogue waves during Hurricane Joaquin ». In: *Scientific reports* 7.1 (2017), pp. 1–15.

[31] N Fonseca and C Guedes Soares. « Experimental investigation of the nonlinear effects on the statistics of vertical motions and loads of a containership in irregular waves ». In: *Journal of Ship Research* 48.02 (2004), pp. 148–167.

[32] George Z Forristall. « Wave crest distributions: Observations and second-order theory ». In: *Journal of physical oceanography* 30.8 (2000), pp. 1931–1943.

[33] Thor I Fossen. *Handbook of marine craft hydrodynamics and motion control*. John Wiley & Sons, 2011.

[34] Amin Ghadirian, Henrik Bredmose, and Signe Schløer. « Prediction of the shape of inline wave force and free surface elevation using First Order Reliability Method (FORM) ». In: *Energy Procedia* 137 (2017), pp. 162–176.

[35] Peter Friis Hansen and Lars P Nielsen. *On the new wave model for the kinematics of large ocean waves*. Tech. rep. American Society of Mechanical Engineers, New York, NY (United States), 1995.

[36] MD Haskind. « The exciting forces and wetting of ships in waves ». In: (2010).

[37] Abraham M Hasofer and Niels C Lind. « Exact and invariant second-moment code format ». In: *Journal of the Engineering Mechanics division* 100.1 (1974), pp. 111–121.

[38] Klaus Hasselmann. « Feynman diagrams and interaction rules of wave-wave scattering processes ». In: *Reviews of Geophysics* 4.1 (1966), pp. 1–32.

[39] Klaus Hasselmann et al. « Measurements of wind-wave growth and swell decay during the Joint North Sea Wave Project (JONSWAP). » In: *Ergaenzungsheft zur Deutschen Hydrographischen Zeitschrift, Reihe A* (1973).

[40] SE Hirdaris et al. « Loads for use in the design of ships and offshore structures ». In: *Ocean engineering* 78 (2014), pp. 131–174.

[41] Sa Young Hong and Byoung Wan Kim. « Experimental investigations of higher-order springing and whipping-WILS project ». In: *International Journal of Naval Architecture and Ocean Engineering* 6.4 (2014), pp. 1160–1181.

[42] Boris Horel et al. « Experimental assessment of vertical shear force and bending moment in severe sea conditions ». In: *International Conference on Offshore Mechanics and Arctic Engineering*. Vol. 58783. American Society of Mechanical Engineers. 2019, V003T02A031.

[43] Zhenjia Huang and Yu Zhang. « Semi-empirical single realization and ensemble crest distributions of long-crest nonlinear waves ». In: *International Conference on Offshore Mechanics and Arctic Engineering*. Vol. 51203. American Society of Mechanical Engineers. 2018, V001T01A032.

[44] Alison C Hunt-Raby et al. « Experimental measurement of focused wave group and solitary wave overtopping ». In: *Journal of Hydraulic Research* 49.4 (2011), pp. 450–464.

[45] January IACS. *Common structural rules for bulk carriers and oil tankers*. 2014.

[46] J Juncher Jensen. « Stochastic procedures for extreme wave load predictions–wave bending moment in ships ». In: *Marine Structures* 22.2 (2009), pp. 194–208.

[47] J Juncher Jensen. *Wave-Induced Bending Moments in Ships–A Quadratic Theory*. Tech. rep. 1978.

[48] Jørgen Juncher Jensen. « Conditional second-order short-crested water waves applied to extreme wave episodes ». In: *Journal of Fluid Mechanics* 545 (2005), pp. 29–40.

[49] Jørgen Juncher Jensen. « Second-order wave kinematics conditional on a given wave crest ». In: *Applied ocean research* 18.2-3 (1996), pp. 119–128.

[50] Jørgen Juncher Jensen and Julien Capul. « Extreme response predictions for jack-up units in second order stochastic waves by FORM ». In: *Probabilistic Engineering Mechanics* 21.4 (2006), pp. 330–337.

[51] Jørgen Juncher Jensen, Ju-hyuck Choi, and Ulrik Dam Nielsen. « Statistical prediction of parametric roll using FORM ». In: *Ocean Engineering* 144 (2017), pp. 235–242.

[52] Shinwoong Kim et al. « Numerical and experimental study of a FORM-based design wave applying the HOS-NWT nonlinear wave solver ». In: *Ocean Engineering* 263 (2022), p. 112287.

[53] Yonghwan Kim and Jung-Hyun Kim. « Benchmark study on motions and loads of a 6750-TEU containership ». In: *Ocean Engineering* 119 (2016), pp. 262–273.

[54] Marco Klein, Günther F Clauss, and Norbert Hoffmann. « Introducing envelope soliton solutions for wave–structure investigations ». In: *Ocean Engineering* 234 (2021), p. 109271.

[55] Korean Register. « Guidance on Strength Assessment of Container Ships Considering the Whipping Effect ». In: *Busan. Korea* (2017).

[56] PAK Lakshmynarayanana and Spyros Hirdaris. « Comparison of nonlinear one- and two-way FFSI methods for the prediction of the symmetric response of a containership in waves ». In: *Ocean engineering* 203 (2020), p. 107179.

[57] Bernard Le Méhauté. *An introduction to hydrodynamics and water waves*. Springer Science & Business Media, 2013.

[58] Yongwon Lee et al. « Comparison of springing and whipping responses of model tests with predicted nonlinear hydroelastic analyses ». In: *The Twenty-first International Offshore and Polar Engineering Conference*. OnePetro. 2011.

[59] Yongwon Lee et al. « Time domain analysis of springing and whipping responses acting on a large container ship ». In: *International Conference on Offshore Mechanics and Arctic Engineering*. Vol. 44380. 2011, pp. 139–147.

[60] Maurice Lemaire. *Structural reliability*. John Wiley & Sons, 2013.

[61] Yuan Lin et al. « Experimental study on the asymmetric impact loads and hydroelastic responses of a very large container ship ». In: *International Journal of Naval Architecture and Ocean Engineering* 12 (2020), pp. 226–240.

[62] Georg Lindgren. « Use and structure of Slepian model processes for prediction and detection in crossing and extreme value theory ». In: *Statistical extremes and applications*. Springer, 1984, pp. 261–284.

[63] George Lindgren. « Some properties of a normal process near a local maximum ». In: *The Annals of Mathematical Statistics* 41.6 (1970), pp. 1870–1883.

[64] Pei-Ling Liu and Armen Der Kiureghian. « Optimization algorithms for structural reliability ». In: *Structural safety* 9.3 (1991), pp. 161–177.

[65] Michael S Longuet-Higgins. « The effect of non-linearities on statistical distributions in the theory of sea waves ». In: *Journal of fluid mechanics* 17.3 (1963), pp. 459–480.

[66] S Malenica. « Hydro structure interactions in seakeeping ». In: *International Workshop on Coupled Methods in Numerical Dynamics*. 2007.

[67] Adolfo Marón and Geert Kapsenberg. « Design of a ship model for hydro-elastic experiments in waves ». In: *International Journal of Naval Architecture and Ocean Engineering* 6.4 (2014), pp. 1130–1147.

[68] John Nicholas Newman. *Marine hydrodynamics*. The MIT press, 2018.

[69] Jorge Nocedal and Stephen Wright. *Numerical optimization*. Springer Science & Business Media, 2006.

[70] Jan Oberhagemann, Vladimir Shigunov, and Ould el Moctar. « Application of CFD in long-term extreme value analyses of wave loads ». In: *Ship Technology Research* 59.3 (2012), pp. 4–22.

[71] Willard J Pierson Jr and Lionel Moskowitz. « A proposed spectral form for fully developed wind seas based on the similarity theory of SA Kitaigorodskii ». In: *Journal of geophysical research* 69.24 (1964), pp. 5181–5190.

[72] Alessio Pipinato. *Innovative bridge design handbook: Construction, rehabilitation and maintenance*. Elsevier, 2021.

[73] Eliot Quon et al. « Application of the most likely extreme response method for wave energy converters ». In: *International Conference on Offshore Mechanics and Arctic Engineering*. Vol. 49972. American Society of Mechanical Engineers. 2016, V006T09A022.

[74] Rüdiger Rackwitz and Bernd Flessler. « Structural reliability under combined random load sequences ». In: *Computers & structures* 9.5 (1978), pp. 489–494.

[75] Suresh Rajendran, Nuno Fonseca, and C Guedes Soares. « A numerical investigation of the flexible vertical response of an ultra large containership in high seas compared with experiments ». In: *Ocean Engineering* 122 (2016), pp. 293–310.

[76] Michelle M Rienecker and John D Fenton. « A Fourier approximation method for steady water waves ». In: *Journal of fluid mechanics* 104 (1981), pp. 119–137.

[77] Reuven Y Rubinstein and Dirk P Kroese. *Simulation and the Monte Carlo method*. John Wiley & Sons, 2016.

[78] SRd Santos, LC Matioli, and AT Beck. « New optimization algorithms for structural reliability analysis ». In: *Computer Modeling in Engineering & Sciences(CMES)* 83.1 (2012), pp. 23–55.

[79] Hemming A Schäffer. « Second-order wavemaker theory for irregular waves ». In: *Ocean Engineering* 23.1 (1996), pp. 47–88.

[80] Christian Schmittner and Janou Hennig. « Optimization of short-crested deterministic wave sequences via a phase-amplitude iteration scheme ». In: *International Conference on Offshore Mechanics and Arctic Engineering*. Vol. 44922. American Society of Mechanical Engineers. 2012, pp. 79–86.

[81] Christian Schmittner, Sascha Kosleck, and Janou Hennig. « A phase-amplitude iteration scheme for the optimization of deterministic wave sequences ». In: *International Conference on Offshore Mechanics and Arctic Engineering*. Vol. 43468. 2009, pp. 653–660.

[82] Betsy R Seiffert and Guillaume Ducrozet. « Simulation of breaking waves using the high-order spectral method with laboratory experiments: wave-breaking energy dissipation ». In: *Ocean Dynamics* 68.1 (2018), pp. 65–89.

[83] Betsy R Seiffert, Guillaume Ducrozet, and Félicien Bonnefoy. « Simulation of breaking waves using the high-order spectral method with laboratory experiments: Wave-breaking onset ». In: *Ocean Modelling* 119 (2017), pp. 94–104.

[84] Kevin M Silva and Kevin J Maki. « Towards a computational fluid dynamics implementation of the critical wave groups method ». In: *Ocean Engineering* 235 (2021), p. 109451.

[85] Shamika N Sirimanne et al. « Review of maritime transport 2019 ». In: *United Nations conference on trade and development, Geneva, Switzerland*. 2019.

[86] Mohammed Khair Al-Solihat and Meyer Nahon. « Stiffness of slack and taut moorings ». In: *Ships and Offshore Structures* 11.8 (2016), pp. 890–904.

[87] Pierre Suret et al. « Nonlinear spectral synthesis of soliton gas in deep-water surface gravity waves ». In: *Physical Review Letters* 125.26 (2020), p. 264101.

[88] Pandeli Temarel et al. « Prediction of wave-induced loads on ships: Progress and challenges ». In: *Ocean Engineering* 119 (2016), pp. 274–308.

[89] Zhigang Tian, Marc Perlin, and Wooyoung Choi. « Energy dissipation in two-dimensional unsteady plunging breakers and an eddy viscosity model ». In: *Journal of fluid mechanics* 655 (2010), pp. 217–257.

[90] Peter S Tromans, Ali R Anaturk, and Paul Hagemeijer. « A new model for the kinematics of large ocean waves-application as a design wave ». In: *The first international offshore and polar engineering conference*. OnePetro. 1991.

[91] Guillermo Vásquez, Nuno Fonseca, and Carlos Guedes Soares. « Experimental and numerical vertical bending moments of a bulk carrier and a roll-on/roll-off ship in extreme waves ». In: *Ocean Engineering* 124 (2016), pp. 404–418.

[92] Bureau Veritas. « Guidance for long-term hydro-structure calculations ». In: *Rule Note NI 638 DT R00 E* (2019).

[93] Bureau Veritas. « Hydrostar for experts user manual ». In: *Bureau Veritas* (2016).

[94] Bureau Veritas. « Structural rules for container ships ». In: *Rule Note NR625 DT R04 E* (2020).

[95] Det Norske Veritas. « Recommended practice DNV-RP-C205: environmental conditions and environmental loads ». In: *DNV, Norway* (2010).

[96] Daniel AG Walker, Paul H Taylor, and R Eatock Taylor. « The shape of large surface waves on the open sea and the Draupner New Year wave ». In: *Applied Ocean Research* 26.3-4 (2004), pp. 73–83.

[97] Daniel AG Walker and R Eatock Taylor. « Wave diffraction from linear arrays of cylinders ». In: *Ocean Engineering* 32.17-18 (2005), pp. 2053–2078.

[98] Peter Welch. « The use of fast Fourier transform for the estimation of power spectra: a method based on time averaging over short, modified periodograms ». In: *IEEE Transactions on audio and electroacoustics* 15.2 (1967), pp. 70–73.

[99] Bruce J West et al. « A new numerical method for surface hydrodynamics ». In: *Journal of Geophysical Research: Oceans* 92.C11 (1987), pp. 11803–11824.

[100] Vladimir E Zakharov. « Stability of periodic waves of finite amplitude on the surface of a deep fluid ». In: *Journal of Applied Mechanics and Technical Physics* 9.2 (1968), pp. 190–194.

[101] Jun Zang et al. « Steep wave and breaking wave impact on offshore wind turbine foundations–ringing re-visited ». In: *25th International Workshop on Water Waves and Floating Bodies*. 2010, pp. 9–12.

[102] Suji Zhu, MingKang Wu, and Torgeir Moan. « Experimental and numerical study of wave-induced load effects of open ships in oblique seas ». In: *Journal of ship research* 55.02 (2011), pp. 100–123.

Titre : Étude expérimentale sur les moments de flexion des vagues sur un modèle de porteconteneurs rigide à vitesse nulle dans des vagues régulières, irrégulières et focalisées

Mots clés : Expérimentation, Modèle rigide, Moments de flexion des vagues, HOS-NWT, FORM

Résumé : La thèse vise à étudier les mouvements et les chargements internes d'un modèle de porte-conteneur rigide formé de 9 segments dans des vagues extrêmes. L'étude est principalement expérimentale et est réalisée avec une maquette sans vitesse d'avance dans une houle de face et une houle oblique (-120 degrés). L'étude aboutit à des résultats soulignant l'importance de la prendre en compte les aspects non linéaires des vagues et des réponses structurelles correspondantes.
Dans des conditions de mer de face, trois types de vagues sont testés. Des vagues régulières sont utilisées pour s'assurer que le modèle se comporte de manière similaire à la campagne précédente effectuée avec la même maquette. Une approche de type Monte Carlo avec un certain nombre de réalisations de 2 heures 30 de vagues irrégulières est ensuite utilisée pour construire des données de référence. Enfin, des vagues equivalentes de design (EDW) sont générées pour vérifier, en particulier, la faisabilité d'une approche EDW irrégulière appelée First Order Reliability Method (FORM). Un algorithme numérique FORM couplé avec le solveur HOSNWT est développé et validé par rapport aux résultats Monte Carlo. Les caractéristiques géométriques des signaux EDW et VBM ainsi que leurs statistiques sont étudiées. L'étude vise peut-être deux quantités. Le premier est la hauteur de crête de la vague dans un scénario de vague seule, et le second est le VBM du modèle segmenté. L'utilisation du solveur de génération d'onde non linéaire HOS-NWT, permet une validation croisée avec la mesure expérimentale car les vagues générées sont comparables. Dans la condition de vagues obliques, l'étude est limitée aux vagues régulières avec différentes cambrure de vagues afin de fournir des données de référence pour les futures études. L'effet de non-linéarité des vagues sur les moments de flexion horizontaux et verticaux des vagues avec une cambrure variable est démontré.

Title : Experimental study on wave bending moments of a zero-speed rigid containership model in regular, irregular, and equivalent design waves

Keywords : Experiment, Rigid model, Wave bending moments, HOS-NWT, FORM

Abstract : The present thesis aims to study the motions and the internal loads of a 9-segmented rigid containership model in extreme waves. The study is mainly experimental and is carried out on a zero-speed model in a 180-degree head sea and a -120 degree oblique sea. The study leads to results highlighting the importance of the consideration of nonlinear wave descriptions and corresponding nonlinear structural responses.
In head sea conditions, three wave approaches are considered. Regular waves are used to ensure that the model behaves similar to the earlier campaign. A Monte Carlo approach with a number of full scale 2h30 irregular wave realizations is used to have reference data. Finally, irregular equivalent design waves (EDW) are studied to check, in particular, the feasibility of one irregular EDW approach called First Order Reliability Method. A numerical algorithm coupling with the HOS-NWT for the FORM EDW is developed and the validation compared to the Monte Carlo results is performed in terms of geometrical characteristics of the EDW and IW signals along with their statistics. The study targets mainly two quantities. The first is the wave crest in a wave-only scenario, and the second is the VBM of the segmented model. The use of the HOSNWT, a nonlinear wave generation solver, enables cross-validation with experimental measurement.
In the oblique wave condition, the study is limited to regular waves with various wave steepness with the intent to provide reference data for future benchmark studies. The wave nonlinearity effect on the horizontal and vertical wave bending moments with varying steepness is shown.